Study of Time Evolution of B Mesons at the KEK B Factory

Tomonobu Tomura

Department of Physics, University of Tokyo

December 2002

Abstract

We report measurements of B meson lifetimes, B^0-$\overline{B}^0$ mixing parameter Δm_d, and CP violation parameter $\sin 2\phi_1$ at the KEK B-Factory experiment. A total of 85×10^6 $B\overline{B}$ pairs produced by the KEKB accelerator are recorded by the Belle detector. Using a partial data sample of 31.3×10^6 $B\overline{B}$ pairs, we reconstruct 7863 neutral and 12047 charged B candidates which decay to several hadronic modes. A fit to the proper decay time differences of neutral and charged B meson pairs yields

$$\begin{aligned} \tau_{B^0} &= 1.554 \pm 0.030(\text{stat}) \pm 0.019(\text{syst})\ \text{ps}, \\ \tau_{B^+} &= 1.695 \pm 0.026(\text{stat}) \pm 0.015(\text{syst})\ \text{ps}, \\ \tau_{B^+}/\tau_{B^0} &= 1.091 \pm 0.023(\text{stat}) \pm 0.014(\text{syst}). \end{aligned}$$

Using the same data sample, we reconstruct 6660 neutral B candidates which decay to flavor-specific hadronic modes, while the flavor of the other is identified from its decay products. From the distributions of proper decay time difference of same- and opposite-flavor B meson pairs, we obtain

$$\Delta m_d = 0.528 \pm 0.017(\text{stat}) \pm 0.011(\text{syst})\ \text{ps}^{-1}.$$

Finally, using the whole data sample, we reconstruct 2958 neutral B candidates which decay to CP eigenstates. From the asymmetry in the distribution of the proper decay time difference, we obtain

$$\sin 2\phi_1 = 0.719 \pm 0.074(\text{stat}) \pm 0.035(\text{syst}).$$

With the data presented in this thesis, we have proved that the Kobayashi-Maskawa mechanism is correct at the electroweak scale.

Acknowledgements

First, I would like to express my great appreciation to my supervisor, Prof. H. Aihara, for giving me an opportunity for these analyses and for his great supervision.

I greatly appreciate Hiroyasu Tajima for giving me a lot of advice. I learned the basic skills for the high energy physics from him.

I would like to thank Masako Iwasaki for the helpful advice.

I am grateful to all the students and OBs of Aihara group: Dr. T. Higuchi, Dr. J. Tanaka, Dr. M. Yokoyama, T. Nakadaira, T. Matsubara, H. Kawai, N. Uozaki, Y. Yamashita, A. Kusaka, K. Tanabe, and R. Ishida.

I would like to express my gratitude to Prof. M. Hazumi and Prof. Y. Sakai for their great leadership in the ICPV group. I thank all the members of the CP-fit and relevant groups for their great teamwork.

Finally, I appreciate all the members of the Belle collaboration and the KEKB accelerator for keeping the good performance of the detector and the high luminosity. Without these excellent conditions of the experiment, this work could not have been completed.

Contents

List of Figures

List of Tables

Chapter 1

Introduction

We live in a universe dominated by matter, containing very little antimatter. In the Big-Bang model, however, the matter and antimatter were created in the equal amounts. Then, where have the antimatters gone?

In 1967, Sakharov showed that three conditions are necessary to explain the dominance of matter over antimatter in the universe [1]:

- The baryon number changing processes in the early universe;
- The violation of CP symmetry (and C symmetry); and
- The out-of-equilibrium situation for the universe.

Here, C and P denote the charge-conjugation and parity-transformation operators, respectively. The charge-conjugation C is not considered to be the transition between matter and antimatter. For instance, we consider the process of the charged pion decaying to the muon and neutrino:

$$\pi^+ \to \mu^+ \nu_\mu. \tag{1.1}$$

The charge conjugation of above process is

$$\pi^- \to \mu^- \overline{\nu}_\mu^L, \tag{1.2}$$

where $\overline{\nu}_\mu^L$ is the left-handed antineutrino and it is not observed in nature. Applying the additional parity transformation to the above, we obtain

$$\pi^- \to \mu^- \overline{\nu}_\mu, \tag{1.3}$$

where $\overline{\nu}_\mu$ is the right-handed antineutrino that is observed in nature. Thus, CP is considered to be the transition between matter and antimatter rather than C itself. Therefore, the CP violation represents the difference between matter and antimatter. The CP violation is one of the most important ingredients of Sakharov's condition and the key to understanding the evolution of the universe.

Although weak interactions are neither invariant under P, nor invariant under C, it was originally believed that the product CP was preserved. For example, the CP transformation to the decay of charged pion described above makes sense and there seems to be no difference between π^+ and π^- decays. However, CP violation was discovered by Christenson *et al.* in the neutral K-meson decays in 1964 [2].

The first theory of the "quark" model was proposed by Gell-Mann in 1964 [3]. This proposal included three "flavors" of quarks: up (u), down (d), and strange (s). Citing the paper written by Cabibbo in 1963 [4], the mixing of the quark flavors was introduced. This theory could explain the weak interactions known at that time with a single coupling constant. In 1970, Glashow, Iliopoulos, and Maiani proposed the fourth flavor of the quark: charm (c) [5]. This theory, which is known as the "GIM mechanism", could explain the suppression of the strangeness-changing neutral weak current, such as $K^0 \to \mu^+\mu^-$. However, these theories still could not explain the CP violation.

Many theoretical attempts to explain the CP violation have been made since its discovery. In 1973, Kobayashi and Maskawa pointed out that a three-generation generalization of the Cabibbo structure gave a theory that allowed CP violation [6]. This meant that at least six flavors of quarks are required to violate CP in the existing framework of the theory, though only three flavors of quarks had experimentally been observed at that time. This predictive theory became reliable as the last three flavors of quarks had been discovered: The fourth flavor, c, was discovered in 1975 [7] as a new resonance J/ψ, which was quickly identified as a $c\bar{c}$ meson. The fifth flavor, bottom (b), was discovered in 1977 [8] as a $b\bar{b}$ meson Υ. Finally, the sixth flavor, top (t), was discovered in 1995 [9]. Now this three-generation quark model is called the "Standard Model" (SM) and has been extremely successful at explaining all forms of elementary particle interactions.

Then the verification of Kobayashi-Maskawa (KM) mechanism came to the next stage: the precise determination of the quark-mixing matrix elements and the check for the phenomena that are predicted by SM but are not measured precisely or have not been observed. In 1981, Bigi, Carter, and Sanda pointed out that the large CP violation in the B meson system is possible in the framework of SM [10]. Since the B meson includes the third-generation quark b, measurements of many properties of the B decays will produce a lot of useful information about the mixing-matrix elements.

The measurements of B decays started after the $\Upsilon(4S)$, which decays to a $B\overline{B}$ pair almost all the time, had been discovered by the CLEO and CUSB collaborations at CESR [11]. Many branching fractions of B meson decays have been measured at the $\Upsilon(4S)$ resonance with the e^+e^- colliders by the CLEO collaboration at CESR and ARGUS collaboration at DORIS. The key discovery that makes B physics more interesting is the long lifetime of the B mesons by the MAC collaboration at PEP [12]. Another key discovery is the B^0-$\overline{B}^0$ oscillation by the ARGUS collaboration [13]. The lifetimes and mixing of B mesons have also been measured with the $z \to b\bar{b}$ events at the e^+e^- and hadron colliders by the ALEPH, DELPHI, and OPAL collaborations at LEP, SLD collaboration at SLC, and CDF collaboration at Tevatron.

The new B-Factory experiment is designed to measure the CP violation in the B-meson system precisely: It produces the high statistics of B decays with low backgrounds, and these B mesons are produced as the $B\overline{B}$ pairs in the coherent state. By employing the asymmetric-energy e^+e^- collider, the produced $B\overline{B}$ pairs are made to move along the beam direction in the laboratory frame. In 1999, two such experiments began their operations at High Energy Accelerator Research Organization (KEK) in Japan and Stanford Linear Accelerator Center (SLAC) in US. Both accelerators are operated at the $\Upsilon(4S)$ energy with the high luminosity. Almost half of the $\Upsilon(4S)$ decays to the neutral B-meson pair and the other half to the charged B-meson pair. Since the produced B-meson pair is boosted in the laboratory frame because of the asymmetric energy of the collider, the decay-time difference between two B mesons corresponds to the separation between the B-decay positions along the beam axis. Using the detectors which have the high position-resolution, we can observe the time evolution of B mesons and can extract many quantities related to the SM parameters.

In this thesis, using the data collected with the Belle detector at the KEKB asymmetric e^+e^- collider, we present the measurements of the three important quantities of B mesons: the B meson lifetimes, the oscillation frequency Δm_d for the B^0-$\overline{B}^0$ mixing, and the CP violation parameter $\sin 2\phi_1$. All these are related with the quark-mixing matrix elements and the measurements of these quantities provide a good test for the validity of SM.

The outline of this thesis is as follows: The theoretical description for the B decays is given in Chapter 2. The experimental apparatus, the KEKB accelerator and the Belle detector, is described in Chapter 3. The reconstruction procedure for the candidate hadronic B decays is explained in Chapter 4. The measurements of the B meson lifetimes, the B^0-$\overline{B}^0$ oscillation frequency Δm_d, and the CP violation parameter $\sin 2\phi_1$ are described in Chapter 5, 6, and 7, respectively. Finally, we conclude in Chapter 8.

Chapter 2

Phenomenology of B mesons

In this chapter, we briefly introduce the theoretical framework for the analyses described in this thesis. First, we describe the KM mechanism, which is the most essential part of SM. Next, we mention the lifetimes of B mesons. The mixing of neutral B mesons is reviewed. Then, we illustrate the mixing-induced CP violation in the B-meson system. Finally, the experimental approach for the measurements of these parameters and the experimental constraints on the KM mechanism are described.

2.1 CKM Matrix and Unitarity Triangle

The Cabibbo-Kobayashi-Maskawa (CKM) matrix [4, 6] connects the electroweak eigenstates (d', s', b') of the down, strange, and bottom quarks with their mass eigenstates (d, s, b) through the following unitary transformation:

$$\begin{pmatrix} d' \\ s' \\ b' \end{pmatrix} = \mathbf{V} \begin{pmatrix} d \\ s \\ b \end{pmatrix} = \begin{pmatrix} V_{ud} & V_{us} & V_{ub} \\ V_{cd} & V_{cs} & V_{cb} \\ V_{td} & V_{ts} & V_{tb} \end{pmatrix} \begin{pmatrix} d \\ s \\ b \end{pmatrix}. \tag{2.1}$$

The elements of the CKM matrix describe the charged-current couplings, as can be seen by expressing the non-leptonic charged-current interaction Lagrangian $\mathcal{L}_{\mathrm{int}}^{\mathrm{CC}}$ in terms of the mass eigenstates appearing in Eq. (2.1):

$$\mathcal{L}_{\mathrm{int}}^{\mathrm{CC}} = -\frac{g_2}{\sqrt{2}} \begin{pmatrix} \bar{u}_{\mathrm{L}}, & \bar{c}_{\mathrm{L}}, & \bar{t}_{\mathrm{L}} \end{pmatrix} \gamma^{\mu} \mathbf{V} \begin{pmatrix} d_{\mathrm{L}} \\ s_{\mathrm{L}} \\ b_{\mathrm{L}} \end{pmatrix} W_{\mu}^{+} + \mathrm{h.c.}, \tag{2.2}$$

where the gauge coupling g_2 is related to the gauge group $SU(2)_{\mathrm{L}}$. Applying the CP operator to Eq. (2.2), we obtain

$$CP(\mathcal{L}_{\mathrm{int}}^{\mathrm{CC}}) = -\frac{g_2}{\sqrt{2}} \left(\overline{u}_{\mathrm{L}}, \quad \overline{c}_{\mathrm{L}}, \quad \overline{t}_{\mathrm{L}}\right) \gamma^\mu \mathbf{V}^* \begin{pmatrix} d_{\mathrm{L}} \\ s_{\mathrm{L}} \\ b_{\mathrm{L}} \end{pmatrix} W_\mu^+ + \mathrm{h.c.}, \tag{2.3}$$

which is identical to Eq. (2.2) except for the complex conjugation on $\mathbf{V}$. Therefore, CP is a good symmetry only if we could find a basis where all the elements of $\mathbf{V}$ are real.

The general $N \times N$ complex matrix has $2N^2$ real parameters. Since the unitarity conditions $\sum_j V_{ij} V_{kj}^* = \delta_{ik}$ offer $N(N-1)/2$ complex ($i \neq k$) and N real ($i = k$) constraints, the $N \times N$ unitary matrix has N^2 real parameters. For the N-generation quark-mixing matrix, since we can absorb a relative phase in each left-handed quark field except for one overall phase, we can reduce $2N-1$ parameters. Thus, N-generation quark-mixing matrix is described by $(N-1)^2$ independent parameters. The real rotation of N dimensions has $N(N-1)/2$ Euler-type angles and the remaining $(N-1)(N-2)/2$ parameters are the irreducible complex phases. In SM, since there are three generations, $\mathbf{V}$ has three Euler angles and one complex phase. If this phase has a non-zero value, CP can be violated.

There are many parameterization to describe the CKM matrix. The most popular one is the Wolfenstein parameterization [14], which is a power-series expansion in the real parameter $\lambda = \sin\theta_{\mathrm{C}} \simeq 0.22$, where θ_{C} is called Cabibbo angle [4]. Up to $\mathcal{O}(\lambda^3)$, it is expressed as

$$\mathbf{V} = \begin{pmatrix} 1 - \frac{1}{2}\lambda^2 & \lambda & A\lambda^3(\rho - i\eta) \\ -\lambda & 1 - \frac{1}{2}\lambda^2 & A\lambda^2 \\ A\lambda^3(1 - \rho - i\eta) & -A\lambda^2 & 1 \end{pmatrix} + \mathcal{O}(\lambda^4), \tag{2.4}$$

where A, ρ, and η are the real parameters and are of order one.

The unitarity conditions for off-diagonal elements, $\sum_j V_{ij} V_{kj}^* = \sum_j V_{ji}^* V_{jk} = 0$ ($i \neq k$), which show that a sum of three complex numbers equals zero, describe a triangle in the complex plane:

$$V_{ud}V_{cd}^* + V_{us}V_{cs}^* + V_{ub}V_{cb}^* = 0, \tag{2.5}$$
$$V_{ud}V_{us}^* + V_{cd}V_{cs}^* + V_{td}V_{ts}^* = 0, \tag{2.6}$$
$$V_{td}V_{cd}^* + V_{ts}V_{cs}^* + V_{tb}V_{cb}^* = 0, \tag{2.7}$$
$$V_{us}V_{ub}^* + V_{cs}V_{cb}^* + V_{ts}V_{tb}^* = 0, \tag{2.8}$$
$$V_{td}V_{ud}^* + V_{ts}V_{us}^* + V_{tb}V_{ub}^* = 0, \tag{2.9}$$
$$V_{ud}V_{ub}^* + V_{cd}V_{cb}^* + V_{td}V_{tb}^* = 0. \tag{2.10}$$

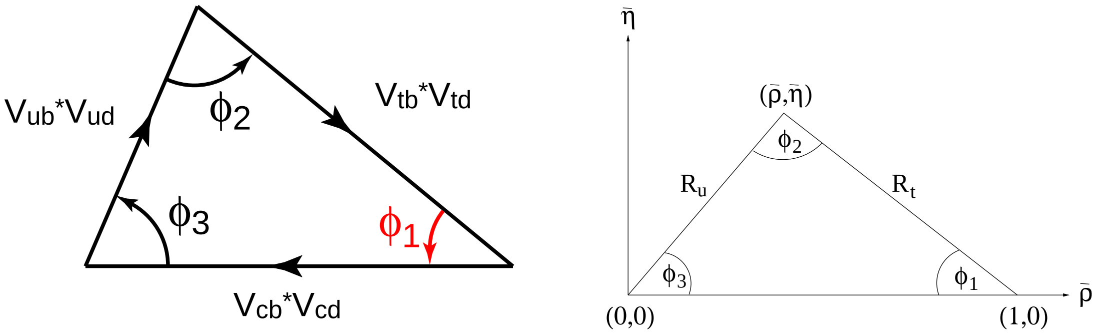

Figure 2.1: Unitarity triangle defined by Eq. (2.10) (left) and the rescaled unitarity triangle in the $\overline{\rho}$-$\overline{\eta}$ plane (right).

The first four triangles have one side much smaller than the other two sides by $\mathcal{O}(\lambda^4)$ or $\mathcal{O}(\lambda^2)$. The remaining two triangles have three sides of the same order $\mathcal{O}(\lambda^3)$. The last equation is the one that is typically used to pictorially represent the irreducible CP violating phase as shown in Fig. 2.1 (left) and is referred to as the "Unitarity Triangle". By dividing all the sides of this triangle by $V_{cd}V_{cb}^*$, the triangle is rescaled so that one side is aligned to the real axis and its length is normalized to one. Then the coordinates of the vertices of the triangle become $(0,0)$, $(1,0)$, and $(\overline{\rho},\overline{\eta})$, where $\overline{\rho}$ and $\overline{\eta}$ are represented using the Wolfenstein parameterization as [15]

$$\overline{\rho} = \left(1 - \frac{\lambda^2}{2}\right)\rho, \qquad \overline{\eta} = \left(1 - \frac{\lambda^2}{2}\right)\eta. \tag{2.11}$$

The normalized unitarity triangle in the $\overline{\rho}$-$\overline{\eta}$ plane is shown in Fig. 2.1 (right).

The lengths of the two sides of the normalized unitarity triangle that are not on the real ($\overline{\rho}$) axis are given by

$$R_u \equiv \frac{|V_{ud}V_{ub}^*|}{|V_{cd}V_{cb}^*|} = \sqrt{\overline{\rho}^2 + \overline{\eta}^2} = \left(1 - \frac{\lambda^2}{2}\right)\frac{1}{\lambda}\left|\frac{V_{ub}}{V_{cb}}\right|, \tag{2.12}$$

$$R_t \equiv \frac{|V_{td}V_{tb}^*|}{|V_{cd}V_{cb}^*|} = \sqrt{(1-\overline{\rho})^2 + \overline{\eta}^2} = \frac{1}{\lambda}\left|\frac{V_{td}}{V_{cb}}\right|. \tag{2.13}$$

The three angles of the triangle are defined as [16] [1]

$$\phi_1 \equiv \pi - \arg\left(\frac{-V_{td}V_{tb}^*}{-V_{cd}V_{cb}^*}\right), \tag{2.14}$$

$$\phi_2 \equiv \arg\left(\frac{V_{td}V_{tb}^*}{-V_{ud}V_{ub}^*}\right), \tag{2.15}$$

$$\phi_3 \equiv \arg\left(\frac{V_{ud}V_{ub}^*}{-V_{cd}V_{cb}^*}\right). \tag{2.16}$$

[1] Another naming convention, $\beta(=\phi_1)$, $\alpha(=\phi_2)$, and $\gamma(=\phi_3)$, is also used in the literature.

The measurements of these angles as well as the lengths of the sides of the unitarity triangle are the crucial tests of the CKM picture of the CP violation.

2.2 Lifetime

In general, the decay of any particular particle is a random process, but we can describe the average evolution for an ensemble of many particles. Its population decreases at a constant fractional rate. Introducing the decay rate Γ, the population at time t, $N(t)$, satisfies the following differential equation:

$$\frac{d}{dt}N(t) = -\Gamma N(t). \tag{2.17}$$

The solution of this equation is

$$N(t) = N(0)e^{-\Gamma t}. \tag{2.18}$$

The decay rate Γ is also called the "decay width" and we define the lifetime τ as

$$\tau \equiv \frac{1}{\Gamma}. \tag{2.19}$$

It corresponds to the time that it takes for $(1 - 1/e) \sim 64\%$ of the population to decay. Then, the probability density function for a particle created at $t = 0$ to decay at time t, $P(t)$, is expressed as

$$P(t) = \Gamma e^{-\Gamma t} = \frac{1}{\tau}e^{-\frac{t}{\tau}}. \tag{2.20}$$

The decay width of the b hadron is dominated by the total width of the b quark. Naively, on the analogy of the muon lifetime τ_μ:

$$\frac{1}{\tau_\mu} = \Gamma_\mu = \frac{G_F^2}{192\pi^3}m_\mu^5, \tag{2.21}$$

the lifetime of the b hadron, τ_b, where the dominant contribution is the $b \to c$ transition, can be expected to be

$$\frac{1}{\tau_b} = \Gamma_b \sim \frac{G_F^2}{192\pi^3}m_b^5|V_{cb}|^2 \times (2 \times 3 + 3), \tag{2.22}$$

where the factor of 2×3 comes from two hadronic channels at quark level ($W^- \to \overline{c}s$ and $\overline{u}d$), each with three colors, and the additional factor of three from three leptonic channels ($W^- \to e^-\overline{\nu}_e$, $\mu^-\overline{\nu}_\mu$, and $\tau^-\overline{\nu}_\tau$).

The total width is related to the partial width of a specific channel in terms of the branching fraction for that channel. For example, using this relation for the semileptonic decays, τ_b can be expressed as

$$\tau_b = \frac{1}{\Gamma_b} = \frac{\mathrm{Br}_{\mathrm{SL}}}{\Gamma_{\mathrm{SL}}}, \tag{2.23}$$

where Γ_{SL} and $\mathrm{Br}_{\mathrm{SL}}$ are the partial width and the branching fraction for the semileptonic b-decays. Γ_{SL} can be theoretically calculated with the very few uncertainties and $\mathrm{Br}_{\mathrm{SL}}$ can be experimentally measured precisely. From a theoretical calculation for the Γ_{SL} in SM, in as much as b quarks only decay into u and c quarks, τ_b can be expressed with a combination of $|V_{ub}|^2$ and $|V_{cb}|^2$ as [17]

$$\tau_b = \frac{\mathrm{Br}_{\mathrm{sl}}}{\Gamma_{\mathrm{sl}}} = \frac{\mathrm{Br}_{\mathrm{sl}}}{\frac{G_{\mathrm{F}}^2 m_b^5}{192\pi^3}\left[F(\epsilon_u)|V_{ub}|^2 + F(\epsilon_c)|V_{cb}|^2\right]} \tag{2.24}$$

where $\epsilon_q \equiv m_q/m_b$ and $F(\epsilon)$ is the phase space factor given by

$$F(\epsilon) = 1 - 8\epsilon^2 + \epsilon^6 - \epsilon^8 - 24\epsilon^4 \ln \epsilon. \tag{2.25}$$

Since $|V_{ub}|^2 \ll |V_{cb}|^2$ as shown in Eq. (2.4), τ_b is mainly a measurement of $|V_{cb}|^2$.

Above discussion is based on the spectator model, in which we assume that the lighter quark in the meson (d for B^0 and u for B^+) is not involved in the decay dynamics. This model, however, cannot explain the difference between the lifetimes of B^0 and B^+. In the framework of Heavy Quark Expansion (HQE) [18], the B lifetime ratio τ_{B^+}/τ_{B^0} is predicted to be equal to one, up to small corrections proportional to $1/m_b^3$ [19]:

$$\frac{\tau_{B^+}}{\tau_{B^0}} = 1 + \mathcal{O}(m_b^{-3}). \tag{2.26}$$

These corrections come from the effects beyond the spectator model, such as Pauli interference and W-exchange. Thus, the ratio of the lifetimes is sensitive to the effects beyond the spectator model and the experimental measurement gives the constraint to the theoretical predictions.

2.3 B^0-$\overline{B}^0$ Mixing

The neutral B meson can mix with its antiparticle through the second order weak interactions called "box diagrams" shown in Fig. 2.2.

An arbitrary linear combination of the neutral B-meson flavor eigenstates $|B^0\rangle$ and $|\overline{B}^0\rangle$,

$$|\Psi(t)\rangle = a(t)|B^0\rangle + b(t)|\overline{B}^0\rangle = \begin{pmatrix} a \\ b \end{pmatrix}, \tag{2.27}$$

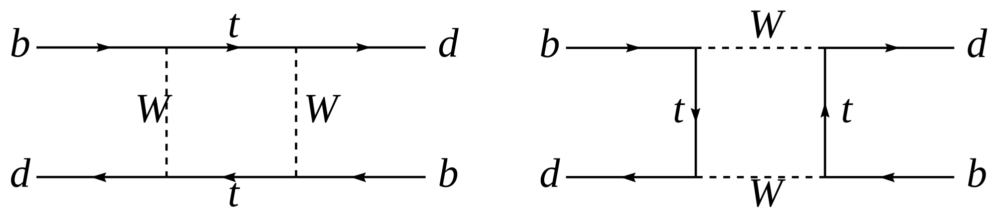

Figure 2.2: Box diagrams for the B^0-B^0 mixing.

is governed by a time-dependent Schrödinger equation:

$$i\frac{\partial}{\partial t}\begin{pmatrix} a \\ b \end{pmatrix} = \mathbf{H}\begin{pmatrix} a \\ b \end{pmatrix} \equiv \left(\mathbf{M} - \frac{i}{2}\mathbf{\Gamma}\right)\begin{pmatrix} a \\ b \end{pmatrix}, \tag{2.28}$$

where $\mathbf{M}$ and $\mathbf{\Gamma}$ are 2×2 Hermitian matrices. Since they are Hermitian matrices, it is required to be $M_{21} = M_{12}^*$ and $\Gamma_{21} = \Gamma_{12}^*$. The CPT symmetry requires $M_{11} = M_{22} \equiv M$ and $\Gamma_{11} = \Gamma_{22} \equiv \Gamma$. Then the eigenvalues λ_+ and λ_- of this Hamiltonian are obtained as

$$\lambda_\pm = M - \frac{i}{2}\Gamma \pm \sqrt{\left(M_{12} - \frac{i}{2}\Gamma_{12}\right)\left(M_{12}^* - \frac{i}{2}\Gamma_{12}^*\right)}. \tag{2.29}$$

The eigenvectors are described as

$$|B_1\rangle = p\big|B^0\big\rangle + q\big|\overline{B}^0\big\rangle \quad \text{for } \lambda_+, \tag{2.30}$$

$$|B_2\rangle = p\big|B^0\big\rangle - q\big|\overline{B}^0\big\rangle \quad \text{for } \lambda_-, \tag{2.31}$$

where

$$|p|^2 + |q|^2 = 1, \tag{2.32}$$

$$\frac{q}{p} = \sqrt{\frac{M_{12}^* - \frac{i}{2}\Gamma_{12}^*}{M_{12} - \frac{i}{2}\Gamma_{12}}}. \tag{2.33}$$

The mass and width of each mass eigenstate are given as

$$m_1 = \mathrm{Re}\lambda_+, \qquad \Gamma_1 = -2\mathrm{Im}\lambda_+, \tag{2.34}$$

$$m_2 = \mathrm{Re}\lambda_-, \qquad \Gamma_2 = -2\mathrm{Im}\lambda_-. \tag{2.35}$$

Then we define the mass and width differences as

$$\Delta m_d \equiv m_2 - m_1 = -2\mathrm{Re}\left[\frac{q}{p}\left(M_{12} - \frac{i}{2}\Gamma_{12}\right)\right], \tag{2.36}$$

$$\Delta\Gamma_d \equiv \Gamma_1 - \Gamma_2 = -4\mathrm{Im}\left[\frac{q}{p}\left(M_{12} - \frac{i}{2}\Gamma_{12}\right)\right]. \tag{2.37}$$

Δm_d and $\Delta\Gamma_d$ satisfy

$$\Delta m_d{}^2 - \frac{1}{4}\Delta\Gamma_d{}^2 = 4|M_{12}|^2 - |\Gamma_{12}|^2, \tag{2.38}$$
$$\Delta m_d \Delta\Gamma_d = -4\mathrm{Re}(M_{12}\Gamma_{12}^*). \tag{2.39}$$

The major contribution to the matrix element M_{12} is given by the box diagrams shown in Fig. 2.2 that contain the top quarks in the loop. Due to the large mass of the top quark, the contribution is dominated by the top quark and $M_{12} \propto m_t^2$ where m_t is the mass of the top quark. On the other hand, the box diagrams can also provide a good approximation for Γ_{12}, but the contribution comes from only the charm and up quarks. Since the charm and up quarks are lighter than the bottom quark, the mass of the bottom quark, m_b, sets the scale and $\Gamma_{12} \propto m_b^2$. Therefore,

$$\left|\frac{\Gamma_{12}}{M_{12}}\right| \simeq \mathcal{O}\left(\frac{m_b^2}{m_t^2}\right) \ll 1. \tag{2.40}$$

With this approximation, the mass and width differences of the mass eigenstates and q/p become simply

$$\Delta m_d \simeq 2|M_{12}|, \tag{2.41}$$
$$\Delta\Gamma_d \simeq -2|M_{12}|\mathrm{Re}\left(\frac{\Gamma_{12}}{M_{12}}\right), \tag{2.42}$$
$$\left|\frac{q}{p}\right|^2 \simeq 1 - \mathrm{Im}\left(\frac{\Gamma_{12}}{M_{12}}\right). \tag{2.43}$$

$\Delta\Gamma_d$ is produced by the decay channels common to B^0 and $\overline{B}^0$. The branching fractions for such channels are at or below the level of 10^{-3}. Thus we can expect $\Delta\Gamma_d/\Gamma \ll 1$. Additionally, $x_d \equiv \Delta m_d/\Gamma$ is known to be of $\mathcal{O}(1)$ from experimental measurements [20]. Then, from Eqs. (2.41) and (2.42), $\Delta\Gamma_d/\Gamma$ can be written as

$$\frac{\Delta\Gamma_d}{\Gamma} \simeq -\mathrm{Re}\left(\frac{\Gamma_{12}}{M_{12}}\right)\frac{\Delta m_d}{\Gamma} \ll 1. \tag{2.44}$$

The time evolution of the generic state $|\Psi\rangle$ in Eq. (2.27) can be written in terms of the mass eigenstates $|B_1\rangle$ and $|B_2\rangle$ as

$$\begin{aligned}|\Psi(t)\rangle &= \alpha_1(t)|B_1\rangle + \alpha_2(t)|B_2\rangle \\ &= e^{-i\lambda_+ t}\alpha_1(0)|B_1\rangle + e^{-i\lambda_- t}\alpha_2(0)|B_2\rangle.\end{aligned} \tag{2.45}$$

Then, the time evolution of the neutral B meson $|B^0(t)\rangle$ ($|\overline{B}^0(t)\rangle$) which is initially created as a pure flavor eigenstate $|B^0\rangle$ ($|\overline{B}^0\rangle$) at $t = 0$ can be written as

$$\left|B^0(t)\right\rangle = f_+(t)\left|B^0\right\rangle + \frac{q}{p}f_-(t)\left|\overline{B}^0\right\rangle, \tag{2.46}$$
$$\left|\overline{B}^0(t)\right\rangle = f_+(t)\left|\overline{B}^0\right\rangle + \frac{p}{q}f_-(t)\left|B^0\right\rangle, \tag{2.47}$$

where the notation $f_\pm$ is

$$f_\pm(t) = \frac{1}{2}\left(e^{-i\lambda_+ t} \pm e^{-i\lambda_- t}\right) = \frac{1}{2}e^{-i\left(m_1 - \frac{i}{2}\Gamma_1\right)t}\left[1 \pm e^{-i\left(\Delta m_d + \frac{i}{2}\Delta\Gamma_d\right)t}\right]. \tag{2.48}$$

The probability of observing a state that is created as B^0 at $t = 0$ decaying as B^0 ($\overline{B}^0$) at the time t is proportional to

$$\begin{aligned}\left|\left\langle B^0 \middle| B^0(t)\right\rangle\right|^2 &= |f_+(t)|^2 \\ &= \frac{1}{2}e^{-\Gamma t}\left[\cosh\left(\frac{\Delta\Gamma_d}{2}t\right) + \cos(\Delta m_d t)\right], \end{aligned}\tag{2.49}$$

$$\begin{aligned}\left|\left\langle \overline{B}^0 \middle| B^0(t)\right\rangle\right|^2 &= \left|\frac{q}{p}f_-(t)\right|^2 \\ &= \frac{1}{2}\left|\frac{q}{p}\right|^2 e^{-\Gamma t}\left[\cosh\left(\frac{\Delta\Gamma_d}{2}t\right) - \cos(\Delta m_d t)\right]. \end{aligned}\tag{2.50}$$

With the approximations $|q/p| \simeq 1$ and $\Delta\Gamma_d/\Gamma \ll 1$, the probabilities can be written as

$$P(B^0 \to B^0; t) = P(\overline{B}^0 \to \overline{B}^0; t) = \frac{1}{2}e^{-\Gamma t}\left[1 + \cos(\Delta m_d t)\right], \tag{2.51}$$

$$P(B^0 \to \overline{B}^0; t) = P(\overline{B}^0 \to B^0; t) = \frac{1}{2}e^{-\Gamma t}\left[1 - \cos(\Delta m_d t)\right], \tag{2.52}$$

where $P(a \to b; t)$ means the probability that the particle generated as a at $t = 0$ is observed as b at t. We can see that B^0 and $\overline{B}^0$ are mixing with a cosine time dependence whose frequency is Δm_d.

The theoretical prediction for Δm_d can be obtained by computing the box-diagram contributions [21]. Neglecting Γ_{12} as shown in Eq. (2.41),

$$\Delta m_d \simeq 2|M_{12}| = \frac{G_F^2}{6\pi^2}B_B f_b^2 m_b |V_{td}V_{tb}^*|^2 m_t^2 F\left(\frac{m_t^2}{m_W^2}\right)\eta_{\mathrm{QCD}}, \tag{2.53}$$

where G_F is the Fermi coupling constant, B_B is the bag parameter of the B meson, f_B is the decay constant, η_{QCD} is the QCD correction, m_W is the W boson mass, and the function $F(z)$ is calculated from the box diagram as

$$F(z) = \frac{1}{4} + \frac{9}{4(1-z)} - \frac{3}{2(1-z)^2} - \frac{3}{2}\frac{z^2 \ln z}{(1-z)^3}. \tag{2.54}$$

The oscillation frequency Δm_d is proportional to the square of $|V_{td}V_{tb}^*|$, which is one of the sides of the unitarity triangle. Accurate measurements of Δm_d therefore provide a mathematical constraint on the unitarity of the CKM matrix.

2.4 CP Violation

We consider the B decays to the CP eigenstates f_{CP} to which both B^0 and $\overline{B}^0$ can decay. We define the amplitudes for the decays of B^0 and $\overline{B}^0$ to f_{CP} as

$$A_{f_{CP}} \equiv \langle f_{CP}|H_{\rm d}|B^0\rangle, \quad \overline{A}_{f_{CP}} \equiv \langle f_{CP}|H_{\rm d}|\overline{B}^0\rangle, \tag{2.55}$$

where $H_{\rm d}$ is the decay Hamiltonian. Using the time evolution of B^0 and $\overline{B}^0$ shown as Eqs. (2.46) and (2.47), the time-dependent decay rate for the particle created as B^0 ($\overline{B}^0$) at $t = 0$ decaying to f_{CP} at time t is given by

$$\begin{aligned}
\Gamma\big(B^0 \to f_{CP}; t\big) &\propto \big|\langle f_{CP}|H_{\rm d}|B^0(t)\rangle\big|^2 \\
&= \left| f_+(t) A_{f_{CP}} + \frac{q}{p} f_-(t)\overline{A}_{f_{CP}} \right|^2 \\
&= e^{-\Gamma t}\,|A_{f_{CP}}|^2 \left[\frac{1+|\lambda_{f_{CP}}|^2}{2} \cosh\!\left(\frac{\Delta\Gamma_d}{2}t\right) - \mathrm{Re}(\lambda_{f_{CP}})\sinh\!\left(\frac{\Delta\Gamma_d}{2}t\right) \right. \\
&\qquad \left. + \frac{1-|\lambda_{f_{CP}}|^2}{2}\cos(\Delta m_d t) - \mathrm{Im}(\lambda_{f_{CP}})\sin(\Delta m_d t) \right],
\end{aligned} \tag{2.56}$$

$$\begin{aligned}
\Gamma\big(\overline{B}^0 \to f_{CP}; t\big) &\propto \big|\langle f_{CP}|H_{\rm d}|\overline{B}^0(t)\rangle\big|^2 \\
&= \left| f_+(t) \overline{A}_{f_{CP}} + \frac{p}{q} f_-(t) A_{f_{CP}} \right|^2 \\
&= e^{-\Gamma t}\,|\overline{A}_{f_{CP}}|^2 \left[\frac{1+|\lambda_{f_{CP}}|^{-2}}{2} \cosh\!\left(\frac{\Delta\Gamma_d}{2}t\right) - \mathrm{Re}(\lambda_{f_{CP}}^{-1})\sinh\!\left(\frac{\Delta\Gamma_d}{2}t\right) \right. \\
&\qquad \left. + \frac{1-|\lambda_{f_{CP}}|^{-2}}{2}\cos(\Delta m_d t) - \mathrm{Im}(\lambda_{f_{CP}}^{-1})\sin(\Delta m_d t) \right] \\
&= e^{-\Gamma t}\,|A_{f_{CP}}|^2 \left|\frac{p}{q}\right|^2 \left[\frac{1+|\lambda_{f_{CP}}|^2}{2} \cosh\!\left(\frac{\Delta\Gamma_d}{2}t\right) - \mathrm{Re}(\lambda_{f_{CP}})\sinh\!\left(\frac{\Delta\Gamma_d}{2}t\right) \right. \\
&\qquad \left. - \frac{1-|\lambda_{f_{CP}}|^2}{2}\cos(\Delta m_d t) + \mathrm{Im}(\lambda_{f_{CP}})\sin(\Delta m_d t) \right],
\end{aligned} \tag{2.57}$$

where the complex parameter $\lambda_{f_{CP}}$ is defined as

$$\lambda_{f_{CP}} \equiv \frac{q}{p}\frac{\overline{A}_{f_{CP}}}{A_{f_{CP}}}. \tag{2.58}$$

With the approximation $|q/p| \simeq 1$ and $\Delta\Gamma_d/\Gamma \ll 1$ as shown in Eqs. (2.43) and (2.44), Eqs. (2.56) and (2.57) can be written as

$$\begin{aligned}\Gamma\big(B^0 \to f_{CP};t\big) \propto |A_{f_{CP}}|^2\, e^{-\Gamma t}\Bigg[&\frac{1+|\lambda_{f_{CP}}|^2}{2} + \frac{1-|\lambda_{f_{CP}}|^2}{2}\cos(\Delta m_d t)\\ &- \mathrm{Im}(\lambda_{f_{CP}})\sin(\Delta m_d t)\Bigg],\end{aligned} \tag{2.59}$$

$$\begin{aligned}\Gamma\big(\overline{B}^0 \to f_{CP};t\big) \propto |A_{f_{CP}}|^2\, e^{-\Gamma t}\Bigg[&\frac{1+|\lambda_{f_{CP}}|^2}{2} - \frac{1-|\lambda_{f_{CP}}|^2}{2}\cos(\Delta m_d t)\\ &+ \mathrm{Im}(\lambda_{f_{CP}})\sin(\Delta m_d t)\Bigg].\end{aligned} \tag{2.60}$$

The time-dependent CP asymmetry A_{CP} is then expressed as

$$\begin{aligned}A_{CP}(t) &\equiv \frac{\Gamma\big(\overline{B}^0 \to f_{CP};t\big) - \Gamma(B^0 \to f_{CP};t)}{\Gamma\big(\overline{B}^0 \to f_{CP};t\big) + \Gamma(B^0 \to f_{CP};t)}\\ &= \frac{|\lambda_{f_{CP}}|^2-1}{|\lambda_{f_{CP}}|^2+1}\cos(\Delta m_d t) + \frac{2\mathrm{Im}(\lambda_{f_{CP}})}{|\lambda_{f_{CP}}|^2+1}\sin(\Delta m_d t).\end{aligned} \tag{2.61}$$

If, in addition to $|q/p| = 1$, $|\overline{A}_{f_{CP}}/A_{f_{CP}}| = 1$ so that $|\lambda_{f_{CP}}| = 1$, Eq. (2.61) can be simplified as

$$A_{CP}(t) = \mathrm{Im}(\lambda_{f_{CP}})\sin(\Delta m_d t). \tag{2.62}$$

Then we consider the $\mathrm{Im}(\lambda_{f_{CP}})$. In the general case, $A_{f_{CP}}$ and $\overline{A}_{f_{CP}}$ can be written as sums of various contributions:

$$A_{f_{CP}} = \sum_i A_i e^{i\delta_i} e^{i\phi_i}, \tag{2.63}$$

$$\overline{A}_{f_{CP}} = \sum_i A_i e^{i\delta_i} e^{-i\phi_i}, \tag{2.64}$$

where A_i is real, ϕ_i is the CKM phase, and δ_i is the strong phase which comes from the strong interaction. Thus, if all the amplitudes that contribute to the decay have the same CKM phase, which we denote by ϕ_{D}, $|\overline{A}_{f_{CP}}/A_{f_{CP}}| = 1$ holds and

$$\frac{\overline{A}_{f_{CP}}}{A_{f_{CP}}} = e^{-2i\phi_{\mathrm{D}}}. \tag{2.65}$$

Since $\Gamma_{12} \ll M_{12}$ as mentioned in Eq. (2.40), Eq. (2.33) can be written as

$$\frac{q}{p} = \sqrt{\frac{M_{12}^*}{M_{12}}} = e^{-2i\phi_{\mathrm{M}}}, \tag{2.66}$$

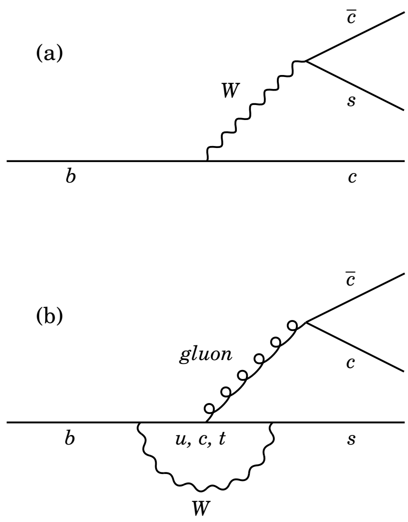

Figure 2.3: (a) Tree and (b) Penguin diagrams for the $b \to c\bar{c}s$ transition.

where $\phi_{\rm M}$ is the CKM phase in the B^0-$\overline{B}^0$ mixing. Thus,

$$\lambda_{f_{CP}} = e^{-2i(\phi_{\rm M}+\phi_{\rm D})}, \tag{2.67}$$

$$\mathrm{Im}(\lambda_{f_{CP}}) = -\sin 2(\phi_{\rm M}+\phi_{\rm D}). \tag{2.68}$$

Next, we examine the relation between $\mathrm{Im}(\lambda_{f_{CP}})$ and the CKM parameters. For the mixing in the B^0 system, since $M_{12} \propto (V_{tb}V_{td}^*)^2$ as expected from the box diagrams,

$$\frac{q}{p} \simeq \sqrt{\frac{M_{12}^*}{M_{12}}} = \frac{V_{tb}^*V_{td}}{V_{tb}V_{td}^*}. \tag{2.69}$$

For f_{CP}, we consider the $b \to c\bar{c}s$ transition, i.e., $B^0(\overline{B}^0) \to$ charmonium K_S^0 or charmonium K_L^0. These decays are dominated by the "Tree" diagram shown in Fig. 2.3(a). The amplitude for this diagram can be written as

$$A_{c\bar{c}s}^{\rm tree} = V_{cb}^*V_{cs}T_{c\bar{c}s}, \tag{2.70}$$

where $T_{c\bar{c}s}$ denotes the contribution from the tree diagram excluding the CKM factors and including the strong phases. There exists the contamination from the "Penguin" diagram shown in Fig. 2.3(b). The amplitude for this diagram can be written as

$$A_{c\bar{c}s}^{\rm penguin} = V_{tb}^*V_{ts}P_{c\bar{c}s}^t + V_{cb}^*V_{cs}P_{c\bar{c}s}^c + V_{ub}^*V_{us}P_{c\bar{c}s}^u, \tag{2.71}$$

where $P_{c\bar{c}s}^i$ $(i = t, c, u)$ denote the contribution from the penguin diagram excluding the CKM factor. Using the unitarity condition of Eq. (2.8), the total amplitude $A_{c\bar{c}s}$

is given by

$$
\begin{aligned}
A_{c\bar{c}s} &= A^{\text{tree}}_{c\bar{c}s} + A^{\text{penguin}}_{c\bar{c}s} \\
&= V^*_{cb}V_{cs}(T_{c\bar{c}s} + P^c_{c\bar{c}s} - P^t_{c\bar{c}s}) + V^*_{ub}V_{us}(P^u_{c\bar{c}s} - P^t_{c\bar{c}s}).
\end{aligned}
\tag{2.72}
$$

Since $|(V^*_{ub}V_{us})/(V^*_{cb}V_{cs})| = \mathcal{O}(\lambda^{-2}) \ll 1$ from Eq. (2.4), the second term containing $V^*_{ub}V_{us}$ can be ignored. Thus, only one CKM phase contributes to the decay amplitude:

$$
\frac{\overline{A}_{c\bar{c}s}}{A_{c\bar{c}s}} = \frac{V_{cb}V^*_{cs}}{V^*_{cb}V_{cs}}. \tag{2.73}
$$

To complete the calculation of $\overline{A}_{f_{CP}}/A_{f_{CP}}$, we have to consider the K^0-$\overline{K}^0$ mixing, since $B^0 \to \psi K^0$ and $\overline{B}^0 \to \psi \overline{K}^0$ are different final states without the K^0-$\overline{K}^0$ mixing. By analogy with the B^0-$\overline{B}^0$ mixing, since $|V_{ts}V^*_{td}| \ll |V_{cs}V^*_{cd}|$, the factor q/p for the neutral K-meson system is given by

$$
\left(\frac{q^*}{p^*}\right)_K \simeq \frac{V_{cs}V^*_{cd}}{V^*_{cs}V_{cd}}. \tag{2.74}
$$

Finally, taking into account the CP eigenvalue of f_{CP}, $\xi_{f_{CP}}$, the CP-asymmetry parameter $\lambda_{f_{CP}}$ is expressed as

$$
\begin{aligned}
\lambda_{f_{CP}} &= \left(\frac{q}{p}\right)\xi_{f_{CP}}\left(\frac{q^*}{p^*}\right)_K \frac{\overline{A}_{c\bar{c}s}}{A_{c\bar{c}s}} \\
&\simeq \xi_{f_{CP}} \frac{V^*_{tb}V_{td}}{V_{tb}V^*_{td}} \frac{V_{cs}V^*_{cd}}{V^*_{cs}V_{cd}} \frac{V_{cb}V^*_{cs}}{V^*_{cb}V_{cs}} \\
&= \xi_{f_{CP}} e^{-2i\phi_1}.
\end{aligned}
\tag{2.75}
$$

Thus, $\text{Im}(\lambda_{f_{CP}})$ and the time-dependent asymmetry $A_{CP}(t)$ defined as Eq. (2.61) are written as

$$
\text{Im}(\lambda_{f_{CP}}) = -\xi_{f_{CP}} \sin 2\phi_1, \tag{2.76}
$$

$$
A_{CP}(t) = -\xi_{f_{CP}} \sin 2\phi_1 \sin(\Delta m_d t). \tag{2.77}
$$

Therefore, by observing the time-dependent CP asymmetry $A_{CP}(t)$ for the B decays to the CP eigenstates that originate from $b \to c\bar{c}s$ transition, one of the angles of the unitarity triangle, ϕ_1, can be directly measured as the amplitude of the sine curve.

2.5 Asymmetric-Energy B-Factory Experiment

To measure above quantities with the high accuracy, the high statistics and the clean experimental environment are required. The B-Factory experiment using an e^+e^-

collider is designed to realize these requirements. The e^+e^- collider environment offers the much cleaner room than the hadron collider experiments. In the B-Factory experiment, the collider is designed to operate at the center-of-mass energy of the $\Upsilon(4S)$ resonance. Since the mass of $\Upsilon(4S)$ is just above the threshold to create the $B^0\overline{B}^0$ or B^+B^- pair and below the $B^*\overline{B}$ or $B_s\overline{B}_s$ creation threshold, $\Upsilon(4S)$ decays only to $B^0\overline{B}^0$ or B^+B^- pair. The ratio between the branching fractions of $\Upsilon(4S) \to B^0\overline{B}^0$ and $\Upsilon(4S) \to B^+B^-$ is almost one.

We consider the time evolution of two neutral B mesons $\big|B\overline{B}(t_1, t_2)\big\rangle$, where t_1 and t_2 denote the proper times of the first and second B mesons, respectively. At $t_1 = t_2 = 0$, i.e., when the $\Upsilon(4S)$ decays, the state consists of $\big|B^0\overline{B}^0\big\rangle$ and $\big|\overline{B}^0B^0\big\rangle$:

$$\big|B\overline{B}(0,0)\big\rangle = c_1\big|B^0\overline{B}^0\big\rangle + c_2\big|\overline{B}^0B^0\big\rangle. \tag{2.78}$$

The $\Upsilon(4S)$ is a vector meson and has the CP eigenvalue of $-1\times-1 = +1$. Since the $\Upsilon(4S)$ decays via the strong interaction, CP is expected to be conserved. Therefore, the $B\overline{B}$ system also has to be $CP = +1$. Because B mesons are pseudoscalar bosons (i.e., spin-0) and the angular momentum $J = L + S = 1$ of the $\Upsilon(4S)$ must be conserved, the orbital angular momentum of $B\overline{B}$ system must be $L = 1$ and hence the orbital part has $CP = -1$. Thus, the flavor part must have $CP = -1$ so that the total CP eigenvalue be $+1$. Considering the normalization condition $|c_1|^2 + |c_2|^2 = 1$, c_1 and c_2 are obtained to be $c_1 = -c_2 = 1/\sqrt{2}$:

$$\big|B\overline{B}(0,0)\big\rangle = \frac{1}{\sqrt{2}}\Big(\big|B^0\overline{B}^0\big\rangle - \big|\overline{B}^0B^0\big\rangle\Big). \tag{2.79}$$

Then, the time evolution of $\big|B\overline{B}(t_1, t_2)\big\rangle$ can be obtained from the Eqs. (2.46) and (2.47) as

$$\begin{aligned}\big|B\overline{B}(t_1,t_2)\big\rangle &= \frac{1}{\sqrt{2}}\Big(\big|B^0(t_1)\overline{B}^0(t_2)\big\rangle - \big|\overline{B}^0(t_1)B^0(t_2)\big\rangle\Big)\\ &= \frac{1}{\sqrt{2}}e^{-i\left(M-\frac{i}{2}\Gamma\right)(t_1+t_2)}\\ &\quad\left\{-\frac{1}{2}\left[e^{i\left(\Delta m_d+\frac{i}{2}\Delta\Gamma_d\right)\frac{t_1-t_2}{2}} - e^{-i\left(\Delta m_d+\frac{i}{2}\Delta\Gamma_d\right)\frac{t_1-t_2}{2}}\right]\left(\frac{p}{q}\big|B^0B^0\big\rangle - \frac{q}{p}\big|\overline{B}^0\overline{B}^0\big\rangle\right)\right.\\ &\quad\left.+\frac{1}{2}\left[e^{i\left(\Delta m_d+\frac{i}{2}\Delta\Gamma_d\right)\frac{t_1-t_2}{2}} + e^{-i\left(\Delta m_d+\frac{i}{2}\Delta\Gamma_d\right)\frac{t_1-t_2}{2}}\right]\left(\big|B^0\overline{B}^0\big\rangle - \big|\overline{B}^0B^0\big\rangle\right)\right\}.\end{aligned} \tag{2.80}$$

If $t_1 = t_2$, the terms containing $|B^0B^0\rangle$ and $\big|\overline{B}^0\overline{B}^0\big\rangle$ vanish and only the terms of $\big|B^0\overline{B}^0\big\rangle$ and $\big|\overline{B}^0B^0\big\rangle$ remain. Therefore, two neutral B mesons cannot be the same flavor states at the same time in this time evolution.

Generally, we consider the event where the first B meson decays to the final state f_1 and the other to f_2. We define the decay amplitudes as

$$A_1 \equiv \langle f_1|H_\mathrm{d}|B^0\rangle, \quad \overline{A}_1 \equiv \langle f_1|H_\mathrm{d}|\overline{B}^0\rangle, \tag{2.81}$$

$$A_2 \equiv \langle f_2|H_\mathrm{d}|B^0\rangle, \quad \overline{A}_2 \equiv \langle f_2|H_\mathrm{d}|\overline{B}^0\rangle. \tag{2.82}$$

Then, the time-dependent decay rate can be calculated as

$$\begin{aligned}\left|\langle f_1 f_2|B\overline{B}(t_1,t_2)\rangle\right|^2 = \frac{1}{2}e^{-\Gamma(t_1+t_2)}|A_1A_2|^2 \\ \Bigg\{c_1\cosh\left[\frac{\Delta\Gamma_d}{2}(t_1-t_2)\right] + c_2\sinh\left[\frac{\Delta\Gamma_d}{2}(t_1-t_2)\right] \\ + c_3\cos[\Delta m_d(t_1-t_2)] + c_4\sin[\Delta m_d(t_1-t_2)]\Bigg\},\end{aligned} \tag{2.83}$$

where the coefficients c_i $(i = 1,\cdots,4)$ are

$$c_1 = \frac{1}{2}\left(\left|\frac{\overline{A}_1}{A_1}\right|^2 + \left|\frac{\overline{A}_2}{A_2}\right|^2 + \left|\frac{p}{q}\right|^2 + \left|\frac{q}{p}\frac{\overline{A}_1\overline{A}_2}{A_1A_2}\right|^2\right) - \mathrm{Re}\left(\frac{\overline{A}_1\overline{A}_2^*}{A_1A_2^*}\right) - \mathrm{Re}\left(\frac{p^*q}{pq^*}\frac{\overline{A}_1\overline{A}_2^*}{A_1A_2^*}\right), \tag{2.84}$$

$$c_2 = -\left|\frac{\overline{A}_2}{A_2}\right|^2\mathrm{Re}\left(\frac{q}{p}\frac{\overline{A}_1}{A_1}\right) - \mathrm{Re}\left(\frac{p}{q}\frac{\overline{A}_1^*}{A_1^*}\right) + \left|\frac{\overline{A}_1}{A_1}\right|^2\mathrm{Re}\left(\frac{q}{p}\frac{\overline{A}_2}{A_2}\right) + \mathrm{Re}\left(\frac{p}{q}\frac{\overline{A}_2^*}{A_2^*}\right), \tag{2.85}$$

$$c_3 = \frac{1}{2}\left(\left|\frac{\overline{A}_1}{A_1}\right|^2 + \left|\frac{\overline{A}_2}{A_2}\right|^2 - \left|\frac{p}{q}\right|^2 - \left|\frac{q}{p}\frac{\overline{A}_1\overline{A}_2}{A_1A_2}\right|^2\right) - \mathrm{Re}\left(\frac{\overline{A}_1\overline{A}_2^*}{A_1A_2^*}\right) + \mathrm{Re}\left(\frac{p^*q}{pq^*}\frac{\overline{A}_1\overline{A}_2^*}{A_1A_2^*}\right), \tag{2.86}$$

$$c_4 = -\left|\frac{\overline{A}_2}{A_2}\right|^2\mathrm{Im}\left(\frac{q}{p}\frac{\overline{A}_1}{A_1}\right) - \mathrm{Im}\left(\frac{p}{q}\frac{\overline{A}_1^*}{A_1^*}\right) + \left|\frac{\overline{A}_1}{A_1}\right|^2\mathrm{Im}\left(\frac{q}{p}\frac{\overline{A}_2}{A_2}\right) + \mathrm{Im}\left(\frac{p}{q}\frac{\overline{A}_2^*}{A_2^*}\right). \tag{2.87}$$

For the neutral B-meson pair, the probability that one B meson is B^0 at time t_1 and the other is $\overline{B}^0(B^0)$ at t_2 is

$$\begin{aligned}\Gamma(B^0\overline{B}^0;t_1,t_2) &\propto \left|\langle B^0\overline{B}^0|B\overline{B}(t_1,t_2)\rangle\right|^2 \\ &= \frac{1}{4}e^{-\Gamma(t_1+t_2)}\left\{\cosh\left[\frac{\Delta\Gamma_d}{2}(t_1-t_2)\right] + \cos[\Delta m_d(t_1-t_2)]\right\},\end{aligned} \tag{2.88}$$

$$\begin{aligned}\Gamma(B^0B^0;t_1,t_2) &\propto \left|\langle B^0B^0|B\overline{B}(t_1,t_2)\rangle\right|^2 \\ &= \frac{1}{4}e^{-\Gamma(t_1+t_2)}\left|\frac{p}{q}\right|^2\left\{\cosh\left[\frac{\Delta\Gamma_d}{2}(t_1-t_2)\right] - \cos[\Delta m_d(t_1-t_2)]\right\}.\end{aligned} \tag{2.89}$$

If one B meson decays to the CP eigenstate f_{CP} at t_1 and the other is $\overline{B}^0(B^0)$ at t_2, then its probability is

$$\begin{aligned}
\Gamma(f_{CP}\overline{B}^0; t_1, t_2) &\propto \left|\left\langle f_{CP}\overline{B}^0 \middle| B\overline{B}(t_1, t_2)\right\rangle\right|^2 \\
&= \frac{1}{2} e^{-\Gamma(t_1+t_2)} \left|A_{f_{CP}}\right|^2 \\
&\quad \left\{ \frac{1+|\lambda_{f_{CP}}|^2}{2} \cosh\left[\frac{\Delta\Gamma_d}{2}(t_1 - t_2)\right] - \mathrm{Re}(\lambda_{f_{CP}}) \sinh\left[\frac{\Delta\Gamma_d}{2}(t_1 - t_2)\right] \right. \\
&\quad \left. + \frac{1-|\lambda_{f_{CP}}|^2}{2} \cos[\Delta m_d(t_1 - t_2)] - \mathrm{Im}(\lambda_{f_{CP}}) \sin[\Delta m_d(t_1 - t_2)] \right\},
\end{aligned} \tag{2.90}$$

$$\begin{aligned}
\Gamma(f_{CP}B^0; t_1, t_2) &\propto \left|\left\langle f_{CP}B^0 \middle| B\overline{B}(t_1, t_2)\right\rangle\right|^2 \\
&= \frac{1}{2} e^{-\Gamma(t_1+t_2)} \left|A_{f_{CP}}\right|^2 \left|\frac{p}{q}\right|^2 \\
&\quad \left\{ \frac{1+|\lambda_{f_{CP}}|^2}{2} \cosh\left[\frac{\Delta\Gamma_d}{2}(t_1 - t_2)\right] - \mathrm{Re}(\lambda_{f_{CP}}) \sinh\left[\frac{\Delta\Gamma_d}{2}(t_1 - t_2)\right] \right. \\
&\quad \left. - \frac{1-|\lambda_{f_{CP}}|^2}{2} \cos[\Delta m_d(t_1 - t_2)] + \mathrm{Im}(\lambda_{f_{CP}}) \sin[\Delta m_d(t_1 - t_2)] \right\}.
\end{aligned} \tag{2.91}$$

Assuming $|q/p| = 1$ and $\Delta\Gamma_d = 0$, the probability that one B meson decays at t_1 and the other at t_2 for the neutral or charged B-meson pair is

$$\Gamma(t_1, t_2) \propto e^{-\Gamma(t_1+t_2)}. \tag{2.92}$$

Since the energy release in the $\Upsilon(4S)$ decay is very small, two B mesons are almost at rest in the $\Upsilon(4S)$ rest frame. This means that the B mesons decay very close to the production point and it is difficult to measure the difference between the production and decay points of the B meson in the symmetric energy collider experiment. However, by colliding e^+ and e^- with the asymmetric energy, the $\Upsilon(4S)$ is boosted in the laboratory frame and thus it is possible to measure the difference between the decay times of two B mesons. If the $\Upsilon(4S)$ is boosted along the beam axis (defined as the z axis) with the Lorentz boost factor $(\beta\gamma)_\Upsilon$, the decay-time difference $\Delta t = t_1 - t_2$ can be obtained from the separation in z between the two B decay vertices, Δz, as

$$\Delta t \simeq \frac{\Delta z}{c(\beta\gamma)_\Upsilon}, \tag{2.93}$$

by neglecting the B momentum in the $\Upsilon(4S)$ rest frame. Since we do not know the sum of proper decay times $t_1 + t_2$, by integrating over this variable, Eq. (2.92)

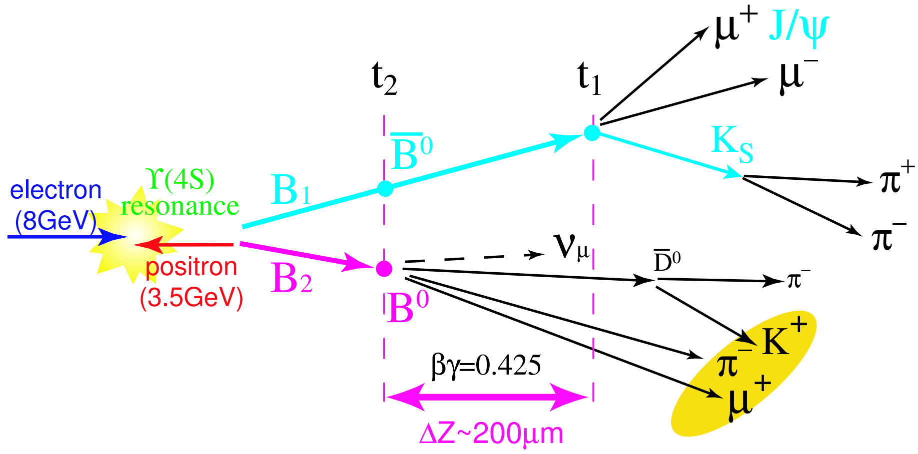

Figure 2.4: Illustration of the event topology in the KEK B Factory.

becomes

$$\Gamma(\Delta t) = \frac{\Gamma}{2} e^{-\Gamma|\Delta t|}. \tag{2.94}$$

For the B^0-$\overline{B}^0$ mixing, with the approximation $|q/p| = 1$ and $\Delta\Gamma_d = 0$, Eqs. (2.88) and (2.89) become

$$\Gamma(B^0\overline{B}^0; \Delta t) = \Gamma(\overline{B}^0 B^0; \Delta t) = \frac{\Gamma}{4} e^{-\Gamma|\Delta t|} \left[1 + \cos(\Delta m_d \Delta t)\right], \tag{2.95}$$

$$\Gamma(B^0 B^0; \Delta t) = \Gamma(\overline{B}^0\overline{B}^0; \Delta t) = \frac{\Gamma}{4} e^{-\Gamma|\Delta t|} \left[1 - \cos(\Delta m_d \Delta t)\right]. \tag{2.96}$$

For the CP asymmetry, with the additional assumption $|\lambda_{f_{CP}}| = 1$, Eqs. (2.90) and (2.91) are

$$\Gamma(f_{CP}\overline{B}^0; \Delta t) = \frac{\Gamma}{4} e^{-\Gamma|\Delta t|} \left[1 + \xi_{f_{CP}} \sin 2\phi_1 \sin(\Delta m_d \Delta t)\right], \tag{2.97}$$

$$\Gamma(f_{CP}B^0; \Delta t) = \frac{\Gamma}{4} e^{-\Gamma|\Delta t|} \left[1 - \xi_{f_{CP}} \sin 2\phi_1 \sin(\Delta m_d \Delta t)\right]. \tag{2.98}$$

Therefore, $\tau = 1/\Gamma$, Δm_d, and $\sin 2\phi_1$ can be obtained from the Δt distributions for several final states.

Figure 2.4 shows an illustration of the event topology in the KEK B-Factory experiment. One of the B mesons, B_1, is fully reconstructed in the hadronic decay modes. By inclusively reconstructing the decay vertex of the other B meson, B_2, we can measure the difference between the two B-meson decay points, Δz. Using Eq. (2.93), we obtain the proper-time difference between the two B-meson decays, Δt, and thus we can extract the lifetimes of B mesons from Eq. (2.94). Since the average separation $\langle \Delta z \rangle$ is about 200 μm in the KEK B Factory, it is crucially

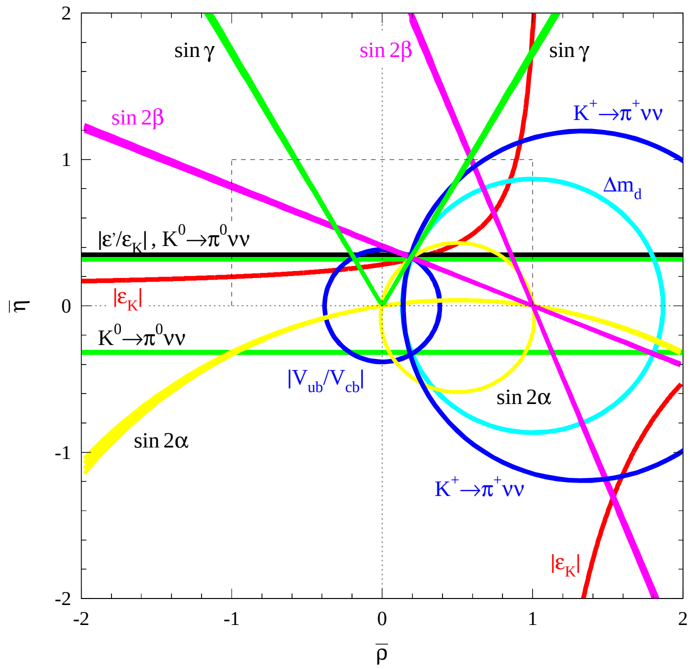

Figure 2.5: Schematic drawing of the constraints in the $\bar{\rho}$-$\bar{\eta}$ plane for the most relevant observables.

important to determine the position of B decay vertex precisely and to understand the resolution closely.

In addition to the reconstruction of Δz, by identifying the flavor of B_2, we can measure the oscillation frequency Δm_d from Eqs. (2.95) and (2.96), and the CP violation parameter $\sin 2\phi_1$ from Eqs. (2.97) and (2.98). The flavor can be identified from the charge and the species of the decay products of B_2. Thus, the particle identification with good performance and the development of the flavor tagging algorithm, as well as the understanding of its performance, are necessary for the Δm_d and $\sin 2\phi_1$ analyses.

2.6 Experimental Constraints on the Unitarity Triangle

In this section, we briefly explain how the unitarity triangle is constrained by the experimental measurements. Each constraint in the $\bar{\rho}$-$\bar{\eta}$ plane is shown schematically in Fig. 2.5. The plot is made by the CKM fitter Group [22]. The detail of the constraints that are not written here is described in Ref. [22].

- $|V_{ub}|$

  Both the inclusive semileptonic b decay to u quark ($b \to X_u \ell^- \overline{\nu}_\ell$) and the exclusive B decays including the b to u transition ($B^0 \to \pi^- \ell^+ \nu_\ell$, $B^0 \to \rho^- \ell^+ \nu_\ell$) allow an extraction of $|V_{ub}|$. These two measurements have different systematics. However, both measurements have large uncertainties, because the statistics are limited and the theoretical uncertainties are large.

- $|V_{cb}|$
  $|V_{cb}|$ is obtained from the exclusive $B \to D^{(*)} \ell \overline{\nu}_\ell$ and the inclusive semileptonic b decay to charm, $b \to X_c \ell^- \overline{\nu}_\ell$. The theoretical frameworks for extracting numerical values for $|V_{cb}|$ from the measured decay rates are the Heavy Quark Effective Theory (HQET) [23] for the exclusive measurements and HQE [18] for the inclusive measurements.

- $|\epsilon_K|$
  The indirect CP violation in the K^0-$\overline{K}^0$ system is measured by

$$\epsilon_K = \frac{2}{3}\eta_{+-} + \frac{1}{3}\eta_{00}, \tag{2.99}$$

  where η_{+-} (η_{00}) is the ratio of the amplitudes of the long-lived and short-lived neutral kaons decaying into two charged (neutral) pions. Theoretically, $|\epsilon_K|$ includes $\overline{\rho}$ and $\overline{\eta}$ in the form of the hyperbola. Though this parameter is measured accurately, the theoretical uncertainties are large.

- Δm_q
  The frequency of B_q^0-$\overline{B}_q^0$ oscillation ($q = d, s$) is given by the mass difference Δm_q. Δm_d is theoretically expressed as Eq. (2.53). Since $|V_{tb}|$ is almost one, the Δm_d measurement gives the constraint on $|V_{td}|$, thus, R_t. Currently, the theoretical uncertainties are large for the $|V_{td}|$ determination.

  The B_s^0-$\overline{B}_s^0$ oscillation frequency Δm_s is given in the same way as Δm_d. By taking the ratio of two oscillation frequencies, some theoretical uncertainties are canceled out:

$$\frac{\Delta m_d}{\Delta m_s} = \frac{B_{B_d} f_{B_d}^2 m_{B_d}}{B_{B_s} f_{B_s}^2 m_{B_s}} \frac{|V_{td}|^2}{|V_{ts}|^2}. \tag{2.100}$$

  Thus, the tighter constraint on R_t is possible, though currently only the upper limit is measured for Δm_s.

- $\sin 2\phi_1$
  As described in Section 2.4, one of the angles of the unitarity triangle, ϕ_1, can be directly measured through the time-dependent asymmetry in the decay rate of the CP eigenstate that is dominated by $b \to c\overline{c}s$ transition. Since we can measure ϕ_1 in the form of $\sin 2\phi_1$, there are four possible values for ϕ_1.

Chapter 3

Experimental Apparatus

In this chapter, we describe the experimental apparatus of the KEK B Factory. The KEK B Factory consists of the KEKB accelerator and the Belle detector.

First, we briefly introduce the KEKB accelerator. Then, overviews of the Belle detector and its sub-detector components are given. We also describe the offline computing environment and software in our experiment.

3.1 KEKB Accelerator

KEKB [24] is a two-ring, asymmetric-energy, e^+e^- collider and aims to produce copious B and anti-B mesons as in a factory. Figure 3.1 shows a schematic layout of KEKB. It consists of two 3-km-long storage rings, an 8-GeV electron ring (HER) and a 3.5-GeV positron ring (LER), and an injection linear accelerator. The two rings cross at one point, called the interaction point (IP), where electrons and positrons collide with a finite crossing angle of ± 11 mrad to avoid parasitic collisions near IP. The Belle detector surrounds IP to catch particles produced by the collisions. The center-of-mass energy is 10.58 GeV, which corresponds to the mass of the $\Upsilon(4S)$ resonance. Due to the energy asymmetry, the $\Upsilon(4S)$ resonance and its daughter B mesons are produced with a Lorentz boost of $(\beta\gamma)_\Upsilon = 0.425$. On average, the separation of the decay vertices of two B mesons is approximately $\langle \Delta z \rangle = c\tau_B(\beta\gamma)_\Upsilon \sim 200\ \mu$m.

The design luminosity of KEKB is 10^{34} cm^{-2}s^{-1}. The peak luminosity that KEKB achieved is 7.35×10^{33} cm^{-2}s^{-1}, which is the world record as of July 2002.

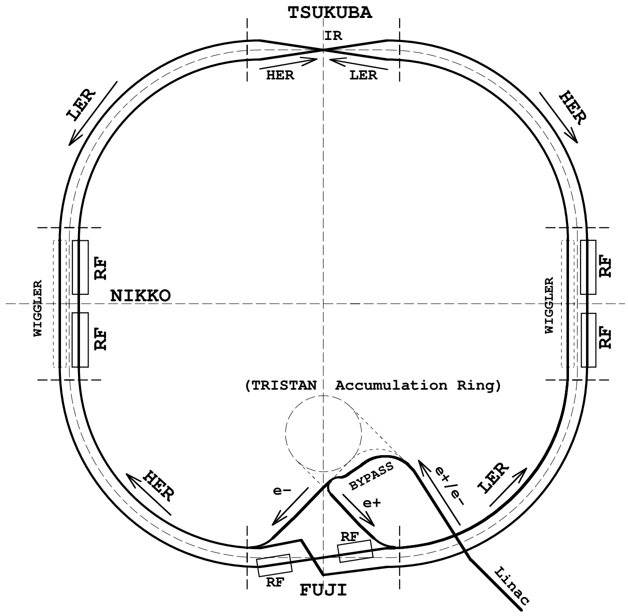

Figure 3.1: Schematic view of the layout of KEKB.

3.2 Belle Detector

The Belle detector [25] is a general-purpose 4-π detector surrounding IP. It consists of a barrel, forward, and rear components. Figures 3.2 and 3.3 show the configuration of the Belle detector.

Precision tracking and vertex measurements are provided by a central drift chamber (CDC) and a silicon vertex detector (SVD). The identification of charged pions and kaons uses three detector systems: the CDC measurements of dE/dx, a set of time-of-flight counters (TOF), and a set of aerogel Cherenkov counters (ACC). Electromagnetic particles are detected in an array of CsI(Tl) crystal calorimeters (ECL). The electron identification is based on a combination of dE/dx measurements in CDC, the response of ACC, and the information of position, shape, and energy of the electromagnetic shower in ECL. The above detectors are located inside a super-conducting solenoid of 1.7 m radius that generates a 1.5 T magnetic field. The outermost detector subsystem is a K_L^0 and muon detector (KLM), which is instrumented from an iron flux-return located outside of the coil. A part of the uncovered small-angle region is instrumented with a pair of BGO crystal arrays (EFC) placed on the surface of the QCS cryostats in forward and backward directions. The performance of detector components are summarized in Table 3.1.

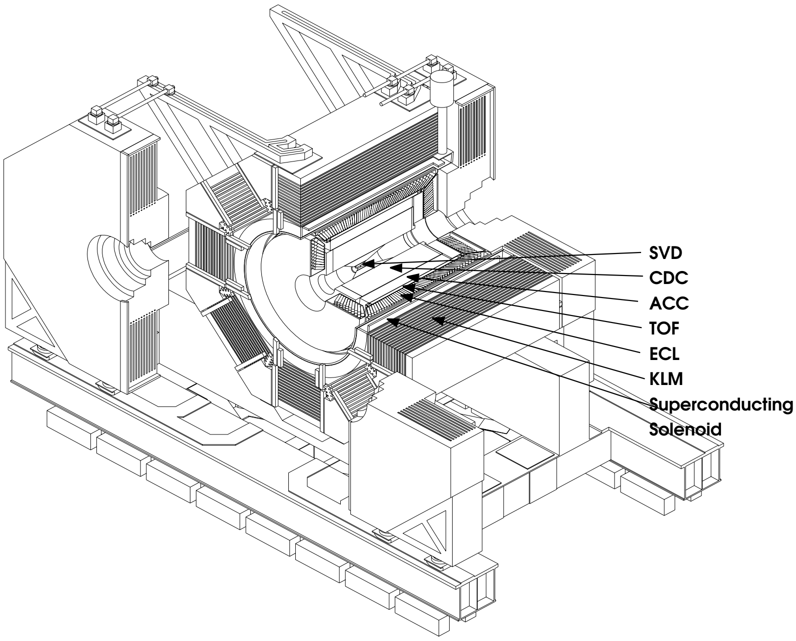

Figure 3.2: Overview of the Belle detector.

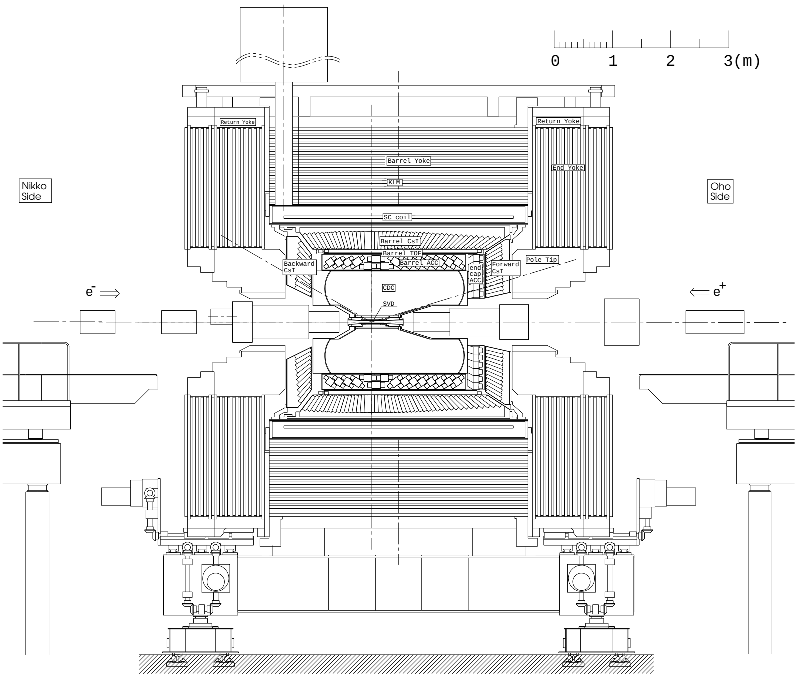

Figure 3.3: Sideview of the Belle detector.

Table 3.1: Performance parameters expected (or achieved) for the Belle detector.

Detector	Type	Configuration	Readout	Performance
SVD	Double sided Si strip	Chip size: 57.5×33.5 mm^2 Strip pitch: 25 (p)/50 (n) μm 3 layers: 8/10/14 ladders	ϕ: 40.96 k z: 40.96 k	$\sigma_{\Delta z} \sim 180$ μm
CDC	Small cell drift chamber	Anode: 50 layers Cathode: 3 layers $r = 8.3$–86.3 cm $-77 \leq z \leq 160$ cm	A: 8.4 k C: 1.8 k	$\sigma_{r\phi} = 130$ μm $\sigma_z = 200 \sim 1400$ μm $\sigma_{p_t}/p_t = 0.3\%\sqrt{{p_t}^2+1}$ $\sigma_{dE/dx} = 8\%$
ACC	Silica aerogel	960 barrel / 228 end-cap FM-PMT readout		$N_{pe} \geq 6$ K/π separation: $1.2 < p < 3.5$ GeV/c
TOF/TSC	Scintillator	128/64 ϕ segmentation $r = 120$ cm, 3-m long	$128 \times 2/64$	$\sigma_t = 100$ ps K/π separation: up to 1.2 GeV/c
ECL	CsI (Towered-structure)	Barrel: $r = 125$–162 cm End-cap: $z =$ -102 cm and $+196$ cm	6624 1152 (F) 960 (B)	$\sigma_E/E = 1.3\%\sqrt{E}$ $\sigma_{pos} = 0.5$ cm$/\sqrt{E}$
KLM	Resistive plate counters	14 layers (5 cm Fe + 4 cm gap) 2 RPCs in each gap	θ: 16 k ϕ: 16 k	$\Delta\phi = \Delta\theta = 30$ mrad for K_L^0 $\sim 1\%$ hadron fake
EFC	BGO	Photodiode readout Segmentation: 32 in ϕ; 5 in θ	160×2	Energy resolution (rms) 7.3% at 8 GeV 5.8% at 3.5 GeV
Beam pipe	Beryllium double-wall	Cylindrical, $r = 20$ mm 0.5/2.5/0.5 (mm) = Be/He/Be		He gas cooled
Magnet	Superconducting	Inner radius = 170 cm		$B = 1.5$ T

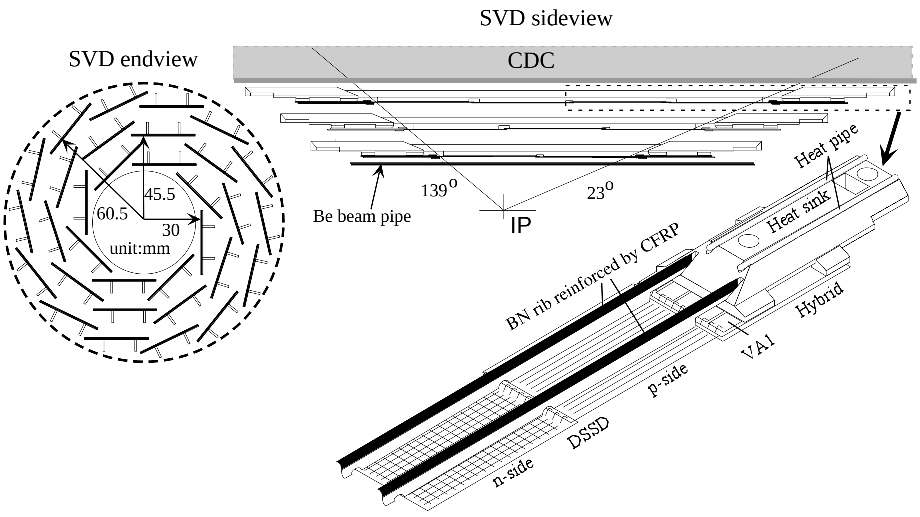

Figure 3.4: Detector configuration of SVD.

3.2.1 Silicon Vertex Detector (SVD)

It is crucially important for the time-evolution study to measure the difference between the flight lengths of the two B mesons in the z direction, where z is defined as the opposite of the positron beam direction. SVD [26] provides essential information for the precise reconstruction of the decay vertices close to IP. Since the average separation of two B-decay vertices is ~ 200 μm, the required Δz resolution is $\lesssim 200$ μm. In addition, the vertex detector is useful for identifying and measuring the decay vertices of D and τ particles.

Since the most particles of interest in Belle have momenta of 1 GeV/c or less, the vertex resolution is dominated by the multiple-Coulomb scattering. This imposes strict constraints on the design of the detector. In particular, the innermost layer of the vertex detector must be placed as close to IP, the support structure must be low in mass but rigid, and the readout electronics must be placed outside the tracking volume.

The design must also withstand large beam backgrounds. With the high luminosity operation of KEKB, the radiation dose to the detector is measured to be 10 kRad/month. Radiation doses of this level both degrade the noise performance of the electronics and induce leakage currents in the silicon detectors.

Figure 3.4 shows the side and end views of SVD. SVD consists of three concentric cylindrical layers arranged in a barrel and covers the angle range $23° < \theta < 139°$ (θ being the polar angle from the z axis), which corresponds to 86% of the full solid angle. The three layers at radii of 30.0 mm, 45.5 mm, and 60.5 mm surround the beam pipe, a double-wall beryllium cylinder of 2.3 cm radius and 1 mm thickness. Three layers are constructed from eight, ten, and fourteen independent ladders from inner to outer, respectively. Each ladder consists of double-sided silicon strip detectors (DSSDs) reinforced by boron-nitride support ribs.

The S6936 DSSDs fabricated by Hamamatsu Photonics (HPK) are used for SVD. Each DSSD consists of 1280 sense strips and 640 readout pads on each side. The overall DSSD size is 57.5×33.5 mm^2 with 300 μm thickness. In total 102 DSSDs are used and the number of readout channels is 81920.

For the z-coordinate measurement, the n-side strips are used and a double-metal structure running parallel to z is employed to route the signals from orthogonal z-sense strips to the ends of the detector. Adjacent strips are connected to a single readout trace on the second metal layer which gives an effective strip pitch of 84 μm. A p-stop structure is employed to isolate the z-sense strips. A relatively large thermal noise ($\sim 600e^-$) is observed due to the common-p-stop design. On the ϕ side, where ϕ is the azimuth angle around the z axis, only every other sense-strip is connected to a readout channel. Charge collected by the floating strips in between is read from adjacent strips by means of capacitive charge division.

The readout chain for DSSDs is based on the VA1 integrated circuit [27]. The VA1 chip is a 128-channel CMOS integrated circuit fabricated in the Austrian Micro Systems (AMS) 1.2-μm CMOS process. It was specially designed for the readout of silicon vertex detectors and other small-signal devices. VA1 has excellent noise performance and reasonably good radiation tolerance of 200 kRad [28].

The track-matching efficiency is defined as the probability that a CDC track within the SVD acceptance has associated SVD hits in at least two layers, and in at least one layer with both the r-ϕ and r-z information, where r is the distance from the z axis. Tracks from K_S^0 decays are excluded since these tracks do not necessarily go through SVD. Figure 3.5 shows the SVD-CDC track matching efficiency for hadronic events as a function of time. The average matching efficiency is better than 98.7%, although slight degradation is observed after one year operation as a result of the gain loss of VA1 from radiation damage [26].

The impact parameter resolution for reconstructed tracks is measured as a function of the track momentum p (measured in GeV/c) and the polar angle θ to be

$$\sigma_{r\phi} = \sqrt{19^2 + \left(\frac{50}{p\beta \sin^{3/2}\theta}\right)^2}\ \mu\text{m}, \tag{3.1}$$

$$\sigma_z = \sqrt{36^2 + \left(\frac{42}{p\beta \sin^{5/2}\theta}\right)^2}\ \mu\text{m}, \tag{3.2}$$

as shown in Fig. 3.6.

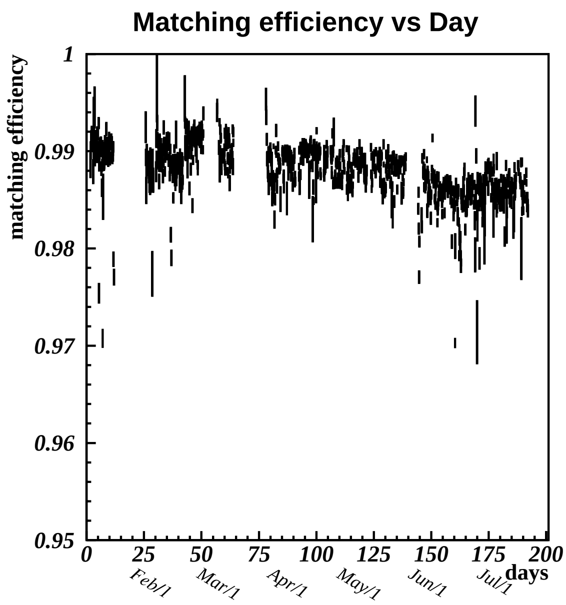

Figure 3.5: SVD-CDC track matching efficiency as a function of the date of data taking.

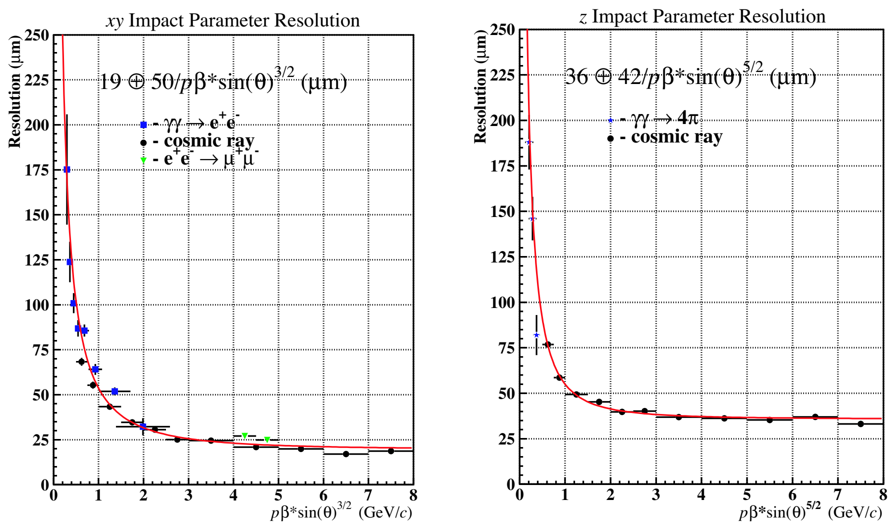

Figure 3.6: Impact parameter resolutions for the r-ϕ plane (left) and z direction (right).

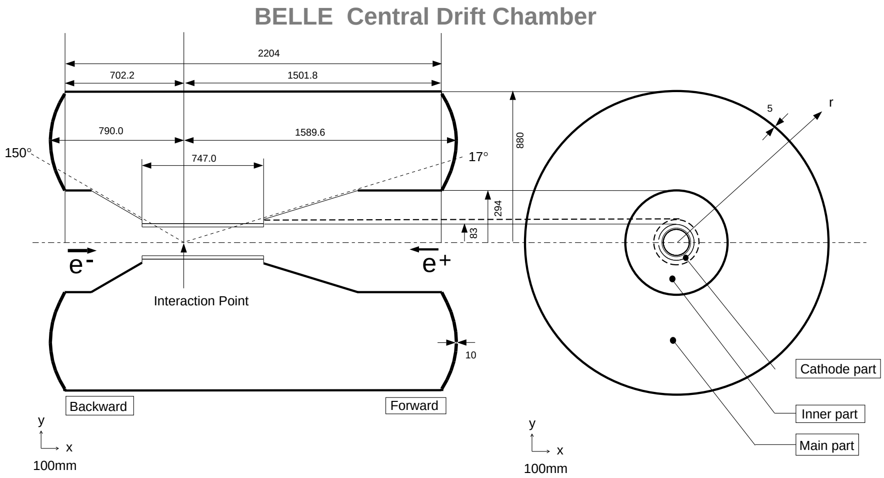

Figure 3.7: Overview of the CDC structure.

3.2.2 Central Drift Chamber (CDC)

The efficient reconstruction of charged particle tracks and precise determination of their momenta are the essential ingredient to almost all of the measurements in the Belle experiment. Specifically, the resolution of a transverse momentum p_t, which is the momentum component transverse to the z axis, is required to be $\sigma_{p_t} \sim 0.5\%\sqrt{1+{p_t}^2}$ (p_t in GeV/c) for all charged particles with $p_t \geq 100$ MeV/c in the polar angle region of $17° \leq \theta \leq 150°$. In addition, the charged particle tracking system is expected to provide important information for the trigger system and particle identification information in the form of precise dE/dx measurements for charged particles.

CDC [29] was designed and constructed to meet above requirements for the central tracking system. Since the majority of the decay particles of a B meson have momenta lower than 1 GeV/c, the minimization of multiple scattering is important for improving the momentum resolution. Therefore, the use of a low-Z gas is desirable, while a good dE/dx resolution must be retained.

The structure of CDC is shown in Fig. 3.7. It is asymmetric in the z direction to provide an angular coverage of $17° \leq \theta \leq 150°$, which corresponds to 92% of the full solid angle. The longest wires are 2400 mm long. The outer radius is 874 mm and the inner one is extended down to 103.5 mm without any walls in order to obtain good tracking efficiency for low-p_t tracks by minimizing the material thickness. The forward and backward small-r regions have conical shapes in order to clear the accelerator components while maximizing the acceptance.

CDC is a small-cell cylindrical drift chamber with 50 layers of anode wires, which consist of 32 axial- and 18 stereo-wire layers, and three cathode strip layers. Axial

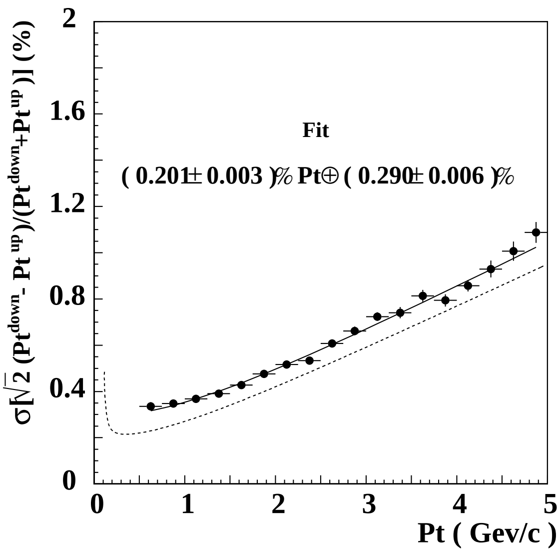

Figure 3.8: $p_{\rm t}$ dependence of $p_{\rm t}$ resolution for cosmic rays. The solid curve shows the fitted result ($0.201\% p_{\rm t} \oplus 0.290\%/\beta$) and the dotted curve ($0.118\% p_{\rm t} \oplus 0.195\%$) shows the ideal expectation for $\beta = 1$ particles.

wires are parallel to the z axis, while stereo wires slant to the z axis to provide z position information. Stereo wires also provide a highly efficient fast z-trigger combined with the cathode strips. CDC has a total of 8400 drift cells.

A low-Z gas mixture, which consists of 50% He and 50% ethane (C_2H_6), is used to minimize multiple Coulomb scattering to ensure a good momentum resolution, especially for low momentum particles. Since low-Z gases have a smaller photo-electric cross-section than argon-based gases, they have the additional advantage of reduced background from synchrotron radiation. Even though the gas mixture has a low Z, a good dE/dx resolution is provided by the large ethane component.

The tracks of charged particles are reconstructed by the Kalman filtering method [30], taking into account the effects of the multiple Coulomb scattering and the energy loss, as well as the effects due to the non-uniformity of the measured magnetic field. The spatial resolution for tracks passing near the middle of the drift space is measured to be $\sim 130\ \mu$m. The $p_{\rm t}$ resolution as a function of $p_{\rm t}$ is shown in Fig. 3.8. The solid curve indicates the result fitted to the data points, i.e.,

$$\sigma_{p_{\rm t}}/p_{\rm t} = \sqrt{\left(\frac{0.29}{\beta}\right)^2 + (0.20 p_{\rm t})^2}\%, \tag{3.3}$$

where $p_{\rm t}$ is measured in GeV/c.

The dE/dx measurement in CDC can distinguish particle species, since the mean energy loss $\langle dE/dx \rangle$ for a charged particle is given as a function of the velocity in

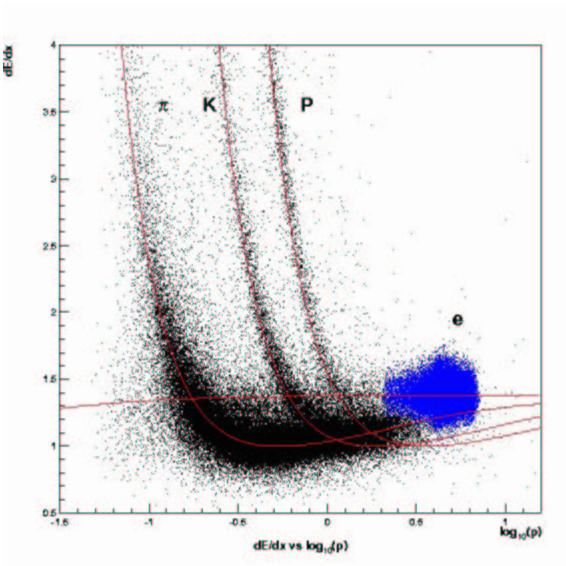

Figure 3.9: Truncated mean of dE/dx versus momentum observed in collision data.

units of c, $\beta \equiv v/c$, by the Bethe-Bloch equation. A scatter plot of measured $\langle dE/dx \rangle$ and particle momentum is shown in Fig. 3.9, together with the expected mean energy losses for different particle species. Populations of pions, kaons, protons, and electrons can be clearly seen. The $\langle dE/dx \rangle$ resolution is measured to be 7.8% in the momentum range from 0.4 to 0.6 GeV/c.

3.2.3 Aerogel Cherenkov Counter System (ACC)

Particle identification, specifically the ability to distinguish $\pi^{\pm}$ from $K^{\pm}$, plays an important role in the many analyses of B decays. An array of silica aerogel threshold Cherenkov counters is selected as a part of the Belle particle identification system to extend the momentum coverage beyond the reach of dE/dx measurements by CDC and time-of-flight measurements by TOF.

The Cherenkov radiations occur in case of

$$n > \frac{1}{\beta} = \sqrt{1 + \left(\frac{m}{p}\right)^2}, \tag{3.4}$$

where m and p are the mass and momentum of the particle, respectively, and n is the refractive index of the matter. Thus, there is the momentum region where the pions emit Cherenkov light, while the heavier than the pions, like kaons, do not.

The configuration of ACC [31] is shown in Fig. 3.10. ACC consists of 960 counter modules segmented into 60 cells in the ϕ direction for the barrel part and 228 modules arranged in five concentric layers for the forward end-cap part of the detector. All

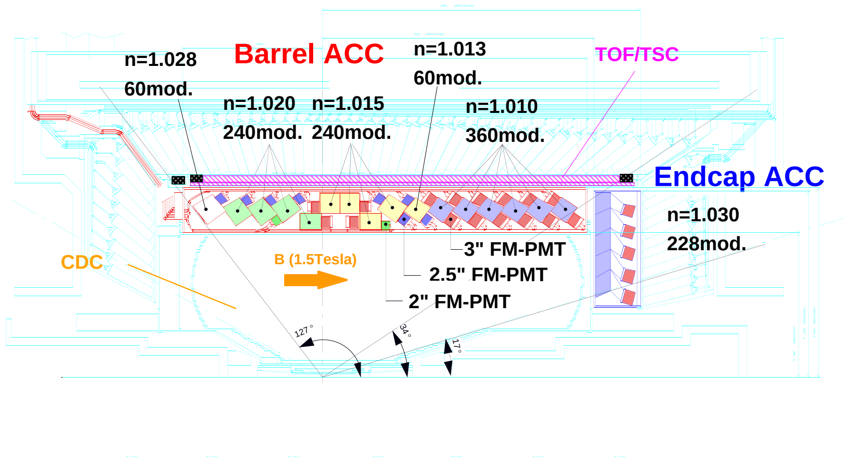

Figure 3.10: Arrangement of ACC at the central part of the Belle detector.

the counters are arranged in a semi-tower geometry, pointing to IP. In order to obtain the good pion/kaon separation for the whole kinematical range, the refractive indices of aerogels are selected to be between 1.01 and 1.03, depending on their polar angle region. Five aerogel tiles are stacked in a thin (0.2 mm thick) aluminum box of approximate dimensions $12 \times 12 \times 12$ cm^3. In order to detect Cherenkov lights effectively, one or two fine mesh-type photomultiplier tubes (FM-PMTs), which are operated in a magnetic field of 1.5 T [32], are attached directly to the aerogels at the sides of the box.

Figure 3.11 shows the measured pulse-height distribution for the barrel ACC for $e^{\pm}$ tracks in Bhabha events and $K^{\pm}$ candidates in hadronic events, which are selected by TOF and dE/dx measurements, together with the expectations from Monte Carlo (MC) simulations. The figure demonstrates a clear separation between high-energy electrons and below-threshold particles. It also indicates good agreement between the data and MC simulations.

3.2.4 Time-of-Flight Counters (TOF)

A time-of-flight (TOF) detector system using plastic scintillation counters is very powerful for particle identification in e^+e^- collider detectors. For a 1.2 m flight path, the TOF system with 100 ps time resolution is effective for particle momenta below about 1.2 GeV/c, which encompasses 90% of the particles produced in $\Upsilon(4S)$ decays. It can provide clean and efficient b-flavor tagging. In addition to particle identification, the TOF counters provide fast timing signals for the trigger system.

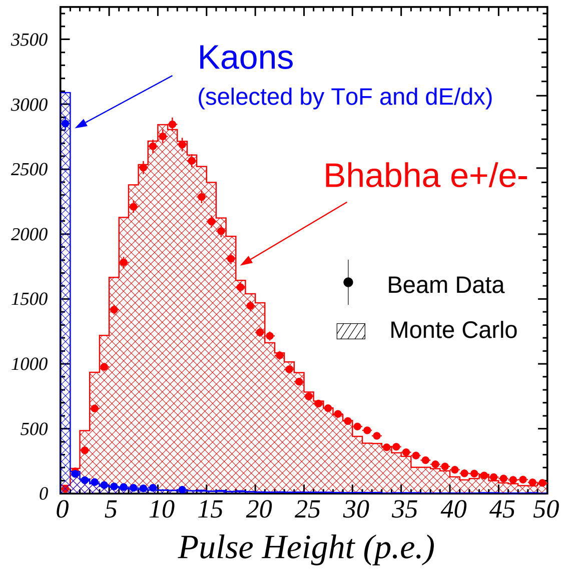

Figure 3.11: Pulse-hight spectra in units of photoelectrons observed by barrel ACC for electrons and kaons. The MC expectations are superimposed.

To avoid pile-up in the trigger queue, the rate of the TOF trigger signals must be kept below 70 kHz. Simulation studies indicate that to keep the fast trigger rate below 70 kHz in any beam background conditions, the TOF counters should be augmented by thin trigger scintillation counters (TSC).

The following equation is satisfied using a measured time-of-flight T with TOF and a measured momentum p with CDC:

$$T = \frac{L}{c\beta} = \frac{L}{c}\sqrt{1 + \left(\frac{m}{p}\right)^2}, \tag{3.5}$$

where L is a length of the flight. For example, when $L = 120$ cm and the particle with momentum $p = 1.2$ GeV/c flies into TOF, if that particle is a pion ($m_\pi = 140$ MeV/c^2) then $T = 4.0$ ns, while if that particle is a kaon ($m_K = 494$ MeV/c^2) then $T = 4.3$ ns. Thus, the difference of T between pion and kaon is ~ 300 ps and 3σ K/π separation is provided with the time resolution of 100 ps.

The Belle TOF system [33] consists of 128 TOF counters and 64 TSC counters. Two trapezoidally shaped TOF counters and one TSC counter, with a 1.5-cm intervening radial gap, form one module. In total 64 TOF/TSC modules located at a radius of 1.2 m from IP cover a polar angle range from 34° to 120°. The minimum transverse momentum to reach the TOF counters is about 0.28 GeV/c. Module dimensions are given in Fig. 3.12. These modules are individually mounted on the inner wall of the barrel ECL container. The 1.5 cm gap between the TOF counters and TSC counters is introduced to isolate TOF from photon conversion

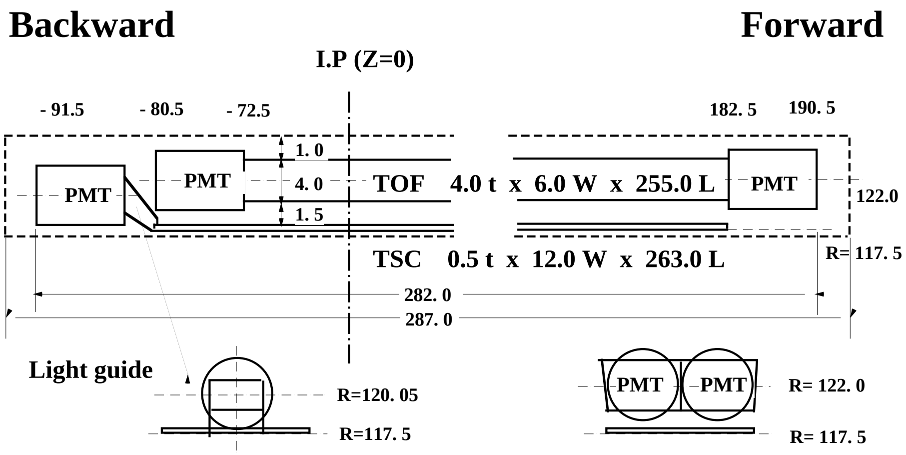

Figure 3.12: Dimensions of a TOF/TSC module.

backgrounds by taking the coincidence between the TOF and TSC counters. Electrons and positrons created in the TSC layer are impeded from reaching the TOF counters due to this gap in a 1.5 T field. The width of the TOF counter is approximately 6 cm. Fine-mesh-dynode photomultiplier tubes (FM-PMTs) are attached to the TOF counter ends with an air gap of ~ 0.1 mm. In the case of the TSC counters the tubes are glued to the light guides at the backward ends. The air gap for the TOF counter selectively passes earlier arrival photons and reduces a gain saturation effect of FM-PMT due to large pulses at a very high rate. As the time resolution is determined by the rising edge of the time profile of arrival photons at PMT, the air gap hardly affects the time resolution.

Figure 3.13 shows time resolutions for forward and backward PMTs and for the weighted average time as a function of z. The resolution for the weighted average time is about 100 ps with a small z dependence. This satisfies the design goal.

Figure 3.14 shows the mass distribution for each track in hadron events, calculated according to Eq. (3.5) using the momentum of the particle determined from the CDC track fit assuming the muon mass. Clear peaks corresponding to $\pi^{\pm}$, $K^{\pm}$, and protons are seen. The data points are in good agreement with a MC prediction (histogram) obtained by assuming $\sigma_{\mathrm{TOF}} = 100$ ps.

3.2.5 Electromagnetic Calorimeter (ECL)

The main purpose of the electromagnetic calorimeter is the detection of photons from B-meson decays with high efficiency and good resolutions in energy and position. Since most of these photons are end products of cascade decays, they have relatively low energies and, thus, good performance below 500 MeV is especially important. On the other hand, since important two-body decay modes, such as $B \to K^{*}\gamma$ and $B^{0} \to$

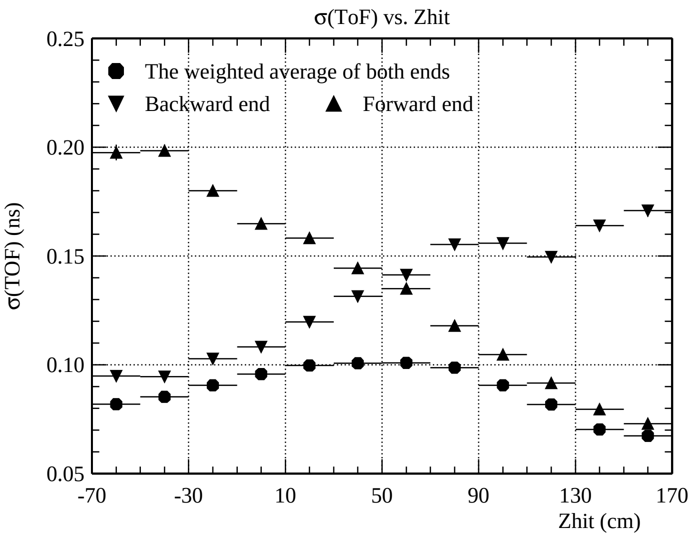

Figure 3.13: Time resolution of TOF for μ-pair events.

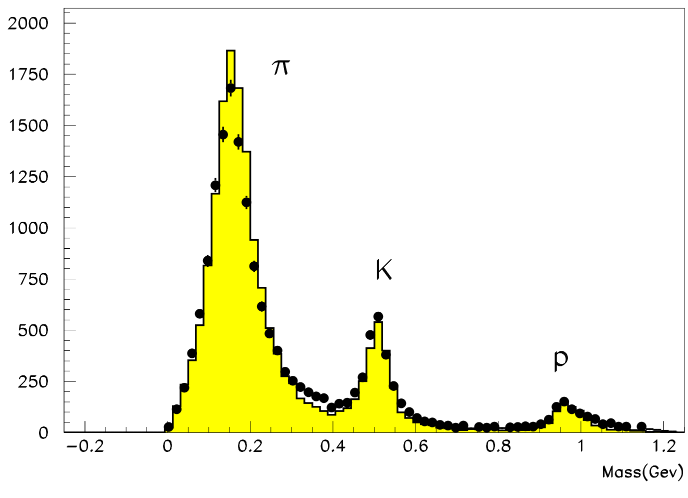

Figure 3.14: Mass distribution from TOF measurements for particle momenta below 1.2 GeV/c. A MC prediction is also shown (histogram).

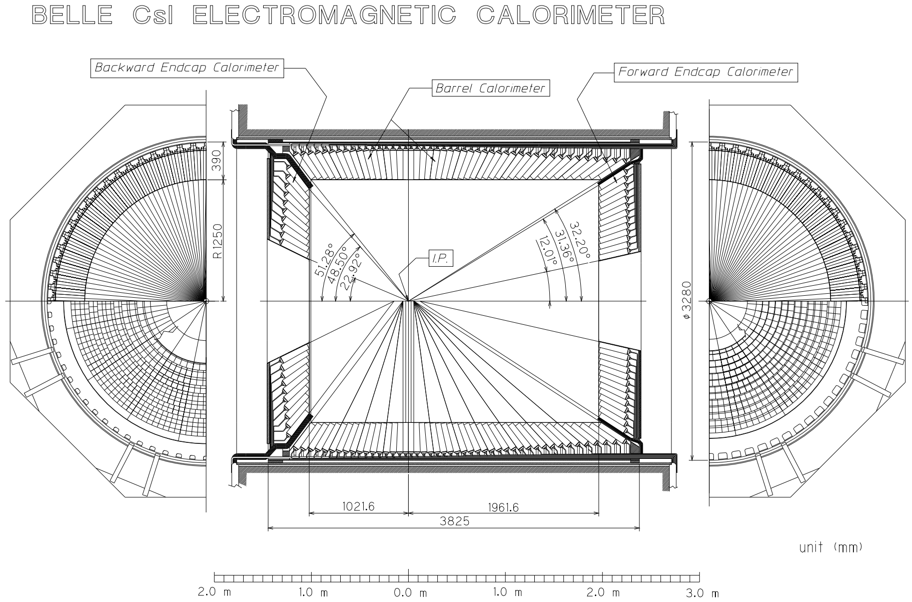

Figure 3.15: Configuration of ECL.

$\pi^0\pi^0$, produce photons energies up to 4 GeV, good resolution for high momentum region is also needed to reduce backgrounds for these modes. Electron identification in Belle relies primarily on a comparison of the charged particle momentum and the energy deposits in the electromagnetic calorimeter. Good electromagnetic energy resolution results in better hadron rejection. High momentum π^0 detection requires the separation of two nearby photons and a precise determination of their opening angle. This requires a fine-grained segmentation in the calorimeter.

In order to satisfy the above requirements, we use a highly segmented array of CsI(Tl) crystals with silicon photodiode readout installed in a magnetic field of 1.5 T inside a superconducting solenoid magnet. CsI(Tl) crystals have various nice features such as a large photon yield, weak hygroscopicity, mechanical stability, and moderate price.

The overall configuration of the Belle calorimeter system, ECL [34], is shown in Fig. 3.15. ECL consists of the barrel section of 3.0 m in length with the inner radius of 1.25 m and the annular end-caps at $z = +2.0$ and -1.0 m from IP. Each crystal has a tower-like shape and is arranged so that it points almost to IP. There is a small tilt angle of $\sim 1.3°$ in the θ and ϕ directions in the barrel section to avoid photons escaping through the gap of the crystals. End-cap crystals are tilted by $\sim 1.5°$ and $\sim 4°$ in the θ direction in the forward and backward sections, respectively. The calorimeter covers the polar angle region of $17.0° < \theta < 150.0°$, corresponding to a total solid-angle coverage of 91% of 4π. Small gaps between the barrel and end-cap crystals provide a pathway for cables and room for supporting members of the inner detectors. The loss of solid angle associated with these gaps is approximately 3% of

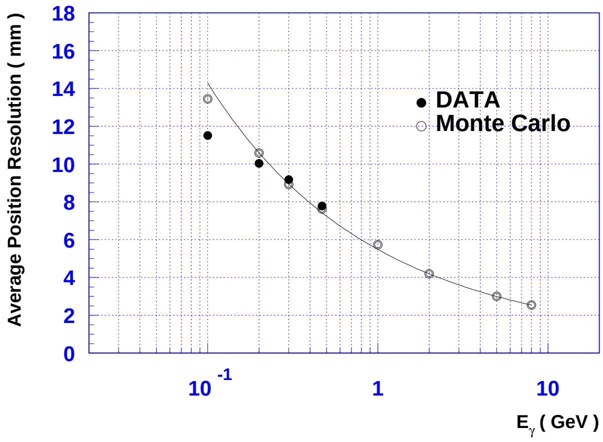

Figure 3.16: Energy dependence of the average position resolution. The solid curve is the result of the fit.

the total acceptance. The entire system contains 8736 CsI(Tl) counters and weighs 43 tons.

The size of each crystal is determined by the condition that approximately 80% of the total energy deposited by a photon injected at the center of the crystal is contained in that crystal. Typical dimension of a crystal is 55 mm × 55 mm (front face) and 65 mm × 65 mm (rear face) for the barrel part. The 30 cm length, which corresponds to 16.2 radiation length (16.2 X_0), is chosen to avoid deterioration of the energy resolution at high energies due to the fluctuations of shower leakages out the rear of the counter.

The energy dependence of the average position resolution is shown in Fig. 3.16 as a function of photon energy. The points above 1 GeV are the MC data. The solid curve is fitted by the relation

$$\sigma_{\text{pos}} = 0.27 + \frac{3.4}{\sqrt{E}} + \frac{1.8}{\sqrt[4]{E}} \text{ mm}, \tag{3.6}$$

where E is measured in units of GeV.

The energy resolution is obtained from the beam test to be

$$\frac{\sigma_E}{E} = \sqrt{\left(\frac{0.066}{E}\right)^2 + \left(\frac{0.81}{\sqrt[4]{E}}\right)^2 + 1.34^2}\%, \tag{3.7}$$

where E is measured in units of GeV. Figures 3.17 show the energy resolutions measured from Bhabha events. The energy resolution was achieved to be 1.7% for the barrel ECL, and 1.74% and 2.85% for the forward and backward ECL, respectively, as shown in Fig. 3.17.

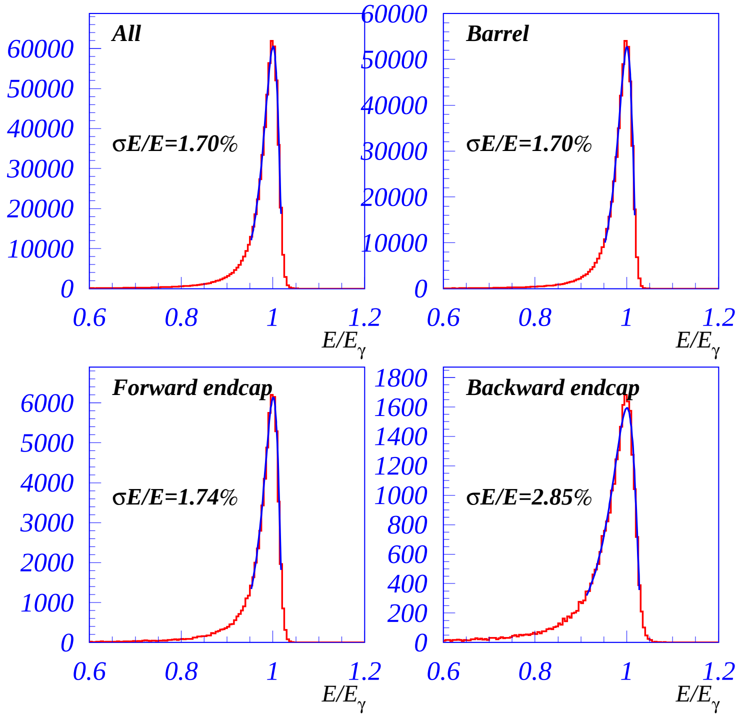

Figure 3.17: Energy resolutions measured from Bhabha event samples for overall (upper-left), barrel (upper-right), forward end-cap (lower-left), and backward end-cap (lower-right).

3.2.6 K_L^0 and Muon Detection System (KLM)

KLM [35] is designed to identify K_L^0's and muons with high efficiency over a broad momentum range greater than 600 MeV/c.

KLM consists of alternating layers of charged particle detectors and 4.7 cm-thick iron plates. The barrel-shaped region around IP covers an angular range from 45° to 125° in the polar angle and the end-caps in the forward and backward directions extend this range to 20° and 155°. There are 15 detector layers and 14 iron layers in the octagonal barrel region and 14 detector layers in each of the forward and backward end-caps. The iron plates provide a total of 3.9 interaction lengths of material for a particle traveling normal to the detector planes. In addition, ECL provides another 0.8 interaction length of material to convert K_L^0's. K_L^0 that interacts in the iron or ECL produces a shower of ionizing particles. The location of this shower determines the direction of K_L^0, but fluctuations in the size of the shower do not allow a useful measurement of the K_L^0 energy. The multiple layers of charged particle detectors and iron allow the discrimination between muons and charged hadrons ($\pi^\pm$ or $K^\pm$) based upon their range and transverse scattering. Muons travel much farther with smaller deflections on average than strongly interacting hadrons.

The detection of charged particles is provided by glass-electrode-resistive plate counters (RPCs) [36]. Resistive plate counters have two parallel plate electrodes with high bulk resistivity ($\geq 10^{10}$ Ωcm) separated by a gas-filled gap. We choose a non-combustible mixture of 62% HFC-134a, 30% argon, and 8% butane silver [37]. Butane silver is a mixture of approximately 70% n-butane and 30% iso-butane. In the streamer mode, an ionizing particle traversing the gap initiates a streamer in the gas that results in a local discharge of the plates. This discharge is limited by the high resistivity of the plates and the quenching characteristics of the gas. The discharge induces a signal on external pickup strips, which can be used to record the location and the time of the ionization.

Figure 3.18 shows the cross-section of a superlayer for the barrel region, in which two RPCs are sandwiched between the orthogonal θ and ϕ pickup-strips with the ground planes for signal reference and proper impedance. This unit structure of two RPCs and two readout-planes is enclosed in an aluminum box and is less than 3.7 cm thick. Each RPC is electrically insulated with a double layer of 0.125 mm thick mylar. Signals from both RPCs are picked up by copper strips above and below the pair of RPCs, providing a three-dimensional space point for particle tracking. Each barrel module has two rectangular RPCs with 48 z pickup strips perpendicular to the beam direction. The smaller seven superlayers closest to IP have 36 ϕ strips and the outer eight superlayers have 48 ϕ strips orthogonal to the z strips. Each end-cap superlayer module contains 10 π-shaped RPCs and have the 96 ϕ and 46 θ pickup-strips.

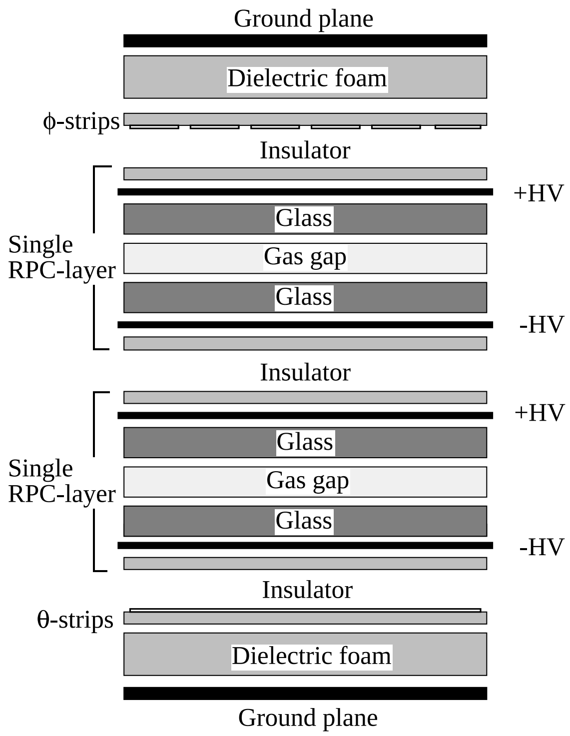

Figure 3.18: Cross-section of a KLM superlayer.

Figure 3.19 shows a histogram of the difference between the direction of the K_L^0 cluster candidate and the missing momentum direction in data. The missing momentum vector is calculated using all the other measured particles in the event. The histogram shows a clear peak where the direction of the neutral cluster measured in KLM is consistent with the missing momentum in the event. A large deviation of the missing momentum direction from the neutral cluster direction is mainly due to undetected neutrinos and particles escaping the detector acceptance.

3.2.7 Extreme Forward Calorimeter (EFC)

In order to improve the experimental sensitivity to some physics processes such as $B \to \tau\nu$, EFC [38] is needed to further extend the polar angle coverage by ECL, $17° < \theta < 150°$. EFC covers the angular range from 6.4° to 11.5° in the forward direction and 163.3° to 171.2° in the backward direction. EFC is also required to function as a beam mask to reduce backgrounds for CDC. In addition, EFC is used for a beam monitor for the KEKB control and a luminosity monitor for the Belle experiment. It can also be used as a tagging device for two-photon physics.

Since EFC is placed in the very high radiation-level area around the beam pipe near IP, it is required to be radiation-hard. Therefore, a radiation-hard BGO (Bis-

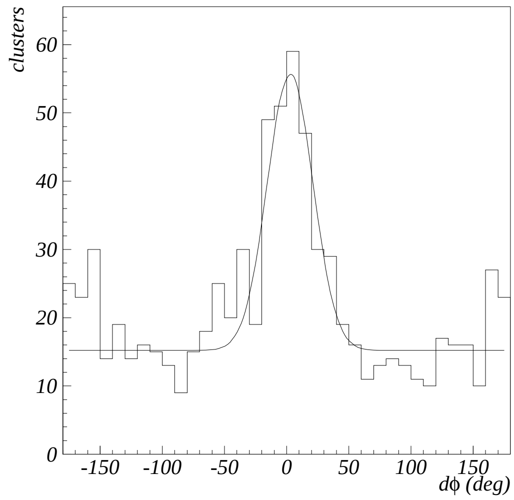

Figure 3.19: Difference between the neutral cluster and the direction of missing momentum in KLM.

muth Germanate, $Bi_4Ge_3O_{12}$) crystal calorimeter is used for EFC. The detector is segmented into 32 in ϕ and 5 in θ for both the forward and backward detectors. The radiation lengths of the forward and backward crystals are 12 and 11, respectively.

The energy sum spectra for Bhabha events show a correlation between the forward and backward EFC detectors. A clear peak at 8 GeV with a resolution of 7.3% (rms) is seen for the forward EFC, while a clear peak at 3.5 GeV with a resolution of 5.8% (rms) is seen in the backward EFC. These results are compatible with the beam test results.

3.2.8 Solenoid Magnet

A superconducting solenoid provides a magnetic field of 1.5 T in a cylindrical volume of 3.4 m in diameter and 4.4 m in length [39]. The coil is surrounded by a multilayer structure consisting of iron plates and calorimeters, which is integrated into a magnetic return circuit. The iron structure of the Belle detector serves as the return path of magnetic flux and an absorber material for KLM. It also provides the overall support for all of the detector components.

3.2.9 Trigger (TRG)

The cross-section for physics events of interest, like $B\overline{B}$ event, is smaller than the background processes. Therefore, they have to be triggered by appropriately re-

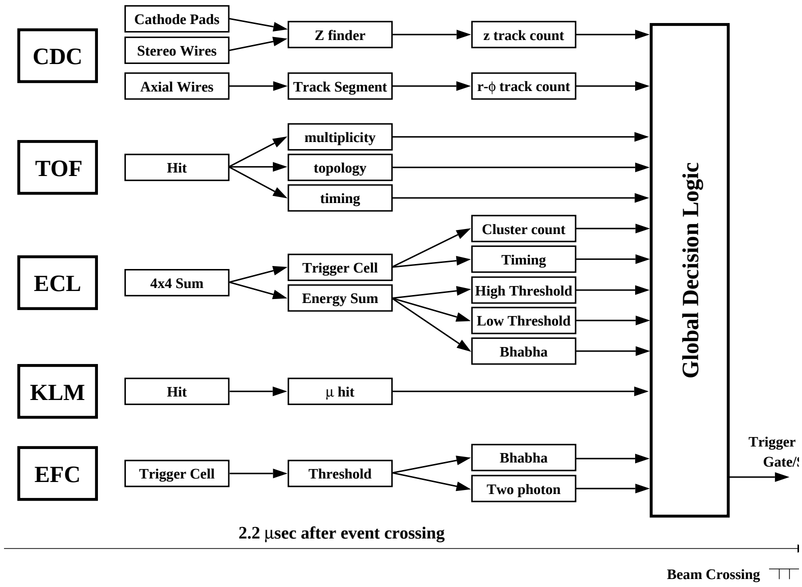

Figure 3.20: Level-1 trigger system for the Belle detector.

strictive conditions. Because of the high beam current, high beam backgrounds are expected. Since the rates are very sensitive to actual accelerator conditions, it is difficult to make a reliable estimate. Therefore, the trigger system is required to be robust against unexpectedly high beam background rates. The trigger conditions should be flexible so that background rates are kept within the tolerance of the data acquisition system, while the efficiency for physics events of interest is kept high. It is important to have redundant triggers to keep the efficiency high even for varying conditions. The Belle trigger system is designed to satisfy these requirements.

The Belle trigger system consists of the Level-1 hardware trigger and the Level-3 software trigger. The latter is designed to be implemented in the online computer farm. Figure 3.20 shows the schematic view of the Belle Level-1 trigger system [40]. It consists of the sub-detector trigger systems and the central trigger system called the Global Decision Logic (GDL). The sub-detector trigger systems are based on two categories: track triggers and energy triggers. CDC and TOF are used to yield trigger signals for charged particles. CDC provides r-ϕ and r-z track trigger signals. The ECL trigger system provides triggers based on the total energy deposit and the cluster counting of crystal hits. These two categories allow sufficient redundancy. The KLM trigger gives additional information on muons and the EFC triggers are used for tagging two photon events as well as Bhabha events. The sub-detectors process event signals in parallel and provide trigger information to GDL, where all information is combined to characterize an event type. Information from SVD is not implemented in the present trigger arrangement. The trigger system provides the trigger signal with the fixed time of 2.2 μs after the event occurrence. The Belle

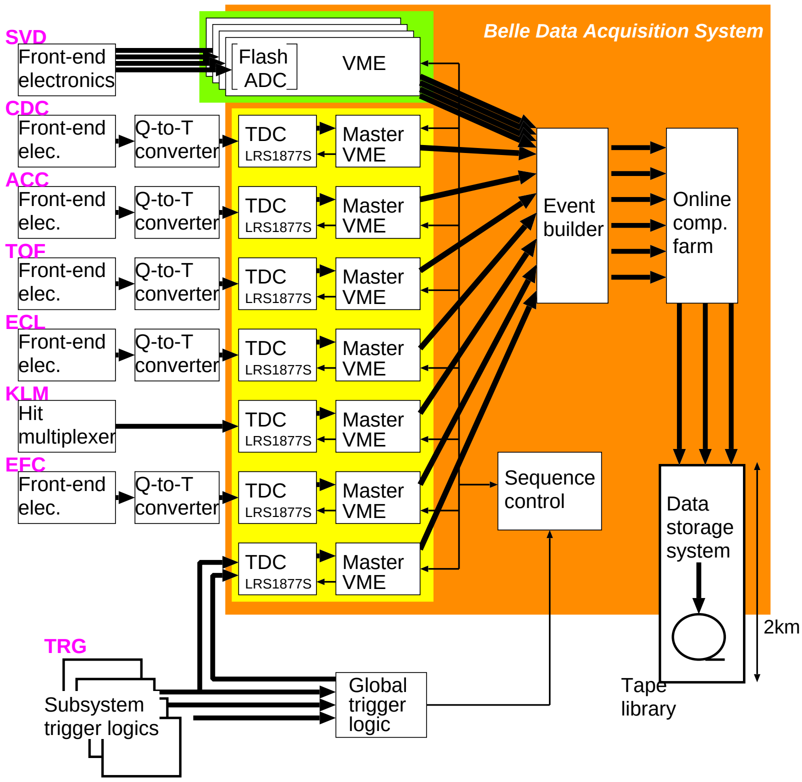

Figure 3.21: Belle DAQ system overview.

trigger system, including most of the sub-detector trigger systems, is operated in a pipelined manner with clocks synchronized to the KEKB accelerator RF signal.

In a typical running condition, the average trigger rate is about 200 Hz. The trigger rate is dominated by the beam background. The trigger efficiency is monitored from the data using the redundant triggers. Each of the multitrack, total energy, and isolated cluster counting triggers provides more than 96% efficiency for multi-hadronic data samples. The combined efficiency is more than 99.5%.

3.2.10 Data Acquisition (DAQ)

In order to satisfy the data acquisition requirements so that it works at 500 Hz with a deadtime fraction of less than 10%, the distributed-parallel system is devised. The global scheme of the system is shown in Fig. 3.21. The entire system is segmented into seven subsystems running in parallel, each handling the data from a sub-detector. Data from each subsystem are combined into a single event record by an event builder, which converts "detector-by-detector" parallel data streams to an "event-by-event" data river. The event builder output is transferred to an online computer farm, where another level of event filtering is done after the fast event reconstruction. The data are then sent to a mass storage system located at the computer center via optical fibers.

A typical data size of a hadronic event by $B\overline{B}$ or $q\overline{q}$ production is measured to be about 30 kB, which corresponds to the maximum data transfer rate of 15 MB/s.

3.3 Offline Computing System and Software

The computing and software system is of great importance to the Belle experiment as very complex data analysis techniques using a large amount of data are required for physics discoveries. A traditional high energy physics (HEP) computing model is adopted by the Belle collaboration. Namely, the Belle collaboration choose to use tape library systems with the sequential access method for the input and output of experimental data as the mass storage system.

All software except for a few HEP-specific and non-HEP-specific free software packages is developed by the members of the Belle collaboration. In particular, the mechanisms to handle event structure and input and output formatting and to process events in parallel on a large Symmetric Multiple Processor (SMP) compute server are developed locally using C and C++ programming languages.

3.3.1 Analysis Framework

The event processing framework, called Belle AnalysiS Framework (BASF) [41], takes users' reconstruction and analysis codes as modules which are dynamically linked at the run time. A module is written as an object of a class of C++. The class, inherited from the module class of BASF which has virtual functions for events, begins and ends run processing and other utility functions such as initialization, termination, and histogram definitions. Modules written in Fortran and C can also be linked using wrapper functions.

The data transfer between modules is managed by PANTHER, an event and I/O management package developed by the Belle collaboration. PANTHER describes the logical structure and inter-relationships of the data using an entity relationship model. In order to store data (structure) in the event structure one writes a description file as an ASCII text file. A PANTHER utility converts the description file into C and C++ header files and source code. The user will include the header files in his/her code and the source code is compiled and linked into the user module to have access to the data structure in the module.

The standard reconstruction modules for subdetectors and global reconstruction of four momenta, production vertices, and likelihoods for being specific species such as electrons, muons, pions, kaons, protons, and gammas of charged and neutral particles are prepared and used to produce physics results as well as detector performance results described in this thesis.

3.3.2 Monte Carlo Simulator

The MC events are generated using the QQ event generator, which was originally developed by the CLEO collaboration [42]. The QQ event generator can handle both $\Upsilon(4S)$ decays and continuum ($e^+e^- \to q\bar{q}$, $q = u, d, s, c$) processes. It is modified for the Belle experiment and the decay modes and their branching ratios are updated by the Belle collaboration to include the up-to-date measurements. The EvtGen event generator, which was originally developed by the BaBar collaboration [43], is also used for some analyses.

The response of the Belle detector is modeled by a GEANT3-based full-simulation program [44]. The simulated events are then reconstructed and analyzed with the same procedure as is used for the real data.

Chapter 4

Event Reconstruction

In this chapter, we describe the event reconstruction procedures of hadronic B decays. First, the $B\overline{B}$ events are selected from the whole data sample. Then, the hadronic B decays are reconstructed.

For the lifetime analysis, the following hadronic B decays are used [1]:

$$B^0 \to D^-\pi^+,\ D^{*-}\pi^+,\ D^{*-}\rho^+,\ J/\psi K_S^0,\ J/\psi K^{*0}, \tag{4.1}$$

$$B^+ \to \overline{D}{}^0\pi^+,\ J/\psi K^+. \tag{4.2}$$

For the mixing analysis, we use the flavor-specific hadronic B decays:

$$B^0 \to D^-\pi^+,\ D^{*-}\pi^+,\ D^{*-}\rho^+. \tag{4.3}$$

We reconstruct B^0 decays to the following CP eigenstates f_{CP} for the $\sin 2\phi_1$ analysis:

$$B^0 \to J/\psi K_S^0,\ \psi(2S)K_S^0,\ \chi_{c1}K_S^0,\ \eta_c K_S^0 \tag{4.4}$$

for the CP eigenvalue $\xi_f = -1$, and

$$B^0 \to J/\psi K_L^0 \tag{4.5}$$

for $\xi_f = +1$. We also use

$$B^0 \to J/\psi K^{*0} \tag{4.6}$$

decays where K^{*0} decays to $K_S^0\pi^0$. Here the final state is a mixture of even and odd CP depending on the relative orbital angular momentum of the J/ψ and K^{*0}.

4.1 Data Sample

Figure 4.1 shows the daily and the total integrated luminosities of KEKB. The

[1] Throughout this thesis, when a decay mode is quoted the inclusion of the charge conjugate mode is implied.

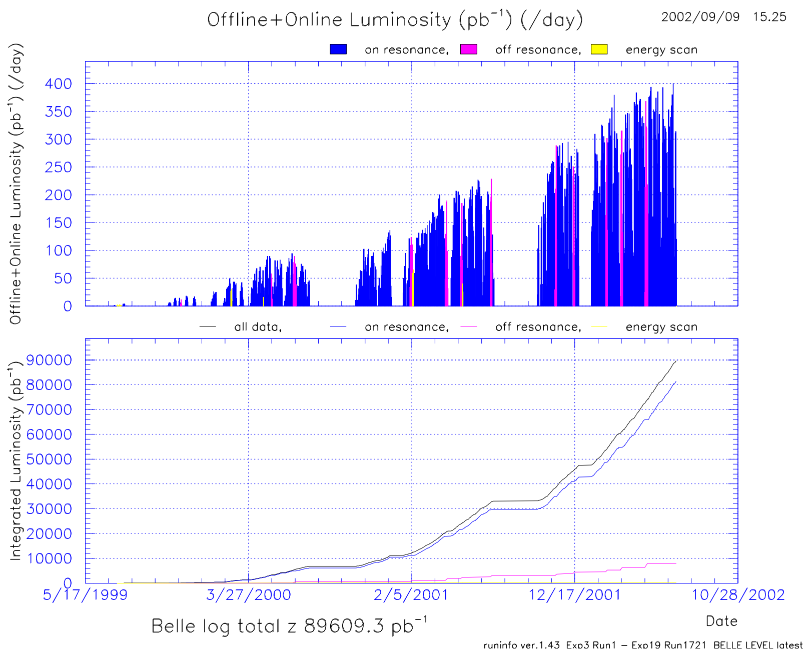

Figure 4.1: Integrated luminosity per day (upper) and total integrated luminosity (lower).

measurements of the B meson lifetimes and the B^0-$\overline{B}^0$ oscillation frequency are based on the data taken from January 2000 to July 2001. The total integrated luminosity on the $\Upsilon(4S)$ resonance in this period is 29.1 fb^{-1}, which corresponds to approximately 31.3×10^6 $B\overline{B}$ pairs.

The measurement of the CP asymmetry is based on 78 fb^{-1} data sample collected from January 2000 through June 2002, corresponding to 85×10^6 $B\overline{B}$ pairs. The entire data sample is analyzed and reconstructed with the same procedure which contains a new track reconstruction algorithm that provides better performance with respect to the analyses for the lifetimes and Δm_d described in Chapter 5 and 6 or the previous measurement of $\sin 2\phi_1$ [45, 46].

4.2 $B\overline{B}$ Event Selection

Other than hadronic events, there exist several processes, QED processes like Bhabha or radiative Bhabha events, μ pair events, τ pair events, two-photon events, and beam-gas interactions, which have the similar or larger cross sections than the $B\overline{B}$ production. First, we need to distinguish hadronic events from such background events. In order to remove non-hadronic events, we apply the following selection criteria [47]:

- At least three "good" tracks must exist, where a "good" track satisfies the criteria, $|r| < 2.0$ cm and $|z| < 4.0$ cm at the closest approach to the beam axis, and transverse momentum $p_{\mathrm{t}} > 0.1$ GeV/c.

- At least two "good" clusters must be detected by ECL within the volume of $-0.7 < \cos\theta < 0.9$, where a "good" cluster has the energy deposit greater than 0.1 GeV.

- The energy sum $E_{\mathrm{sum}}^{\mathrm{cms}}$, which is the sum of the "good" cluster energies in ECL within $17° < \theta < 150°$ in the center of mass system (cms), is required to be between 10% and 80% of the total cms energy:

$$0.1 < E_{\mathrm{sum}}^{\mathrm{cms}}/\sqrt{s} < 0.8, \tag{4.7}$$

  where s is the square of the total cms energy.

- The sum of the z components of momenta of "good" tracks and "good" photons in the cms must be less than 50% of the total cms energy:

$$\left|\sum p_z^{\mathrm{cms}}\right| < 0.5\sqrt{s}, \tag{4.8}$$

  where "good" photons are defined as the "good" clusters within the CDC acceptance, i.e., $17° < \theta < 150°$, that are not associated with any tracks in CDC.

- The total visible energy $E_{\mathrm{vis}}^{\mathrm{cms}}$, which is calculated in the cms as a sum of the energies of "good" tracks assuming the pion mass and the energies of "good" photons, should be greater than 20% of the total cms energy:

$$E_{\mathrm{vis}}^{\mathrm{cms}} \geq 0.2\sqrt{s}. \tag{4.9}$$

- The event primary vertex, which is formed by all "good" tracks, must be within 1.5 cm and 3.5 cm from the detector origin in r and z directions, respectively.

From a MC study, the above selections retain more than 99% of $B\overline{B}$ events and 84% of continuum events, while the contribution from non-hadronic events, mainly the beam-gas and τ-pair events, is about 15% of the selected events.

For the reconstruction of the decay modes which include J/ψ, no further preselection is needed because $J/\psi \to \ell^+\ell^-$ signal is very clean. For the reconstruction of the other modes, we apply some more selection criteria to reduce the non-hadronic contribution:

- The ratio of the heavy-jet mass to the visible energy is greater than 0.25, or the heavy-jet mass is larger than 1.8 GeV/c^2:

$$M_{\mathrm{HJ}}/E_{\mathrm{vis}}^{\mathrm{cms}} > 0.25 \quad \text{or} \quad M_{\mathrm{HJ}} > 1.8 \text{ GeV}/c^2. \tag{4.10}$$

  The heavy-jet mass is calculated as follows: The event is split into two hemispheres by the plane perpendicular to the thrust axis; Form a jet by associating all "good" tracks in the same hemisphere; Then calculate the invariant mass of the jet using the "good" tracks by assuming the pion mass; The larger invariant mass is regarded as the heavy-jet mass. The heavy-jet mass is essentially the τ invariant mass.

- The modified energy sum $E_{\mathrm{sum}}^{\mathrm{cms}\prime}$, which is the sum of all "good" cluster energies in ECL in the cms without the requirement for the polar angle region, is greater than 18% of the cms energy, or the heavy-jet mass M_{HJ} is greater than 1.8 GeV/c^2:

$$E_{\mathrm{sum}}^{\mathrm{cms}\prime} > 0.18\sqrt{s} \quad \text{or} \quad M_{\mathrm{HJ}} > 1.8 \text{ GeV}/c^2. \tag{4.11}$$

- The averaged cluster energy $E_{\mathrm{sum}}^{\mathrm{cms}\prime}/N_{\mathrm{ECL}}$ is smaller than 1 GeV:

$$E_{\mathrm{sum}}^{\mathrm{cms}\prime}/N_{\mathrm{ECL}} < 1 \text{ GeV}, \tag{4.12}$$

  where N_{ECL} is the number of "good" clusters.

A MC study shows these selections can suppress the contributions of non-hadronic events to be less than 5%, while the efficiency of the $B\overline{B}$ events is still 99%.

To reduce the continuum background after the hadronic event selection, additional selections based on the event shape variables are applied for some decay modes. One is the ratio of second to zeroth Fox-Wolfram moments R_2. The i-th Fox-Wolfram moment H_i is defined as [48]

$$H_i = \sum_{j,k} \frac{|\vec{p}_j||\vec{p}_k|}{s} P_i(\cos\phi_{jk}), \tag{4.13}$$

where the indices j and k run over all the particles produced in that event, $\vec{p}_j$ is the momentum vector of j-th particle in the cms, ϕ_{jk} is the angle between $\vec{p}_j$ and $\vec{p}_k$, and $P_i(x)$ is the Legendre polynomial of order i. R_2 is defined as $R_2 \equiv H_2/H_0$. R_2, which varies from 0 to 1, is close to 1 if the event is jet-like, and is close to 0 if the event is spherical. Since $B\overline{B}$ events are spherical while continuum events are jet-like, we can reject continuum events by applying the selection of R_2. Figure 4.2 shows R_2 distribution for the whole data sample after the hadronic event selection. The R_2 distribution for continuum events is obtained from the off-resonance data which

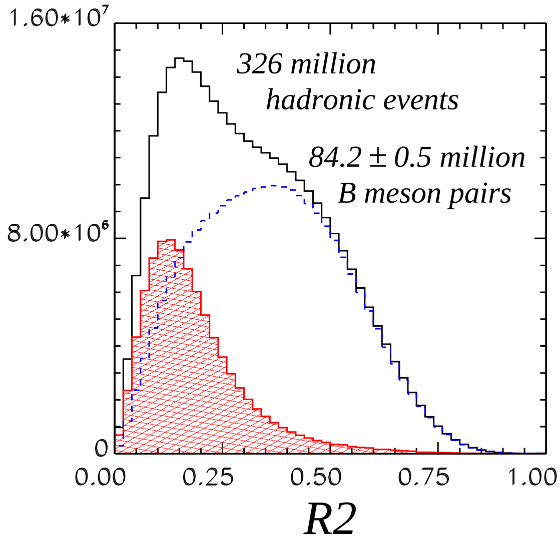

Figure 4.2: Distributions of R_2 for whole hadronic events (solid open histogram), continuum events (dashed open histogram), and $B\overline{B}$ events (solid hatched histogram).

are taken 50 MeV below the $\Upsilon(4S)$ resonance. The distribution for $B\overline{B}$ events is obtained by subtracting the continuum distribution. Another event shape variable is $\theta_{\rm th}$, the angle between the thrust axes of two B mesons. The thrust axis $\vec{n}_T$ is a unit vector which is set, for each event, such that the thrust T is maximized. The thrust T is defined by

$$T = \frac{\sum_i |\vec{p}_i \cdot \vec{n}_T|}{\sum_i |\vec{p}_i|}, \tag{4.14}$$

where the summation is over all final-state particles and $\vec{p}_i$ is the momentum vector of i-th particle in the cms. The $\cos\theta_{\rm th}$ distribution tends to be flat for $B\overline{B}$ signal events, while it tends to have a peak at $\cos\theta_{\rm th} = \pm 1$ for the continuum background. Figure 4.3 shows $\cos\theta_{\rm th}$ distributions for $B\overline{B}$ signal events and continuum background obtained from the MC sample. The selection criteria for R_2 and $\cos\theta_{\rm th}$ for each decay mode are described in the next section.

4.3 Reconstruction of the Hadronic B Decays

In this section, we describe the reconstruction of B mesons.

First, we reconstruct the B-decay products that further decay. Then, the B mesons are reconstructed by combining their decay products.

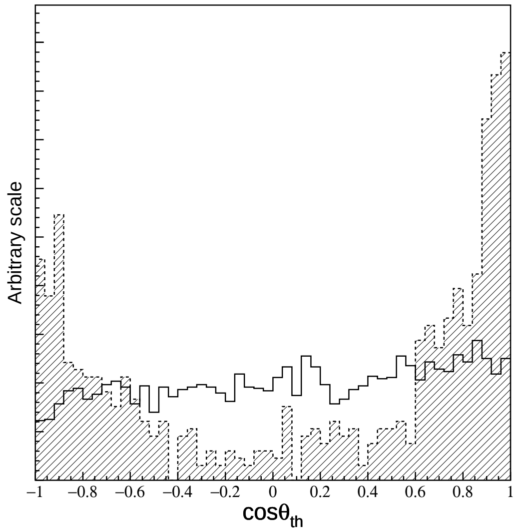

Figure 4.3: Distributions of $\cos\theta_{\rm th}$ for $B\overline{B}$ signal MC events (open histogram) and continuum background MC events (hatched histogram).

Table 4.1: Decay modes and mass ranges used to select the light mesons.

Decay Mode	Mass ranges (MeV/c^2)
$\pi^0 \to \gamma\gamma$	$124 < M_{\gamma\gamma} < 146$
$\rho^+ \to \pi^+\pi^0$	$\lvert M_{\pi^+\pi^0} - M_{\rho^+}\rvert < 150$
$K_S^0 \to \pi^+\pi^-$	$482 < M_{\pi^+\pi^-} < 514$
$K^{*0} \to K^+\pi^-$	$\lvert M_{K^+\pi^-} - M_{K^{*0}}\rvert < 75$

4.3.1 Reconstruction of Light Mesons

Decay modes of several light mesons that are used in the lifetime and mixing analyses are summarized in Table 4.1. Mass ranges used to select them are also shown.

π^0 Reconstruction

π^0 candidates are reconstructed from pairs of photon candidates with invariant masses between 124 and 146 MeV/c^2. The photon candidates are defined as isolated ECL clusters which have the energy more than 30 MeV and are not matched to any charged track. A mass-constrained fit is performed to improve the π^0 momentum resolution. A minimum π^0 momentum of 200 MeV/c is required.

ρ^+ Reconstruction

ρ^+ candidates are selected as $\pi^+\pi^0$ pairs which have invariant masses within 150 MeV/c^2 of the average ρ^+ mass [20]. Charged pion candidates are required to satisfy the loose particle identification (PID) selection that they are not tagged as kaons ($P(K/\pi) < 0.9$, where it is likely to be a kaon if $P(K/\pi)$ is close to one). The detail of PID is described in Appendix A.

K_S^0 Reconstruction

For $K_S^0 \to \pi^+\pi^-$ reconstruction, we select oppositely charged tracks pairs. A K_S^0 candidate is required to pass a kinematic fit with vertex constraint [49] to improve the momentum resolution. No PID selection is required for charged pion candidates. Instead, we select the candidates that satisfy the following requirements [50]:

- When both pions have associated SVD hits, the distance of the closest approach of both pion tracks in the z direction should be smaller than 1 cm.
- When only one of the two pions has associated SVD hits, the distance of the closest approach of both pion tracks to the nominal IP should be larger than 250 μm in r-ϕ plane.
- When neither of the two pions has an associated SVD hit, the ϕ coordinate of the $\pi^+\pi^-$ vertex point and the ϕ direction of the $\pi^+\pi^-$ candidate's momentum vector should agree within 0.1 rad.

The invariant mass of the K_S^0 candidate calculated after a kinematic fit is required to be between 482 and 514 MeV/c^2.

K^{*0} Reconstruction

K^{*0} candidates are reconstructed via $K^{*0} \to K^+\pi^-$ decays. Charged kaons are identified by requiring the kaon likelihood of a track to be consistent with that expected for a kaon track ($P(K/\pi) > 0.4$). Tracks which are not identified as kaons and not used as leptons in the J/ψ reconstruction (described later) are treated as charged pion candidates. If the difference between the invariant mass of $K^+\pi^-$ pair and the nominal K^{*0} mass is within 75 MeV/c^2, the pair is identified as K^{*0}.

4.3.2 Reconstruction of J/ψ

The reconstruction of J/ψ is performed using dilepton decays, $J/\psi \to e^+e^-$ and $\mu^+\mu^-$. For the $B^0 \to J/\psi K^{*0}$ mode, we detect oppositely charged tracks pairs where both tracks are required to be positively identified as leptons. The detail

Table 4.2: Invariant mass requirements for J/ψ reconstruction.

B decay mode	J/ψ decay mode	Mass range (MeV/c^2)
$B^0 \to J/\psi K_S^0, B^+ \to J/\psi K^+$	$J/\psi \to e^+e^-$	$-150 < M_{e^+e^-} - M_{J/\psi} < 36$
	$J/\psi \to \mu^+\mu^-$	$-60 < M_{\mu^+\mu^-} - M_{J/\psi} < 36$
$B^0 \to J/\psi K^{*0}$	$J/\psi \to e^+e^-$	$-147 < M_{e^+e^-} - M_{J/\psi} < 53$
	$J/\psi \to \mu^+\mu^-$	$-47 < M_{\mu^+\mu^-} - M_{J/\psi} < 53$

of the lepton identification is described in Appendix A. For $B^0 \to J/\psi K_S^0$ and $B^+ \to J/\psi K^+$ modes, the requirement for one of the tracks is relaxed: a track with an ECL energy deposit consistent with a minimum ionizing particle is accepted as a muon and a track that satisfies either the dE/dx or the ECL shower energy requirements as an electron. In order to remove either poorly reconstructed tracks or tracks that do not come from the interaction region, we require the closest approach of the track to the nominal IP to be within 5 cm in z direction for both lepton tracks. We accept the muon pairs which satisfy $-60 < M_{\mu^+\mu^-} - M_{J/\psi} < 36$ MeV/c^2 for $B^0 \to J/\psi K_S^0$ and $B^+ \to J/\psi K^+$, and $-47 < M_{\mu^+\mu^-} - M_{J/\psi} < 53$ MeV/c^2 for $B^0 \to J/\psi K^{*0}$, where $M_{\mu^+\mu^-}$ is the invariant mass of the muon pair and $M_{J/\psi}$ is the nominal J/ψ mass.

For e^+e^- pairs, a partial correction for final-state radiation or real bremsstrahlung in the detectors before ECL is performed by including the four-momentum of every photon detected within 50 mrad of the original e^+ or e^- directions in the e^+e^- invariant mass calculation. Nevertheless a radiative tail remains and we require the invariant mass of the electron pairs, $M_{e^+e^-}$, to be $-150 < M_{e^+e^-} - M_{J/\psi} < 36$ MeV/c^2 for $B^0 \to J/\psi K_S^0$ and $B^+ \to J/\psi K^+$, and $-147 < M_{e^+e^-} - M_{J/\psi} < 53$ MeV/c^2 for $B^0 \to J/\psi K^{*0}$. These invariant mass requirements for J/ψ selections are summarized in Table 4.2. Kinematical fits with vertex constraint and then with mass constraint are performed for the candidate lepton pairs to improve the resolution of J/ψ momentum. The candidate J/ψ momentum in the cms is required to be less than 2.0 GeV/c.

Figure 4.4 shows the invariant mass distributions of $J/\psi \to \ell^+\ell^-$ with the selection criteria applied for $B^0 \to J/\psi K_S^0$, for $\mu^+\mu^-$ pairs (upper), and for e^+e^- pairs (lower).

4.3.3 Reconstruction of Charm Mesons

$\overline{D}^0$, D^- Reconstruction

Three $\overline{D}^0$ decay modes, $\overline{D}^0 \to K^+\pi^-$, $\overline{D}^0 \to K^+\pi^-\pi^0$, and $\overline{D}^0 \to K^+\pi^-\pi^-\pi^+$, are used to reconstruct the $\overline{D}^0$ meson. $D^- \to K^+\pi^-\pi^-$ decay is used to reconstruct

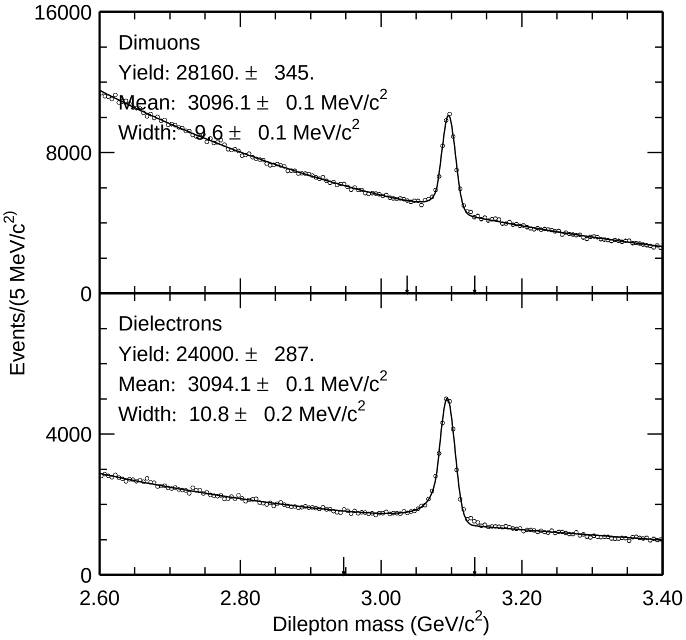

Figure 4.4: Invariant mass distributions for $J/\psi \to \mu^+\mu^-$ (upper) and $J/\psi \to e^+e^-$ (lower).

the D^- meson. Charged kaon candidates are required to pass the PID selections: $P(K/\pi) > 0.4$ and $P(p/K) < 0.9$. Charged pion candidates need to be tagged as a not-kaon: $P(K/\pi) < 0.9$. In order to reconstruct the position and momentum vector of the D meson precisely, at least two charged tracks are required to satisfy the SVD hit association criterion: we use tracks that have the associated z and r-ϕ hits in at least one layer and at least one additional layer with a z hit in the SVD to fit the vertex. First, the vertex position of the D meson is obtained from a kinematical fit to these tracks with a vertex constraint. Then, other tracks are refitted with the constraint that they come from this vertex point [49]. The position, momentum, and their error matrix of gammas from π^0 are also calculated again from the vertex point, and π^0 momentum is recalculated. By summing up these fitted momenta, four-momentum of D is obtained. The invariant mass distribution of each D decay mode is shown in Fig. 4.5. The requirement for the invariant mass is optimized for each decay mode of the B and D meson decays and is described in Section 4.3.4.

D^{*-} Reconstruction

D^{*-} candidates are formed by combining $\overline{D}^0$ candidates with soft π^-'s. No PID selection is required for the soft pions. The selection of D^{*-} is based on the mass difference $\Delta M \equiv M_{\overline{D}^0\pi^-} - M_{\overline{D}^0}$, where $M_{\overline{D}^0\pi^-}$ is the invariant mass of the combination of the $\overline{D}^0$ and soft pion candidates and $M_{\overline{D}^0}$ is the invariant mass of the

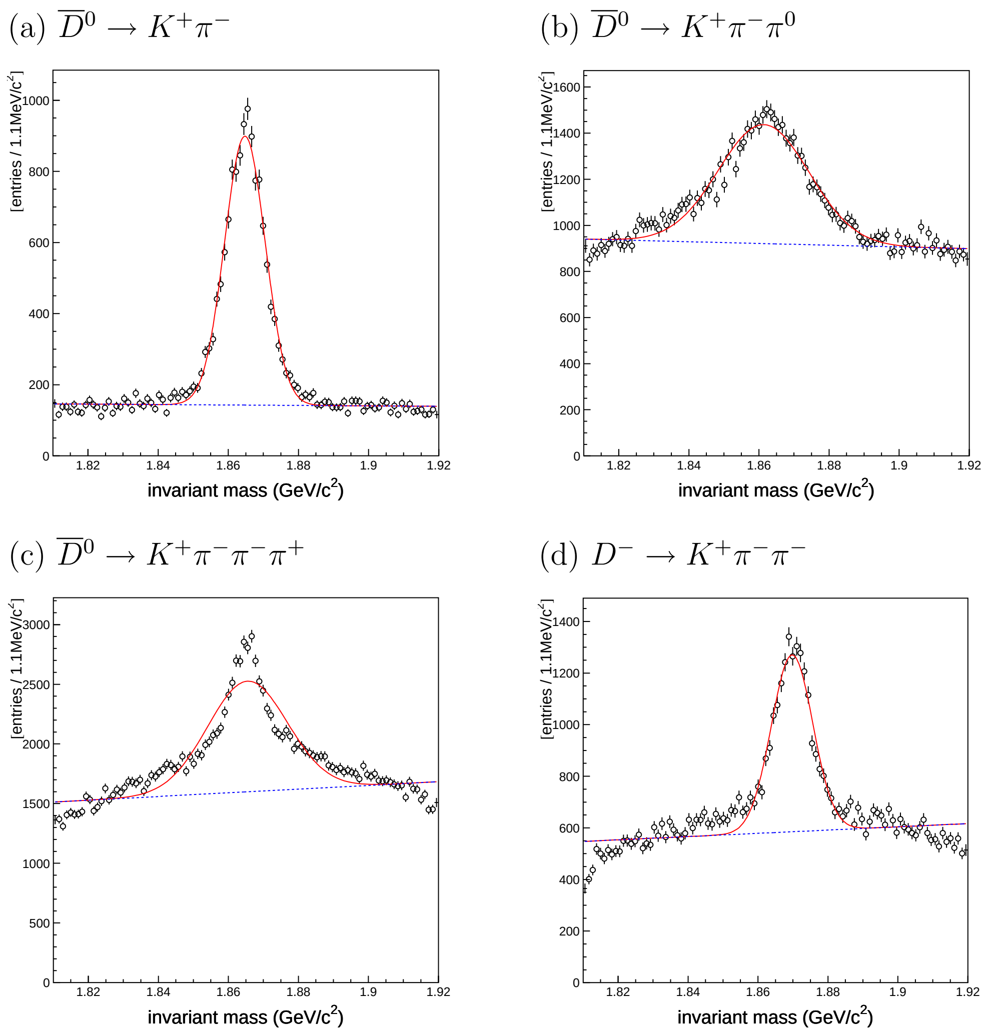

Figure 4.5: Invariant mass distributions of (a) $\overline{D}^0 \to K^+\pi^-$, (b) $\overline{D}^0 \to K^+\pi^-\pi^0$, (c) $\overline{D}^0 \to K^+\pi^-\pi^-\pi^+$, and (d) $D^- \to K^+\pi^-\pi^-$.

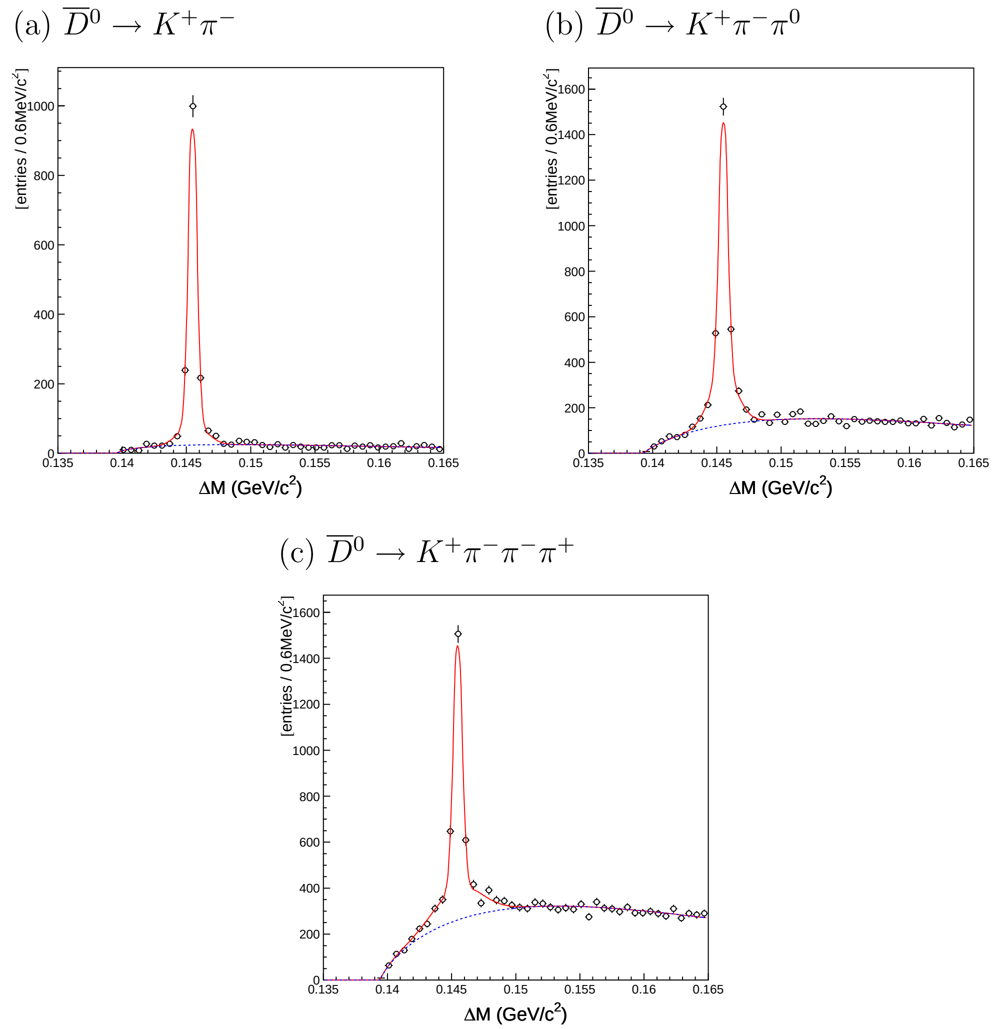

Figure 4.6: Distributions of ΔM for D^{*-} candidates. $\overline{D}^0$ candidates are reconstructed via (a) $\overline{D}^0 \to K^+\pi^-$, (b) $\overline{D}^0 \to K^+\pi^-\pi^0$, and (c) $\overline{D}^0 \to K^+\pi^-\pi^-\pi^+$.

$\overline{D}^0$ candidate. Since the energy released from the D^{*-} decay is very small and the $\overline{D}^0$ mass resolution is canceled by taking the difference, we expect to obtain better resolution for ΔM than that for $M_{\overline{D}^0\pi^-}$. The ΔM resolution is improved by refitting the soft π^- track subject to the constraint that it originates from the $\overline{D}^0$ production point, i.e., B decay point, which is described in the next chapter. Figures 4.6(a)–4.6(c) show ΔM distributions for D^{*-} candidates. The points with error bar indicate data points while the solid curve indicates the fit result. Signal is represented by a sum of two Gaussians while background is represented by a phase-space function, $a(x - x_0)^b \exp[-c(x - x_0)]$. The background function is indicated by the dotted curve in the figure. The requirement for ΔM is optimized for each D decay mode separately and is described in Section 4.3.4.

4.3.4 Reconstruction of B Mesons

Lifetime and Mixing Analyses

B mesons are reconstructed by combining their daughter particles reconstructed in the above sections. For $B^0 \to D^-\pi^+$, $D^{*-}\pi^+$, and $B^+ \to \overline{D}^0\pi^+$ modes, pion candidates are required to satisfy the loose PID selection: $P(K/\pi) < 0.9$. No PID selection is applied to kaon candidates for $B^+ \to J/\psi K^+$.

For $B \to D^{(*)}X$ modes, the vertex constrained fit is applied to the tracks which are originated from the same B decay vertex and have enough hits in SVD. The detail of the B decay vertex reconstruction is described in the next chapter. The tracks that are not used for the vertex reconstruction are refitted with the constraint that they come from the B decay vertex, in order to improve the B momentum resolution. In $B^0 \to D^{*-}\rho^+$ case, photons from π^0 of $\rho^+ \to \pi^+\pi^0$ are also calculated again using the B decay vertex. For $B \to J/\psi X$ modes, no further vertex constraint on the B vertex is applied.

For the reconstruction of the B mesons, two variables are used to select the candidate events: the energy difference ΔE and the beam-energy constrained mass $M_{\rm bc}$. The energy difference is defined as

$$\Delta E \equiv E_B^{\rm cms} - E_{\rm beam}^{\rm cms}, \tag{4.15}$$

where $E_{\rm beam}^{\rm cms}$ is the beam energy in the cms (i.e., $\sqrt{s}/2$) and $E_B^{\rm cms}$ is the energy of the fully reconstructed B candidate in the cms. The beam-energy constrained mass is defined as

$$M_{\rm bc} \equiv \sqrt{(E_{\rm beam}^{\rm cms})^2 - (p_B^{\rm cms})^2}, \tag{4.16}$$

where $p_B^{\rm cms}$ is the momentum of the fully reconstructed B candidate in the cms. By substituting $E_{\rm beam}^{\rm cms}$ for $E_B^{\rm cms}$ in the invariant mass calculation, the mass resolution is greatly improved. The typical resolution of ΔE is 10–30 MeV depending on the decay mode, and that of $M_{\rm bc}$ is about 3 MeV/c^2.

If there exist multiple candidates in a single event, the most probable candidate is chosen based on the information of ΔE, $M_{\rm bc}$, and the invariant mass of the D candidate, $M_{Kn\pi}$. χ^2 for the B candidate is calculated by

$$\chi^2 = \left(\frac{\Delta E}{\sigma_{\Delta E}}\right)^2 + \left(\frac{M_{\rm bc} - M_B}{\sigma_{M_{\rm bc}}}\right)^2 + \left(\frac{M_{Kn\pi} - M_D}{\sigma_{M_{Kn\pi}}}\right)^2 \tag{4.17}$$

for the analysis of $B \to D^{(*)}X$, and

$$\chi^2 = \left(\frac{\Delta E}{\sigma_{\Delta E}}\right)^2 + \left(\frac{M_{\rm bc} - M_B}{\sigma_{M_{\rm bc}}}\right)^2 \tag{4.18}$$

Table 4.3: Selection criteria for $B \to D^{(*)}X$ modes.

B decay mode	D decay mode	M_D	ΔM	R_2	$\cos\theta_{\rm th}$
$B^0 \to D^-\pi^+$	$D^- \to K^+\pi^-\pi^-$	$< 2.5\sigma$	—	< 0.5	< 0.995
	$\overline{D}^0 \to K^+\pi^-$	$< 10\sigma$	< 5 MeV/c^2	—	—
$B^0 \to D^{*-}\pi^+$	$\overline{D}^0 \to K^+\pi^-\pi^0$	$< 3.5\sigma$	< 3 MeV/c^2	—	< 0.98
	$\overline{D}^0 \to K^+\pi^-\pi^-\pi^+$	$< 4\sigma$	< 4 MeV/c^2	< 0.6	—
	$\overline{D}^0 \to K^+\pi^-$	$< 7\sigma$	< 4 MeV/c^2	< 0.6	< 0.95
$B^0 \to D^{*-}\rho^+$	$\overline{D}^0 \to K^+\pi^-\pi^0$	$< 3.5\sigma$	< 12 MeV/c^2	< 0.7	< 0.98
	$\overline{D}^0 \to K^+\pi^-\pi^-\pi^+$	$< 3.5\sigma$	< 3 MeV/c^2	—	< 0.92
	$\overline{D}^0 \to K^+\pi^-$	$< 4\sigma$	—	—	—
$B^+ \to \overline{D}^0\pi^+$	$\overline{D}^0 \to K^+\pi^-\pi^0$	$< 3\sigma$	—	< 0.45	—
	$\overline{D}^0 \to K^+\pi^-\pi^-\pi^+$	$< 2\sigma$	—	< 0.45	—

for the analysis of $B \to J/\psi X$, where M_B and M_D are the masses of B and D mesons, respectively, and $\sigma_{\Delta E}$, $\sigma_{M_{\rm bc}}$, and $\sigma_{M_{Kn\pi}}$ are the errors of ΔE, $M_{\rm bc}$, and $M_{Kn\pi}$, respectively. The candidate with the least χ^2 is chosen.

As described in Section 4.2, event shape parameters R_2 and $\cos\theta_{\rm th}$ are used to reduce the continuum background. For $B \to J/\psi X$ events, R_2 is required to be less than 0.5 and no selection is applied on $\cos\theta_{\rm th}$. For $B \to D^{(*)}X$ events, selection criteria on R_2 and $\cos\theta_{\rm th}$, as well as the D candidate mass M_D and the mass-difference of the D^{*-} candidate ΔM, are determined so that the figure of merit FOM $= S/\sqrt{S+B}$ is maximized for the data, where S and B are the numbers of signal and background events determined from the fit to the ΔE distribution, respectively. These selection criteria for the B and D decay modes are listed in Table 4.3.

Figures 4.7(a)– 4.7(g) show the two dimensional histograms of ΔE versus $M_{\rm bc}$ for all the decay modes used in the lifetime analysis after all the selections, including the selections on the vertexing quality and Δt which are described in the next chapter. The signal boxes in the ΔE-$M_{\rm bc}$ plane shown in Fig. 4.7 are listed in Table 4.4.

$\sin 2\phi_1$ Analysis

The $\psi(2S)$ meson is reconstructed via its decays to $\ell^+\ell^-$ ($\ell = \mu, e$) and $J/\psi\pi^+\pi^-$. The χ_{c1} is reconstructed via $J/\psi\gamma$. The η_c is detected in the $K_S^0K^-\pi^+$, $K^+K^-\pi^0$, and $p\overline{p}$ modes. For the $J/\psi K_S^0$ mode, we use $K_S^0 \to \pi^+\pi^-$ and $\pi^0\pi^0$ decays; for the other modes we only use $K_S^0 \to \pi^+\pi^-$. The reconstruction of $B^0 \to J/\psi K_S^0(\pi^+\pi^-)$ is the same as that for the lifetime analysis. The reconstruction and selection criteria for the other f_{CP} channels used in the measurement are described in more detail in Ref. [46]. For reconstructed $B \to f_{CP}$ candidates other than $J/\psi K_L^0$, we identify B

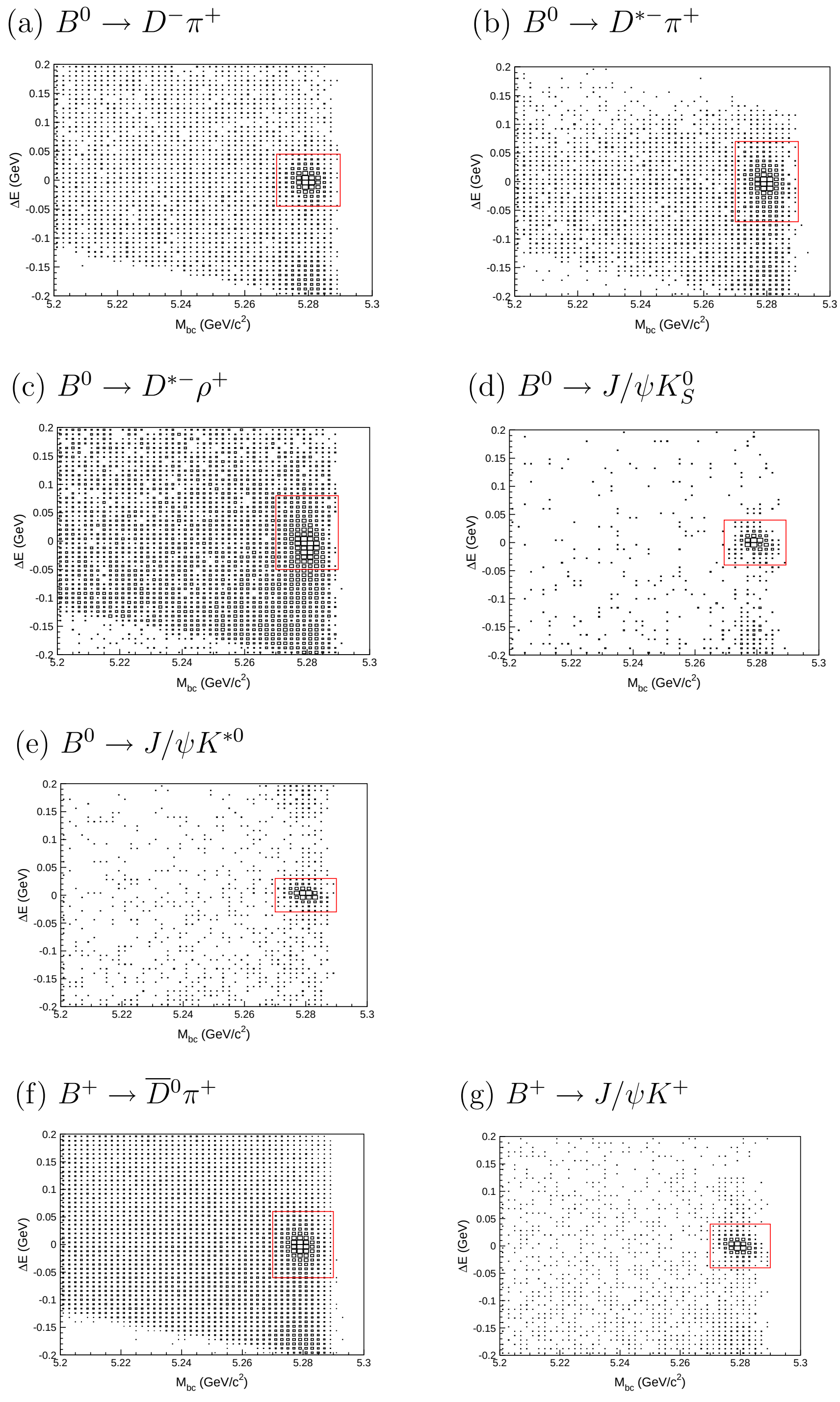

Figure 4.7: Two dimensional histograms of ΔE versus $M_{\rm bc}$ for (a) $B^0 \to D^-\pi^+$, (b) $B^0 \to D^{*-}\pi^+$, (c) $B^0 \to D^{*-}\rho^+$, (d) $B^0 \to J/\psi K^0_S$, (e) $B^0 \to J/\psi K^{*0}$, (f) $B^+ \to \overline{D}^0\pi^+$, and (g) $B^+ \to J/\psi K^+$ events. The boxes represent the signal regions.

Table 4.4: Signal box for each decay mode used in the lifetime and mixing analyses.

Decay mode	ΔE range (GeV)	$M_{\rm bc}$ range (GeV/c^2)
$B^0 \to D^-\pi^+$	$-0.045 < \Delta E < 0.045$	$5.270 < M_{\rm bc} < 5.290$
$B^0 \to D^{*-}\pi^+$	$-0.07 < \Delta E < 0.07$	$5.270 < M_{\rm bc} < 5.290$
$B^0 \to D^{*-}\rho^+$	$-0.05 < \Delta E < 0.08$	$5.270 < M_{\rm bc} < 5.290$
$B^0 \to J/\psi K_S^0$	$-0.04 < \Delta E < 0.04$	$5.2694 < M_{\rm bc} < 5.2894$
$B^0 \to J/\psi K^{*0}$	$-0.03 < \Delta E < 0.03$	$5.270 < M_{\rm bc} < 5.290$
$B^+ \to \overline{D}{}^0\pi^+$	$-0.06 < \Delta E < 0.06$	$5.270 < M_{\rm bc} < 5.290$
$B^+ \to J/\psi K^+$	$-0.04 < \Delta E < 0.04$	$5.270 < M_{\rm bc} < 5.290$

Table 4.5: Summary of ΔE-$M_{\rm bc}$ signal regions and the numbers of candidates $N_{\rm rec}$ for the $\sin 2\phi_1$ analysis.

Decay mode	ΔE range (GeV)	$M_{\rm bc}$ range (GeV/c^2)	$N_{\rm rec}$
$J/\psi K_S^0(\pi^+\pi^-)$	$-0.04 < \Delta E < 0.04$	$5.2694 < M_{\rm bc} < 5.2894$	1285
$J/\psi K_S^0(\pi^0\pi^0)$	$-0.15 < \Delta E < 0.10$	$5.27 < M_{\rm bc} < 5.29$	188
$\psi(2S)(\ell^+\ell^-)K_S^0$	$-0.04 < \Delta E < 0.04$	$5.2694 < M_{\rm bc} < 5.2894$	91
$\psi(2S)(J/\psi\pi^+\pi^-)K_S^0$	$-0.04 < \Delta E < 0.03$	$5.2694 < M_{\rm bc} < 5.2894$	112
$\chi_{c1}(J/\psi\gamma)K_S^0$	$-0.04 < \Delta E < 0.03$	$5.2694 < M_{\rm bc} < 5.2894$	77
$\eta_c(K_S^0K^-\pi^+)K_S^0$	$-0.035 < \Delta E < 0.035$	$5.27 < M_{\rm bc} < 5.29$	72
$\eta_c(K^+K^-\pi^0)K_S^0$	$-0.055 < \Delta E < 0.045$	$5.27 < M_{\rm bc} < 5.29$	49
$\eta_c(p\overline{p})K_S^0$	$-0.025 < \Delta E < 0.025$	$5.27 < M_{\rm bc} < 5.29$	21
$J/\psi K^{*0}(K_S^0\pi^0)$	$-0.05 < \Delta E < 0.03$	$5.27 < M_{\rm bc} < 5.29$	101

decays using the energy difference ΔE and the beam-energy constrained mass $M_{\rm bc}$ defined in Eqs. (4.15) and (4.16), respectively. Figure 4.8 shows the $M_{\rm bc}$ distributions for all B^0 candidates except for $B^0 \to J/\psi K_L^0$ that have ΔE values in the signal regions. The B^0 candidates are selected by applying the mode-dependent requirements on ΔE and $M_{\rm bc}$ listed in Table 4.5. The number of observed candidates, $N_{\rm rec}$, for each decay mode is also shown.

Candidate $B^0 \to J/\psi K_L^0$ decays are selected by requiring the ECL and/or KLM hit patterns that are consistent with the presence of a shower induced by a K_L^0 meson. The centroid of the shower is required to be within a 45° cone centered on the K_L^0 direction inferred from two-body decay kinematics and the measured four-momentum of the J/ψ. The detail of the reconstruction and selection for the $B^0 \to J/\psi K_L^0$ channel is described in Refs. [46, 51, 52]. For the $B^0 \to J/\psi K_L^0$ mode, since the energy of the K_L^0 meson cannot be measured, ΔE and $M_{\rm bc}$ cannot be used to identify B^0 candidates. However, using the four-momentum of a reconstructed J/ψ candidate and the flight direction of the K_L^0, we can calculate the momentum

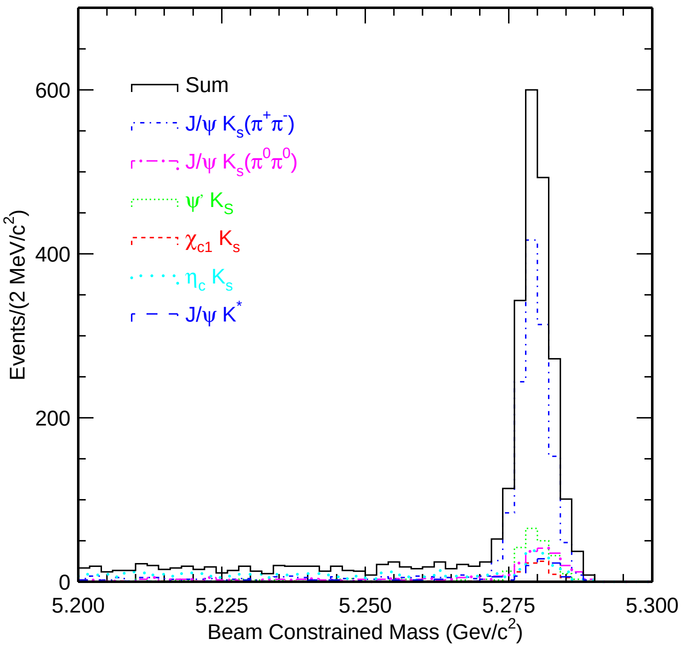

Figure 4.8: Beam-energy constrained mass distribution for all decay modes other than $J/\psi K_L^0$.

of the K_L^0 candidate with the $B^0 \to J/\psi K_L^0$ two-body decay hypothesis. We then calculate the $p_B^{\rm cms}$ which is used for the final selection. For this $p_B^{\rm cms}$ calculation, the effect of the run-dependent variation of the beam energy is corrected [52]. Figure 4.9 shows the $p_B^{\rm cms}$ distribution. The histograms are the results of a fit to the signal and background distributions described in Section 7.4.1. There are 1330 entries in total in the $0.20 \leq p_B^{\rm cms} \leq 0.45$ GeV/c signal region; the fit indicates a signal purity of 63%.

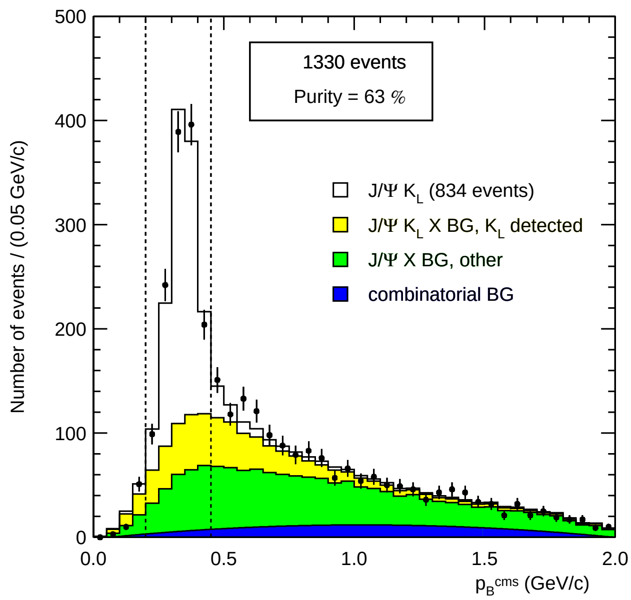

Figure 4.9: Distribution of p_B^{cms} for $B^0 \to J/\psi K_L^0$ candidates with the results of the fit.

Chapter 5

Measurement of Lifetimes

In this chapter, we describe the analysis procedure for the B lifetimes measurement [53]. First, the proper-time interval for each event is reconstructed from two B decay vertices. The effects from the resolution of proper-time interval and background events are studied. Then, lifetimes of B mesons are extracted using an unbinned maximum likelihood fit to the observed proper-time interval distributions. Finally, the systematic uncertainties of the result are estimated.

5.1 Fitting Method

In order to make maximal use of the available statistics, an unbinned maximum likelihood fit [54] is used for the lifetime analysis and other two time-evolution analyses.

5.1.1 Unbinned Maximum Likelihood Fit

We suppose that a set of N independent measurements of quantities x_i comes from a probability density function (PDF) $P(x; \boldsymbol{\alpha})$, where $\boldsymbol{\alpha} = (\alpha_1, \cdots, \alpha_n)$ is a set of n parameters whose values are unknown. The maximum likelihood method takes the estimators $\hat{\boldsymbol{\alpha}}$ to be those values that maximize the *likelihood function*

$$L(\boldsymbol{\alpha}) = \prod_{i=1}^{N} P(x_i; \boldsymbol{\alpha}). \tag{5.1}$$

The likelihood function L is the joint PDF for the data, evaluated with the data obtained in the experiment and regarded as a function of the parameters $\boldsymbol{\alpha}$.

It is usually easier to work with $\ln L$, since L can be very small and exceed the limit of the computer and both L and $\ln L$ are maximized for the same parameter values $\hat{\boldsymbol{\alpha}}$. Using the logarithm has the additional advantage that the quantity $-2 \ln L$

behaves like a χ^2 in the large sample limit. In this case, s-standard-deviation errors are determined from the contour given by the $\boldsymbol{\alpha}'$ such that

$$-2 \ln L(\boldsymbol{\alpha}') = -2 \ln L(\hat{\boldsymbol{\alpha}}) + s^2. \tag{5.2}$$

We use the MINUIT fitting package [55] to find the set of parameters $\hat{\boldsymbol{\alpha}}$ which minimize the quantity $-2 \ln L$ and to calculate the statistical uncertainties on these parameters.

5.1.2 Probability Density Function

As described in Section 2.5, the theoretical proper-time difference distribution $\mathcal{P}_{\rm sig}$ is given by

$$\mathcal{P}_{\rm sig}(\Delta t; \tau_B) = \frac{1}{2\tau_B} \exp\left(-\frac{|\Delta t|}{\tau_B}\right), \tag{5.3}$$

where Δt is the proper-time interval between two B mesons and τ_B is, depending on the reconstructed mode in the event, either the B^0 or the B^+ lifetime. This $\mathcal{P}_{\rm sig}$ cannot be directly used as the PDF to calculate the likelihood function L, because observed Δt is smeared by the finite detector resolution and there exist the background events in the data. Taking into account these effects, the overall PDF $P(\Delta t)$ can be expressed as

$$P(\Delta t) = (1 - f_{\rm ol}) \left[f_{\rm sig} P_{\rm sig}(\Delta t) + (1 - f_{\rm sig}) P_{\rm bkg}(\Delta t) \right] + f_{\rm ol} P_{\rm ol}(\Delta t), \tag{5.4}$$

where $f_{\rm sig}$ is the signal purity determined on an event-by-event basis, $P_{\rm sig}$ and $P_{\rm bkg}$ are the PDFs for the signal and background events, respectively. To account for a small number of events that give large Δt in both the signal and background (outlier components), we introduce a fraction of outliers $f_{\rm ol}$ and a function $P_{\rm ol}(\Delta t)$ to model its distribution. $P_{\rm sig}$ is described as the convolution of a theoretical PDF $\mathcal{P}_{\rm sig}$ with a resolution function $R_{\rm sig}$:

$$P_{\rm sig}(\Delta t) = \int_{-\infty}^{+\infty} d(\Delta t') \mathcal{P}_{\rm sig}(\Delta t') R_{\rm sig}(\Delta t - \Delta t'). \tag{5.5}$$

We describe the reconstruction of Δt and the detail of $R_{\rm sig}$, $P_{\rm ol}$, $f_{\rm sig}$, and $P_{\rm bkg}$ in the following sections.

5.2 Proper-time Interval Reconstruction

We need to reconstruct the proper-time interval Δt of each event for the lifetime analysis or any other time-evolution analyses. As described in Section 2.5, Δt can be calculated by

$$\Delta t = \frac{z_{\rm ful} - z_{\rm asc}}{c(\beta\gamma)_\Upsilon} \equiv \frac{\Delta z}{c(\beta\gamma)_\Upsilon}, \tag{5.6}$$

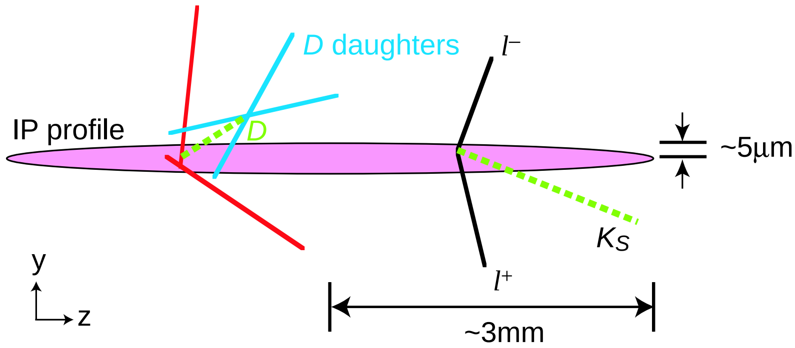

Figure 5.1: Illustration of vertex reconstruction of two B decay vertices.

where $z_{\rm ful}$ and $z_{\rm asc}$ are the z coordinates of the fully-reconstructed and associated B decay vertices, respectively.

Figure 5.1 illustrates the reconstruction of the decay vertices. The decay vertices of the two B mesons in each event are fitted using tracks which have sufficient number of associated SVD hits; Having both z and r-ϕ hits in at least one layer and at least one additional layer with a z hit in SVD. We impose the constraint that they are consistent with the IP profile [49], smeared in the r-ϕ plane by 21 μm to account for the transverse B decay length. The IP profile is described as a three-dimensional Gaussian, where the parameters are determined in each run (every 60,000 events in case of the mean position) using hadronic events. The size of the IP region is typically $\sigma_x \simeq 100$ μm, $\sigma_y \simeq 5$ μm, and $\sigma_z \simeq 3$ mm, where x and y denote the horizontal and vertical (upward) directions, respectively. The detail of the determination of parameters for IP profile is described in Appendix B. This IP profile constraint makes it possible to reconstruct a decay vertex even with a single track.

We reject a small fraction ($\sim 0.2\%$) of the events by requiring $\Delta t < 70$ ps ($\sim 45\tau_B$), to reject poorly reconstructed events. This selection affects the normalization of PDF. We use the notation such that each PDF $P_x(\Delta t)$ ($P_{\rm sig}$, $P_{\rm bkg}$, and $P_{\rm ol}$) satisfies

$$\int_{-\infty}^{+\infty} d(\Delta t) P_x(\Delta t) = 1. \tag{5.7}$$

This naturally satisfies the normalization of $P(\Delta t)$:

$$\int_{-\infty}^{+\infty} d(\Delta t) P(\Delta t) = 1. \tag{5.8}$$

But for the likelihood function used in the final fit, we use

$$\tilde{P}_x(\Delta t) \equiv \frac{P_x(\Delta t)}{\int_{-70\ \rm ps}^{+70\ \rm ps} d(\Delta t) P_x(\Delta t)} \tag{5.9}$$

instead of $P_x(\Delta t)$, which satisfies

$$\int_{-70\ \mathrm{ps}}^{+70\ \mathrm{ps}} d(\Delta t)\tilde{P}_x(\Delta t) = 1. \tag{5.10}$$

5.2.1 Reconstruction of Fully-reconstructed B Vertex

The decay vertex of the fully reconstructed B meson (B_{ful}) is obtained using all tracks with associated SVD hits.

In the case of a fully reconstructed $B \to D^{(*)}X$ decay, the vertex is obtained from the reconstructed D pseudo-track (the vertex position and momentum vector obtained after D vertex fit) and tracks other than the slow π^- candidate from D^{*-} decay, i.e., the primary π^+. We do not use the single track vertexing for $B \to D^{(*)}X$.

For a fully reconstructed $B \to J/\psi X$ decay, the vertex is determined using lepton tracks from J/ψ. In this case, at least one track is required to satisfy the SVD hit selection criterion, and the single track vertexing is allowed.

5.2.2 Reconstruction of Associated B Vertex

The decay vertex of the associated B meson (B_{asc}) is determined inclusively from tracks that are not assigned to B_{ful} and have enough SVD hits. Here, poorly reconstructed tracks as well as tracks that are likely to come from K_S^0 decays are not used. These poor-quality tracks meet one or more of the following conditions:

- A track with a longitudinal position error greater than 500 μm.
- A track forming the K_S^0 mass (within ± 15 MeV/c^2) with another oppositely charged track.
- A track more than 500 μm away from the fully reconstructed B vertex in the r-ϕ plane.

We repeat the vertex reconstruction by removing the track that gives the largest contribution to the reduced χ^2 (χ^2 divided by the number of degrees of freedom for the vertex fit [n.d.f.]) until the resulting χ^2 satisfies χ^2/n.d.f. < 20 or only one track is left. However, we do not remove the lepton track with momentum greater than 1.1 GeV/c in the cms, because the high-momentum leptons are likely to come from primary semileptonic B decays, and we remove the track with the second largest contribution to the χ^2/n.d.f. instead.

The presence of the secondary charm ($b \to c$) decay vertex in the associated B meson causes a shift of the reconstructed vertex point toward charm flight direction and degrades the vertex resolution.

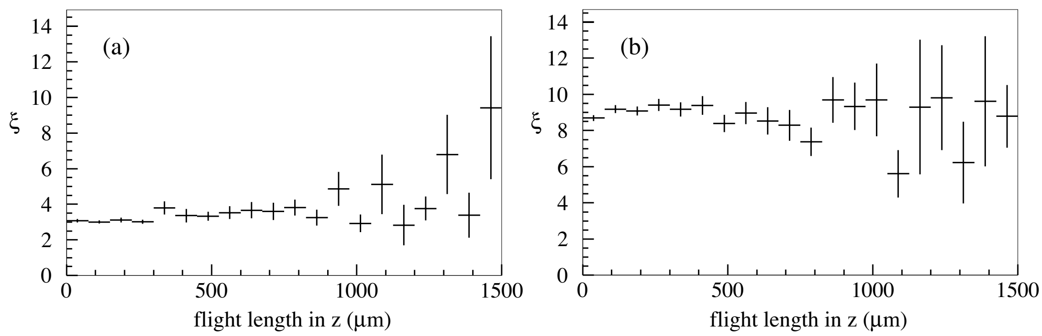

Figure 5.2: Distributions of ξ as a function of B flight length for (a) $B_{\rm ful}$ and (b) $B_{\rm asc}$.

5.2.3 Quality of the Vertex Fit

We use only well-reconstructed vertices for the Δt calculation. The ordinary $\chi^2$of the vertex fit depends on the flight length of B meson because of the tight IP constraint in the transverse plane, which may result in a bias to the lifetime measurement. Therefore, the assessment of the quality of the vertex fit is done only in the z direction for both $B_{\rm ful}$ and $B_{\rm asc}$ vertices. We use the following variable

$$\xi = \frac{1}{2n} \sum_{i=1}^{n} \left(\frac{z^i_{\rm after} - z^i_{\rm before}}{\varepsilon^i_{\rm before}} \right)^2 , \tag{5.11}$$

where n is the number of tracks used in the fit, $z^i_{\rm before}$ and $z^i_{\rm after}$ are the z positions of the i-th track at the closest approach to the origin before and after the vertex fit, respectively, and $\varepsilon^i_{\rm before}$ is the error of $z^i_{\rm before}$. The MC simulation study shows that ξ does not depend on the B decay length, as indicated in Fig. 5.2. Figure 5.3 shows the ξ distributions for the fully reconstructed B decay vertices and for the associated B decay vertices, obtained from a MC simulation. We require $\xi < 100$ for both vertices to eliminate poorly reconstructed vertices. We find that about 3% of the fully reconstructed and 1% of the associated B decay vertices are rejected in the data.

5.3 Resolution Function

The resolution function of the signal is constructed as the convolution of four different contributions [56]: the detector resolution on $z_{\rm ful}$ and $z_{\rm asc}$ ($R_{\rm ful}$ and $R_{\rm asc}$), an additional smearing on $z_{\rm asc}$ to account for the tracks which do not originate from the associated B vertex ($R_{\rm np}$), mostly from charm or K^0_S decays, and the kinematic approximation that the B mesons are at rest in the cms ($R_{\rm k}$). The overall resolution

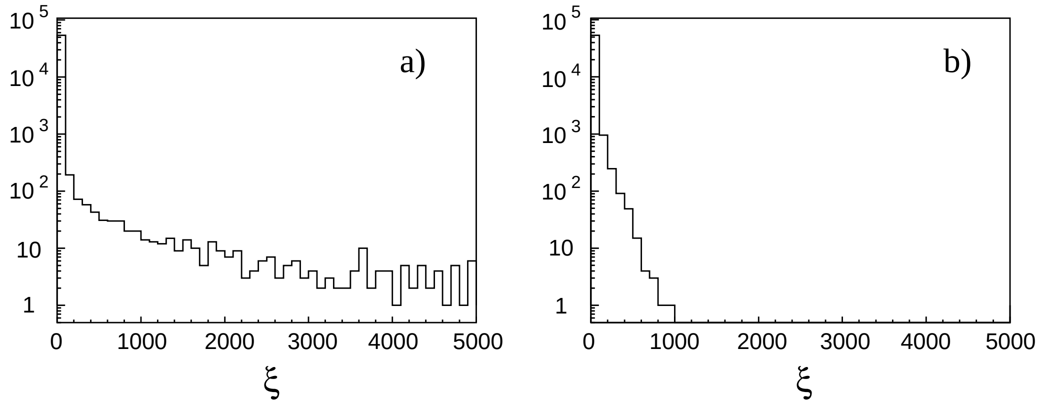

Figure 5.3: Distributions of ξ for (a) $B_{\rm ful}$ and (b) $B_{\rm asc}$.

function, $R_{\rm sig}(\Delta t)$, is expressed as

$$R_{\rm sig}(\Delta t) = \iiint_{-\infty}^{+\infty} d(\Delta t')d(\Delta t'')d(\Delta t''')R_{\rm ful}(\Delta t - \Delta t')R_{\rm asc}(\Delta t' - \Delta t'') \times R_{\rm np}(\Delta t'' - \Delta t''')R_{\rm k}(\Delta t'''). \quad (5.12)$$

We use a MC simulation to understand the resolution function and determine its functional form. One of B mesons in each event is forced to decay to the modes that are used to fully reconstruct the B meson while the other decays generically to one of all possible final states.

5.3.1 Detector Resolution

In order to separate the intrinsic detector resolution from smearing due to non-primary tracks, we use a MC simulation in which all secondary particles from $B_{\rm asc}$ are generated with zero lifetime at the B decay vertex. Figures 5.4(a) and 5.4(b) show the distributions of difference in z between the reconstructed and generated vertex positions:

$$\delta z_q = z_q^{\rm rec} - z_q^{\rm gen}, \quad (5.13)$$

where q = ful (asc) is for the fully reconstructed (associated) B vertex, and the superscripts 'rec' and 'gen' denote the reconstructed and generated vertex positions, respectively. Results of the fit with a sum of two Gaussians are also shown. The fitted curves do not represent the δz distributions in tail regions. We also find that even a sum of three or more Gaussians with constant standard deviations cannot represent δz properly. We therefore consider a more elaborate function that uses the vertex-by-vertex z-coordinate error of the reconstructed vertex (σ^z) as an input parameter. The σ^z is computed from the error matrix of the tracks used in the

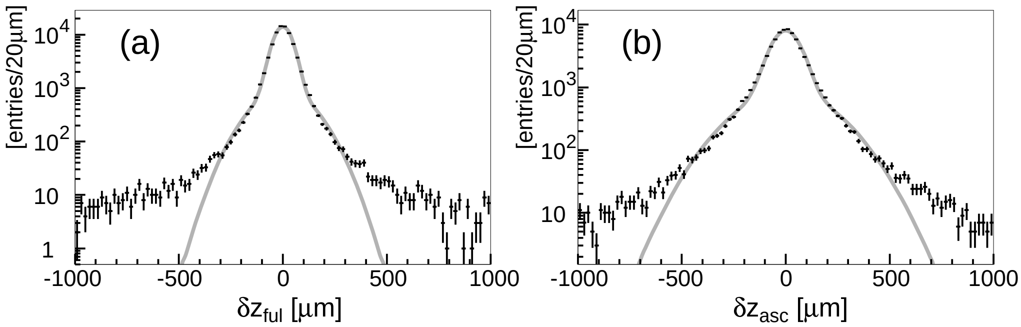

Figure 5.4: Distributions of δz for (a) fully reconstructed and (b) associated B vertices obtained from the $B^0 \to J/\psi K_S^0$ MC sample. Superimposed are the results of the fit to a sum of two Gaussians.

vertex fit and the size of the IP region. To construct functional forms of $R_{\rm ful}$ and $R_{\rm asc}$, we investigate the distribution of a pull, defined as δz divided by σ^z. If the σ^z estimation is correct on average, the pull distribution is expected to be a single Gaussian with the standard deviation of unity.

Because of the IP profile constraint, it is possible to reconstruct a decay vertex by a single track. The resolution for such a vertex is worse than that for the vertex reconstructed by multiple tracks, and is considered separately.

Multiple-track Vertex

We evaluate the vertex-fit-quality dependence of the resolution using the value of ξ defined in Eq. (5.11). We find that a pull distribution for vertices with similar ξ values can be expressed as a single Gaussian. This can be seen in Fig. 5.5 which shows the pull distributions for eight different ξ ranges. The result of a fit to a single Gaussian for each ξ range is superimposed. Furthermore, we find that the standard deviation of the distribution has a linear dependence on ξ as shown in Fig. 5.6. Results from this MC study lead us to model the detector resolution of the multiple-track vertex using the following function:

$$R_q^{\rm multiple}(\delta z_q) = G(\delta z_q; (s_q^0 + s_q^1 \xi_q)\sigma_q^z) \qquad (q = {\rm ful, asc}), \tag{5.14}$$

where G is the Gaussian function,

$$G(x;\sigma) \equiv \frac{1}{\sqrt{2\pi}\sigma} \exp\left(-\frac{x^2}{2\sigma^2}\right). \tag{5.15}$$

The scale factors s_q^0 and s_q^1 are treated as free parameters and determined from the lifetime fit to the data. Figures 5.7(a) and 5.7(b) show the $\delta z_{\rm ful}$ and $\delta z_{\rm asc}$ distributions, respectively. Superimposed are results of a fit to $R_q^{\rm multiple}(\delta z_q)$, which

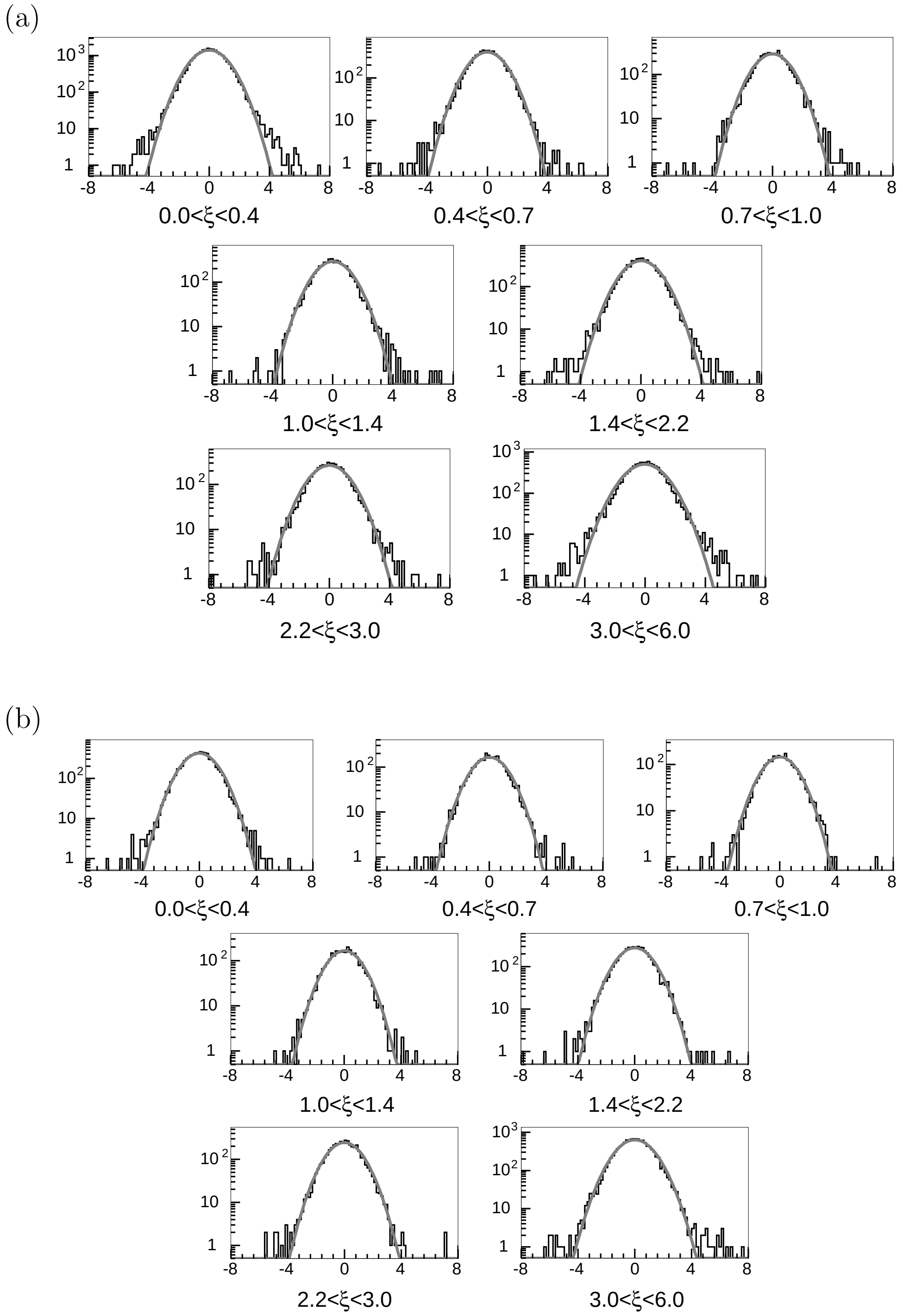

Figure 5.5: Pull ($\delta z/\sigma^z$) distributions of (a) fully reconstructed and (b) associated B vertices, for each ξ range. Only vertices reconstructed with multiple tracks are shown. Results of a fit to a single Gaussian are superimposed. These distributions are obtained from $B^0 \to J/\psi K_S^0$ MC samples.

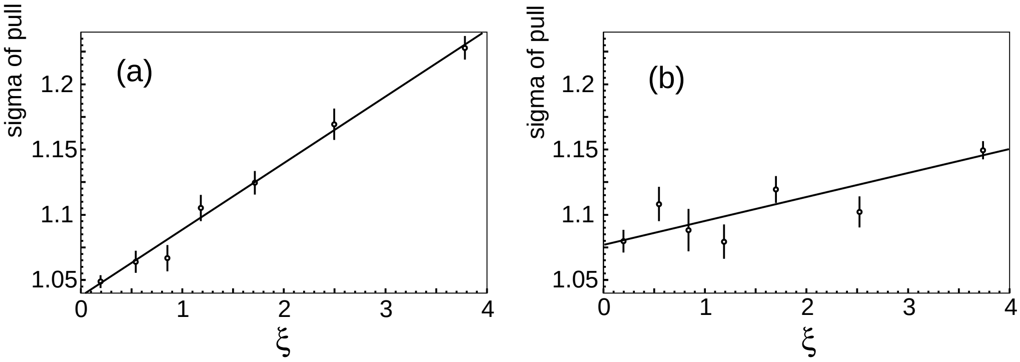

Figure 5.6: Standard deviations of the pull distributions as a function of ξ for (a) fully reconstructed and (b) associated B meson vertices. The distributions are obtained form $B^0 \to J/\psi K_S^0$ MC samples.

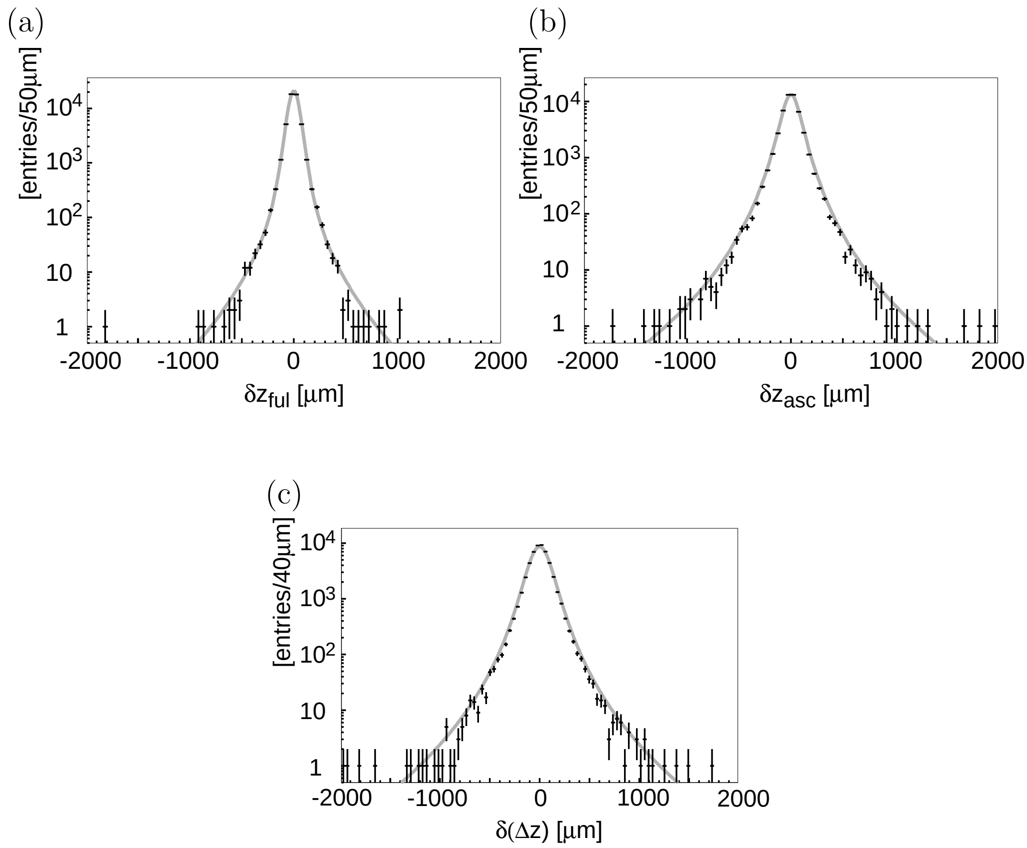

Figure 5.7: Distributions of (a) δz_{ful} and (b) δz_{asc} for multiple-track vertices, with $R_{\mathrm{ful}}^{\mathrm{multiple}}(\delta z_{\mathrm{ful}})$ and $R_{\mathrm{asc}}^{\mathrm{multiple}}(\delta z_{\mathrm{asc}})$, respectively. Figure (c) is the $\delta(\Delta z)$ distribution and the convolution of $R_{\mathrm{ful}}^{\mathrm{multiple}}(\delta z_{\mathrm{ful}})$ and $R_{\mathrm{asc}}^{\mathrm{multiple}}(\delta z_{\mathrm{asc}})$.

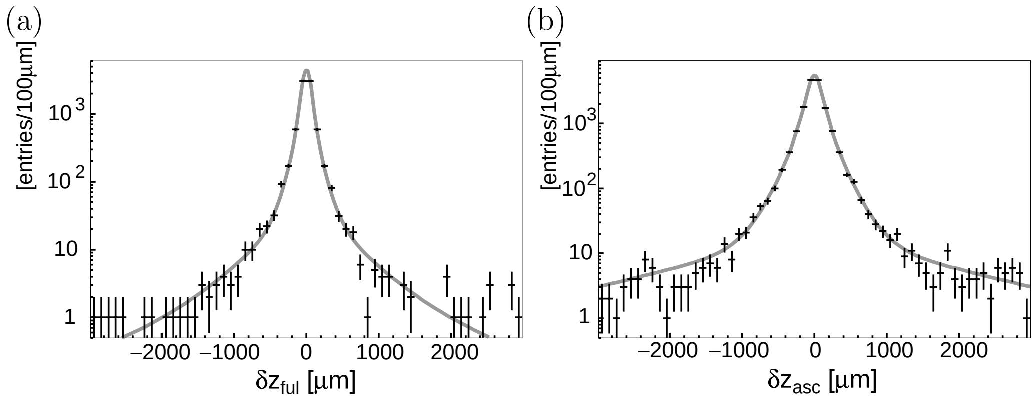

Figure 5.8: Distributions of (a) $\delta z_{\rm ful}$ and (b) $\delta z_{\rm asc}$ for single-track vertices with $R_{\rm ful}^{\rm single}$ and $R_{\rm asc}^{\rm single}$.

well reproduce the δz_q distributions. Figure 5.7(c) shows the distribution of the residual of Δz, $\delta(\Delta z) \equiv \Delta z^{\rm rec} - \Delta z^{\rm gen}$ together with the convolution of $R_{\rm ful}^{\rm multiple}(\delta z_{\rm ful})$ and $R_{\rm asc}^{\rm multiple}(\delta z_{\rm asc})$.

Single-track Vertex

For the single-track vertices, the ξ is not available. The resolution function of the single-track vertices, $R_q^{\rm single}(\delta z_q)$ (q = ful, asc), is expressed as a sum of two Gaussians, one for the main part of the detector resolution and the other for the tail part from the poorly reconstructed tracks:

$$R_q^{\rm single}(\delta z_q) = (1 - f_{\rm tail})G(\delta z_q; s_{\rm main}\sigma_q^z) + f_{\rm tail}G(\delta z_q; s_{\rm tail}\sigma_q^z), \tag{5.16}$$

where $s_{\rm main}$ and $s_{\rm tail}$ are global scale factors which are common to all single-track vertices. The parameters $s_{\rm main}$, $s_{\rm tail}$, and $f_{\rm tail}$ are treated as free parameters and determined from the lifetime fit to the data. Figure 5.8 shows the residual distributions of the single-track $z_{\rm ful}$ and $z_{\rm asc}$ vertices, together with a fit to $R_q^{\rm single}(\delta z_q)$.

The resolution functions $R_{\rm ful}(\delta z_{\rm ful})$ and $R_{\rm asc}(\delta z_{\rm asc})$ described above are the resolutions for $\delta z_{\rm ful}$ and $\delta z_{\rm asc}$. The δz resolution can be easily converted into the Δt resolution by replacing σ_q^z with $\sigma_q \equiv \sigma_q^z/[c(\beta\gamma)_\Upsilon]$.

5.3.2 Smearing due to Non-primary Tracks

The shape of $R_{\rm np}$ is determined from MC data samples, separately for B^0 and B^+ events, because the yield of each charmed meson, D^0, D^+, and D_s^+, is different

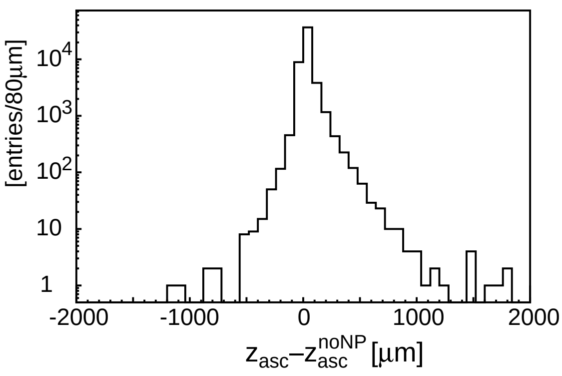

Figure 5.9: Distribution of $z_{\rm asc} - z_{\rm asc}^{\rm noNP}$ for multi-track vertex, where $z_{\rm asc}^{\rm noNP}$ is $z_{\rm asc}$ obtained from a MC sample in which secondary decays are turned off. In making this plot the events in which $z_{\rm asc}^{\rm noNP} = z_{\rm asc}$ are removed. The histogram is obtained from $B^0 \to J/\psi K_S^0$ MC whose associated B vertex is reconstructed with multiple tracks.

between neutral and charged B mesons. Figure 5.9 shows the distribution of the difference between $z_{\rm asc}$ from the nominal MC sample and that from the special MC sample in which secondary decays are turned off to eliminate the smearing due to non-primary tracks. We assume $R_{\rm np}$ consists of a prompt component, expressed by Dirac's δ-function $\delta(\delta z_{\rm asc})$, and components which account for smearing due to K_S^0 and charm decays, expressed by a function defined as $f_{\rm p} E_{\rm p}(\delta z_{\rm asc}; c(\beta\gamma)_\Upsilon \tau_{\rm np}^{\rm p}) + (1 - f_{\rm p}) E_{\rm n}(\delta z_{\rm asc}; c(\beta\gamma)_\Upsilon \tau_{\rm np}^{\rm n})$, where $f_{\rm p}$ is a fraction of $\delta z_{\rm asc} > 0$ component and $E_{\rm p}$ and $E_{\rm n}$ are

$$E_{\rm p}(x;\tau) \equiv \frac{1}{\tau}\exp\Big(-\frac{x}{\tau}\Big) \qquad \text{for } x \geq 0, \text{ otherwise } 0, \tag{5.17}$$

$$E_{\rm n}(x;\tau) \equiv \frac{1}{\tau}\exp\Big(+\frac{x}{\tau}\Big) \qquad \text{for } x < 0, \text{ otherwise } 0. \tag{5.18}$$

Thus, $R_{\rm np}$ is given by

$$\begin{aligned} R_{\rm np}(\delta z_{\rm asc}) \equiv f_\delta \delta(\delta z_{\rm asc}) + (1 - f_\delta) \big[& f_{\rm p} E_{\rm p}(\delta z_{\rm asc}; c(\beta\gamma)_\Upsilon \tau_{\rm np}^{\rm p}) \\ & + (1 - f_{\rm p}) E_{\rm n}(\delta z_{\rm asc}; c(\beta\gamma)_\Upsilon \tau_{\rm np}^{\rm n}) \big] , \end{aligned} \tag{5.19}$$

where f_δ is a fraction of the prompt component. We find that the vertex position shift is correlated with $\sigma_{\rm asc}^z$ and $\xi_{\rm asc}$ as shown in Fig. 5.10 for multi-track vertices. Consequently, we define $\tau_{\rm np}^{\rm p}$ and $\tau_{\rm np}^{\rm n}$ as

$$\tau_{\rm np}^{\rm p} = \tau_{\rm p}^0 + \tau_{\rm p}^1 (s_{\rm asc}^0 + s_{\rm asc}^1 \xi_{\rm asc}) \sigma_{\rm asc}, \quad \text{and} \tag{5.20}$$

$$\tau_{\rm np}^{\rm n} = \tau_{\rm n}^0 + \tau_{\rm n}^1 (s_{\rm asc}^0 + s_{\rm asc}^1 \xi_{\rm asc}) \sigma_{\rm asc}. \tag{5.21}$$

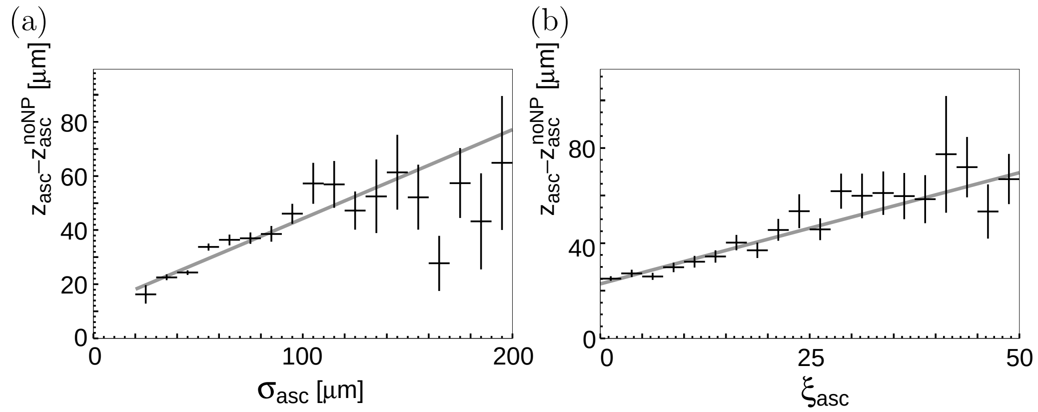

Figure 5.10: Vertex position shift ($z_{\rm asc} - z_{\rm asc}^{\rm noNP}$) versus (a) $\sigma^z_{\rm asc}$ and (b) $\xi_{\rm asc}$. $z_{\rm asc}^{\rm noNP}$ is obtained from a MC sample in which secondary decays are turned off. The events with $z_{\rm asc} < z_{\rm asc}^{\rm noNP}$ are excluded.

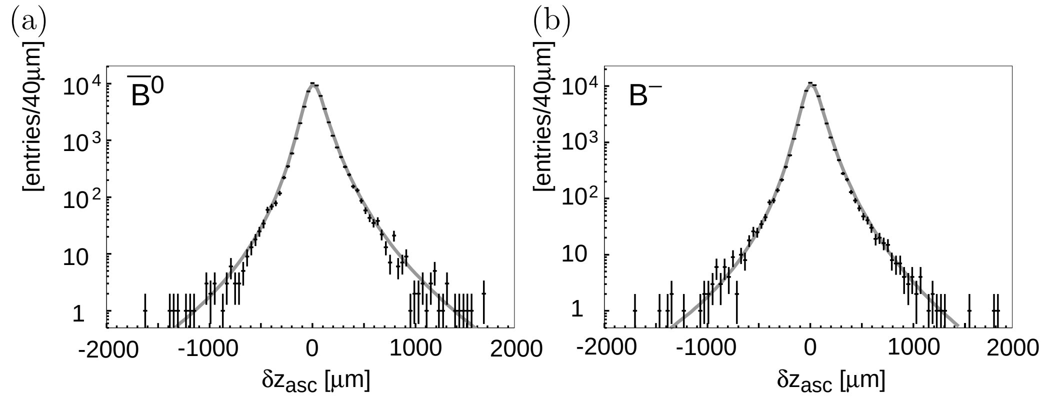

Figure 5.11: Distributions of $\delta z_{\rm asc}$ for multiple-track vertices of (a) $B^0 \to J/\psi K^0_S$ and (b) $B^+ \to J/\psi K^+$ decays.

Since these values can be zero or negative according to parameters, we set the lower limit of $\tau^{\rm p}_{\rm np}$ and $\tau^{\rm n}_{\rm np}$ to 1.0×10^{-4} ps. Figure 5.11 shows the $\delta z_{\rm asc}$ distributions for multiple-track vertices. We fit the convolution of $R_{\rm asc}$ and $R_{\rm np}$ to the distribution, in which f_δ, $f_{\rm p}$, $\tau^0_{\rm p}$, $\tau^1_{\rm p}$, $\tau^0_{\rm n}$, and $\tau^1_{\rm n}$ are free parameters, and the scale parameters, $s^0_{\rm asc}$ and $s^1_{\rm asc}$, for $R_{\rm asc}$ are fixed to the value obtained from the fit to the $\delta z^{\rm noNP}_{\rm asc}$ distribution. Results, shown as superimposed, well represent the distributions.

For single-track vertices we can only consider the correlation between the vertex position shift and $\sigma^z_{\rm asc}$. Figure 5.12 shows the vertex position shift versus $\sigma^z_{\rm asc}$ for the single-track vertices. Since $R_{\rm asc}$ for the single-track vertices is defined as a sum of main and tail Gaussians, we also introduce $R^{\rm main}_{\rm np}$ and $R^{\rm tail}_{\rm np}$ for main and tail parts, respectively. Each of $R^{\rm main}_{\rm np}$ and $R^{\rm tail}_{\rm np}$ is expressed by the function of Eq. (5.19) with

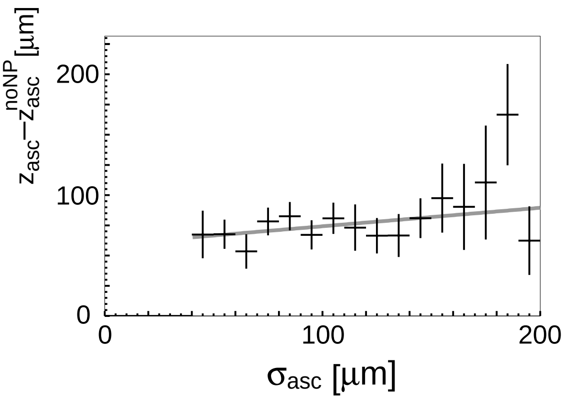

Figure 5.12: Vertex position shift ($z_{\rm asc} - z_{\rm asc}^{\rm noNP}$) versus $\sigma^z_{\rm asc}$ for single-track vertices. The events where $z_{\rm asc} < z_{\rm asc}^{\rm noNP}$ are excluded.

parameters defined as

$$(\tau^{\rm p}_{\rm np})_{\rm main} = \tau^0_{\rm p} + \tau^1_{\rm p} s_{\rm main}\sigma_{\rm asc}, \tag{5.22}$$

$$(\tau^{\rm n}_{\rm np})_{\rm main} = \tau^0_{\rm n} + \tau^1_{\rm n} s_{\rm main}\sigma_{\rm asc}, \tag{5.23}$$

$$(\tau^{\rm p}_{\rm np})_{\rm tail} = \tau^0_{\rm p} + \tau^1_{\rm p} s_{\rm tail}\sigma_{\rm asc}, \quad \text{and} \tag{5.24}$$

$$(\tau^{\rm n}_{\rm np})_{\rm tail} = \tau^0_{\rm n} + \tau^1_{\rm n} s_{\rm tail}\sigma_{\rm asc}. \tag{5.25}$$

The convolution of $R_{\rm asc}$ and $R_{\rm np}$ for single-track vertices is, thus, defined as

$$\begin{aligned} R^{\rm single}_{\rm asc} \otimes R^{\rm single}_{\rm np}(\delta z_{\rm asc}) = \int_{-\infty}^{+\infty} d\delta z'_{\rm asc} \Big[&(1-f_{\rm tail}) G(\delta z_{\rm asc} - \delta z'_{\rm asc}; s_{\rm main}\sigma^z_{\rm asc}) R^{\rm main}_{\rm np}(\delta z'_{\rm asc}) \\ &+ f_{\rm tail} G(\delta z_{\rm asc} - \delta z'_{\rm asc}; s_{\rm tail}\sigma^z_{\rm asc}) R^{\rm tail}_{\rm np}(\delta z'_{\rm asc}) \Big] . \end{aligned} \tag{5.26}$$

Figure 5.13 shows the $\delta z_{\rm asc}$ distributions for the single-track vertices. Superimposed curves are the results of the fit to the function given by Eq. (5.26).

Table 5.1 lists the shape parameters of $R_{\rm np}$ determined by fitting $R_{\rm asc} \otimes R_{\rm np}(\delta z_{\rm asc})$ to the MC $\delta z_{\rm asc}$ distributions. These parameter values are held fixed when the lifetime fit to the data is performed.

Again, above $R_{\rm np}(\delta z_{\rm asc})$ is the resolution for $\delta z_{\rm asc}$. The Δt resolution $R_{\rm np}(\Delta t)$ can be written as

$$R_{\rm np}(\Delta t) \equiv f_\delta \delta(\Delta t) + (1-f_\delta)\left[f_{\rm p} E_{\rm p}(\Delta t; \tau^{\rm p}_{\rm np}) + (1-f_{\rm p}) E_{\rm n}(\Delta t; \tau^{\rm n}_{\rm np}) \right] . \tag{5.27}$$

5.3.3 Kinematic Approximation

$R_{\rm k}$ is calculated analytically as a function of $E^{\rm cms}_B$ and $\cos\theta^{\rm cms}_B$ from the kinematics of the $\Upsilon(4S)$ two-body decay, where $E^{\rm cms}_B$ and $\theta^{\rm cms}_B$ are the energy and polar angle of

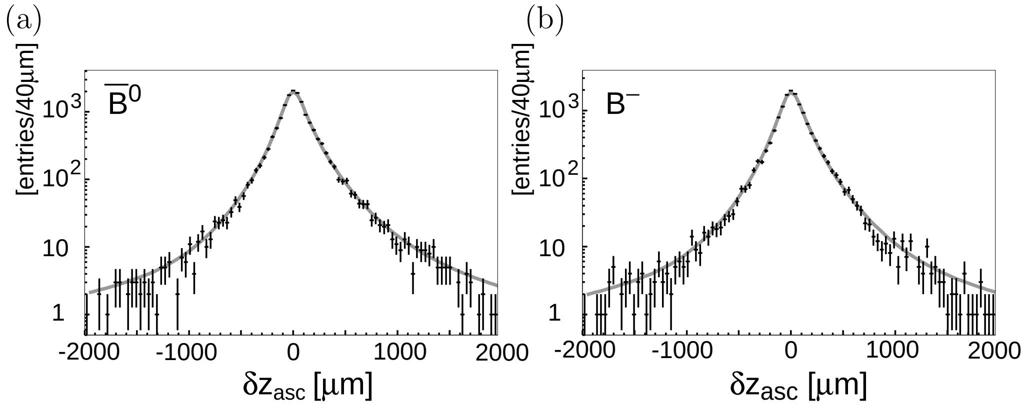

Figure 5.13: Distributions of $\delta z_{\rm asc}$ for single-track vertices of (a) B^0 and (b) B^+ mesons.

Table 5.1: Shape parameters of $R_{\rm np}$ used for the lifetime fit. They are determined for multiple- and single-track vertices, separately, using MC $\delta z_{\rm asc}$ distributions.

Parameters	B^0		B^+	
	multiple	single	multiple	single
f_δ	0.676 ± 0.007	$0.787^{+0.010}_{-0.011}$	0.650 ± 0.010	$0.763^{+0.017}_{-0.018}$
$f_{\rm p}$	0.955 ± 0.004	$0.790^{+0.020}_{-0.021}$	0.963 ± 0.004	$0.757^{+0.025}_{-0.026}$
$\tau^0_{\rm p}$ (ps)	-0.010 ± 0.011	$0.108^{+0.068}_{-0.067}$	0.037 ± 0.012	$-0.019^{+0.066}_{-0.065}$
$\tau^1_{\rm p}$	$0.927^{+0.025}_{-0.024}$	$1.321^{+0.099}_{-0.094}$	0.674 ± 0.025	$1.113^{+0.099}_{-0.092}$
$\tau^0_{\rm n}$ (ps)	$-0.194^{+0.078}_{-0.077}$	$-0.281^{+0.130}_{-0.147}$	-0.269 ± 0.099	$-0.375^{+0.111}_{-0.122}$
$\tau^1_{\rm n}$	$1.990^{+0.182}_{-0.169}$	$1.583^{+0.213}_{-0.184}$	$2.070^{+0.235}_{-0.213}$	$1.548^{+0.207}_{-0.182}$

the fully reconstructed B in the cms. The difference between the true proper-time interval $\Delta t_{\rm true} = t_{\rm ful} - t_{\rm asc}$, where $t_{\rm ful}$ and $t_{\rm asc}$ are the proper decay times of $B_{\rm ful}$ and $B_{\rm asc}$, respectively, and Δt defined in Eq. (5.6) can be given by:

$$\begin{aligned} x \equiv \Delta t - \Delta t_{\rm true} &= \frac{z_{\rm ful} - z_{\rm asc}}{c(\beta\gamma)_\Upsilon} - (t_{\rm ful} - t_{\rm asc}) \\ &= \frac{c(\beta\gamma)_{\rm ful} t_{\rm ful} - c(\beta\gamma)_{\rm asc} t_{\rm asc}}{c(\beta\gamma)_\Upsilon} - (t_{\rm ful} - t_{\rm asc}) \\ &= \left[\frac{(\beta\gamma)_{\rm ful}}{(\beta\gamma)_\Upsilon} - 1\right] t_{\rm ful} - \left[\frac{(\beta\gamma)_{\rm asc}}{(\beta\gamma)_\Upsilon} - 1\right] t_{\rm asc}, \end{aligned} \tag{5.28}$$

where $(\beta\gamma)_{\rm ful}$ and $(\beta\gamma)_{\rm asc}$ are Lorentz boost factors of the fully reconstructed and associated B mesons, respectively, and can be expressed as:

$$(\beta\gamma)_{\rm ful} = (\beta\gamma)_\Upsilon \left(\frac{E_B^{\rm cms}}{m_B c^2} + \frac{p_B^{\rm cms} \cos\theta_B^{\rm cms}}{m_B c \beta_\Upsilon} \right), \quad \text{and} \tag{5.29}$$

$$(\beta\gamma)_{\rm asc} = (\beta\gamma)_\Upsilon \left(\frac{E_B^{\rm cms}}{m_B c^2} - \frac{p_B^{\rm cms} \cos\theta_B^{\rm cms}}{m_B c \beta_\Upsilon} \right), \tag{5.30}$$

where $\beta_\Upsilon = 0.391$ is the velocity of $\Upsilon(4S)$ in units of c. Defining $a_{\rm k} \equiv E_B^{\rm cms}/(m_B c^2)$ and $c_{\rm k} \equiv p_B^{\rm cms} \cos\theta_B^{\rm cms}/(m_B c \beta_\Upsilon)$, x can be written as:

$$x = (a_{\rm k} + c_{\rm k} - 1) t_{\rm ful} - (a_{\rm k} - c_{\rm k} - 1) t_{\rm asc}. \tag{5.31}$$

Here, $a_{\rm k} \simeq 1$. Because the distribution of $t_{\rm ful}$ and $t_{\rm asc}$ is given by

$$P_{\rm true}(t_{\rm ful}, t_{\rm asc}; \tau_B) = \frac{1}{\tau_B^2} \exp\left(-\frac{t_{\rm ful} + t_{\rm asc}}{\tau_B} \right) \tag{5.32}$$

as shown in Eq. (2.92), the probability of obtaining x and $\Delta t_{\rm true}$ simultaneously is given by

$$\begin{aligned} F(x, \Delta t_{\rm true}) = \int_0^{+\infty} dt_{\rm ful} \int_0^{+\infty} & dt_{\rm asc} P_{\rm true}(t_{\rm ful}, t_{\rm asc}; \tau_B) \delta(\Delta t_{\rm true} - (t_{\rm ful} - t_{\rm asc})) \\ & \times \delta(x - [(a_{\rm k} + c_{\rm k} - 1) t_{\rm ful} - (a_{\rm k} - c_{\rm k} - 1) t_{\rm asc}]) \,, \end{aligned} \tag{5.33}$$

and the probability of obtaining $\Delta t_{\rm true}$ is given by

$$F(\Delta t_{\rm true}) = \int_0^{+\infty} dt_{\rm ful} \int_0^{+\infty} dt_{\rm asc} P_{\rm true}(t_{\rm ful}, t_{\rm asc}; \tau_B) \delta(\Delta t_{\rm true} - (t_{\rm ful} - t_{\rm asc})) \,. \tag{5.34}$$

$R_{\rm k}(x)$ can, then, be expressed as $R_{\rm k}(x) = F(x, \Delta t_{\rm true})/F(\Delta t_{\rm true})$ which gives

$$R_{\rm k}(x) = \begin{cases} E_{\rm p}(x - [(a_{\rm k} - 1)\Delta t_{\rm true} + c_{\rm k}|\Delta t_{\rm true}|] \,; |c_{\rm k}|\, \tau_B) & (c_{\rm k} > 0) \\ \delta(x - (a_{\rm k} - 1)\Delta t_{\rm true}) & (c_{\rm k} = 0) \\ E_{\rm n}(x - [(a_{\rm k} - 1)\Delta t_{\rm true} + c_{\rm k}|\Delta t_{\rm true}|] \,; |c_{\rm k}|\, \tau_B) & (c_{\rm k} < 0) \end{cases} . \tag{5.35}$$

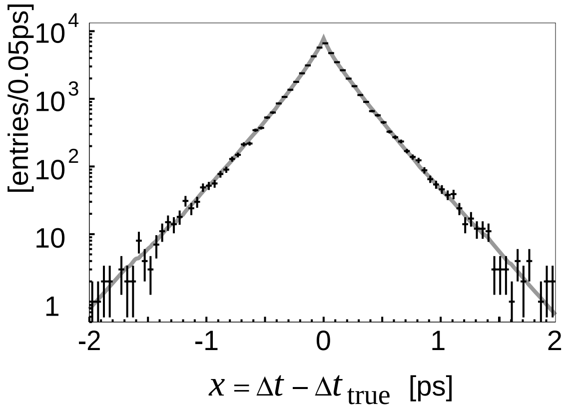

Figure 5.14: $x = \Delta t - \Delta t_{\rm true}$ distribution for $B^0 \to J/\psi K^0_S$ events together with $R_{\rm k}(x)$.

Figure 5.14 shows the x distribution for $B^0 \to J/\psi K^0_S$ events with the function $R_{\rm k}(x)$. The expected theoretical Δt distribution $P(\Delta t)$ can be expressed as a convolution of the true PDF $\mathcal{P}_{\rm sig}(\Delta t_{\rm true}; \tau_B)$ with $R_{\rm k}(x)$:

$$P(\Delta t) = \begin{cases} \frac{1}{2a_{\rm k}\tau_B} \exp\left[-\frac{|\Delta t|}{(a_{\rm k}+c_{\rm k})\tau_B}\right] & (\Delta t \geq 0) \\ \frac{1}{2a_{\rm k}\tau_B} \exp\left[-\frac{|\Delta t|}{(a_{\rm k}-c_{\rm k})\tau_B}\right] & (\Delta t < 0) \end{cases}. \tag{5.36}$$

More generally, if the probability of obtaining $t_{\rm ful}$ and $t_{\rm asc}$ simultaneously, $f(t_{\rm ful}, t_{\rm asc})$, can be expressed as

$$f(t_{\rm ful}, t_{\rm asc}) = \frac{1}{\tau_B^2} \exp\left(-\frac{t_+}{\tau_B}\right) g(t_-), \tag{5.37}$$

where $t_+ \equiv t_{\rm ful} + t_{\rm asc}$ and $t_- \equiv t_{\rm ful} - t_{\rm asc}$, Eq. (5.33) is written as

$$\begin{aligned} F(x, \Delta t_{\rm true}) &= \int_0^{+\infty} dt_{\rm ful} \int_0^{+\infty} dt_{\rm asc} f(t_{\rm ful}, t_{\rm asc}) \delta(\Delta t_{\rm true} - (t_{\rm ful} - t_{\rm asc})) \\ &\quad \times \delta(x - [(a_{\rm k} + c_{\rm k} - 1)t_{\rm ful} - (a_{\rm k} - c_{\rm k} - 1)t_{\rm asc}]) \\ &= \int_{-\infty}^{+\infty} dt_- \int_{|t_-|}^{+\infty} dt_+ \frac{1}{2}\frac{1}{\tau_B^2} \exp\left(-\frac{t_+}{\tau_B}\right) g(t_-)\delta(\Delta t_{\rm true} - t_-) \\ &\quad \times \delta(x - [(a_{\rm k} - 1)t_- + c_{\rm k} t_+]) \end{aligned} \tag{5.38}$$

and Eq. (5.34) as

$$\begin{aligned} F(\Delta t_{\rm true}) &= \int_0^{+\infty} dt_{\rm ful} \int_0^{+\infty} dt_{\rm asc} f(t_{\rm ful}, t_{\rm asc}) \delta(\Delta t_{\rm true} - (t_{\rm ful} - t_{\rm asc})) \\ &= \int_{-\infty}^{+\infty} dt_- \int_{|t_-|}^{+\infty} dt_+ \frac{1}{2}\frac{1}{\tau_B^2} \exp\left(-\frac{t_+}{\tau_B}\right) g(t_-)\delta(\Delta t_{\rm true} - t_-). \end{aligned} \tag{5.39}$$

Then, $R_{\rm k}(x) = F(x, \Delta t_{\rm true})/F(\Delta t_{\rm true})$ gives the same result as Eq. (5.35). Therefore, this $R_{\rm k}$ can be applied to any distributions that satisfy Eq. (5.37), including B^0-$\overline{B}^0$ mixing and CP asymmetry distributions.

5.3.4 Outliers

We find that there still exists a very long tail that cannot be described by the resolution functions discussed above. The outlier term is introduced to describe this long tail and is represented by a single Gaussian with zero mean and event-independent width:

$$P_{\rm ol}(\Delta t) = G(\Delta t; \sigma_{\rm ol}). \tag{5.40}$$

Since this width $\sigma_{\rm ol}$ is very large (~ 40 ps), we ignore the effect of the convolution with the lifetime distribution or other resolution components, and ignore the effect of the offset.

This outlier component exists also in the background events described in the next section. Since this long tail is considered to be caused by the mis-reconstruction of the track and independent on whether the event is signal or background, we assign the same fraction and shape of the outlier for both signal and background events. Therefore, the outlier term is regarded as the third component other than signal and background components, as shown in Eq. (5.4).

The global fraction of outliers $f_{\rm ol}$ and its width $\sigma_{\rm ol}$ are left as free parameters in the lifetime fit. Different values are used for $f_{\rm ol}$ depending on whether both vertices are reconstructed with multiple tracks or not ($f_{\rm ol}^{\rm multiple}$ or $f_{\rm ol}^{\rm single}$).

5.4 Background

For each of the reconstructed events, the signal probability $f_{\rm sig}$ is assigned using ΔE and $M_{\rm bc}$ information. The remaining fraction of the event is considered as the background. The PDF of Δt distribution for the background component is different from the signal PDF. In this section, first we describe the method of $f_{\rm sig}$ assignment to an event, and then we discuss the PDF of Δt distribution for the background components.

5.4.1 Signal Probability

The signal fraction $f_{\rm sig}$ is calculated based on ΔE and $M_{\rm bc}$ for each event. The ΔE and $M_{\rm bc}$ distribution is fitted with a sum of two dimensional signal and background functions ($F_{\rm sig}$ and $F_{\rm bkg}$) in each mode. The signal function $F_{\rm sig}$ is represented by the two dimensional Gaussian and the background function $F_{\rm bkg}$ is represented by a

Table 5.2: Region where the event is used for $F_{\rm sig}+F_{\rm bkg}$ fit for each decay mode.

Decay mode	ΔE range (GeV)	$M_{\rm bc}$ range (GeV/c^2)
$B^0 \to D^-\pi^+$	$-0.10 < \Delta E < 0.20$	$5.20 < M_{\rm bc} < 5.29$
$B^0 \to D^{*-}\pi^+$	$-0.10 < \Delta E < 0.20$	$5.20 < M_{\rm bc} < 5.29$
$B^0 \to D^{*-}\rho^+$	$-0.05 < \Delta E < 0.20$	$5.20 < M_{\rm bc} < 5.29$
$B^0 \to J/\psi K^0_S$	$-0.10 < \Delta E < 0.20$	$5.20 < M_{\rm bc} < 5.29$
$B^0 \to J/\psi K^{*0}$	$-0.20 < \Delta E < 0.10$	$5.20 < M_{\rm bc} < 5.29$
$B^+ \to \overline{D}{}^0\pi^+$	$-0.10 < \Delta E < 0.20$	$5.20 < M_{\rm bc} < 5.29$
$B^+ \to J/\psi K^+$	$-0.10 < \Delta E < 0.20$	$5.20 < M_{\rm bc} < 5.29$

first order polynomial in the ΔE axis and an ARGUS background function [57] in the $M_{\rm bc}$ axis:

$$F_{\rm sig}(\Delta E, M_{\rm bc}) = aG(\Delta E - \mu_{\Delta E};\sigma_{\Delta E})G(M_{\rm bc}-\mu_{M_{\rm bc}};\sigma_{M_{\rm bc}}), \tag{5.41}$$

$$F_{\rm bkg}(\Delta E, M_{\rm bc}) = b(1+c\Delta E)M_{\rm bc}\sqrt{1-\left(\frac{M_{\rm bc}}{E^{\rm cms}_{\rm beam}}\right)^2}\exp\left\{d\left[1-\left(\frac{M_{\rm bc}}{E^{\rm cms}_{\rm beam}}\right)^2\right]\right\}. \tag{5.42}$$

Using these functions, $f_{\rm sig}$ is obtained as a function of both ΔE and $M_{\rm bc}$:

$$f_{\rm sig}(\Delta E, M_{\rm bc}) = \frac{F_{\rm sig}(\Delta E, M_{\rm bc})}{F_{\rm sig}(\Delta E, M_{\rm bc}) + F_{\rm bkg}(\Delta E, M_{\rm bc})}. \tag{5.43}$$

An unbinned maximum likelihood fit is used for the parameter determination of $F_{\rm sig}$ and $F_{\rm bkg}$. The region used for the fit of each mode is listed in Table 5.2. The ΔE range is chosen to avoid the satellite peak from the cross-feed. Figures 5.15 and 5.16 show the ΔE and $M_{\rm bc}$ distributions of B candidates found in the $M_{\rm bc}$ and ΔE signal regions, respectively.

5.4.2 Background Shape

The background PDF $P_{\rm bkg}(\Delta t)$ is modeled as a sum of prompt and exponential components ($\mathcal{P}_{\rm bkg}(\Delta t)$) convoluted with a sum of two Gaussians ($R_{\rm bkg}(\Delta t)$):

$$P_{\rm bkg}(\Delta t) = \int_{-\infty}^{+\infty} d(\Delta t')\mathcal{P}_{\rm bkg}(\Delta t - \Delta t')R_{\rm bkg}(\Delta t'), \tag{5.44}$$

where

$$\mathcal{P}_{\rm bkg}(\Delta t) = f^{\rm bkg}_\delta \delta(\Delta t - \mu^{\rm bkg}_\delta) + (1-f^{\rm bkg}_\delta)\frac{1}{2\tau_{\rm bkg}}\exp\left(-\frac{|\Delta t - \mu^{\rm bkg}_\tau|}{\tau_{\rm bkg}}\right) \tag{5.45}$$

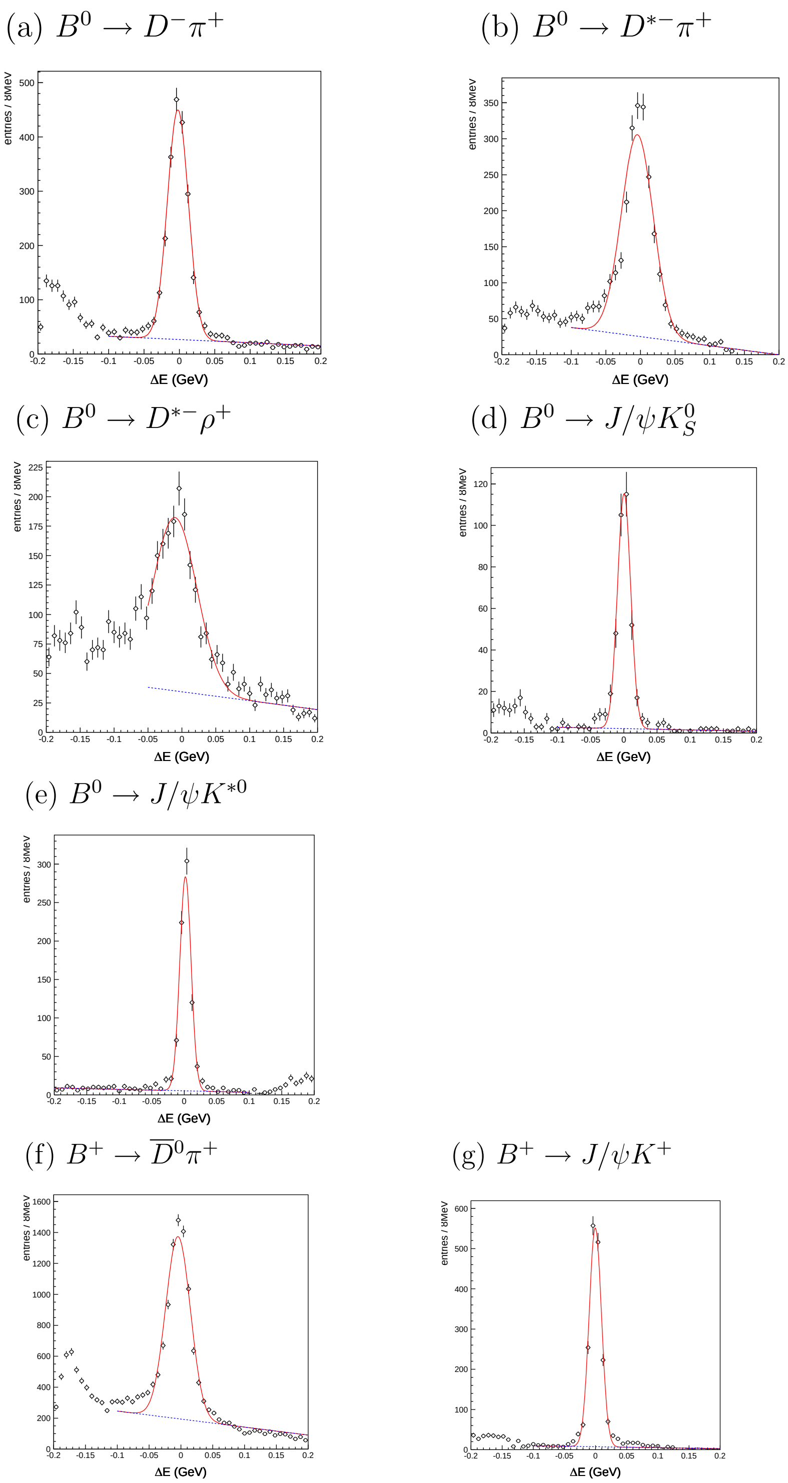

Figure 5.15: Distributions of ΔE for the B candidates found in the $M_{\rm bc}$ signal regions. The projections of the fit results are superimposed. Dashed lines represent the background contribution $F_{\rm bkg}$.

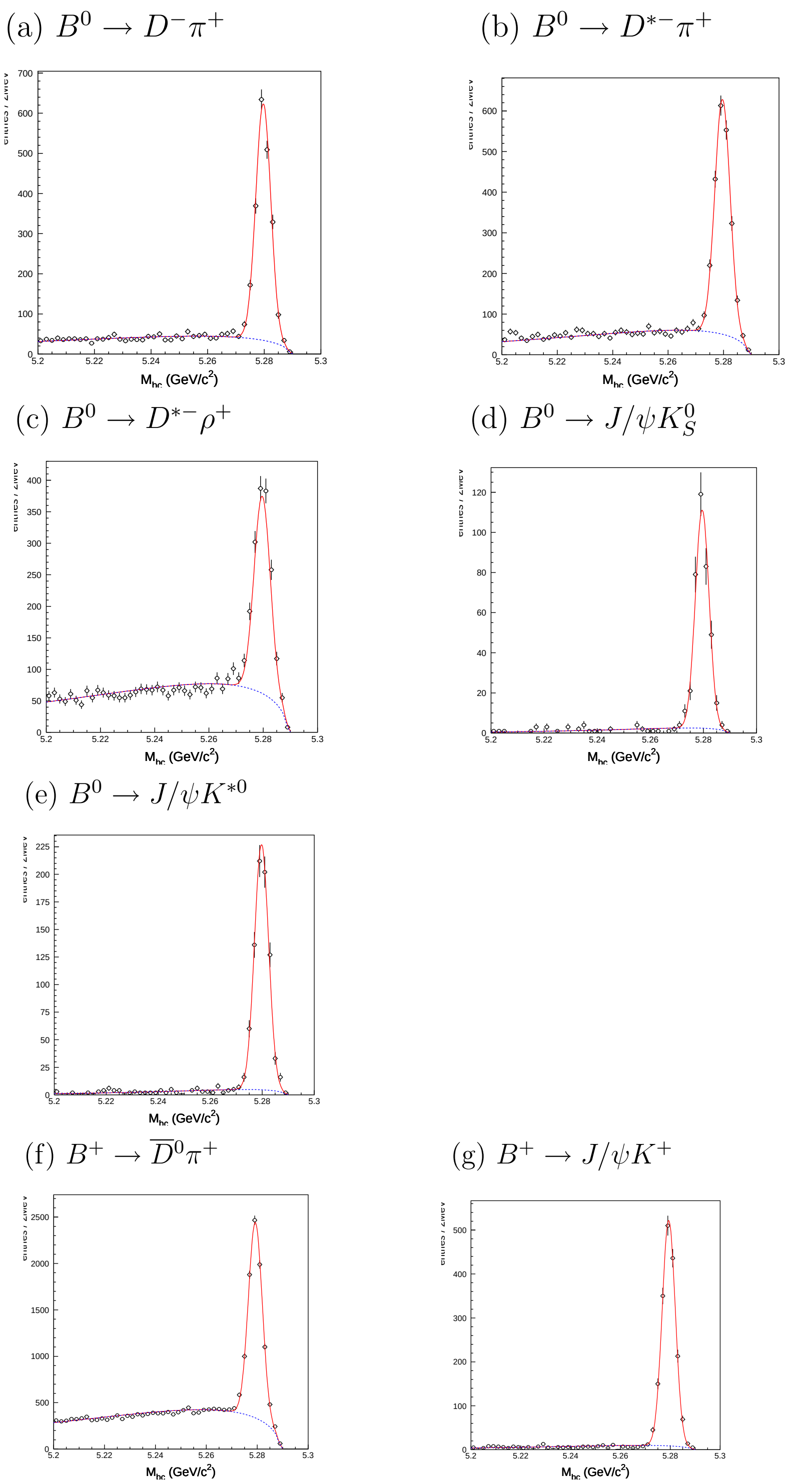

Figure 5.16: Distributions of $M_{\rm bc}$ for the B candidates found in the ΔE signal regions. The projections of the fit results are superimposed. Dashed lines represent the background contribution $F_{\rm bkg}$.

Table 5.3: Excluded area where the event is not used to fit the $P_{\rm bkg}$ for each decay mode.

Decay mode	ΔE range (GeV)	$M_{\rm bc}$ range (GeV/c^2)
$B^0 \to D^-\pi^+$	$-0.10 < \Delta E < 0.09$	$5.26 < M_{\rm bc} < 5.29$
$B^0 \to D^{*-}\pi^+$	$-0.10 < \Delta E < 0.14$	$5.26 < M_{\rm bc} < 5.29$
$B^0 \to D^{*-}\rho^+$	$-0.05 < \Delta E < 0.17$	$5.26 < M_{\rm bc} < 5.29$
$B^0 \to J/\psi K_S^0$	$-0.10 < \Delta E < 0.08$	$5.26 < M_{\rm bc} < 5.29$
$B^0 \to J/\psi K^{*0}$	$-0.08 < \Delta E < 0.10$	$5.26 < M_{\rm bc} < 5.29$
$B^+ \to \overline{D}{}^0\pi^+$	$-0.10 < \Delta E < 0.12$	$5.26 < M_{\rm bc} < 5.29$
$B^+ \to J/\psi K^+$	$-0.10 < \Delta E < 0.08$	$5.26 < M_{\rm bc} < 5.29$

with $\mu_\delta^{\rm bkg}$ and $\mu_\tau^{\rm bkg}$ being offsets of the distribution, and

$$R_{\rm bkg}(\Delta t) = (1 - f_{\rm tail}^{\rm bkg})G\left(\Delta t; s_{\rm main}^{\rm bkg}\sqrt{\sigma_{\rm ful}^2 + \sigma_{\rm asc}^2}\right) + f_{\rm tail}^{\rm bkg}G\left(\Delta t; s_{\rm tail}^{\rm bkg}\sqrt{\sigma_{\rm ful}^2 + \sigma_{\rm asc}^2}\right). \tag{5.46}$$

Different values are used for $s_{\rm main}^{\rm bkg}$, $s_{\rm tail}^{\rm bkg}$, $f_{\rm tail}^{\rm bkg}$, and $f_\delta^{\rm bkg}$ depending on whether both vertices are reconstructed with multiple tracks or not. The parameters for the background function $P_{\rm bkg}$ are determined by the unbinned maximum likelihood fit to the Δt distribution of the background-enhanced control sample for each decay mode. For the background-enhanced control sample we use the ΔE-$M_{\rm bc}$ sideband region which is basically the same as the region used for $f_{\rm sig}$ fit shown in Table 5.2, but the signal region which is slightly wider than the signal box shown in Table 4.4 is excluded. This excluded area for each mode is listed in Table 5.3. The fitted parameters of the background shape for each mode are listed in Table 5.4. The Δt distribution of the background-enhanced control sample is shown in Fig. 5.17 mode by mode, with the fitted curve to the background shape listed in Table 5.4.

A MC study shows that the fraction of prompt component $f_\delta^{\rm bkg}$ in the signal region is smaller (by ∼10–50% depending on the decay mode) than that in the sideband region for $B \to D^{(*)}X$ modes. Therefore, in the lifetime fitting, we correct $P_{\rm bkg}$ to take account for this effect by multiplying the ratio of $f_\delta^{\rm bkg}$ in the signal box to that in the sideband region obtained from MC sample, $(f_\delta^{\rm bkg})^{\rm signal\ box}/(f_\delta^{\rm bkg})^{\rm sideband}$. The ratio obtained from MC sample for each mode is listed in Table 5.5.

5.5 Fit Result

Using the PDF described above, an unbinned maximum likelihood fit is applied to the Δt distribution. In the lifetime fit, following twelve parameters are determined simultaneously;

Table 5.4: Background shape parameters for each decay mode.

Parameter	$B^0 \to D^-\pi^+$	$B^0 \to D^{*-}\pi^+$	$B^0 \to D^{*-}\rho^+$	$B^+ \to \overline{D}^0\pi^+$
$(s^{\rm bkg}_{\rm main})_{\rm multiple}$	1.03 ± 0.04	$0.69^{+0.18}_{-0.14}$	0.90 ± 0.07	1.02 ± 0.02
$(s^{\rm bkg}_{\rm tail})_{\rm multiple}$	$3.03^{+0.68}_{-0.37}$	$2.33^{+0.39}_{-0.32}$	$5.19^{+0.74}_{-0.58}$	$6.27^{+0.38}_{-0.34}$
$(f^{\rm bkg}_{\rm tail})_{\rm multiple}$	$0.14^{+0.06}_{-0.05}$	$0.67^{+0.12}_{-0.17}$	$0.13^{+0.04}_{-0.03}$	0.060 ± 0.008
$(f^{\rm bkg}_{\delta})_{\rm multiple}$	$0.67^{+0.08}_{-0.09}$	$0.70^{+0.07}_{-0.08}$	0.34 ± 0.09	0.52 ± 0.03
$(s^{\rm bkg}_{\rm main})_{\rm single}$	0.73 ± 0.07	$0.87^{+0.09}_{-0.10}$	0.93 ± 0.08	0.79 ± 0.03
$(s^{\rm bkg}_{\rm tail})_{\rm single}$	$4.69^{+0.90}_{-0.76}$	$4.54^{+4.05}_{-1.34}$	$3.52^{+0.47}_{-0.39}$	$5.99^{+0.55}_{-0.52}$
$(f^{\rm bkg}_{\rm tail})_{\rm single}$	0.12 ± 0.04	$0.08^{+0.06}_{-0.04}$	0.17 ± 0.05	0.09 ± 0.01
$(f^{\rm bkg}_{\delta})_{\rm single}$	0.35 ± 0.10	0.54 ± 0.11	0.34 ± 0.13	0.33 ± 0.05
$\tau_{\rm bkg}$ (ps)	$1.10^{+0.14}_{-0.13}$	$1.68^{+0.26}_{-0.20}$	$0.87^{+0.11}_{-0.10}$	0.98 ± 0.05
$\mu^{\rm bkg}_{\delta}$ (ps)	-0.03 ± 0.03	0.00 ± 0.03	$0.11^{+0.07}_{-0.06}$	-0.02 ± 0.01
$\mu^{\rm bkg}_{\tau}$ (ps)	$0.00^{+0.08}_{0.07}$	$-0.11^{+0.13}_{-0.15}$	$-0.13^{+0.06}_{-0.07}$	-0.11 ± 0.02

Parameter	$B^0 \to J/\psi K^0_S$	$B^0 \to J/\psi K^{*0}$	$B^+ \to J/\psi K^+$
$(s^{\rm bkg}_{\rm main})_{\rm multiple}$	$0.40^{+0.13}_{-0.10}$	$1.09^{+0.24}_{-0.26}$	$0.79^{+0.22}_{-0.24}$
$(s^{\rm bkg}_{\rm tail})_{\rm multiple}$	$9.46^{+4.26}_{-2.57}$	$6.97^{+6.39}_{-2.30}$	$1.90^{+0.64}_{-0.37}$
$(f^{\rm bkg}_{\rm tail})_{\rm multiple}$	$0.29^{+0.11}_{-0.12}$	$0.03^{+0.05}_{-0.03}$	$0.66^{+0.21}_{-0.28}$
$(f^{\rm bkg}_{\delta})_{\rm multiple}$	$0.39^{+0.18}_{-0.17}$	0.08 ± 0.08	$0.85^{+0.04}_{-0.05}$
$(s^{\rm bkg}_{\rm main})_{\rm single}$	$0.96^{+0.19}_{-0.23}$	$0.82^{+0.15}_{-0.14}$	$1.03^{+0.09}_{-0.10}$
$(s^{\rm bkg}_{\rm tail})_{\rm single}$	$4.90^{+2.15}_{-1.29}$	$8.33^{+2.96}_{-2.13}$	$11.2^{+4.7}_{-3.0}$
$(f^{\rm bkg}_{\rm tail})_{\rm single}$	$0.16^{+0.16}_{-0.07}$	$0.09^{+0.04}_{-0.03}$	$0.05^{+0.03}_{-0.02}$
$(f^{\rm bkg}_{\delta})_{\rm single}$	$0.38^{+0.28}_{-0.34}$	$0.18^{+0.14}_{-0.12}$	$0.65^{+0.09}_{-0.11}$
$\tau_{\rm bkg}$ (ps)	$0.39^{+0.24}_{-0.25}$	1.43 ± 0.16	$2.14^{+0.41}_{-0.33}$
$\mu^{\rm bkg}_{\delta}$ (ps)	-0.56 ± 0.09	$-0.70^{+0.28}_{-0.27}$	-0.00 ± 0.05
$\mu^{\rm bkg}_{\tau}$ (ps)	$0.23^{+0.17}_{-0.19}$	$-0.00^{+0.14}_{-0.13}$	$-0.21^{+0.33}_{-0.37}$

Table 5.5: Ratio of $f^{\rm bkg}_{\delta}$ in the signal box to that in the sideband region, $(f^{\rm bkg}_{\delta})^{\rm signal\ box}/(f^{\rm bkg}_{\delta})^{\rm sideband}$.

Decay mode	$(f^{\rm bkg}_{\delta})^{\rm signal\ box}_{\rm multiple}/(f^{\rm bkg}_{\delta})^{\rm sideband}_{\rm multiple}$	$(f^{\rm bkg}_{\delta})^{\rm signal\ box}_{\rm single}/(f^{\rm bkg}_{\delta})^{\rm sideband}_{\rm single}$
$B^0 \to D^-\pi^+$	0.59 ± 0.10	$0.82^{+0.28}_{-0.30}$
$B^0 \to D^{*-}\pi^+$	0.54 ± 0.10	0.59 ± 0.31
$B^0 \to D^{*-}\rho^+$	0.65 ± 0.08	$0.55^{+0.20}_{-0.21}$
$B^+ \to \overline{D}^0\pi^+$	0.82 ± 0.02	0.89 ± 0.07

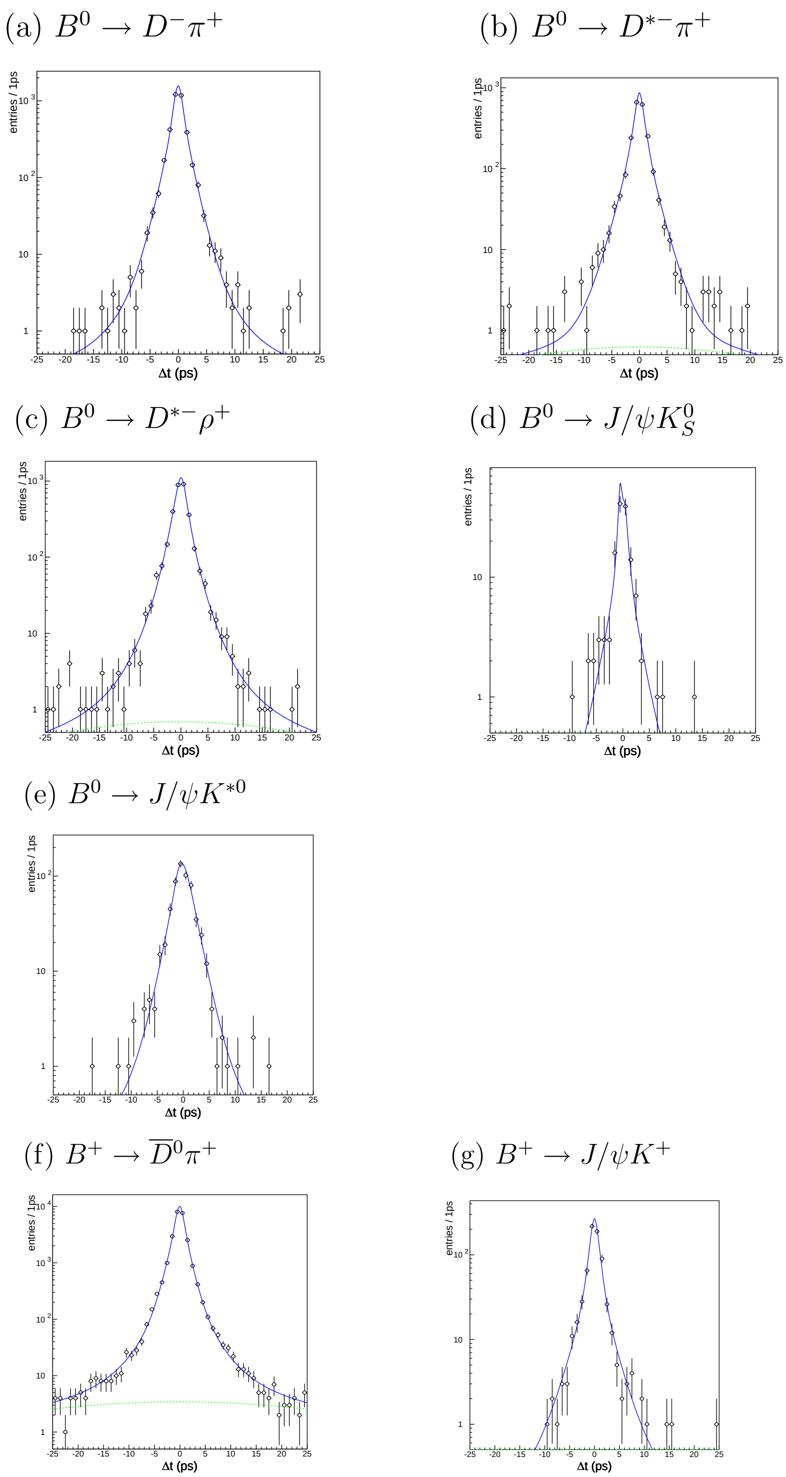

Figure 5.17: Distribution of Δt in the ΔE-$M_{\rm bc}$ sideband region for each mode. Fitted curves to the background shapes listed in Table 5.4 are superimposed. The dashed lines represent the outlier distribution of Δt.

Table 5.6: Number of events used in the lifetime fit for each mode.

Mode	Number of events
$B^0 \to D^-\pi^+$	2269
$B^0 \to D^{*-}\pi^+$	2495
$B^0 \to D^{*-}\rho^+$	1902
$B^0 \to J/\psi K^0_S$	386
$B^0 \to J/\psi K^{*0}$	811
B^0 total	7863
$B^+ \to \overline{D}{}^0\pi^+$	10243
$B^+ \to J/\psi K^+$	1804
B^+ total	12047
Total	19910

- The lifetimes of B mesons: τ_{B^0} and τ_{B^+}.
- The detector resolution
  - Parameters for multiple-track vertices: $s^0_{\rm rec}$, $s^1_{\rm rec}$, $s^0_{\rm asc}$, and $s^1_{\rm asc}$.
  - Parameters for single-track vertices: $s_{\rm main}$, $s_{\rm tail}$, and $f_{\rm tail}$.
- The outlier parameters: $\sigma_{\rm ol}$, $f^{\rm multiple}_{\rm ol}$, and $f^{\rm single}_{\rm ol}$.

The parameters for $R_{\rm np}$ are fixed to the values obtained from the MC sample as listed in Table 5.1, because $R_{\rm np}$ is considered to be determined from the physics. In order to reduce the dependence on the MC sample and as a result to reduce the systematic error, we determine the detector resolution during the fit of the B meson lifetimes. The detector resolution could be the most dominating part of the systematic error, since the detector resolution is as broad as the lifetime distribution being fitted. Because we use common detector resolution parameters for both neutral and charged B mesons as described in Section 5.3, B^0 and B^+ should be fitted simultaneously through the determination of the detector resolution parameters.

We also measure the lifetime ratio of the charged B meson to the neutral B meson, $r \equiv \tau_{B^+}/\tau_{B^0}$, by repeating the final fit after replacing τ_{B^+} with $r\tau_{B^0}$.

Using 29.1 fb^{-1} data which correspond to 31.3×10^6 $B\overline{B}$ pairs, we find 7863 B^0 and 12047 B^+ events in the signal boxes after all vertexing and selection requirements are applied. The number of events used in the lifetime fit for each mode is listed in Table 5.6. The unbinned maximum likelihood fit to these data sample yields

$$\tau_{B^0} = 1.554 \pm 0.030 \text{ ps}, \tag{5.47}$$

$$\tau_{B^+} = 1.695 \pm 0.026 \text{ ps}. \tag{5.48}$$

Table 5.7: Result of the lifetime fit.

Parameter	Value
τ_{B^0} (ps)	1.554 ± 0.030
τ_{B^+} (ps)	1.695 ± 0.026
$s^0_{\rm rec}$	$0.809^{+0.146}_{-0.150}$
$s^1_{\rm rec}$	0.154 ± 0.013
$s^0_{\rm asc}$	$0.753^{+0.064}_{-0.065}$
$s^1_{\rm asc}$	0.064 ± 0.005
$s_{\rm main}$	$0.647^{+0.074}_{-0.083}$
$s_{\rm tail}$	$3.00^{+2.23}_{-0.99}$
$f_{\rm tail}$	$0.083^{+0.083}_{-0.045}$
$\sigma_{\rm ol}$ (ps)	$36.2^{+5.0}_{-3.5}$
$f^{\rm multiple}_{\rm ol}$	$(5.83^{+3.02}_{-2.25}) \times 10^{-4}$
$f^{\rm single}_{\rm ol}$	0.0306 ± 0.0036

Table 5.8: Result of lifetime fit for each decay mode. All lifetimes are determined simultaneously with sharing the same resolution function.

Decay mode	Lifetime (ps)
$B^0 \to D^-\pi^+$	$1.535^{+0.046}_{-0.045}$
$B^0 \to D^{*-}\pi^+$	$1.576^{+0.050}_{-0.048}$
$B^0 \to D^{*-}\rho^+$	$1.618^{+0.065}_{-0.063}$
$B^0 \to J/\psi K^0_S$	$1.778^{+0.125}_{-0.116}$
$B^0 \to J/\psi K^{*0}$	$1.368^{+0.068}_{-0.065}$
$B^+ \to \overline{D}^0\pi^+$	1.694 ± 0.029
$B^+ \to J/\psi K^+$	$1.704^{+0.053}_{-0.051}$

The fit results of all the parameters are listed in Table 5.7. The Δt distributions with the fitted curves for neutral and charged B mesons are shown in Fig. 5.18. The resulting Δt resolution for the signal is ~ 1.56 ps (rms). The fit for the lifetime ratio yields

$$\tau_{B^+}/\tau_{B^0} = 1.091 \pm 0.023. \tag{5.49}$$

The result of the lifetime fit in which lifetimes are different for each decay mode is listed in Table 5.8. All lifetimes are determined simultaneously with sharing the same resolution function.

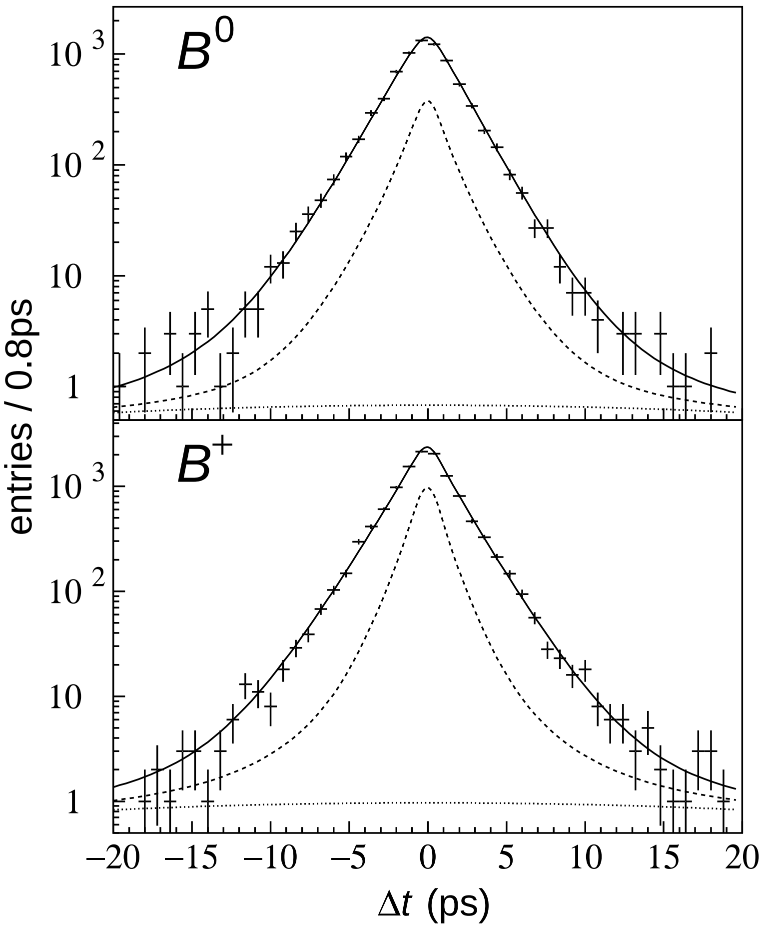

Figure 5.18: Distributions of Δt for neutral (upper) and charged (lower) B mesons, with fitted curves. The dashed lines represent the sum of the background and outlier components, and the dotted lines represent the outlier component.

Table 5.9: Summary of the systematic errors for neutral and charged B lifetimes, and their ratio. The errors are combined in quadrature.

Source	τ_{B^0} (ps)	τ_{B^+} (ps)	τ_{B^+}/τ_{B^0}
IP constraint	0.004	0.003	0.001
Track selection	0.006	0.004	0.001
Vertex selection	0.003	0.002	0.002
Δt range	0.003	0.002	0.001
ΔE-$M_{\rm bc}$ signal region	0.003	0.004	0.003
Signal fraction	0.001	0.001	0.001
$R_{\rm sig}$ parameterization	0.008	0.008	Cancels
$R_{\rm np}$ parameters	0.006	0.004	0.006
Background shape	0.012	0.007	0.011
Fit bias	0.006	0.007	0.005
Total	0.019	0.015	0.014

5.6 Systematic Uncertainties

We consider the systematic uncertainties from various sources listed bellow. The results are summarized in Table 5.9. All systematic errors are combined in quadrature.

IP Constraint The IP constraint vertex fit includes the uncertainty of the B decay point due to the transverse B flight length. This uncertainty is estimated to be 21 μm assuming a Gaussian function although it is actually an exponential function. The systematic error due to the IP constraint is estimated by varying the smearing by ± 10 μm.

The nominal IP position for each run is also determined using Bhabha events instead of hadronic events. The systematic error due to the IP position is studied using the IP position obtained from Bhabha events. We find the uncertainty from the IP position to be negligible.

Track Selection Possible systematic effects due to the track quality selection of the associated B decay vertices are studied. Each track selection criterion is varied by $\pm 10\%$.

Vertex Selection The uncertainty on the vertex selection is studied by varying the vertex-fit quality cut from $\xi < 50$ to $\xi < 200$.

Δt Range We estimate the systematic uncertainty due to the maximum $|\Delta t|$ requirement by varying the $|\Delta t|$ range by ± 30 ps and taking the maximum excursion to be the systematic error.

Δt Scale We examine the uncertainty in the scale of Δt arising from the measurement error of the SVD sizes and thermal expansion during the operation. We find that its contribution to the lifetimes is negligibly small.

Δt Dependence of Reconstruction Efficiency The Δt dependence of the reconstruction efficiency is assessed by performing unbinned maximum likelihood fits on the generated Δt distribution for all generated events, and then on the reconstructed events, with a pure exponential function $\mathcal{P}_{\rm sig}(\Delta t; \tau_B)$ defined by Eq. (5.3). The difference of the lifetimes obtained from the two fits is considered to be from the bias in the reconstruction efficiency. There is no difference between two fits beyond the statistical error.

ΔE-$M_{\rm bc}$ Signal Region ΔE-$M_{\rm bc}$ signal regions listed in Table 4.4 are varied by ± 10 MeV for ΔE and ± 3 MeV/c^2 for $M_{\rm bc}$, to estimate the systematic error on the signal region selection.

Signal Fraction The signal fraction $f_{\rm sig}$ is calculated from the signal and background distributions of ΔE and $M_{\rm bc}$ as described in Section 5.4.1. The parameters determining $f_{\rm sig}$ are varied by $\pm 1\sigma$ to estimate the associated systematic error.

$R_{\rm sig}$ Parameterization The systematic error due to the modeling of $R_{\rm sig}$ is estimated by comparing the results with different $R_{\rm sig}$ parameterizations. For this estimation, we use modified $R_{\rm ful}^{\rm multiple}$ and $R_{\rm asc}^{\rm multiple}$ defined as

$$R_{\rm ful}^{\rm multiple}(\delta z_{\rm ful}) = (1 - f_{\rm tail}^{\rm ful}) G(\delta z_{\rm ful}; s_{\rm main}^{\rm ful}\sigma_{\rm ful}) + f_{\rm tail}^{\rm ful} G(\delta z_{\rm ful}; s_{\rm tail}^{\rm ful} s_{\rm main}^{\rm ful}\sigma_{\rm ful}) \quad (5.50)$$

$$R_{\rm asc}^{\rm multiple}(\delta z_{\rm asc}) = (1 - f_{\rm tail}^{\rm asc}) G(\delta z_{\rm asc}; s_{\rm main}^{\rm asc}\sigma_{\rm asc}) + f_{\rm tail}^{\rm asc} G(\delta z_{\rm asc}; s_{\rm tail}^{\rm asc} s_{\rm main}^{\rm asc}\sigma_{\rm asc}), \quad (5.51)$$

where $s_{\rm main}^{\rm ful}$ and $s_{\rm main}^{\rm asc}$ are the first order polynomials of ξ like Eq. (5.14). The parameters for $R_{\rm np}$ and $s_{\rm tail}^{\rm ful}$, $f_{\rm tail}^{\rm ful}$, $s_{\rm tail}^{\rm asc}$, and $f_{\rm tail}^{\rm asc}$ are obtained from MC. We consider that this effect is same for B^0 and B^+, and regard the average of the differences of the fit results as the systematic error for the lifetimes. No systematic error is assigned for the lifetime ratio.

$R_{\rm np}$ Parameters The effects of smearing on $z_{\rm asc}$ reconstruction due to the non-primary tracks are determined from the MC data sample as described in Section 5.3.2. The lifetime fit is repeated after varying the $R_{\rm np}$ parameters which are obtained from the MC data sample, by $\pm 2\sigma$.

Dependence on *B* Meson Mass The lifetime dependence on the B meson mass, which is the input for $R_{\rm k}$ as shown in Section 5.3.3, is measured by varying the mass by $\pm 1\sigma$ from the world average value. The differences is found to be negligible.

Background Shape The parameters of the background Δt distribution are determined from the fit to the Δt distribution of the ΔE-$M_{\rm bc}$ sideband region in the data, as described in Section 5.4.2. The systematic error due to the background shape is estimated by varying its parameters by their errors. The ratio of $f_\delta^{\rm bkg}$ in the signal box to that in the sideband region, obtained from the MC data sample, is varied by $\pm 2\sigma$.

Fit bias The possible bias in the fitting procedure and the effect of SVD alignment error are studied with MC samples. The difference between the results of the fit on the generated Δt distribution for reconstructed events with a pure exponential function and the fit on the reconstructed Δt distribution with the nominal probability density function is considered to be the bias from the lifetime fit procedure. Since we find no bias, we do not introduce the correction and regard the MC statistics as a systematic error.

5.7 Summary of Lifetime Fit

We have presented the measurements of the B^0 and B^+ meson lifetimes using 29.1 fb^{-1} of data sample collected with the Belle detector at the $\Upsilon(4S)$ resonance. Unbinned maximum likelihood fits to the distributions of the proper-time difference between the two B meson decays yield

$$\tau_{B^0} = 1.554 \pm 0.030(\text{stat}) \pm 0.019(\text{syst})\ \text{ps}, \tag{5.52}$$

$$\tau_{B^+} = 1.695 \pm 0.026(\text{stat}) \pm 0.015(\text{syst})\ \text{ps}, \tag{5.53}$$

$$\tau_{B^+}/\tau_{B^0} = 1.091 \pm 0.023(\text{stat}) \pm 0.014(\text{syst}). \tag{5.54}$$

A value of unity for τ_{B^+}/τ_{B^0} is ruled out at a level greater than 3σ.

Chapter 6

Measurement of Δm_d

In this chapter, we describe the analysis procedure for the measurement of the oscillation frequency for B^0-$\overline{B}^0$ mixing, Δm_d [58]. One neutral B meson is fully reconstructed in a flavor-specific hadronic decay mode as described in Section 4.3.4. The flavor of the other B is extracted through a likelihood calculated using the b-flavor information in its final decay products. An unbinned maximum likelihood fit is applied to the distributions of the proper decay time difference of B pairs in events tagged as same- and opposite-flavor decays.

6.1 Unbinned Maximum Likelihood Fit

The value of Δm_d is extracted from the time evolution of opposite-flavor (OF; $B^0\overline{B}^0$) and same-flavor (SF; B^0B^0, $\overline{B}^0\overline{B}^0$) neutral B decays.

For the reconstruction of proper-time interval, we follow the same procedure as in the lifetime analysis described in Section 5.2. The selection criteria to assure the vertexing quality and those on Δt are also the same as in the lifetime analysis.

The theoretical proper-time difference distributions for OF events ($\mathcal{P}_{\rm sig}^{\rm OF}$) and for SF events ($\mathcal{P}_{\rm sig}^{\rm SF}$) are given by

$$\mathcal{P}_{\rm sig}^{\rm OF}(\Delta t; \Delta m_d) = \frac{1}{4\tau_{B^0}} \exp\left(-\frac{|\Delta t|}{\tau_{B^0}}\right) [1 + \cos(\Delta m_d \Delta t)]\,, \text{ and} \tag{6.1}$$

$$\mathcal{P}_{\rm sig}^{\rm SF}(\Delta t; \Delta m_d) = \frac{1}{4\tau_{B^0}} \exp\left(-\frac{|\Delta t|}{\tau_{B^0}}\right) [1 - \cos(\Delta m_d \Delta t)]\,, \tag{6.2}$$

respectively, as discussed in Section 2.5. Including the probability of the wrong flavor assignment for the associated B meson, w, the above distributions are diluted as

$$\mathcal{P}_{\rm sig}^{\rm OF}(\Delta t; \Delta m_d) = \frac{1}{4\tau_{B^0}} \exp\left(-\frac{|\Delta t|}{\tau_{B^0}}\right) \left[1 + (1-2w)\cos(\Delta m_d \Delta t)\right], \tag{6.3}$$

$$\mathcal{P}_{\rm sig}^{\rm SF}(\Delta t; \Delta m_d) = \frac{1}{4\tau_{B^0}} \exp\left(-\frac{|\Delta t|}{\tau_{B^0}}\right) \left[1 - (1-2w)\cos(\Delta m_d \Delta t)\right]. \tag{6.4}$$

To take account for the effects of the detector resolution and the background events in the data, the overall PDFs become

$$\begin{aligned} P^{\rm OF}(\Delta t; \Delta m_d) = (1 - f_{\rm ol}) &\left[f_{\rm sig} P_{\rm sig}^{\rm OF}(\Delta t; \Delta m_d) + (1 - f_{\rm sig}) P_{\rm bkg}^{\rm OF}(\Delta t)\right] \\ &+ f_{\rm ol}\left[f_{\rm sig} f_{\rm sig}^{\rm OF} + (1 - f_{\rm sig}) f_{\rm bkg}^{\rm OF}\right] P_{\rm ol}(\Delta t), \end{aligned} \tag{6.5}$$

$$\begin{aligned} P^{\rm SF}(\Delta t; \Delta m_d) = (1 - f_{\rm ol}) &\left[f_{\rm sig} P_{\rm sig}^{\rm SF}(\Delta t; \Delta m_d) + (1 - f_{\rm sig}) P_{\rm bkg}^{\rm SF}(\Delta t)\right] \\ &+ f_{\rm ol}\left[f_{\rm sig}(1 - f_{\rm sig}^{\rm OF}) + (1 - f_{\rm sig})(1 - f_{\rm bkg}^{\rm OF})\right] P_{\rm ol}(\Delta t), \end{aligned} \tag{6.6}$$

where $f_{\rm sig}$ is the signal purity determined on an event-by-event basis, $P_{\rm sig}^{\rm OF}$ and $P_{\rm bkg}^{\rm OF}$ ($P_{\rm sig}^{\rm SF}$ and $P_{\rm bkg}^{\rm SF}$) are the PDFs for the signal and background OF (SF) events, respectively, and $f_{\rm sig}^{\rm OF}$ and $f_{\rm bkg}^{\rm OF}$ are the fractions of the OF events in the signal and background events, respectively. $f_{\rm ol}$ and $P_{\rm ol}(\Delta t)$ are the fraction and the function of the outlier described in Section 5.3.4, respectively. $P_{\rm sig}^{\rm OF}$ and $P_{\rm sig}^{\rm SF}$ are described as the convolution of the theoretical PDFs $\mathcal{P}_{\rm sig}^{\rm OF}$ and $\mathcal{P}_{\rm sig}^{\rm SF}$ defined in Eqs. (6.3) and (6.4) with a resolution function $R_{\rm sig}$ described in Section 5.3:

$$P_{\rm sig}^{\rm OF}(\Delta t; \Delta m_d) = \int_{-\infty}^{+\infty} d(\Delta t') \mathcal{P}_{\rm sig}^{\rm OF}(\Delta t') R_{\rm sig}(\Delta t - \Delta t'), \tag{6.7}$$

$$P_{\rm sig}^{\rm SF}(\Delta t; \Delta m_d) = \int_{-\infty}^{+\infty} d(\Delta t') \mathcal{P}_{\rm sig}^{\rm SF}(\Delta t') R_{\rm sig}(\Delta t - \Delta t'). \tag{6.8}$$

The likelihood function is constructed from these PDFs:

$$L(\Delta m_d) = \prod_i P^{\rm OF}(\Delta t_i; \Delta m_d) \prod_j P^{\rm SF}(\Delta t_j; \Delta m_d), \tag{6.9}$$

where the indices i and j run over all selected OF and SF events in the signal region, respectively.

Note that the PDFs are normalized as

$$\int d(\Delta t)\left[P^{\rm OF}(\Delta t) + P^{\rm SF}(\Delta t)\right] = 1. \tag{6.10}$$

By using this normalization, not only the shapes of Δt distributions, but also the ratio of the number of the SF events to that of the OF events can be used for the determination of Δm_d.

6.2 Flavor Tagging

To measure the oscillation frequency Δm_d, we need to know the flavor of the associated B meson at its decay time. This determination is called "flavor tagging." We refer to the associated B meson as the tag-side B meson or B_{tag}.

We determine the flavor based on the charge information of the final state particles that belong to B_{tag}. The charge of high-momentum leptons coming from $B^0 \to X\ell^+\nu$ semileptonic decays provides the cleanest B flavor information. The charges of final-state kaons can also be used, since the majority of them comes from the $B^0 \to K^+X$ through the cascade transition $\bar{b} \to \bar{c} \to \bar{s}$. In addition to these two leading discriminants, the charge of intermediate-momentum leptons coming from $c \to s\ell^+\nu$ decay, high-momentum pions that originate from decays like $B^0 \to D^{(*)-}(\pi^+, \rho^+, a_1^+$, etc.), slow pions from $D^{*-} \to \overline{D}^0\pi^-$ decay, and flavor of Λ baryons from the cascade decay $b \to c \to s$ also make some contributions for flavor assignment.

The performance of the flavor tagging is characterized by two parameters: ϵ and w. The parameter ϵ is the raw tagging efficiency, while w is the probability that the flavor tagging is wrong (wrong tag fraction). A non-zero value of w results in a dilution of the true asymmetry. For example, if the true numbers of reconstructed OF and SF events are n_{OF} and n_{SF}, the corresponding asymmetry is $\mathcal{A}_{\text{mix}} = (n_{\text{OF}} - n_{\text{SF}})/(n_{\text{OF}} + n_{\text{SF}})$. With realistic flavor tagging, the observed numbers are $N_{\text{OF}} = \epsilon[(1-w)n_{\text{OF}} + wn_{\text{SF}}]$ for OF events and $N_{\text{SF}} = \epsilon[(1-w)n_{\text{SF}} + wn_{\text{OF}}]$ for SF events, and the observed asymmetry becomes $(1-2w)\mathcal{A}_{\text{mix}}$. Since the statistical error of the measured asymmetry is proportional to $\epsilon^{-1/2}$, the number of events required to have the asymmetry for a certain statistical significance is proportional to $\epsilon_{\text{eff}} = \epsilon(1-2w)^2$, which is called the "effective efficiency." The tagging algorithm has been designed to maximize ϵ_{eff}.

We use two parameters, q and r, to represent the tagging information. The parameter q corresponds to the sign of the b-quark charge of the tag-side B meson, where $q = +1$ for $\bar{b}$ and hence B^0, and $q = -1$ for b and $\overline{B}^0$. The parameter r is an event-by-event flavor-tagging dilution factor that ranges from $r = 0$ for no flavor discrimination to $r = 1$ for unambiguous flavor assignment. The values of q and r are determined for each event from a look-up table prepared by a large statistics MC sample [59]. Each entry of the table contains

$$q \cdot r \equiv \frac{N(B^0) - N(\overline{B}^0)}{N(B^0) + N(\overline{B}^0)}, \tag{6.11}$$

where $N(B^0)$ and $N(\overline{B}^0)$ are the numbers of B^0 and $\overline{B}^0$ in the MC sample, respectively.

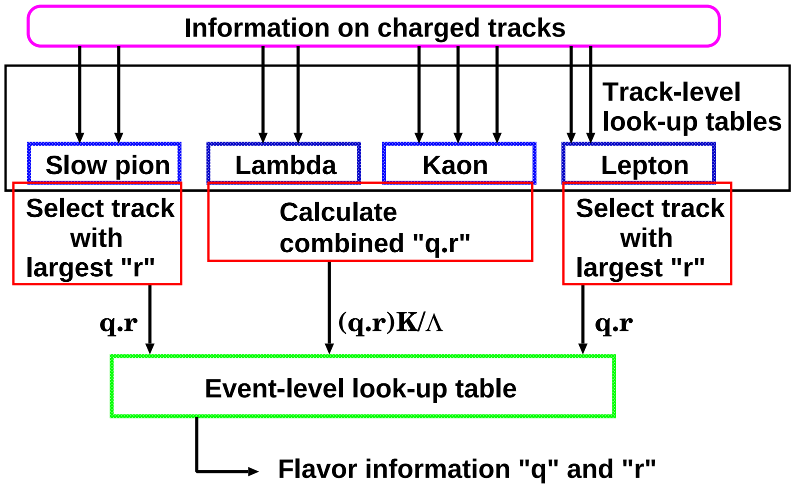

Figure 6.1: Schematic diagram of the flavor tagging.

The flavor tagging proceeds in two stages: the track-level and the event-level flavor tagging. Initially, the b-flavor determination is performed at the track level. Each track is examined and classified into four categories, namely those that resemble leptons, kaons, Λ baryons, and slow pions. For each category, we consider several tagging discriminants, such as the charge of tagging particle, the track momentum, the polar angle, and the particle-identification information, as well as the other kinematic and event shape quantities. The values of q and r for each track are assigned based on the MC-generated look-up tables that take the tagging discriminants as inputs. In the second stage, the results from the separate track categories are combined to determine the values of q and r for each event, taking into account correlations in the case of multiple track-level tags. Again a look-up table is prepared to provide $q \cdot r$.

Figure 6.1 shows a schematic diagram of the flavor-tagging method. The event-level parameter r should satisfy $r \simeq 1 - 2w$.

In this analysis, we sort flavor-tagged events into six bins in r. For each r bin, we determine w directly from data.

6.2.1 Track-level Flavor Tagging

We select tracks that do not belong to the fully reconstructed B and that satisfy $|dr| < 2$ cm and $|dz| < 10$ cm, where dz and dr are the distances from the nominal IP in r-ϕ plane and z direction, respectively. Tracks that belong to a K_S^0 candidate are not used. Each selected tag-side track is examined and assigned to one of the four track categories.

Lepton Category

Tracks in the lepton category are subdivided into categories for electron-like and muon-like tracks. If the cms momentum $p_\ell^{\rm cms}$ of a track is larger than 0.4 GeV/c and the ratio of its electron and kaon likelihoods is larger than 0.8, the track is assigned to the electron-like category. If a track has $p_\ell^{\rm cms}$ larger than 0.8 GeV/c and the ratio of its muon and kaon likelihoods is larger than 0.95, it is assigned to the muon-like category.

In the lepton category, leptons from semileptonic B decays yield the largest effective efficiency. Leptons from $B \to D$ cascade decays and high-momentum pions from $B^0 \to D^{(*)-}\pi^+ X$ also make a small contribution to this category.

We choose the following six discriminants:

- The track charge;
- The magnitude of the momentum in the cms $p_\ell^{\rm cms}$;
- The polar angle in the laboratory frame $\theta_{\rm lab}$;
- The recoil mass $M_{\rm recoil}$ calculated using all the tag-side tracks except the lepton candidate;
- The magnitude of the missing momentum in the cms $P_{\rm miss}^{\rm cms}$; and
- The lepton-identification quality value.

The track charge directly provides the b-flavor q. The lepton-identification quality distinguishes leptons from pions. Its performance is reinforced by variables $p_\ell^{\rm cms}$ and $\theta_{\rm lab}$, which have distributions that are different for leptons and pions. The variables $p_\ell^{\rm cms}$, $M_{\rm recoil}$, and $P_{\rm miss}^{\rm cms}$ discriminate semileptonic B decays from $B \to D$ cascade decays where the D decays semileptonically.

The number of divisions for each discriminant is two for the lepton flavor (e or μ), two for the track charge, eleven for $p_\ell^{\rm cms}$, six for $\theta_{\rm lab}$, ten for $M_{\rm recoil}$, six for $P_{\rm miss}^{\rm cms}$, four for the lepton-identification quality, and $2 \times 2 \times 11 \times 6 \times 10 \times 6 \times 4 = 63360$ bins in total.

Slow-Pion Category

If a track cannot be positively identified as a kaon and its momentum is less than 0.25 GeV/c, it is assigned to the slow-pion category, since low-momentum pions often come from charged $D^* \to D\pi$ decays. Here the discriminant variables are:

- The track charge;

- The momentum and polar angle in the laboratory frame, $p_{\rm lab}$ and $\theta_{\rm lab}$;
- The ratio of the probability for a particle to be an electron to that for the particle to be a pion, where the probability is calculated using dE/dx information; and
- $\cos\alpha_{\rm thr}$, the cosine of the angle between the slow pion candidate and the thrust axis of the tag-side particles in the cms.

The main background sources in this category are other (i.e., non-D^* daughter) low momentum pions and electrons from photon conversions and π^0 Dalitz decays. To separate slow pions from those electrons, we use only dE/dx, because they do not reach ECL. Due to the small Q value, the direction of the slow pion is approximately the same as the D^* direction, consequently is also almost the same as the thrust axis. The variables $\cos\alpha_{\rm thr}$, $p_{\rm lab}$, and $\theta_{\rm lab}$, thus, are effective to identify the slow pions from D^* decays.

The number of divisions for each discriminant is two for the track charge, ten for $p_{\rm lab}$, ten for $\theta_{\rm lab}$, five for the electron to pion probability, seven for $\cos\alpha_{\rm thr}$, and $2 \times 10 \times 10 \times 5 \times 7 = 7000$ bins in total.

Λ Baryon Category

If a track forms a Λ candidate with another track, it is assigned to the Λ category. The Λ category is subdivided into two parts: events with and without K^0_S decays, since they have different wrong tag fractions. In this category the discriminant variables are:

- The flavor (Λ or $\overline{\Lambda}$);
- The invariant mass of the reconstructed Λ candidate;
- The angle difference between the Λ momentum vector and the direction of the Λ vertex point from the nominal IP; and
- The mismatch in the z direction of the two tracks at the Λ vertex point.

Since the number of Λ candidates is small, each discriminant is subdivided into two regions. The total number of bins is $2 \times 2 \times 2 \times 2 \times 2 = 32$.

Kaon Category

If a track does not fall into any of the categories described above, and is not positively identified as a proton, it is classified as a kaon. The kaon category is subdivided into two parts, one for events with K_S^0 decays, and the other for events without K_S^0's. Separate treatment is necessary, since events with K_S^0 have a larger wrong tag fraction because of their additional strange-quark content. We use:

- The track charge;
- $p^{\rm cms}$;
- $\theta_{\rm lab}$; and
- The ratio of the probability for a particle to be a kaon to that for the particle to be a pion

as the tagging discriminants. The charge of kaons is the most important discriminant. The other three variables separate kaons from pions.

Although high-momentum pions have the weaker discriminating power than charged kaons, they provide some tagging information. Therefore we include them in the kaon category. Approximately a half of the pions with $p^{\rm cms} > 1.0$ GeV/c are included in the kaon category, while the other half falls into the lepton class, mostly in the muon-like category.

The number of divisions for each discriminant is two for the existence of K_S^0, two for the track charge, 21 for $p^{\rm cms}$, 18 for $\theta_{\rm lab}$, 13 for the probability ratio, and $2 \times 2 \times 21 \times 18 \times 13 = 19656$ bins in total.

6.2.2 Event-level Flavor Tagging

For the event-level flavor tagging, we combine the results from each of the track categories to determine overall q and r. For the lepton and slow-pion track categories, we take the b-flavor assignment from the track with the highest r-value in each category. For the kaon and Λ categories, a combined b-flavor output is calculated as the product of likelihood values for all tracks:

$$(q \cdot r)_{K/\Lambda} = \frac{\prod_i [1 + (q \cdot r)_i] - \prod_i [1 - (q \cdot r)_i]}{\prod_i [1 + (q \cdot r)_i] + \prod_i [1 - (q \cdot r)_i]}, \tag{6.12}$$

where the subscript i runs over all tracks in the kaon and Λ categories. The product likelihood is designed to use the information from the sum of the strangeness, which provides better flavor-tagging performance than simply choosing the best candidate.

Using the three track-level $q \cdot r$ values, lepton, slow pion, and kaon and Λ combination, the event-level q and r values are obtained from a look-up table determined by a MC simulation. The MC sample for the look-up table is independent of the sample used to obtain $q \cdot r$ values in the track categories. The number of divisions for each category is 25 for the lepton, 35 for the kaon and Λ, 19 for the slow pion, and $25 \times 35 \times 19 = 16625$ bins in total.

The probability that we can assign a non-zero value for r is 99.6% in MC; i.e., almost all the reconstructed candidates can be used to extract Δm_d. The events where the flavor of $B_{\rm tag}$ cannot be assigned (i.e., $r = 0$) are not used for the Δm_d fit.

We group events into six bins: $0 < r \le 0.25$, $0.25 < r \le 0.5$, $0.5 < r \le 0.625$, $0.625 < r \le 0.75$, $0.75 < r \le 0.875$, and $0.875 < r \le 1$. For each bin we obtain the wrong tag fraction w_l, where l is the bin ID ($l = 1, \cdots, 6$), from the mixing fit to the data. In this way, the analysis is not biased by systematic differences between the MC simulation and the data due to imperfections in the modeling of the detector response, decay branching fractions, and fragmentation in the MC simulation.

6.3 Background

For each reconstructed event, the signal probability $f_{\rm sig}$ is assigned using ΔE and $M_{\rm bc}$ information. The remaining fraction of the event is considered as the background. The method of $f_{\rm sig}$ assignment and the determination of background Δt distribution are basically the same as in the lifetime measurement, except the information for the flavor-tagging purity r is used.

6.3.1 Signal Probability

The signal fraction $f_{\rm sig}$ is calculated based on ΔE and $M_{\rm bc}$ for each event using the signal and background functions, $F_{\rm sig}$ and $F_{\rm bkg}$, defined as Eqs. (5.41) and (5.42), respectively. Since the signal purity also depends on the flavor-tagging purity r, i.e., the high r region has less background, we account for this dependence. The normalizations of signal and background components, a and b in Eqs. (5.41) and (5.42), are fitted again for each r region. The other parameters are fixed to the values obtained from the fit for the lifetime measurement described in Section 5.4.1.

6.3.2 Background Shape

The Δt distributions for the background, $P^{\rm OF}_{\rm bkg}(\Delta t)$ and $P^{\rm SF}_{\rm bkg}(\Delta t)$, are basically the same as those for the lifetime fit. They are modeled as a sum of prompt and exponential components ($\mathcal{P}^{\rm OF}_{\rm bkg}(\Delta t)$ and $\mathcal{P}^{\rm SF}_{\rm bkg}(\Delta t)$) convoluted with a sum of two

Gaussians ($R_{\rm bkg}(\Delta t)$):

$$P^{\rm OF}_{\rm bkg}(\Delta t) = \int_{-\infty}^{+\infty} d(\Delta t')\mathcal{P}^{\rm OF}_{\rm bkg}(\Delta t - \Delta t')R_{\rm bkg}(\Delta t'), \tag{6.13}$$

$$P^{\rm SF}_{\rm bkg}(\Delta t) = \int_{-\infty}^{+\infty} d(\Delta t')\mathcal{P}^{\rm SF}_{\rm bkg}(\Delta t - \Delta t')R_{\rm bkg}(\Delta t'), \tag{6.14}$$

where

$$\mathcal{P}^{\rm OF}_{\rm bkg}(\Delta t) = f^{\rm OF}_{\rm bkg}\left[f^{\rm bkg}_{\delta}\delta(\Delta t - \mu^{\rm bkg}_{\delta}) + (1 - f^{\rm bkg}_{\delta})\frac{1}{2\tau_{\rm bkg}}\exp\left(-\frac{|\Delta t - \mu^{\rm bkg}_{\tau}|}{\tau_{\rm bkg}}\right)\right], \tag{6.15}$$

$$\mathcal{P}^{\rm SF}_{\rm bkg}(\Delta t) = (1 - f^{\rm OF}_{\rm bkg})\left[f^{\rm bkg}_{\delta}\delta(\Delta t - \mu^{\rm bkg}_{\delta}) + (1 - f^{\rm bkg}_{\delta})\frac{1}{2\tau_{\rm bkg}}\exp\left(-\frac{|\Delta t - \mu^{\rm bkg}_{\tau}|}{\tau_{\rm bkg}}\right)\right], \tag{6.16}$$

and $R_{\rm bkg}$ is the same as defined in Eq. (5.46).

For the parameters of $P^{\rm OF}_{\rm bkg}$ and $P^{\rm SF}_{\rm bkg}$ other than $f^{\rm OF}_{\rm bkg}$, we use the values obtained from the lifetime analysis described in Section 5.4.2. The fraction of OF events in the background, $f^{\rm OF}_{\rm bkg}$, as well as the fraction of OF events in the signal, $f^{\rm OF}_{\rm sig}$, is determined from the fit of $F_{\rm sig}(\Delta E, M_{\rm bc}) + F_{\rm bkg}(\Delta E, M_{\rm bc})$ to the ΔE-$M_{\rm bc}$ distribution in each r region, where the parameters of $F_{\rm sig}$ and $F_{\rm bkg}$ other than their normalization a and b are fixed to the result of global fit described in Section 5.4.1.

6.4 Fit Result

Using the PDFs described above, an unbinned maximum likelihood fit is applied to the Δt distributions for OF and SF events. In the final fit, we fix τ_{B^0} to the world average value [20] and determine Δm_d and w_l ($l = 1, \cdots, 6$) simultaneously. The parameters of the resolution function are fixed to the result of the lifetime fit. We use the values listed in Table 5.1 and 5.7.

Using 29.1 fb^{-1} data which correspond to 31.3×10^6 $B\overline{B}$ pairs, we find 6660 events in the signal boxes after all vertexing and flavor-tagging requirements. The number of events used in the mixing fit for each mode is listed in Table 6.1. The unbinned maximum likelihood fit to these data sample yields

$$\Delta m_d = 0.528 \pm 0.017 \text{ ps}^{-1}. \tag{6.17}$$

Here the error is statistical only. The fit result of all the parameters is listed in Table 6.2. Figures 6.2(a) and 6.2(b) show the Δt distributions for SF and OF events with the fitted curves superimposed. Figure 6.3 shows the asymmetry between OF

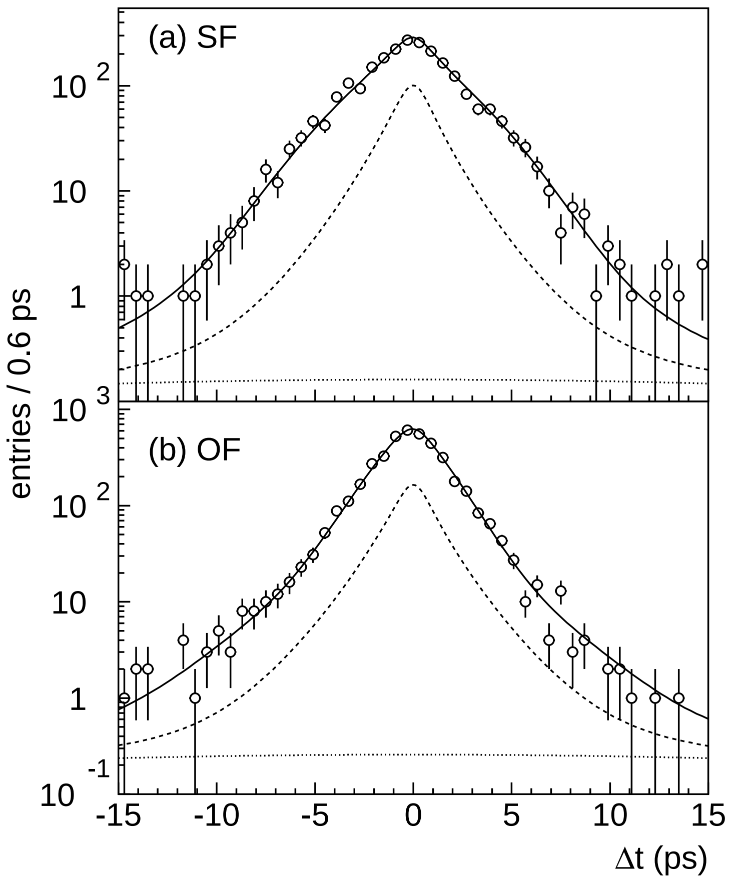

Figure 6.2: Distributions of Δt for (a) SF and (b) OF events with the fitted curves superimposed. The dashed, dotted, and solid curves show the background, outliers, and the sum of backgrounds and signal, respectively.

Table 6.1: Number of events used in the mixing fit for each mode.

Mode	Number of events
$B^0 \to D^-\pi^+$	2269
$B^0 \to D^{*-}\pi^+$	2490
$B^0 \to D^{*-}\rho^+$	1901
Total	6660

Table 6.2: Summary of fit result.

Parameter	Value
Δm_d (ps^{-1})	0.528 ± 0.017
w_1	0.478 ± 0.017
w_2	0.313 ± 0.027
w_3	0.212 ± 0.030
w_4	0.187 ± 0.027
w_5	0.088 ± 0.022
w_6	0.016 ± 0.013

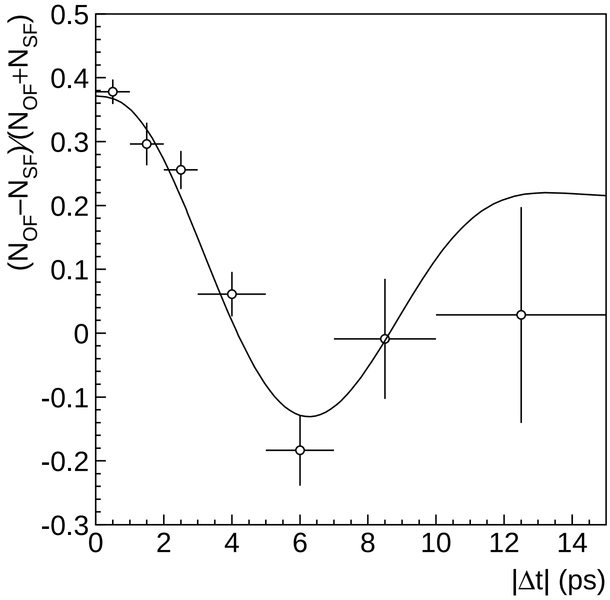

Figure 6.3: Time dependence of the asymmetry between OF and SF events. The curve shows the result of the Δm_d fit.

Table 6.3: Summary of the systematic errors for Δm_d. The errors are combined in quadrature.

Source	Error (ps^{-1})
Resolution parameters	0.008
Resolution parameterization	0.003
IP constraint	0.001
Track selection	0.002
Vertex selection	0.003
ΔE-$M_{\rm bc}$ signal box	0.001
Signal fraction	0.001
Background shape	0.002
Mixing in the background	0.002
B^0 lifetime	0.002
Fit bias	0.005
Total	0.011

and SF events, $(N_{\rm OF} - N_{\rm SF})/(N_{\rm OF} + N_{\rm SF})$, as a function of $|\Delta t|$.

Separate fits to the $D^-\pi^+$, $D^{*-}\pi^+$, and $D^{*-}\rho^+$ decay modes give consistent Δm_d values: 0.536 ± 0.027 ps^{-1}, 0.543 ± 0.027 ps^{-1}, and 0.497 ± 0.032 ps^{-1}, respectively.

6.5 Systematic Uncertainties

We consider the systematic uncertainties from various sources listed bellow. The major contributions to the systematic error are found to be the uncertainties in the resolution function. The results are summarized in Table 5.9. All systematic errors are combined in quadrature.

Resolution Parameters To estimate the uncertainty from the resolution function parameters, we vary the parameters determined from the data (parameters for the detector resolution and outlier) by $\pm 1\sigma$, and the parameters obtained from MC sample ($R_{\rm np}$ parameters) by $\pm 2\sigma$.

Resolution Parameterization The systematic error due to the modeling of the resolution function is estimated by comparing the results with different parameterizations. For this estimation, we use modified $R_{\rm ful}^{\rm multiple}$ and $R_{\rm asc}^{\rm multiple}$ that are used in the study of systematic errors for the lifetime measurement and defined as Eqs. (5.50) and (5.51). We use the parameters obtained from the result of the lifetime fit for these modified detector resolution functions.

IP Constraint The systematic error due to the IP constraint is estimated by varying the smearing used to account for the transverse B decay length by ± 10 μm.

The nominal IP position obtained from Bhabha events is also used instead of that obtained from hadronic events to estimate the systematic error due to the IP position. We find the difference between the two results is negligibly small.

Track Selection Possible systematic effects due to the track quality selection of the associated B decay vertices are studied by varying each criterion by 10%.

Vertex Selection The fit quality criterion for reconstructed vertices is varied from $\xi < 50$ to $\xi < 200$, to estimate the systematic dependence on ξ selection criteria.

Δt Dependence of Reconstruction Efficiency The Δt dependence of the reconstruction efficiency is assessed by performing unbinned maximum likelihood fits on the generated $|\Delta t|$ distributions for all generated events, and then on the reconstructed events, with a pure mixing function. The difference of Δm_d obtained from the two fits is considered to be due to the bias in the reconstruction efficiency. Since we find no difference between the two fits beyond the statistical error, no systematic uncertainty is listed.

ΔE-$M_{\rm bc}$ Signal Box ΔE-$M_{\rm bc}$ signal regions are varied by ± 10 MeV for ΔE and ± 3 MeV/c^2 for $M_{\rm bc}$, to estimate the uncertainty.

Signal Fraction The parameters determining the signal fraction $f_{\rm sig}$, obtained from the fits to the ΔE-$M_{\rm bc}$ distributions, are varied by $\pm 1\sigma$ to estimate the associated systematic error.

Background Shape The systematic error due to the background shape is estimated by varying its parameters by their errors. The parameters obtained from the fit to the ΔE-$M_{\rm bc}$ sideband data are varied by $\pm 1\sigma$, and the ratio of $f_\delta^{\rm bkg}$ in the signal box to that in the sideband region is varied by $\pm 2\sigma$.

Mixing in the Background In the nominal fit, we do not include any oscillation component in the background. Such a component may arise from the B^0 originated background. To estimate this effect, we apply the fit with a background PDF including a mixing term:

$$\mathcal{P}_{\mathrm{bkg}}^{\mathrm{OF}}(\Delta t) = f_{\mathrm{bkg}}^{\mathrm{OF}} f_{\delta}^{\mathrm{bkg}} \delta(\Delta t - \mu_{\delta}^{\mathrm{bkg}}) + (1 - f_{\delta}^{\mathrm{bkg}}) \frac{1}{4\tau_{\mathrm{bkg}}} \exp\left(-\frac{|\Delta t - \mu_{\tau}^{\mathrm{bkg}}|}{\tau_{\mathrm{bkg}}}\right)$$
$$\left\{1 + (1 - 2w_l^{\mathrm{bkg}}) \cos\left[\Delta m_d^{\mathrm{bkg}} (\Delta t - \mu_{\tau}^{\mathrm{bkg}})\right]\right\}, \tag{6.18}$$
$$\mathcal{P}_{\mathrm{bkg}}^{\mathrm{SF}}(\Delta t) = (1 - f_{\mathrm{bkg}}^{\mathrm{OF}}) f_{\delta}^{\mathrm{bkg}} \delta(\Delta t - \mu_{\delta}^{\mathrm{bkg}}) + (1 - f_{\delta}^{\mathrm{bkg}}) \frac{1}{4\tau_{\mathrm{bkg}}} \exp\left(-\frac{|\Delta t - \mu_{\tau}^{\mathrm{bkg}}|}{\tau_{\mathrm{bkg}}}\right)$$
$$\left\{1 - (1 - 2w_l^{\mathrm{bkg}}) \cos\left[\Delta m_d^{\mathrm{bkg}} (\Delta t - \mu_{\tau}^{\mathrm{bkg}})\right]\right\}, \tag{6.19}$$

where $\Delta m_d^{\mathrm{bkg}}$ and w_l^{bkg} $(l = 1, \cdots, 6)$ are determined from the fit to the sideband Δt distribution for each decay mode.

B^0 Lifetime The dependence on the B^0 lifetime is measured by varying the lifetime by $\pm 1\sigma$ from the world average value.

Δt Range We check the systematic uncertainty due to outliers by varying the Δt range to ± 40 ps and ± 100 ps, and find a negligibly small effect.

Fit Bias The possible bias in the fitting procedure and the effect of SVD alignment error are studied with MC samples. Since we find no bias, no correction is made. The MC statistical error is associated as a systematic error for these sources.

6.6 Summary of Δm_d Fit

We have presented the measurement of Δm_d using 29.1 fb^{-1} of data sample collected with the Belle detector at the $\Upsilon(4S)$ energy. An unbinned maximum likelihood fit to the distribution of the proper-time difference of a flavor-tagged sample with one of the neutral B mesons fully reconstructed in hadronic decays yields

$$\Delta m_d = 0.528 \pm 0.017(\mathrm{stat}) \pm 0.011(\mathrm{syst})\ \mathrm{ps}^{-1}. \tag{6.20}$$

Chapter 7

Measurement of $\sin 2\phi_1$

In this chapter, we describe the analysis procedure for the measurement of the CP violation parameter $\sin 2\phi_1$ [60]. One neutral B meson is reconstructed in a CP-eigenstate decay channel as described in Section 4.3.4. The flavor of the accompanying B meson is identified by the flavor-tagging procedure used in the Δm_d analysis. From an unbinned maximum likelihood fit applied to the distribution of the proper-time interval between the two B meson decays, the value of $\sin 2\phi_1$ is extracted.

7.1 Unbinned Maximum Likelihood Fit

We determine $\sin 2\phi_1$ by performing an unbinned maximum likelihood fit of a CP violating probability density function to the observed Δt distribution. As discussed in Section 2.5, the theoretical proper-time interval distribution $\mathcal{P}_{\rm sig}$ is given by

$$\mathcal{P}_{\rm sig}(\Delta t; \sin 2\phi_1) = \frac{1}{4\tau_{B^0}} \exp\left(-\frac{|\Delta t|}{\tau_{B^0}}\right) \left[1 - q\xi_f \sin 2\phi_1 \sin(\Delta m_d \Delta t)\right], \tag{7.1}$$

where ξ_f is the CP eigenvalue of the reconstructed CP eigenstate and q is the sign of the b-quark charge: $q = +1$ (-1) if the tag side is B^0 $(\overline{B}^0)$. However, since the determination of the flavor of the tag-side B meson is not perfect, above distributions for $q = +1$ and $q = -1$ are mixed and the observed amplitude of the asymmetry is diluted. Therefore, $\mathcal{P}_{\rm sig}$ should be written as

$$\mathcal{P}_{\rm sig}(\Delta t; \sin 2\phi_1) = \frac{1}{4\tau_{B^0}} \exp\left(-\frac{|\Delta t|}{\tau_{B^0}}\right) \left[1 - q\xi_f (1-2w) \sin 2\phi_1 \sin(\Delta m_d \Delta t)\right], \tag{7.2}$$

where w is the probability of the wrong flavor assignment. For the $B^0 \to J/\psi K^{*0}$ fit, we use the event-by-event angular information. The signal PDF for $J/\psi K^{*0}$ is written as

$$\begin{aligned}\mathcal{P}_{\rm sig}(\Delta t;\sin 2\phi_1) &= \frac{1}{4\tau_{B^0}}\exp\left(-\frac{|\Delta t|}{\tau_{B^0}}\right)\\ &\times\left\{(1-f_{\rm odd})\frac{3}{8}(1+\cos^2\theta_{\rm tr})\left[1-q(1-2w)\sin 2\phi_1\sin(\Delta m_d\Delta t)\right]\right.\\ &\left.+f_{\rm odd}\frac{3}{4}(1-\cos^2\theta_{\rm tr})\left[1+q(1-2w)\sin 2\phi_1\sin(\Delta m_d\Delta t)\right]\right\},\quad (7.3)\end{aligned}$$

where $f_{\rm odd}$ is the fraction of $\xi_f=-1$ decays in the $B^0\to J/\psi K^{*0}$ ($K^{*0}\to K_S^0\pi^0$) mode, determined from a full angular analysis to be $0.19\pm0.02(\rm stat)\pm0.03(\rm syst)$ [61], and $\theta_{\rm tr}$ is defined in the transversity basis [62] as the angle between the positive J/ψ decay lepton direction and the axis normal to the K^{*0} decay plane in the J/ψ rest frame.

There also exists the smearing due to the finite detector resolution or the background events in the data. Taking into account these effects, the overall PDF is expressed as

$$\begin{aligned}P(\Delta t;\sin 2\phi_1) = (1-f_{\rm ol})&\left[f_{\rm sig}P_{\rm sig}(\Delta t;\sin 2\phi_1)+(1-f_{\rm sig})P_{\rm bkg}(\Delta t)\right]\\ &+f_{\rm ol}P_{\rm ol}(\Delta t),\quad (7.4)\end{aligned}$$

where $f_{\rm sig}$ is the signal purity determined on an event-by-event basis, $P_{\rm sig}$ and $P_{\rm bkg}$ are the PDFs for the signal and background events, respectively. $f_{\rm ol}$ and $P_{\rm ol}(\Delta t)$ are the fraction and the function of the outlier described in Section 5.3.4, respectively. $P_{\rm sig}$ is described as the convolution of the theoretical PDF $\mathcal{P}_{\rm sig}$ defined in Eqs. (7.2) and (7.3) with a resolution function $R_{\rm sig}$ described in Section 5.3:

$$P_{\rm sig}(\Delta t;\sin 2\phi_1) = \int_{-\infty}^{+\infty} d(\Delta t')\mathcal{P}_{\rm sig}(\Delta t';\sin 2\phi_1)R_{\rm sig}(\Delta t-\Delta t'). \quad (7.5)$$

The likelihood function is constructed as

$$L(\sin 2\phi_1) = \prod_i P(\Delta t_i;\sin 2\phi_1), \quad (7.6)$$

where the index i runs over all selected events in the signal region.

7.2 Resolution Function

The procedure for the reconstruction of the proper-time interval Δt is the same as those for the lifetime and Δm_d analyses which are described in Section 5.2. The resolution function $R_{\rm sig}$ is almost identical to those used in the lifetime and Δm_d

Table 7.1: Shape parameters of R_{np} used for the $\sin 2\phi_1$ fit.

Parameters	B^0		B^+	
	multiple	single	multiple	single
f_{p}	0.959 ± 0.003	0.818 ± 0.013	0.971 ± 0.003	$0.804^{+0.016}_{-0.017}$
τ^0_{p} (ps)	-0.049 ± 0.010	$0.374^{+0.084}_{-0.082}$	0.015 ± 0.009	$0.214^{+0.070}_{-0.069}$
τ^1_{p}	$1.008^{+0.023}_{-0.022}$	$1.472^{+0.105}_{-0.102}$	0.736 ± 0.020	$1.234^{+0.104}_{-0.099}$
τ^0_{n} (ps)	$-0.138^{+0.083}_{-0.082}$	$0.193^{+0.146}_{-0.141}$	$-0.070^{+0.099}_{-0.100}$	$-0.148^{+0.193}_{-0.189}$
τ^1_{n}	$2.057^{+0.188}_{-0.176}$	$1.811^{+0.221}_{-0.205}$	$1.927^{+0.231}_{-0.212}$	$2.086^{+0.318}_{-0.286}$

analyses described in Section 5.3. However, since the track reconstruction algorithm is improved and whole data sample is analyzed using this new algorithm, a new set of parameters of the resolution function is obtained by repeating the lifetime analysis. A MC sample is also remade with the new tracking algorithm.

We find the fraction f_{tail} for the tail part of the detector resolution is consistent with zero in the case of single-track vertexing, and therefore set $f_{\mathrm{tail}} = 0$ for this data sample. Consequently, s_{tail} is not used. In addition, an improved statistics enables us to determine some parameters that are previously determined only by MC simulations: The fractions of the prompt component in R_{np} for multiple- and single-track vertices ($f^{\mathrm{multiple}}_{\delta,B^0}$, $f^{\mathrm{single}}_{\delta,B^0}$ for B^0 mesons, and $f^{\mathrm{multiple}}_{\delta,B^+}$, $f^{\mathrm{single}}_{\delta,B^+}$ for B^+ mesons) are determined by the lifetime fit to the data.

As we did in the lifetime analysis, first we determine the parameters for R_{np} using the MC data. Table 7.1 lists the R_{np} parameters obtained from the new MC sample. Then we apply the lifetime fit to the 78 fb^{-1} data sample. Table 7.2 lists the parameter values for $R_{\mathrm{sig}}(\Delta t)$ determined from the lifetime fit. The Δt distributions with the fitted curves for neutral and charged B mesons are shown in Fig. 7.1. We find the resulting Δt resolution to be ~ 1.43 ps (rms), improved over the resolution of ~ 1.56 ps obtained for the 29.1 fb^{-1} sample.

7.3 Flavor Tagging

We use the same flavor-tagging method used in the Δm_d analysis described in Section 6.2. However, the contents of look-up tables are updated using the EvtGen event generator, which shows the better agreement with data in the flavor specific charged track multiplicity than the QQ event generator [63]. Therefore, the performance of the flavor tagging is evaluated again using 78 fb^{-1} data sample.

The wrong tag fraction w is estimated from the time-dependent B^0-$\overline{B}^0$ oscillation. The Δt distributions for OF and SF events are fitted in the similar way as described in Chapter 6. For this estimation, we use the semileptonic decay

Table 7.2: Result of the lifetime fit.

Parameter	Value
τ_{B^0} (ps)	1.551 ± 0.018
τ_{B^+} (ps)	1.658 ± 0.016
$s^0_{\rm rec}$	$0.987^{+0.117}_{-0.124}$
$s^1_{\rm rec}$	0.094 ± 0.008
$s^0_{\rm asc}$	0.778 ± 0.048
$s^1_{\rm asc}$	0.044 ± 0.002
$s_{\rm main}$	0.972 ± 0.045
$f^{\rm multiple}_{\delta,B^0}$	$0.555^{+0.041}_{-0.043}$
$f^{\rm multiple}_{\delta,B^+}$	$0.440^{+0.045}_{-0.046}$
$f^{\rm single}_{\delta,B^0}$	$0.701^{+0.039}_{-0.042}$
$f^{\rm single}_{\delta,B^+}$	$0.764^{+0.042}_{-0.045}$
$\sigma_{\rm ol}$ (ps)	$42.0^{+4.6}_{-3.5}$
$f^{\rm multiple}_{\rm ol}$	$(1.65^{+1.13}_{-0.82}) \times 10^{-4}$
$f^{\rm single}_{\rm ol}$	$0.0269^{+0.0019}_{-0.0018}$

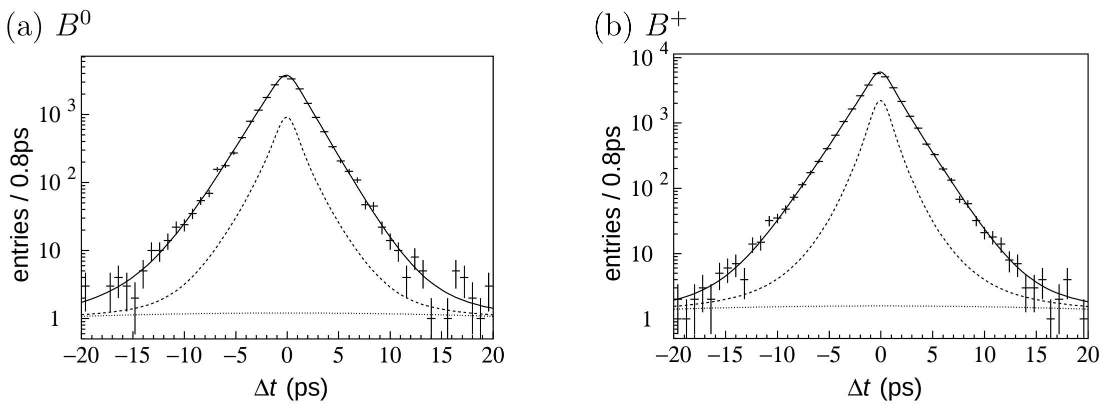

Figure 7.1: Distributions of Δt for (a) neutral and (b) charged B mesons, with fitted curves. The dashed lines represent the sum of the background and outlier components, and the dotted lines represent the outlier component.

Table 7.3: Event fraction ϵ_l, wrong tag fraction w_l, and effective tagging efficiency $\epsilon^l_{\rm eff} = \epsilon_l(1-2w_l)^2$ for each r interval. The first and second errors of w_l are statistical and systematic uncertainties, respectively. The errors of $\epsilon^l_{\rm eff}$ are statistical and systematic combined. The event fractions are obtained from the $J/\psi K^0_S$ MC.

l	r interval	ϵ_l	w_l	$\epsilon^l_{\rm eff}$
1	0.000 – 0.250	0.398	$0.458 \pm 0.005 \pm 0.003$	0.003 ± 0.001
2	0.250 – 0.500	0.146	$0.336 \pm 0.008 \pm 0.004$	0.016 ± 0.002
3	0.500 – 0.625	0.104	$0.228 \pm 0.009 \,^{+0.004}_{-0.006}$	0.031 ± 0.002
4	0.625 – 0.750	0.122	$0.160 \pm 0.007 \,^{+0.005}_{-0.004}$	0.056 ± 0.003
5	0.750 – 0.875	0.094	$0.112 \pm 0.008 \pm 0.004$	0.056 ± 0.003
6	0.875 – 1.000	0.136	$0.020 \,^{+0.005}_{-0.004} \,^{+0.005}_{-0.004}$	$0.126 \,^{+0.003}_{-0.004}$

$B^0 \to D^{*-}\ell^+\nu$ as well as the hadronic modes $B^0 \to D^-\pi^+$, $D^{*-}\pi^+$, and $D^{*-}\rho^+$ as the flavor-specific B decays. The reconstruction and selection procedures for the hadronic modes are same as those for the Δm_d analysis described in Chapter 6. The event selection and reconstruction methods for the semileptonic decay are described in Ref. [64]. An unbinned maximum likelihood fit is applied to the reconstructed Δt distributions for OF and SF events. The likelihood function is defined as Eq. (6.9) and the probability density functions are defined in Eqs. (6.5) and (6.6). The fraction and Δt distribution of the background events for the hadronic and semileptonic modes are described in Section 6.3 and Ref. [64], respectively, but the parameters are updated for 78 fb^{-1} data. We use the parameters for resolution function $R_{\rm sig}(\Delta t)$ described in the previous section. However, since we cannot obtain $\cos\theta^{\rm cms}_B$ for the semileptonic decay due to the missing neutrino, $R_{\rm k}$ part is modeled from the MC study for the semileptonic sample [56]. From a 78 fb^{-1} data sample, we select 47317 semileptonic decay candidates and 18015 hadronic decay candidates. The overall efficiency of the flavor tagging is 99.8%. In the fit, we fix the B^0 lifetime τ_{B^0} and the B^0-$\overline{B}^0$ oscillation frequency Δm_d to the world average values [65] and determine the wrong tag fraction for each r interval, w_l ($l = 1, \cdots, 6$), simultaneously. The fit results are summarized in Table 7.3. The event fraction ϵ obtained from the $B^0 \to J/\psi K^0_S$ MC and the effective tagging efficiency $\epsilon_{\rm eff} = \epsilon(1-2w)^2$ for each r interval are also listed in Table 7.3. Figure 7.2 shows the measured asymmetry between the OF and SF events, $(N_{\rm OF} - N_{\rm SF})/(N_{\rm OF} + N_{\rm SF})$, as a function of $|\Delta t|$ for each r interval. Figure 7.3 plots the measured $1-2w$ with respect to r. It is close to linear and confirms the validity of the flavor-tagging method.

The total effective tagging efficiency is calculated to be

$$\epsilon_{\rm eff} = \sum_l \epsilon_l (1-2w_l)^2 = (28.8 \pm 0.6)\%, \tag{7.7}$$

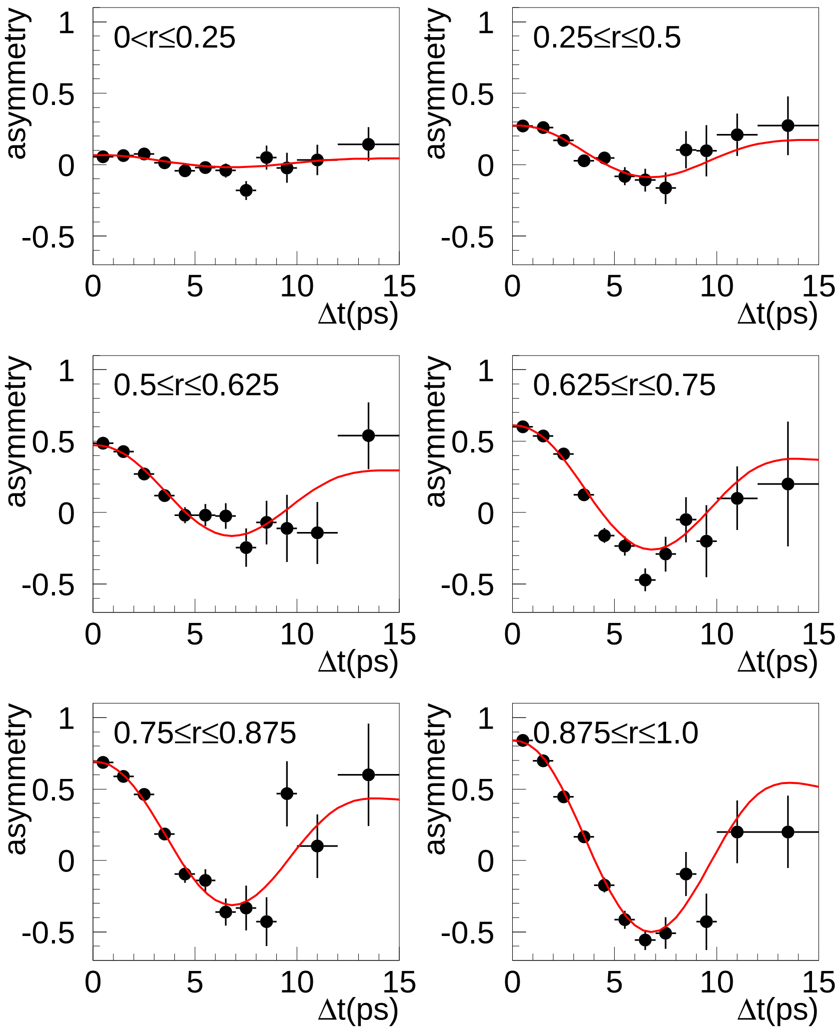

Figure 7.2: Measured asymmetries between the OF and SF events, $(N_{\rm OF} - N_{\rm SF})/(N_{\rm OF} + N_{\rm SF})$, for the six r regions as functions of $|\Delta t|$. The results of the fit are superimposed.

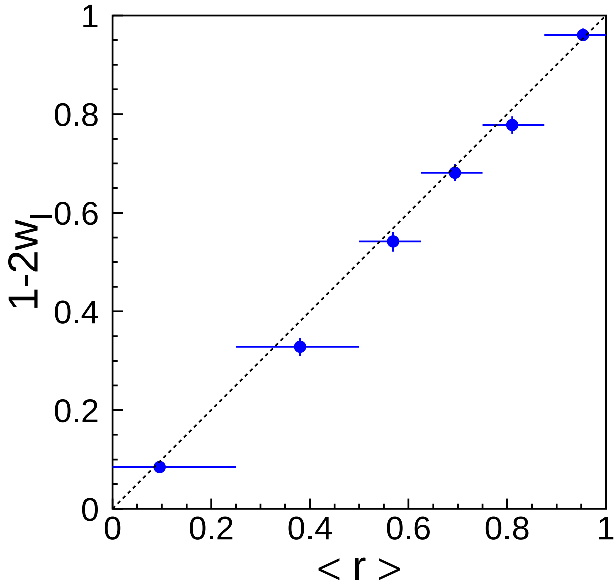

Figure 7.3: Measured dilution factor $1 - 2w$ as a function of the mean of r, $\langle r \rangle$, in each r region. $\langle r \rangle$ is taken from the $B^0 \to J/\psi K_S^0$ MC.

where the error includes both statistical and systematic uncertainties. This value is higher by 6.7% (relative) than that in the previous $\sin 2\phi_1$ measurement [45].

7.4 Background

For each of the reconstructed events, the signal probability $f_{\rm sig}$ is assigned using ΔE and $M_{\rm bc}$ information for the modes other than $J/\psi K_L^0$ and using $p_B^{\rm cms}$ for $J/\psi K_L^0$. The remaining fraction of the event is considered as the background. The PDF of Δt distribution for the background component is different from the signal PDF. In this section, first we describe the method of $f_{\rm sig}$ assignment to an event, and then we discuss the PDF of Δt distribution for the background components.

7.4.1 Signal Probability

The signal fractions are determined in the different ways for $B^0 \to (c\bar{c})K_S^0$, $J/\psi K^{*0}$, and $J/\psi K_L^0$ modes.

$B^0 \to$ charmonium K_S^0

The signal fraction $f_{\rm sig}$ is calculated based on ΔE and $M_{\rm bc}$ for each event. The ΔE and $M_{\rm bc}$ distributions are fitted with a sum of two dimensional signal and background functions ($F_{\rm sig}$ and $F_{\rm bkg}$) in each mode. Using these functions, $f_{\rm sig}$ is obtained as a function of both ΔE and $M_{\rm bc}$:

$$f_{\rm sig}(\Delta E, M_{\rm bc}) = \frac{F_{\rm sig}(\Delta E, M_{\rm bc})}{F_{\rm sig}(\Delta E, M_{\rm bc}) + F_{\rm bkg}(\Delta E, M_{\rm bc})}. \tag{7.8}$$

In the cases of $B^0 \to J/\psi K_S^0$ ($K_S^0 \to \pi^+\pi^-$) and $\eta_c K_S^0$ ($\eta_c \to p\overline{p}$), the signal distribution of ΔE is represented by a sum of two Gaussians and $M_{\rm bc}$ by a single Gaussian:

$$\begin{aligned} F_{\rm sig}(\Delta E, M_{\rm bc}) = a \left[f_{\rm main} G(\Delta E - \mu_{\Delta E}; \sigma_{\Delta E}^{\rm main}) + (1 - f_{\rm main}) G(\Delta E - \mu_{\Delta E}; \sigma_{\Delta E}^{\rm tail}) \right] \\ \times G(M_{\rm bc} - \mu_{M_{\rm bc}}; \sigma_{M_{\rm bc}}). \end{aligned} \tag{7.9}$$

The ΔE and $M_{\rm bc}$ distributions for $B^0 \to \psi(2S) K_S^0$ ($\psi(2S) \to \ell^+\ell^-$), $\psi(2S) K_S^0$ ($\psi(2S) \to J/\psi \pi^+\pi^-$), $\chi_{c1} K_S^0$ ($\chi_{c1} \to J/\psi\gamma$), and $\eta_c K_S^0$ ($\eta_c \to K_S^0 K^-\pi^+$), are represented by the two dimensional Gaussian:

$$F_{\rm sig}(\Delta E, M_{\rm bc}) = a\, G(\Delta E - \mu_{\Delta E}; \sigma_{\Delta E})\, G(M_{\rm bc} - \mu_{M_{\rm bc}}; \sigma_{M_{\rm bc}}). \tag{7.10}$$

For the modes that include π^0 mesons, i.e., $B^0 \to J/\psi K_S^0$ ($K_S^0 \to \pi^0\pi^0$) and $\eta_c K_S^0$ ($\eta_c \to K^+K^-\pi^0$), the ΔE distribution is represented by the Crystal Ball function $f_{\rm CB}$ [66] and $M_{\rm bc}$ distribution by a single Gaussian:

$$F_{\rm sig}(\Delta E, M_{\rm bc}) = a\, f_{\rm CB}(\Delta E; \mu_{\Delta E}, \sigma_{\Delta E}, \alpha, n)\, G(M_{\rm bc} - \mu_{M_{\rm bc}}; \sigma_{M_{\rm bc}}), \tag{7.11}$$

where $f_{\rm CB}$ is defined as

$$\begin{aligned} & f_{\rm CB}(\Delta E; \mu_{\Delta E}, \sigma_{\Delta E}, \alpha, n) \\ & = \begin{cases} \frac{1}{A} \exp\left(-\frac{(\Delta E - \mu_{\Delta E})^2}{2\sigma_{\Delta E}^2} \right) & \text{for } \Delta E \geq \mu_{\Delta E} - \alpha\sigma_{\Delta E} \\ \frac{1}{A} \exp\left(-\frac{\alpha^2}{2} \right) \left[1 - \frac{(\Delta E - \mu_{\Delta E})\alpha}{n\sigma_{\Delta E}} - \frac{\alpha^2}{n} \right]^{-n} & \text{for } \Delta E < \mu_{\Delta E} - \alpha\sigma_{\Delta E} \end{cases} . \end{aligned} \tag{7.12}$$

The background function $F_{\rm bkg}$ is represented by a first order polynomial in the ΔE axis and the ARGUS background function [57] in the $M_{\rm bc}$ axis:

$$F_{\rm bkg}(\Delta E, M_{\rm bc}) = b(1 + c\Delta E) M_{\rm bc} \sqrt{1 - \left(\frac{M_{\rm bc}}{E_{\rm beam}^{\rm cms}} \right)^2} \exp\left\{ d \left[1 - \left(\frac{M_{\rm bc}}{E_{\rm beam}^{\rm cms}} \right)^2 \right] \right\}. \tag{7.13}$$

An unbinned maximum likelihood fit is used for the parameter determination of $F_{\rm sig}$ and $F_{\rm bkg}$. For $B^0 \to J/\psi K_S^0$ ($K_S^0 \to \pi^0\pi^0$), $\eta_c K_S^0$ ($\eta_c \to K^+K^-\pi^0$), and $\eta_c K_S^0$ ($\eta_c \to p\overline{p}$), some parameters are determined from the MC simulation because the data samples for these modes are too small to estimate the parameters reliably.

$B^0 \to J/\psi K^{*0}$

The background for the $B^0 \to J/\psi K^{*0}$ mode consists of three components:

- The cross-feed background from the other $B \to J/\psi K^*$ modes;
- The background from non-resonant $B^0 \to J/\psi K^0_S \pi^0$ decay; and
- The combinatorial background.

The fraction of the combinatorial background $f_{\rm cmb}$ is calculated from the result of the fit to the ΔE and the $M_{\rm bc}$ distributions like $(c\bar{c})K^0_S$ case. The ΔE and $M_{\rm bc}$ distribution for the combinatorial background, $F_{\rm cmb}(\Delta E, M_{\rm bc})$, is defined in the same way as Eq. (7.13) and that for the other components (the signal, cross-feed background, and non-resonant background), $F_{J/\psi K^*}(\Delta E, M_{\rm bc})$, is defined as Eq. (7.11). Then, $f_{\rm cmb}$ is obtained as a function of both ΔE and $M_{\rm bc}$:

$$f_{\rm cmb}(\Delta E, M_{\rm bc}) = \frac{F_{\rm cmb}(\Delta E, M_{\rm bc})}{F_{\rm cmb}(\Delta E, M_{\rm bc}) + F_{J/\psi K^*}(\Delta E, M_{\rm bc})}. \tag{7.14}$$

The ratio of the fraction of the signal to that of the cross-feed and non-resonant backgrounds is obtained as the function of $M_{\rm bc}$ from the MC simulation and the K^{*0} mass sideband data. The fraction of the signal, $f_{\rm sig}$, is then calculated from this ratio and the value of $1 - f_{\rm cmb}$. Finally, the correction for the $\cos\theta_{\rm tr}$ dependence of the signal reconstruction efficiency to $f_{\rm sig}$ determined from the MC study is applied. The detail can be found in Refs. [61, 51].

$B^0 \to J/\psi K^0_L$

For the $B^0 \to J/\psi K^0_L$ fit, we define the signal probability as a function of $p_B^{\rm cms}$ using the fitted $p_B^{\rm cms}$ distribution shown in Fig. 4.9.

The $J/\psi K^0_L$ signal yield is extracted by fitting the $p_B^{\rm cms}$ distribution of the data to a sum of four components:

- The signal;
- The background with K^0_L;
- The background without K^0_L; and
- The combinatorial J/ψ mesons.

The shapes of the first three components are determined from the J/ψ inclusive MC sample and look-up tables are used in the fit. The normalizations of these three components are treated as free parameters in the fit to minimize the effect of the aforementioned uncertainty in the K_L^0 detection efficiency in the MC simulation. The combinatorial component is evaluated using events with e-μ pairs that satisfy the requirements for J/ψ reconstruction. The shape is modeled by a second-order polynomial. The normalization of this combinatorial component is also free in the fit. An additional parameter of the fit is an offset in p_B^{cms}, allowing the signal shape to shift with respect to the background distribution. The detail of the fit to the p_B^{cms} distribution is described in Refs. [51, 52].

The result of the fit to the p_B^{cms} distribution is shown in Fig. 4.9. Then, f_{sig} is calculated as a function of p_B^{cms} from the ratio of the heights of the signal and total p_B^{cms} distributions.

7.4.2 Background Shape

The background Δt distributions are also determined in the different ways for above three cases.

$B^0 \to$ charmonium K_S^0

The background PDF $P_{\mathrm{bkg}}(\Delta t)$ for the modes other than $B^0 \to J/\psi K_L^0$ and the combinatorial background for $J/\psi K^{*0}$ mode is modeled as a sum of prompt and exponential components ($\mathcal{P}_{\mathrm{bkg}}(\Delta t)$) convoluted with a sum of two Gaussians ($R_{\mathrm{bkg}}(\Delta t)$):

$$P_{\mathrm{bkg}}(\Delta t) = \int_{-\infty}^{+\infty} d(\Delta t')\mathcal{P}_{\mathrm{bkg}}(\Delta t - \Delta t')R_{\mathrm{bkg}}(\Delta t'), \tag{7.15}$$

where

$$\mathcal{P}_{\mathrm{bkg}}(\Delta t) = f_\delta^{\mathrm{bkg}}\frac{1}{2}\delta(\Delta t - \mu_{\mathrm{bkg}}) + (1 - f_\delta^{\mathrm{bkg}})\frac{1}{4\tau_{\mathrm{bkg}}}\exp\left(-\frac{|\Delta t - \mu_{\mathrm{bkg}}|}{\tau_{\mathrm{bkg}}}\right), \tag{7.16}$$

$$R_{\mathrm{bkg}}(\Delta t) = (1 - f_{\mathrm{tail}}^{\mathrm{bkg}})G\left(\Delta t; s_{\mathrm{main}}^{\mathrm{bkg}}\sqrt{\sigma_{\mathrm{ful}}^2 + \sigma_{\mathrm{asc}}^2}\right) + f_{\mathrm{tail}}^{\mathrm{bkg}}G\left(\Delta t; s_{\mathrm{tail}}^{\mathrm{bkg}}\sqrt{\sigma_{\mathrm{ful}}^2 + \sigma_{\mathrm{asc}}^2}\right). \tag{7.17}$$

Different values are used for $s_{\mathrm{main}}^{\mathrm{bkg}}$, $s_{\mathrm{tail}}^{\mathrm{bkg}}$, $f_{\mathrm{tail}}^{\mathrm{bkg}}$, and f_δ^{bkg} depending on whether both vertices are reconstructed with multiple tracks or not. The parameters for the background function P_{bkg} are determined by the unbinned maximum likelihood fit to the Δt distribution of the background-enhanced control sample in the ΔE-M_{bc} sideband region. The $B^0 \to J/\psi K_S^0$, $\psi(2S)K_S^0$, $\chi_{c1}K_S^0$, and $J/\psi K^{*0}$ modes are fitted simultaneously with the same parameter set. For the $B^0 \to \eta_c K_S^0$ mode, the different parameter set is used.

$B^0 \to J/\psi K^{*0}$

As described in Section 7.4.1, the background of the $J/\psi K^{*0}$ mode consists of three components. The fraction of each component in the background is obtained from the ΔE and the $M_{\rm bc}$ distributions as described in Section 7.4.1. Then, the background Δt distribution for $J/\psi K^{*0}$ is defined as

$$P_{\rm bkg}(\Delta t) = (f_{\rm cf}^{\rm bkg} + f_{\rm nr}^{\rm bkg}) \int_{-\infty}^{+\infty} d(\Delta t') \mathcal{P}_{\rm life}^{\rm bkg}(\Delta t - \Delta t'; \tau_{B^0}) R_{\rm sig}(\Delta t') + f_{\rm cmb}^{\rm bkg} P_{\rm cmb}^{\rm bkg}(\Delta t), \quad (7.18)$$

where $f_{\rm cf}^{\rm bkg}$, $f_{\rm nr}^{\rm bkg}$, and $f_{\rm cmb}^{\rm bkg}$ are the fractions of the background components from the cross-feed, the non-resonant decay, and the combinatorial, respectively, and satisfy $f_{\rm cf}^{\rm bkg} + f_{\rm nr}^{\rm bkg} + f_{\rm cmb}^{\rm bkg} = 1$. The Δt distribution of the combinatorial background $P_{\rm cmb}^{\rm bkg}$ is defined in Eq. (7.15) as described above and $\mathcal{P}_{\rm life}^{\rm bkg}$ is defined as

$$\mathcal{P}_{\rm life}^{\rm bkg}(\Delta t; \tau) = \frac{1}{4\tau} \exp\left(-\frac{|\Delta t|}{\tau}\right). \quad (7.19)$$

The MC study shows that the effective lifetimes for the cross-feed and non-resonant backgrounds are consistent with the nominal B^0 lifetime. Thus we use the nominal B^0 lifetime in the fit. We use the signal resolution function $R_{\rm sig}$ for these backgrounds since the vertices are reconstructed in the same way as the signal.

$B^0 \to J/\psi K_L^0$

The background in the $B^0 \to J/\psi K_L^0$ mode is dominated by $B \to J/\psi X$ decays, including CP eigenstates that have to be treated differently from non-CP states. The $P_{\rm bkg}$ for the $J/\psi K_L^0$ mode is determined by the MC simulation study separately for each background component:

- $J/\psi K^{*0}(K_L^0 \pi^0)$;
- $\xi_f = -1$ CP modes ($J/\psi K_S^0$);
- $\xi_f = +1$ CP modes ($\psi(2S) K_L^0$, $\chi_{c1} K_L^0$, and $J/\psi \pi^0$);
- The other B^0 decay modes;
- The B^+ decays; and
- The combinatorial background.

The fraction of each background component is a function of p_B^{cms}. Their shapes are determined from the MC simulation study except for the combinatorial background which is determined from the fit to the data described in Section 7.4.1. The fractions of the background components other than the combinatorial one are calculated using the p_B^{cms} distributions obtained from the MC study, for each of the background with and without K_L^0 components described in Section 7.4.1. Then the fraction of the background component for the event is given as the sum of the products of the above MC-determined fraction and the fraction determined from the fit to data in Section 7.4.1. The detail can be found in Ref. [51].

For the CP-mode backgrounds, we use the signal PDF given in Eq. (7.5) with the appropriate ξ_f values. For the $J/\psi K^{*0}(K_L^0\pi^0)$ mode, which is a mixture of $\xi_f = -1$ (about 81%) and $\xi_f = +1$ (about 19%) states [61], we use a net CP eigenvalue of $\xi_{J/\psi K^{*0}} = -0.62 \pm 0.07$. The MC study shows that the effective lifetime for the background from B^+, $\tau_{B^+}^{\text{bkg}}$, is shorter than the B^+ lifetime due to the contamination of charged tracks from the fully reconstructed side (mostly π^+ from $J/\psi K^{*+}(K_L^0\pi^+)$) into the tag-side vertex. The value of $\tau_{B^+}^{\text{bkg}}$ is determined from the MC simulation to be 1.558 ± 0.026 ps. The same MC study shows that the effective lifetime for the B^0 background is consistent with the nominal B^0 lifetime. Thus we use the nominal B^0 lifetime in the fit. For the $J/\psi X$ background in the $J/\psi K_L^0$ mode, we use the signal resolution function R_{sig} to model the background since both the CP- and tag-side vertices are reconstructed with similar combinations of tracks for these backgrounds. For the Δt distribution of the combinatorial background $P_{\text{cmb}}^{\text{bkg}}$, we use the same function as defined in Eq. (7.15). Their parameters are determined from the fit to the e-μ combinations described in Section 7.4.1.

Accordingly, we obtain the background PDF for $J/\psi K_L^0$

$$
\begin{aligned}
P_{\text{bkg}}(\Delta t) = \int_{-\infty}^{+\infty} d(\Delta t') \Big[& f_{J/\psi K^{*0}}^{\text{bkg}} \mathcal{P}_{CP}^{\text{bkg}}(\Delta t - \Delta t'; \xi_{J/\psi K^{*0}}) \\
& + f_{CP_{\text{odd}}}^{\text{bkg}} \mathcal{P}_{CP}^{\text{bkg}}(\Delta t - \Delta t'; -1) \\
& + f_{CP_{\text{even}}}^{\text{bkg}} \mathcal{P}_{CP}^{\text{bkg}}(\Delta t - \Delta t'; +1) \\
& + f_{B^0}^{\text{bkg}} \mathcal{P}_{\text{life}}^{\text{bkg}}(\Delta t - \Delta t'; \tau_{B^0}) \\
& + f_{B^+}^{\text{bkg}} \mathcal{P}_{\text{life}}^{\text{bkg}}(\Delta t - \Delta t'; \tau_{B^+}^{\text{bkg}}) \Big] R_{\text{sig}}(\Delta t') \\
+ f_{\text{cmb}}^{\text{bkg}} P_{\text{cmb}}^{\text{bkg}}(\Delta t), &
\end{aligned} \tag{7.20}
$$

where $\mathcal{P}_{\text{life}}^{\text{bkg}}$ is defined in Eq. (7.19) and $\mathcal{P}_{CP}^{\text{bkg}}$ is defined as

$$
\mathcal{P}_{CP}^{\text{bkg}}(\Delta t; \xi_f) = \frac{1}{4\tau_{B^0}} \exp\left(-\frac{|\Delta t|}{\tau_{B^0}}\right) \left[1 - q\xi_f(1-2w)\sin(\Delta m_d \Delta t)\right]. \tag{7.21}
$$

$f_{J/\psi K^{*0}}^{\text{bkg}}$, $f_{CP_{\text{odd}}}^{\text{bkg}}$, $f_{CP_{\text{even}}}^{\text{bkg}}$, $f_{B^0}^{\text{bkg}}$, $f_{B^+}^{\text{bkg}}$, and $f_{\text{cmb}}^{\text{bkg}}$ are the fractions of the background components from $J/\psi K^{*0}(K_L^0\pi^0)$, $\xi_f = -1$ CP-modes, $\xi_f = +1$ CP-modes, the re-

Table 7.4: Number of events used in the $\sin 2\phi_1$ fit for each mode.

Mode	Number of events
$J/\psi(\ell^+\ell^-)K_S^0(\pi^+\pi^-)$	1116
$J/\psi(\ell^+\ell^-)K_S^0(\pi^0\pi^0)$	162
$\psi(2S)(\ell^+\ell^-)K_S^0(\pi^+\pi^-)$	76
$\psi(2S)(J/\psi\pi^+\pi^-)K_S^0(\pi^+\pi^-)$	96
$\chi_{c1}(J/\psi\gamma)K_S^0(\pi^+\pi^-)$	67
$\eta_c(K_S^0K^-\pi^+)K_S^0(\pi^+\pi^-)$	63
$\eta_c(K^+K^-\pi^0)K_S^0(\pi^+\pi^-)$	44
$\eta_c(p\overline{p})K_S^0(\pi^+\pi^-)$	15
All with $\xi_f = -1$	1639
$J/\psi(\ell^+\ell^-)K^{*0}(K_S^0\pi^0)$	89
$J/\psi(\ell^+\ell^-)K_L^0$	1230
Total	2958

maining B^0, B^+, and combinatorial, respectively, and they satisfy $f^{\rm bkg}_{J/\psi K^{*0}} + f^{\rm bkg}_{CP_{\rm odd}} + f^{\rm bkg}_{CP_{\rm even}} + f^{\rm bkg}_{B^0} + f^{\rm bkg}_{B^+} + f^{\rm bkg}_{\rm cmb} = 1$.

7.5 Fit Result

Using the PDF described above, an unbinned maximum likelihood fit is applied to the Δt distribution. In the final fit, we fix τ_{B^0} and Δm_d to the world average value [65]. The parameters of the resolution function and wrong tag fractions are fixed to the values described above. The only free parameter in the fit is $\sin 2\phi_1$.

Using 78 fb^{-1} data which correspond to 85×10^6 $B\overline{B}$ pairs, we find 2958 events in the signal boxes after all vertexing and flavor-tagging requirements are applied. The number of events used in the $\sin 2\phi_1$ fit for each mode is listed in Table 7.4. The unbinned maximum likelihood fit to these data sample yields

$$\sin 2\phi_1 = 0.719 \pm 0.074. \tag{7.22}$$

Figure 7.4 shows the observed Δt distributions for the $q\xi_f = +1$ and $q\xi_f = -1$ event samples together with the results from the fit. Figure 7.5(a) shows the raw asymmetry and the fit result.

We examine the value of $\sin 2\phi_1$ in various subsamples. Table 7.5 lists the results obtained by applying the same analysis to the subsamples. All values are statistically consistent with each other. Figures 7.5(b) and 7.5(c) show the raw asymmetries and the fit results for $(c\overline{c})K_S^0$ and $J/\psi K_L^0$, respectively.

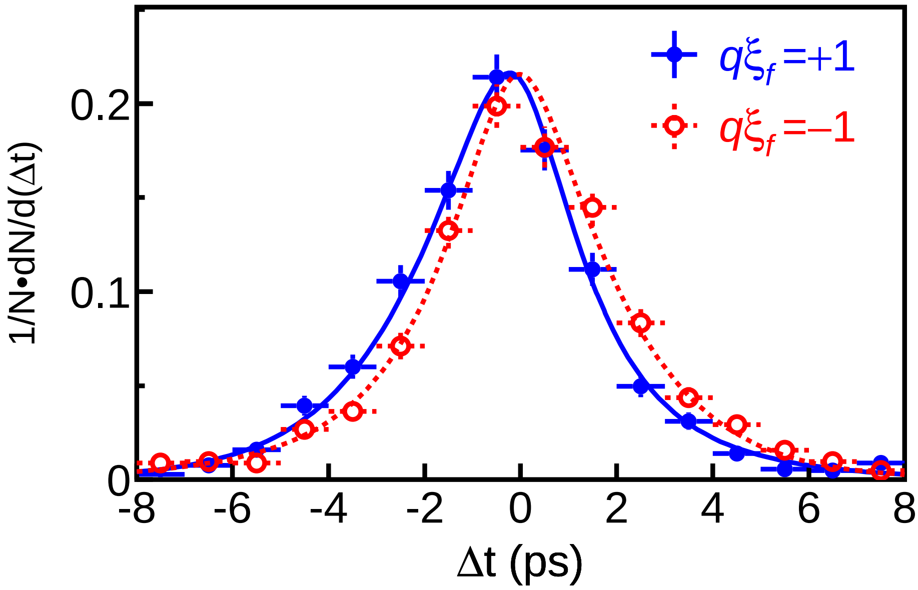

Figure 7.4: Distributions of Δt for the events with $q\xi_f = +1$ (solid points) and $q\xi_f = -1$ (open points). The results of the global fit with $\sin 2\phi_1 = 0.719$ are shown as solid and dashed curves, respectively.

Table 7.5: Numbers of candidate events and values of $\sin 2\phi_1$ for various subsamples (statistical errors only).

Sample	Number of events	$\sin 2\phi_1$
$J/\psi K_S^0(\pi^+\pi^-)$	1116	0.73 ± 0.10
$(c\bar{c})K_S^0$ except $J/\psi K_S^0(\pi^+\pi^-)$	523	0.67 ± 0.17
$J/\psi K_L^0$	1230	0.78 ± 0.17
$J/\psi K^{*0}(K_S^0\pi^0)$	89	0.04 ± 0.63
$B_{\rm tag} = B^0$ $(q = +1)$	1465	0.65 ± 0.12
$B_{\rm tag} = \overline{B}^0$ $(q = -1)$	1493	0.77 ± 0.09
$0 < r \leq 0.5$	1600	1.27 ± 0.36
$0.5 < r \leq 0.75$	658	0.62 ± 0.15
$0.75 < r \leq 1$	700	0.72 ± 0.09
data before 2002	1587	0.78 ± 0.10
data in 2002	1371	0.65 ± 0.11
All	2958	0.72 ± 0.07

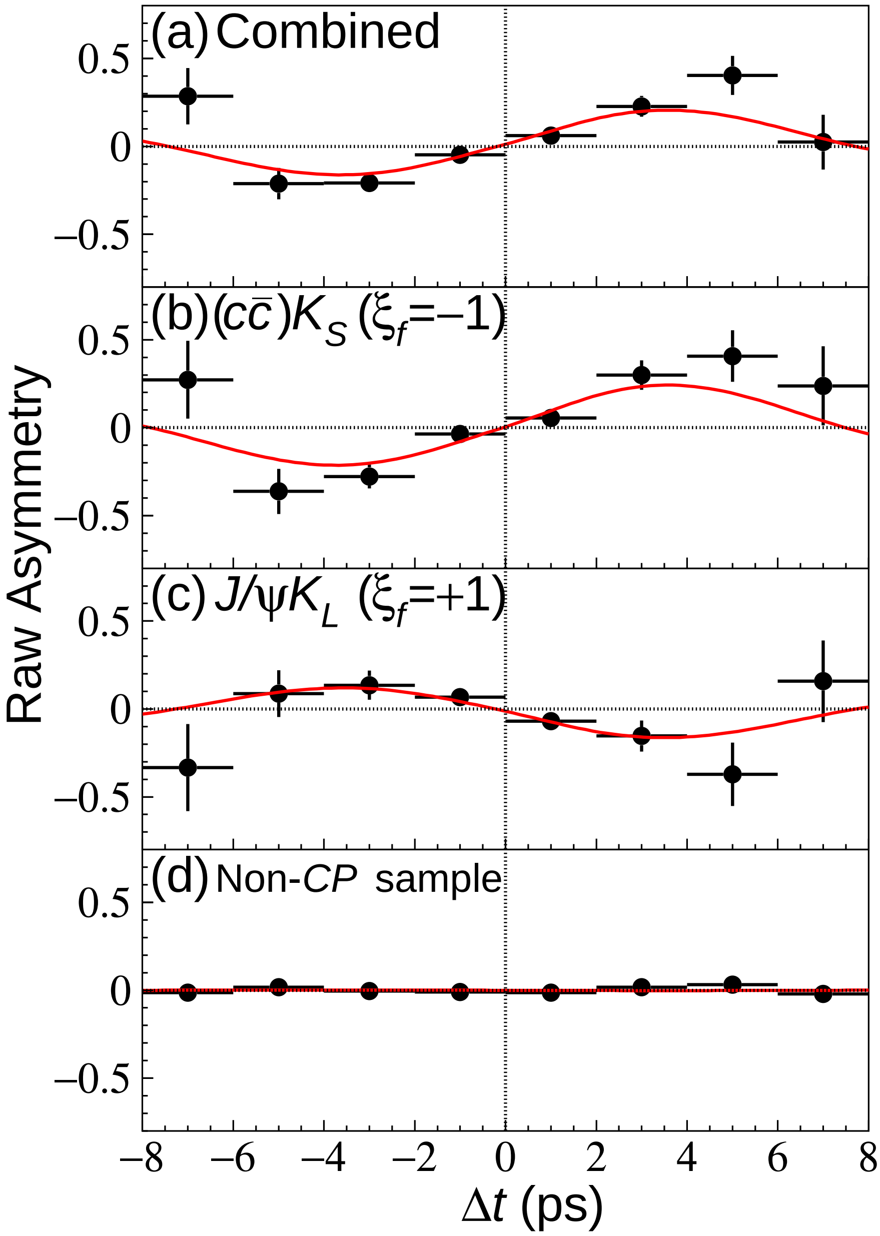

Figure 7.5: (a) Raw asymmetry for all modes combined. The asymmetry for $J/\psi K_L^0$ and $J/\psi K^{*0}$ is inverted to account for the opposite CP eigenvalue. The corresponding plots for (b) $(c\bar{c})K_S^0$, (c) $J/\psi K_L^0$, and (d) non-CP control samples are also shown. The curves are the results of the unbinned maximum likelihood fit applied separately to the individual data samples.

Table 7.6: Results of the $|\lambda|$ fit for subsamples (statistical errors only).

Sample	$|\lambda|$
$J/\psi K^0_S(\pi^+\pi^-)$	0.95 ± 0.07
$(c\bar{c})K^0_S$ except $J/\psi K^0_S(\pi^+\pi^-)$	0.98 ± 0.12
$J/\psi K^0_L$	0.95 ± 0.09
$J/\psi K^{*0}(K^0_S\pi^0)$	0.66 ± 0.34
All	0.95 ± 0.05

We also apply the same fit to the non–CP-eigenstate modes: $B^0 \to D^-\pi^+$, $D^{*-}\pi^+$, $D^{*-}\rho^+$, $J/\psi K^{*0}(K^+\pi^-)$, and $D^{*-}\ell^+\nu$. The data samples are same as those used for the determination of the resolution and wrong tag fraction described in Section 7.2 and 7.3. The fit to these samples, where no asymmetry is expected, yields

$$0.005 \pm 0.015(\text{stat}). \tag{7.23}$$

The result is consistent with zero, and no systematic bias is observed. Figure 7.5(d) shows the raw asymmetry for these non-CP control samples.

The signal PDF for a neutral B meson decaying into a CP eigenstate [Eq. (7.2)] can be expressed in a more general form as

$$\mathcal{P}_{\text{sig}}(\Delta t) = \frac{1}{4\tau_{B^0}} \exp\left(-\frac{|\Delta t|}{\tau_{B^0}}\right) \Bigg\{ 1 + q(1-2w) \\ \left[\frac{2\text{Im}\lambda}{|\lambda|^2+1} \sin(\Delta m_d \Delta t) + \frac{|\lambda|^2-1}{|\lambda|^2+1} \cos(\Delta m_d \Delta t) \right] \Bigg\}, \tag{7.24}$$

where λ is a complex parameter that depends on both B^0-$\overline{B}^0$ mixing and on the amplitudes for B^0 and $\overline{B}^0$ decay to a CP eigenstate, as described in Sections 2.4 and 2.5. The presence of the cosine term ($|\lambda| \neq 1$) would indicate direct CP violation. The value for $\sin 2\phi_1$ reported above is determined with the assumption $|\lambda| = 1$, as $|\lambda|$ is expected to be very close to one in SM. In order to test this assumption, we also perform a fit using the above expression with $a_{CP} = -\text{Im}\lambda/(\xi_f|\lambda|)$ and $|\lambda|$ as free parameters, keeping everything else the same. The fit result for each subsample is listed in Table 7.6. We obtain

$$|\lambda| = 0.950 \pm 0.049(\text{stat}) \pm 0.025(\text{syst}) \tag{7.25}$$

and $a_{CP} = 0.720 \pm 0.074(\text{stat})$ for all CP modes combined, where the sources of the systematic error for $|\lambda|$ are the same as those for $\sin 2\phi_1$ described in Section 7.6. This result is consistent with the assumption used in the analysis.

Table 7.7: Summary of the systematic errors for $\sin 2\phi_1$. The errors are combined in quadrature.

Source	Error
Vertex reconstruction	0.022
Resolution function	0.014
Wrong tag fraction	0.015
Physics (τ_{B^0}, Δm_d, $J/\psi K^{*0}$)	0.007
Background fraction (except for $J/\psi K_L^0$)	0.004
Background fraction ($J/\psi K_L^0$)	0.010
Background shape	0.005
Fit bias	0.011
Total	0.035

7.6 Systematic Uncertainties

We consider the systematic uncertainties from various sources listed bellow. The major contributions to the systematic error are from the vertex reconstruction. The results are summarized in Table 7.7. All systematic errors are combined in quadrature.

Vertex Reconstruction The largest contribution comes from vertex reconstruction.

The fit quality criterion for reconstructed vertices is varied from $\xi < 50$ to $\xi < 200$.

Possible systematic effects due to the track quality selection of the tag-side B decay vertices are studied by varying each criterion by 10%.

We check the systematic uncertainty due to outliers and tails of the resolution by varying the Δt range from $|\Delta t| < 5$ ps to $|\Delta t| < \infty$, i.e., no requirement for the Δt range.

The systematic error due to the IP constraint is estimated by varying the smearing used to account for the transverse B decay length by ± 10 μm.

Possible charge-dependent bias in the track position in z is studied using the cosmic and $\gamma\gamma \to \rho^0\rho^0 \to \pi^+\pi^-\pi^+\pi^-$ two-photon events. This bias may cause the systematic shift in $\sin 2\phi_1$. Since we find no systematic bias in the track position between the positive and negative tracks, we apply no correction in the nominal fit. Systematic error is estimated by shifting the z position of the track by ± 3 μm for the positive and ∓ 3 μm for the negative track.

The errors of the track parameters are calibrated using the cosmic data and the cosmic and hadronic MC samples [67]. The systematic uncertainty due to this calibration is studied by comparing the result of the fit where this calibration is turned off with the nominal result.

Resolution Function We estimate the contribution due to the uncertainty in the parameters of the resolution function by varying its parameters given in Section 7.2 by $\pm 1\sigma$ for the parameters determined from the real data (parameters for the detector resolution and outlier, and f_δ's for $R_{\rm np}$) and $\pm 2\sigma$ for those determined from the MC sample ($R_{\rm np}$ parameters other than f_δ's).

We also estimate the uncertainty due to the resolution function form by using the resolution function whose detector parts ($R_{\rm ful}$ and $R_{\rm asc}$) are the sum of two Gaussians.

Wrong Tag Fraction Systematic errors due to the uncertainties in the wrong tag fractions given in Section 7.3 (Table 7.3) are studied by varying the wrong tag fraction individually for each r region by its error.

We estimate the uncertainty due to the difference of wrong tag fractions between $q = +1$ and -1 events by using the wrong tag fractions obtained for $q = +1$ and -1 events separately.

The uncertainties due to the difference of wrong tag fractions between the CP events and flavor-specific events are also studied using the MC samples.

Physics Parameters The B meson mass, lifetime, and mixing parameter are fixed to the world average values [65] in the fit, i.e., $m_{B^0} = 5.2794 \pm 0.0005$ GeV/c^2, $\tau_{B^0} = 1.542 \pm 0.016$ ps, and $\Delta m_d = 0.489 \pm 0.008$ ps^{-1}. We estimate the systematic error by repeating the fit varying these parameters by their errors.

Another physics-related uncertainty is the CP eigenvalue of $J/\psi K^{*0}$ ($\xi_{J/\psi K^{*0}}$) measured from the angular distribution of the decay daughters [61]. This systematic uncertainty is determined from the $\pm 1\sigma$ uncertainty in the measurement.

Background Fraction except for $J/\psi K_L^0$ The background fraction in the PDF, $1 - f_{\rm sig}$, is calculated from the signal and background distribution functions of ΔE and $M_{\rm bc}$ as described in Section 7.4.1. These functions are determined from the data or the MC simulation depending on the decay mode. To estimate the systematic errors associated with the choice of parameterization, we vary the parameters obtained from the MC simulation by $\pm 2\sigma$ and those obtained from the data by $\pm 1\sigma$.

Background Fraction for $J/\psi K_L^0$ As described in Section 7.4.1, the background fraction for the $J/\psi K_L^0$ sample is obtained from a fit to the $p_B^{\rm cms}$ distribution. In this fit, the sum of the components is automatically constrained to the total number of events in the signal region. Thus, the signal yield and the size of other backgrounds are strongly anticorrelated. To determine the systematic error on $\sin 2\phi_1$ that comes from the uncertainty of the background fraction, we need to take this anticorrelation into account. To this end, we repeat the fit to the $p_B^{\rm cms}$ distribution with the fraction of one component fixed $+1\sigma$ or -1σ away from the central value obtained in the nominal fit and with the fractions of the other components as free parameters. We obtain $\sin 2\phi_1$ using the resultant background yields. This procedure is repeated for all the four component (the signal, the background with K_L^0, without K_L^0, and the combinatorial background). We regard the maximum difference between the thus obtained value and the nominal $\sin 2\phi_1$ value as the systematic error.

We also check the systematic error due to the uncertainty in the CP content of the background. We repeat the fit varying the parameters to determine the various background fractions. Since these parameters are obtained from the MC simulation, we estimate the systematic error by conservatively changing each parameter by $\pm 2\sigma$ and adding the resulting changes in quadrature.

Background Shape The parameters that determine $P_{\rm bkg}(\Delta t)$ for the modes other than $B^0 \to J/\psi K_L^0$ and $P_{\rm cmb}^{\rm bkg}(\Delta t)$ for $J/\psi K_L^0$ are varied within their errors and fits are repeated to estimate the uncertainties due to the background shape.

The effective lifetime of the B^+ background for $J/\psi K_L^0$, $\tau_{B^+}^{\rm bkg}$, which is determined from the MC study as described in Section 7.4.2, is varied by $\pm 2\sigma$ to estimate its contribution.

In the background of the $B^0 \to \chi_{c1} K_S^0$ sample, there may be the contamination from the $B^0 \to \chi_{c2} K_S^0$ mode, which has the opposite CP eigenvalue. We neglect this effect in the nominal fit, but the systematic uncertainty due to this effect is estimated by regarding all the background events in the $\chi_{c1} K_S^0$ mode as the $\chi_{c2} K_S^0$ events.

Fit Bias The possible bias in the fitting procedure and the effect of SVD alignment error are studied with MC samples. Since we find no bias, no correction is made. The MC statistical error is associated as a systematic error for these sources.

7.7 Summary of $\sin 2\phi_1$ Fit

We have presented the measurement of the CP violating parameter $\sin 2\phi_1$ using 78 fb^{-1} of data sample collected with the Belle detector at the $\Upsilon(4S)$ energy. An unbinned maximum likelihood fit to the distribution of the proper-time difference between the two B meson decays with one of the neutral B mesons fully reconstructed in the CP eigenstate yields

$$\sin 2\phi_1 = 0.719 \pm 0.074(\text{stat}) \pm 0.035(\text{syst}). \tag{7.26}$$

Chapter 8

Discussions and Conclusion

8.1 Discussions

8.1.1 Lifetimes

The comparisons of the measurements of τ_{B^0}, τ_{B^+}, and τ_{B^+}/τ_{B^0} described in Chapter 5 with other experiments are shown in Figs. 8.1, 8.2, and 8.3, respectively. These plots are made by the LEP B lifetimes working group as of July 2002 [68]. As shown in these figures, our results are ones of the most precise measurements. They are the first precise measurements of B-meson lifetimes at the asymmetric energy B-Factory experiment operated on the $\Upsilon(4S)$ resonance. It is remarkable that the B-Factory experiments reached these precisions with only two- to three-year operation.

The measurements in the B-Factory experiments have different systematics from the experiments at the e^+e^- colliders operated on the Z-boson mass or the hadron colliders. The B-Factory experiments on the $\Upsilon(4S)$ resonance offer the much cleaner signal than the other experiments. The high luminosity at the B Factory offers the advantage of the high statistics with respect to the other experiments. On the other hand, B mesons produced in the KEK B-Factory experiment travel only ~ 200 μm, while those produced in the other experiments travel an order of millimeters. This results in the fact that the resolution of the proper-time interval in the KEK B-Factory experiment is the same order as the lifetimes of the B mesons and worse than the other experiments. In addition, the proper-time interval distributes to both positive and negative sides since we only know the difference of two B-meson decay points, while both the production and decay points of B meson can be measured at the other experiments. These facts make the lifetime measurements difficult in the B Factory. Nevertheless we successfully measured the lifetimes precisely and determined the resolution function that is applicable to other time-evolution

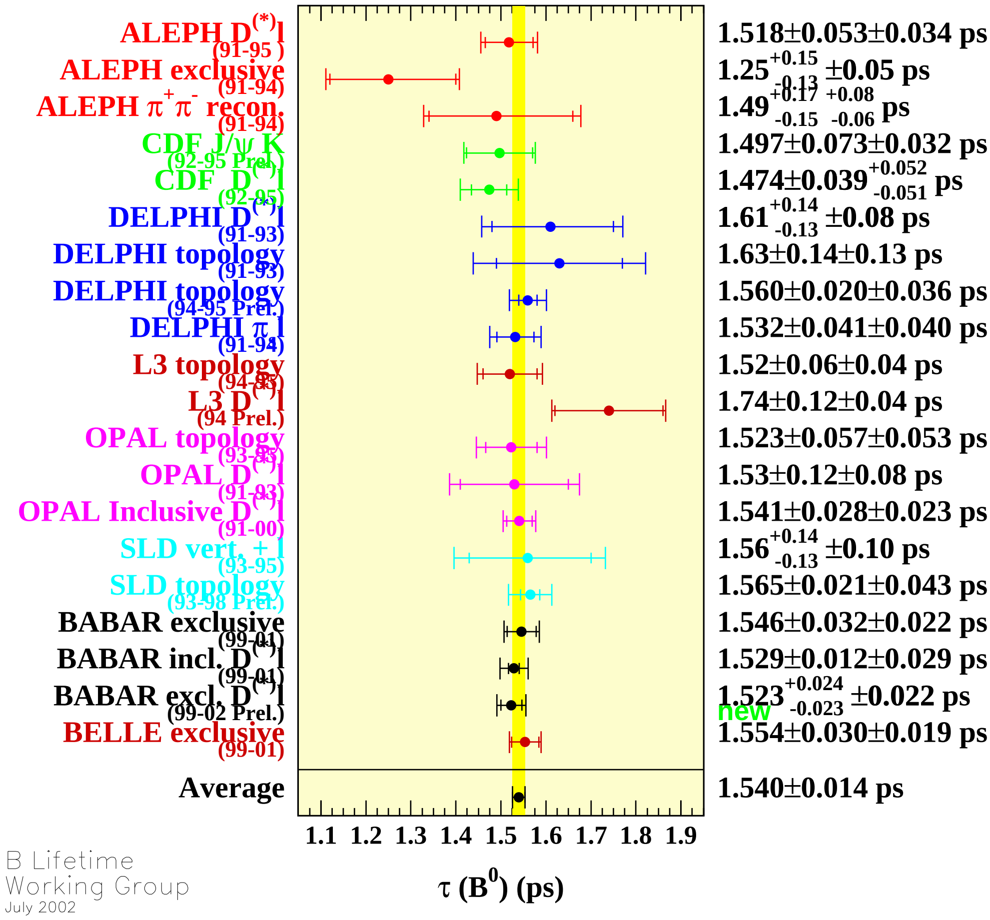

Figure 8.1: Comparison of the results for B^0 lifetime measurements and the world average as of July 2002 [68]. The result shown in this thesis is presented as “BELLE exclusive (99–01)”.

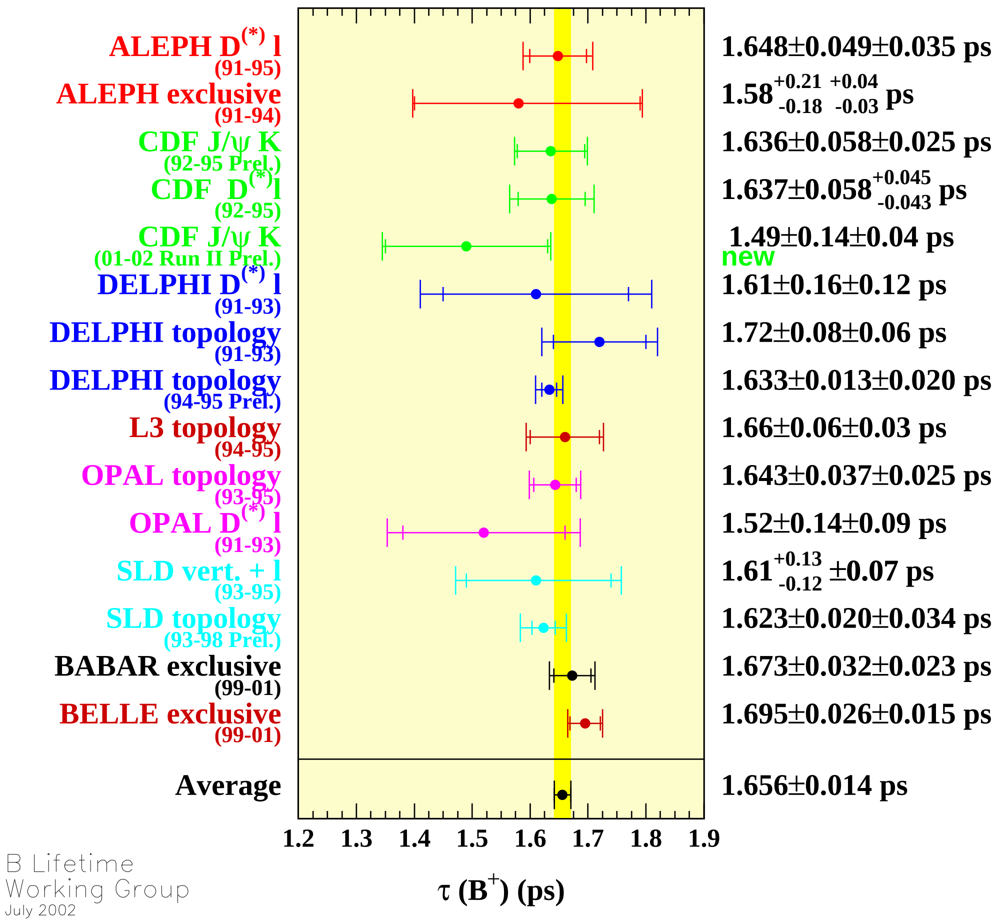

Figure 8.2: Comparison of the results for B^+ lifetime measurements and the world average as of July 2002 [68]. The result shown in this thesis is presented as "BELLE exclusive (99–01)".

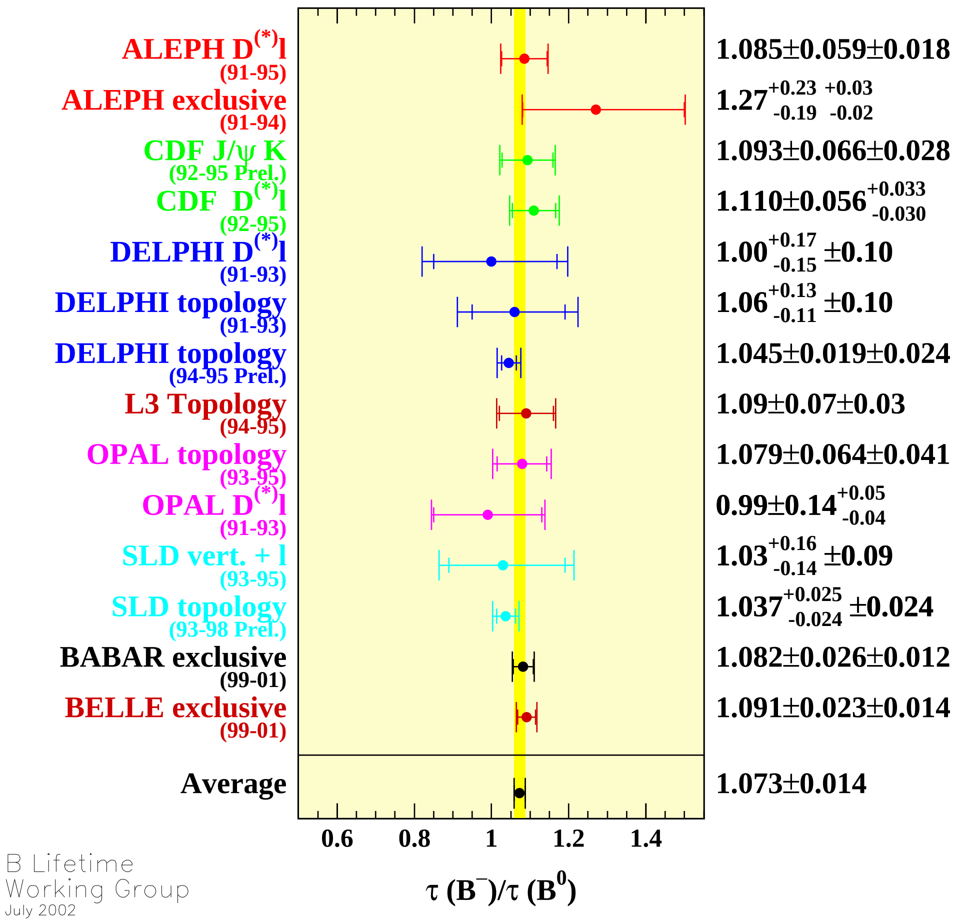

Figure 8.3: Comparison of the results for τ_{B^+}/τ_{B^0} measurements and the world average as of July 2002 [68]. The result shown in this thesis is presented as “BELLE exclusive (99–01)”.

analyses. We established the precise measurements of the B-meson time-evolution at the B-Factory experiment.

Since the lifetimes are the basic parameters of B mesons, the precise determination of them contributes to the precision of other experiments. For example, in the Δm_d measurement using the dilepton events [69], the dominant systematic uncertainty comes from the lifetime ratio τ_{B^+}/τ_{B^0}.

Our result of $\tau_{B^+}/\tau_{B^0} = 1.091 \pm 0.023(\text{stat}) \pm 0.014(\text{syst})$ is consistent with the recent theoretical prediction of 1.07 ± 0.03 [70]. Therefore, the current framework of the heavy quark expansion seems to be successful to explain the experimental data.

8.1.2 Oscillation Frequency Δm_d

The B^0-$\overline{B}^0$ oscillation was first observed as the time-integrated probability χ_d with the $e^+e^- \to \Upsilon(4S)$ data by the ARGUS collaboration at DORIS and the CLEO collaboratin at CESR. The world average value of χ_d from these time-integrated measurements is 0.187 ± 0.015 [65]. The relation between χ_d and Δm_d is expressed as

$$\chi_d = \frac{x_d^2}{2(1 + x_d^2)}, \tag{8.1}$$

where $x_d \equiv \Delta m_d/\Gamma$. The value of Δm_d derived from χ_d world average and Eq. (8.1) is 0.491 ± 0.032 ps^{-1}, and is consistent with our result of direct Δm_d measurement.

Figure 8.4 shows the comparison of the time-evolution Δm_d measurements between several experiments. This plot is made by the Working group on B oscillation as of July 2002 [71]. We provide the Δm_d measurement of 4% accuracy and it is one of the most precise measurements.

The Δm_d measurements in the B-Factory experiments also have different systematics from the other experiments. In addition to the differences described in the previous subsection, the B-Factory experiments have the great advantage in the flavor tagging because of the clean signal environment and the powerful particle identification. The effective tagging efficiency of $\sim 30\%$ is much higher than that in the other experiments (typically $\lesssim 10\%$). This is the first measurement of the oscillation frequency for the B^0-$\overline{B}^0$ mixing using the flavor tagging method developed for the KEK B-Factory experiment. We demonstrated the high performance of our flavor tagging algorithm and the successful application of the resolution function determined in the lifetime measurement to the other time-evolution analyses.

Since the oscillation frequency Δm_d is related to $|V_{td}|$ as described in Section 2.3, accurate measurements of Δm_d provide a mathematical constraint on the unitarity of the CKM matrix. However, currently there exists the large theoretical uncertainties on the V_{td} determination. The result of the constraint on the unitarity triangle is shown in the next subsection.

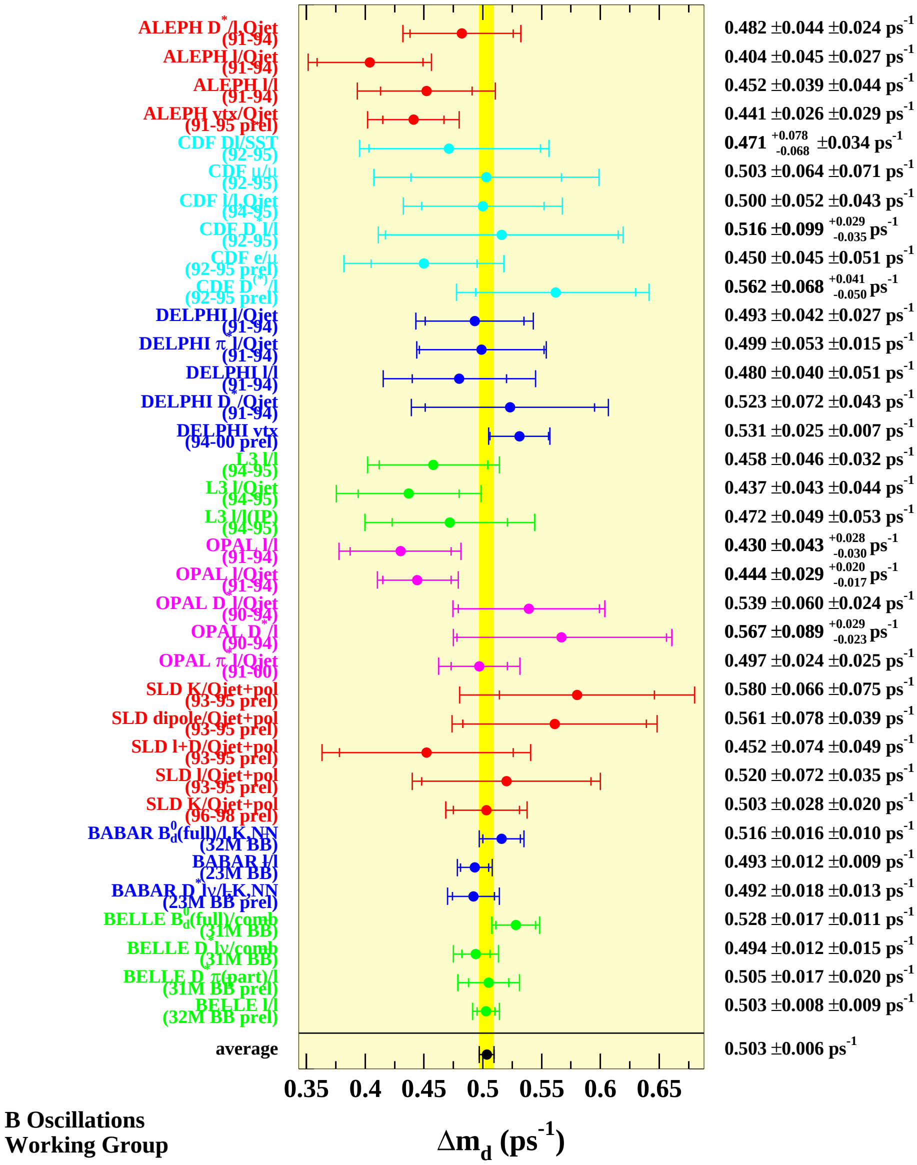

Figure 8.4: Comparison of the results for Δm_d measurements and the world average as of July 2002 [71]. The result shown in this thesis is presented as “BELLE B_d^0 (full)/comb (31M $B\overline{B}$)”.

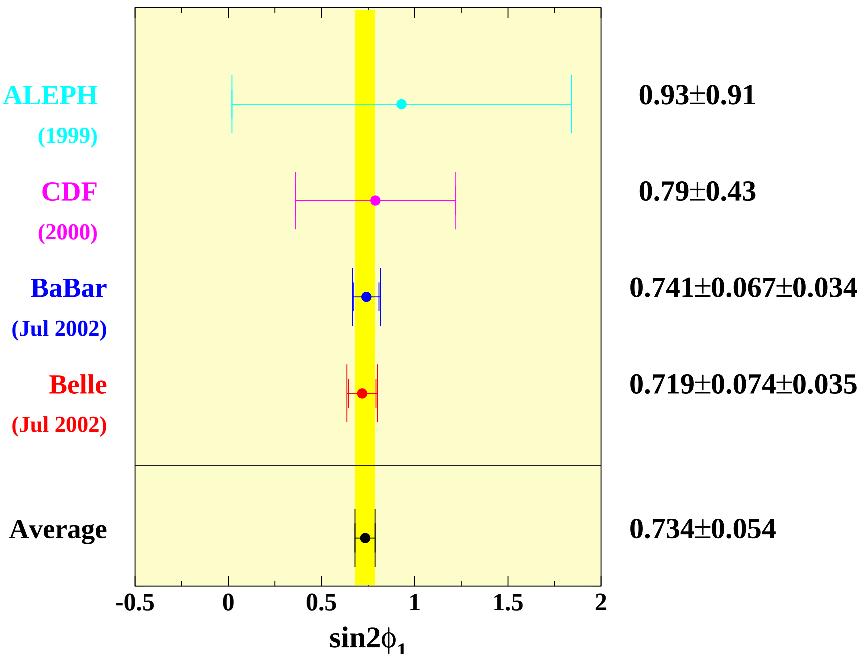

Figure 8.5: Comparison of the results for $\sin 2\phi_1$ measurements and the world average as of July 2002. The result shown in this thesis is presented as "Belle (Jul 2002)".

8.1.3 CP Violation Parameter $\sin 2\phi_1$

The comparison of the $\sin 2\phi_1$ measurement described in Chapter 7 with the other experiments [72, 73] is shown in Fig. 8.5. The average shown in the plot is the weighted mean of the listed measurements. In all measurements, our measurement is the most precise together with the BaBar experiment. The result in this thesis is further precise than the previous result obtained in 2001 [45], not only due to the $\sim$ 3-times larger statistics, but also because of the improved tracking and flavor-tagging algorithms and the improved resolution function.

The parameters of the CKM matrix are fitted by the CKM Fitter working group [22] using the recent experimental and theoretical results as of July 2002, including the results shown in this thesis. For the oscillation frequency of the B^0-$\overline{B}^0$ mixing Δm_d, the world average obtained by the Working group on B oscillation [71] shown in Fig. 8.4 is used. Our Δm_d result is also used to calculate the average. For the CP violation parameter $\sin 2\phi_1$, the weighted mean of the measured values listed in Fig. 8.5 includes our result.

The results of the global fit including all the constraints are presented in the $(\overline{\rho}, \overline{\eta})$ plane shown in Fig. 8.6. The regions of 10% and 95% confidence levels (CLs)

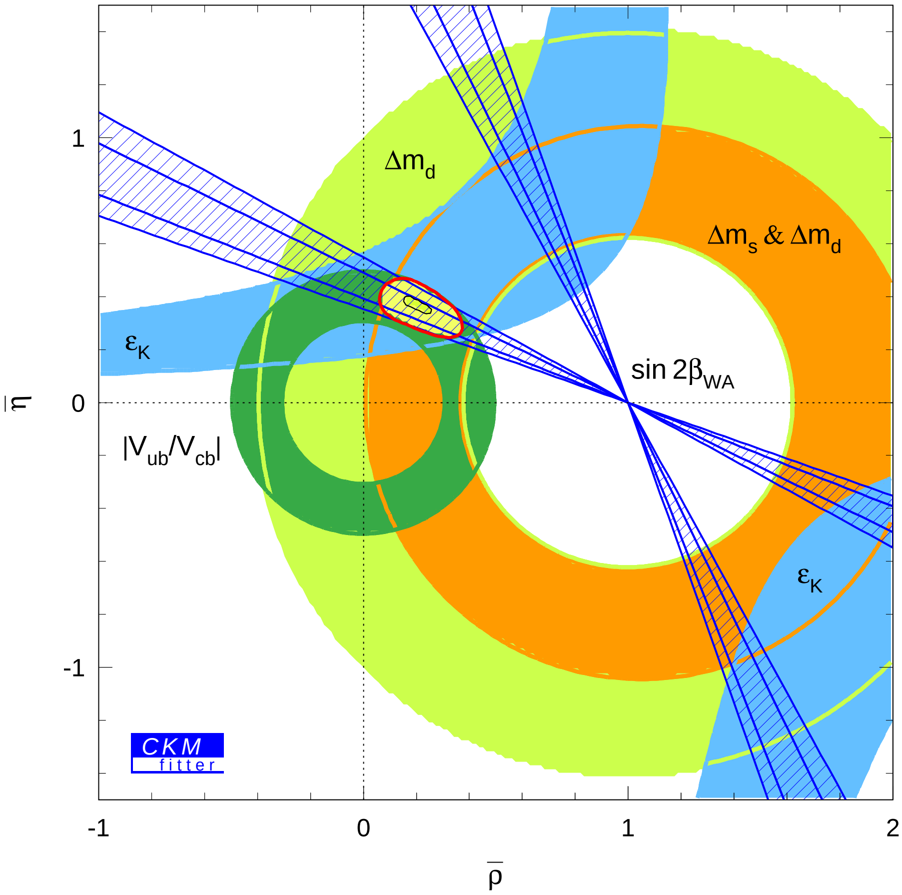

Figure 8.6: Confidence levels in the $(\bar{\rho}, \bar{\eta})$ plane for the global CKM fit as of July 2002 [22]. The regions of 10% and 95% CLs are shown. Also shown are the 95% CL contours of the individual constraints. For the world average of the $\sin 2\phi_1$ measurements indicated as "$\sin 2\beta_{\rm WA}$", the 68% and 95% CL constraints are depicted by the hatched areas.

are shown in the figure. The 95% CL contours of the individual constraints as well as the 68% and 95% CL regions corresponding to the world average of the $\sin 2\phi_1$ measurements (hatched areas) are also shown.

As we can see in the Fig. 8.6, the directly measured $\sin 2\phi_1$ value provides the most precise and robust constraint on the unitarity triangle. The directly measured $\sin 2\phi_1$ value extraordinarily agrees with the indirect determination from the theories and the measurements of the other parameters. The global CKM fit result gives the consistent picture of SM. Thus, KM mechanism is most probably the dominant source of the CP violation at the electroweak scale. We enter the new stage of the CP violation: We seek for the new-physics corrections to the CKM picture rather than search for the new-physics alternatives to the CKM picture.

8.2 Conclusion

We have measured the neutral and charged B-meson lifetimes, τ_{B^0} and τ_{B^+}, the oscillation frequency Δm_d for the B^0-$\overline{B}^0$ mixing, and the CP violation parameter $\sin 2\phi_1$ at the KEK B-Factory experiment, employing the Belle detector and the KEKB asymmetric e^+e^- collider operating with the energy of $\Upsilon(4S)$ resonance.

Using 29.1 fb^{-1} of data sample, we reconstruct 7863 neutral and 12047 charged B candidates which decay to several hadronic modes. Unbinned maximum likelihood fits to the distributions of the proper-time difference between the two B meson decays yield

$$\tau_{B^0} = 1.554 \pm 0.030(\text{stat}) \pm 0.019(\text{syst}) \text{ ps}, \tag{8.2}$$

$$\tau_{B^+} = 1.695 \pm 0.026(\text{stat}) \pm 0.015(\text{syst}) \text{ ps}, \tag{8.3}$$

$$\tau_{B^+}/\tau_{B^0} = 1.091 \pm 0.023(\text{stat}) \pm 0.014(\text{syst}). \tag{8.4}$$

Using the same data set, we reconstruct 6660 neutral B candidates which decay to flavor-specific hadronic modes, while the flavor of the other is identified from its decay products. From the distributions of proper decay time difference of same- and opposite-flavor B meson pairs, we obtain

$$\Delta m_d = 0.528 \pm 0.017(\text{stat}) \pm 0.011(\text{syst}) \text{ ps}^{-1}. \tag{8.5}$$

Using 78 fb^{-1} of data sample with the improved track reconstruction and flavor tagging algorithms, we reconstruct 2958 neutral B candidates that decay to the CP eigenstates. An unbinned maximum likelihood fit to the distribution of the proper-time difference between the two B meson decays, where one is fully reconstructed in a CP eigenstate and the flavor of the other is determined from its decay products, yields

$$\sin 2\phi_1 = 0.719 \pm 0.074(\text{stat}) \pm 0.035(\text{syst}). \tag{8.6}$$

We have provided the most precise measurements for these parameters. These results make tighter constraints to the CKM unitarity triangle. Thus, we have shown that the study of time evolution of B mesons at the B Factory offers very sensitive tests of SM. With the data presented in this thesis we have proved that the KM mechanism is correct at the electroweak scale. We have opened a new era for the understanding of the CP violation to search for the new-physics corrections to the CKM picture. Further increase of the statistics enables us to probe the physics beyond SM.

Appendix A

Particle Identification

In this appendix, we describe the algorithms for PID.

First, the K/π identification is explained. Then, the electron identification is described. Finally, we mention the muon identification.

A.1 K/π Identification

The K/π identification is carried out by combining information from three nearly independent measurements [74]:

- dE/dx measurement by CDC;
- TOF measurement; and
- Measurement of the number of photoelectrons ($N_{\rm pe}$) in ACC.

The momentum coverage of each detector for K/π separation is shown in Fig. A.1. We make PDF for each measurement beforehand. Based on each PDF, the likelihood function for each measurement is calculated and the product of the three likelihood functions yields the overall likelihood probability for being a kaon or a pion, L_K or L_π. A particle is then identified as a kaon or a pion by the selection based on the likelihood ratio P:

$$P(K/\pi) = \frac{L_K}{L_K + L_\pi}, \tag{A.1}$$

$$P(\pi/K) = 1 - P(K/\pi). \tag{A.2}$$

The validity of the K/π identification is demonstrated using the charm decay, $D^{*+} \to D^0\pi^+$, followed by $D^0 \to K^-\pi^+$. The characteristic slow π^+ from the D^{*+} decay allows these decays to be selected with a good S/N ratio (better than 30), without relying on PID. Therefore, the detector performance can be directly probed

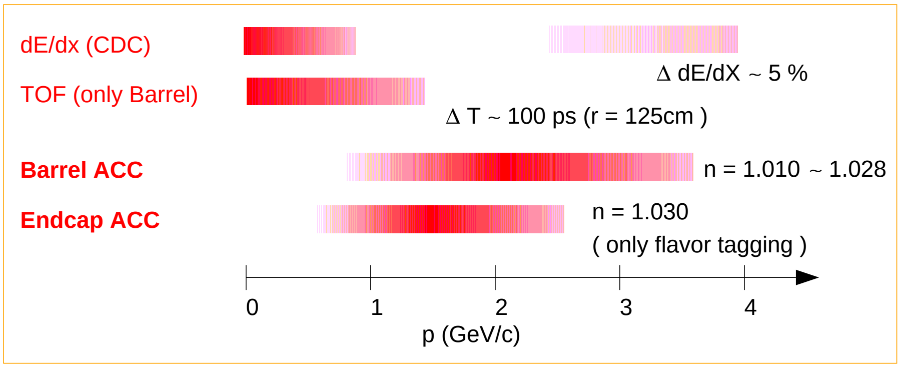

Figure A.1: Momentum coverage of each detector used for K/π separation.

with the daughter K and π mesons from the D decay, which can be tagged by their relative charge with respect to the slow pion. Figure A.2 shows two-dimensional plots of the likelihood ratio $P(K/\pi)$ and measured momenta for the kaon and pion tracks. The figure demonstrates the clear separation of kaons and pions up to around 4 GeV$/c$. The measured K efficiency and π fake rate in the barrel region are plotted as functions of the track momentum from 0.5 to 4.0 GeV$/c$ in Fig. A.3. The likelihood ratio selection, $P(K/\pi) \geq 0.6$, is applied in this figure. For most of the region, the measured K efficiency exceeds 80%, while the π fake rate is kept below 10%.

A.2 Electron Identification

Electrons are identified by using the following discriminants [75]:

- Ratio of energy deposited in ECL and charged track momentum measured by CDC;
- Transverse shower shape at ECL;
- Matching between a cluster at ECL and charged track position extrapolated to ECL;
- dE/dx measured by CDC;
- Light yield in ACC; and
- Time-of-flight measured by TOF.

As in the case of K/π identification, the PDFs for the discriminants are made beforehand. Based on each PDF, likelihood probabilities are calculated with track-by-track basis, and unified into a final likelihood output. This likelihood calculation

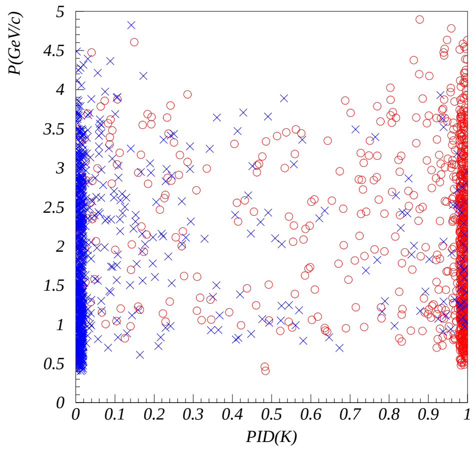

Figure A.2: Likelihood ratio $P(K/\pi)$ versus momenta for daughter tracks from $D^0 \to K^-\pi^+$ decays, tagged by the charge of the slow π^+'s. The open circles correspond to kaons and the cross-points to pions.

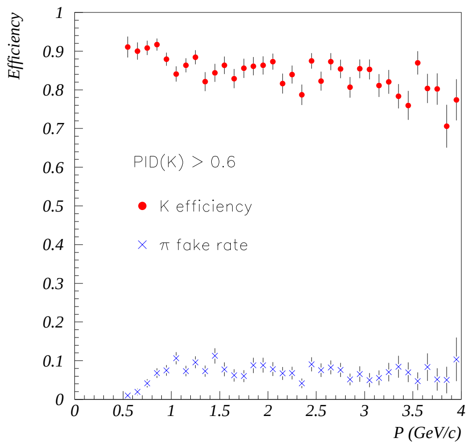

Figure A.3: K efficiency and π fake rate, measured with $D^{*+} \to D^0(K^-\pi^+) + \pi^+$ decays, for the barrel region. The likelihood ratio selection $P(K/\pi) \geq 0.6$ is applied.

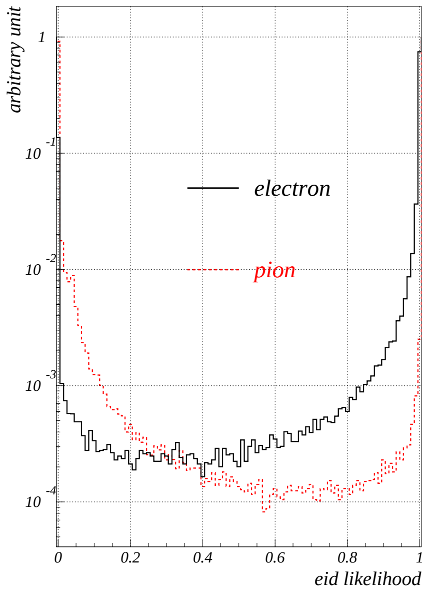

Figure A.4: Distribution of final unified discriminant to identify electrons. The solid histogram is for electrons in $e^+e^- \to e^+e^-e^+e^-$ events and the dashed one for charged pion.

is carried out taking into account the momentum and angular dependence. Figure A.4 shows the output from the above procedure. Closer to unity the particle is more likely to be an electron. The solid (dashed) histogram shows for $e^\pm$ in $e^+e^- \to e^+e^-e^+e^-$ data ($\pi^\pm$ in $K^0_S \to \pi^+\pi^-$ decays in data). The clear separation can be seen.

The efficiency and fake rate are displayed in Fig. A.5 using electrons in real $e^+e^- \to e^+e^-e^+e^-$ events for the efficiency measurement, and $K^0_S \to \pi^+\pi^-$ decays in real data for the fake rate evaluation. For momentum greater than 1 GeV/c, the electron identification efficiency is maintained to be above 90% while the fake rate to be around 0.2–0.3%.

A.3 Muon Identification

Muon identification [76] begins with the extrapolation of the track reconstructed in CDC, through the outer detectors. A track is considered to be within the KLM acceptance if it crosses at least one RPC layer: This requires at least 0.6 GeV/c of momentum. Then, associated RPC hits in KLM are searched. The outermost layer crossed by the extrapolated track defines the predicted range of the track assuming the track has no hadronic interaction with the materials. The actual

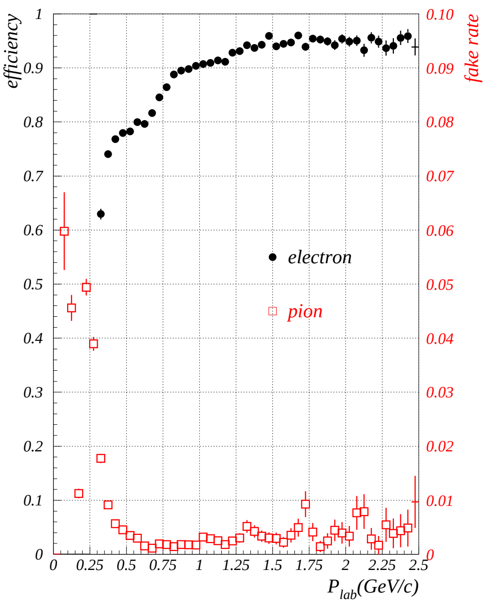

Figure A.5: Electron identification efficiency (circles) and fake rate for charged pions (squares). The different scales are used for the efficiency and fake rate.

range of the track is measured by the outermost layer with an associated RPC hit. The difference between the predicted and measured ranges and the goodness of fit of the transverse deviations of the associated hits from the extrapolated crossings provide the two variables used in a likelihood ratio to test the hypothesis that the track resembles a muon rather than a charged hadron.

Probability density distributions of two discriminant variables are constructed beforehand using simulated singletrack events containing a muon, pion, or kaon with measured chamber efficiencies. Then, the probability densities p_μ, p_π, and p_K for muons, pions, and kaons, respectively, are obtained from the distributions. We use the normalized muon likelihood

$$L_\mu = \frac{p_\mu}{p_\mu + p_\pi + p_K}, \tag{A.3}$$

for muon identification.

The measured efficiencies are shown as a function of momentum in Fig. A.6 for $L_\mu > 0.9$ and 0.1, for the KLM barrel only and for the entire KLM acceptance. The efficiencies have a plateau above 1.0 GeV/c. Some fraction of charged pions and kaons will be misidentified as muons. A sample of $K^0_S \to \pi^+\pi^-$ events in the e^+e^- collision data was used to determine this fake rate. The measured pion fake rates as a function of momentum are shown in Fig. A.7 for $L_\mu > 0.9$ (0.1), presented separately for the pions in the KLM barrel and those in the entire acceptance. The fake rates

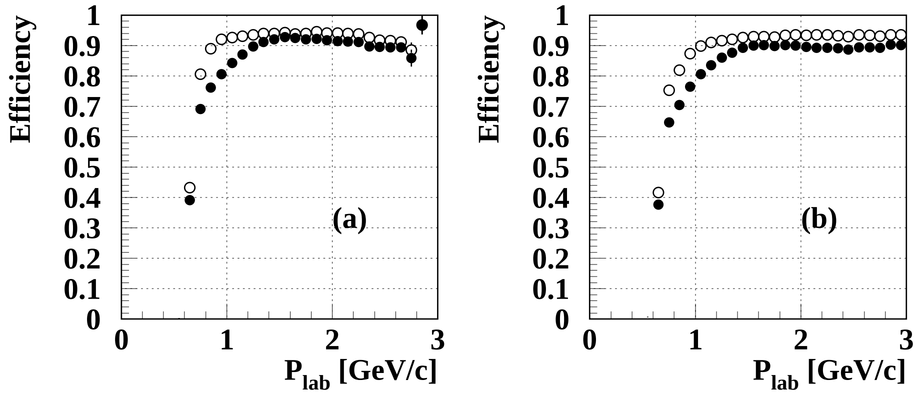

Figure A.6: Measured efficiency of muon identification as a function of momentum, measured by $e^+e^- \to e^+e^-\mu^+\mu^-$: (a) barrel ($51^\circ < \theta < 117^\circ$), (b) whole polar angle region ($25^\circ < \theta < 145^\circ$), for $L_\mu > 0.9$ (closed circles) and $L_\mu > 0.1$ (open circles).

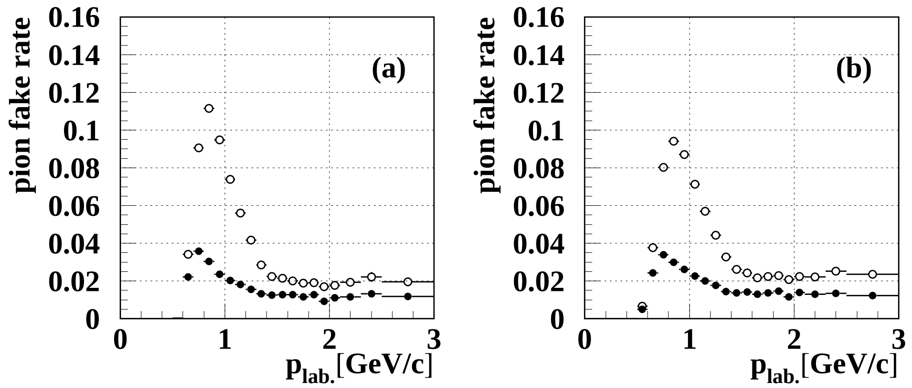

Figure A.7: Measured fake rate of pions versus momentum by $K_S^0 \to \pi^+\pi^-$: (a) barrel, (b) whole polar angle region, for $L_\mu > 0.9$ (closed circles) and $L_\mu > 0.1$ (open circles).

are approximately constant at momenta above 1.5 GeV/c. In the momentum region 1.5–3.0 GeV/c, we have a muon identification efficiency $\sim$ 90% with a fake rate of less than 5%.

Appendix B

IP Profile

The IP profile is calculated from the hadronic data sample and the information from the KEKB accelerator group.

First, the IP position is calculated event by event using hadronic data sample. Then, IP distribution is fitted with the three-dimensional Gaussian run by run. Finally, fit results are combined with the information from the accelerator and the parameters for the IP profile are determined.

B.1 Event-by-Event IP Reconstruction

Hadronic events are selected as described in Section 4.2. Initially, the IP position is calculated using all charged tracks. Then, the IP position is recalculated using only the tracks coming from the initial IP position. At least two SVD hits are required in both r-ϕ and z strips to ensure the good vertex resolution for the recalculation.

An example of the reconstructed IP distribution for a typical run is shown in Fig. B.1.

B.2 Fit for IP Distribution

The IP distribution for the run is fitted with three-dimensional Gaussian using the unbinned maximum likelihood method.

The axes of the Gaussian are not necessarily parallel to the detector axes. Since the electron beam is tilted 22 mrad from the z axis in the horizontal plane while the positron beam is parallel to the z axis, IP distribution is rotated at least around the y axis. In addition, the detector coordinate may be tilted from the beam axis. Considering this rotation, the IP profile coordinate (x', y', z') where the axes are parallel to the Gaussian axes and the origin is the mean point of the Gaussian,

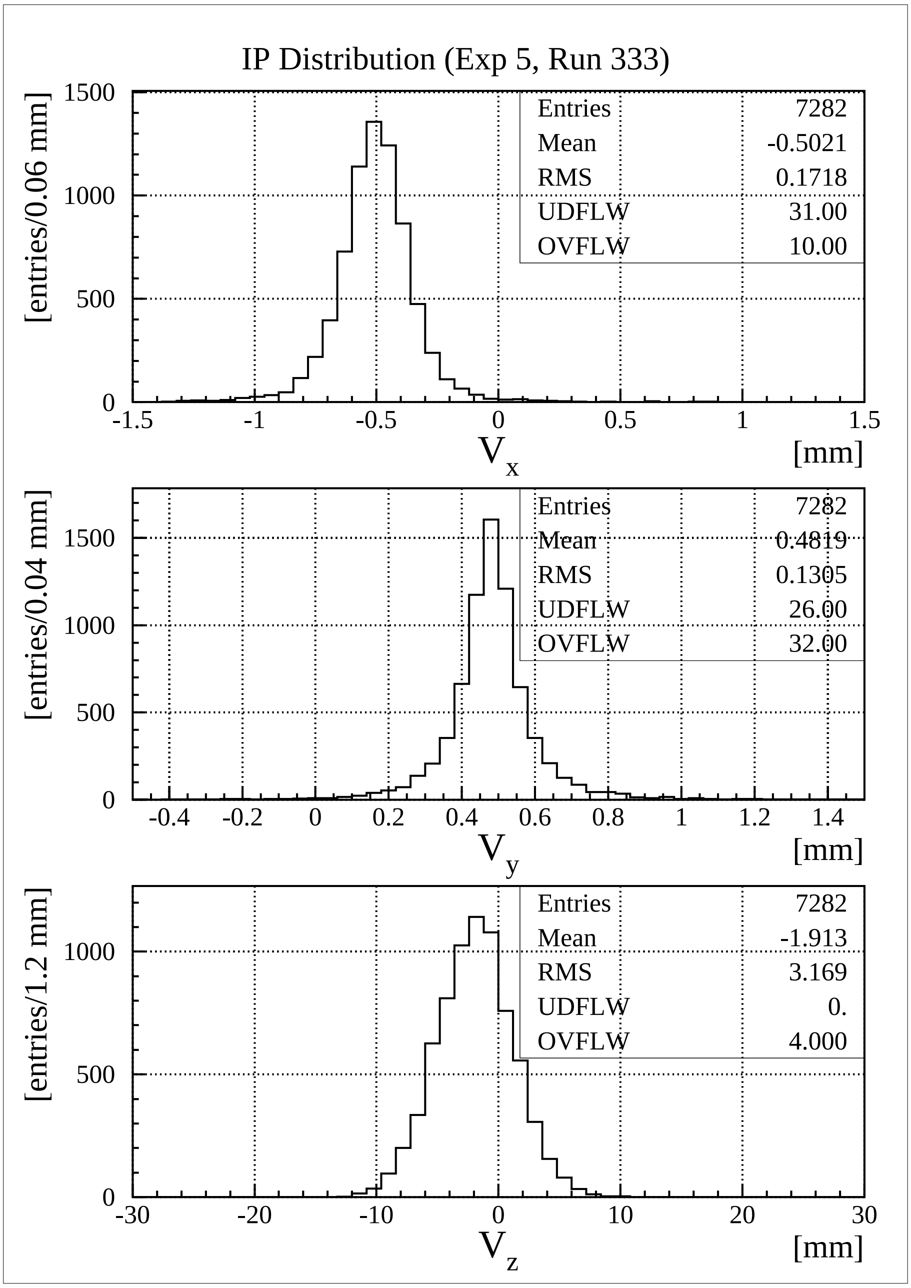

Figure B.1: Reconstructed IP distribution in x (top), y (middle), and z (bottom) for a typical run.

(μ_x, μ_y, μ_z), is defined. The transformation between the detector coordinate (x, y, z) and the IP profile coordinate (x', y', z') is defined as

$$\begin{pmatrix} x \\ y \\ z \end{pmatrix} = \mathbf{R}_z(\theta_z)\mathbf{R}_y(\theta_y)\mathbf{R}_x(\theta_x) \begin{pmatrix} x' \\ y' \\ z' \end{pmatrix} + \begin{pmatrix} \mu_x \\ \mu_y \\ \mu_z \end{pmatrix} \tag{B.1}$$

where $\mathbf{R}_i(\theta)$ is the rotation matrix around i axis with angle θ. Since the IP distribution has non-Gaussian tails in the x and y directions while it seems to be a single Gaussian in z as in Fig. B.1, a sum of two Gaussians with a same mean is used for the fit in x' and y' direction. The tail is considered to be due to mis-reconstructed events. The same value is used for the width of the wider Gaussian in x' and y'. The PDF becomes

$$\begin{aligned} \mathrm{PDF} = & \left[(1-f)\exp\left(-\frac{x'^2}{2\sigma_{x'}^2}\right) + f\exp\left(-\frac{x'^2}{2\sigma_{\mathrm{wide}}^2}\right)\right] \\ & \times \left[(1-f)\exp\left(-\frac{y'^2}{2\sigma_{y'}^2}\right) + f\exp\left(-\frac{y'^2}{2\sigma_{\mathrm{wide}}^2}\right)\right] \\ & \times \exp\left(-\frac{z'^2}{2\sigma_{z'}^2}\right), \end{aligned} \tag{B.2}$$

where $\sigma_{x'}$, $\sigma_{y'}$, and $\sigma_{z'}$ are the sizes of the IP distribution along the x', y', and z' axes, respectively, f is the fraction of the wider Gaussian, and σ_{wide} is the width of the wider Gaussian. Thus, the free parameters are μ_x, μ_y, μ_z, $\sigma_{x'}$, $\sigma_{y'}$, $\sigma_{z'}$, θ_x, θ_y, θ_z, f, and σ_{wide}. However, since $\sigma_{x'}$ and $\sigma_{y'}$ are on the same order while $\sigma_{z'}$ is far larger than them, it is difficult to determine the rotation around the z axis while the determination of the rotation around the x or y axis is just like a fit of a line and is easy. Therefore, if the number of events used for the fit is less than 10000, the rotation around the z axis is fixed to be 0.

The results of the fits for a certain range of runs are plotted on Fig. B.2.

However, we know that the mean IP position sometimes moves even during a run. To accommodate this variation, we fit the mean position with the other parameters (the widths and the rotation angles) fixed for every 60000 events [1].

B.3 Determination of IP Profile

Finally, the parameters of the IP profile are determined from the fit results described above and the information from the KEKB accelerator.

[1] From September 2001, we fit the mean position for every 10000 events.

(a) mean position

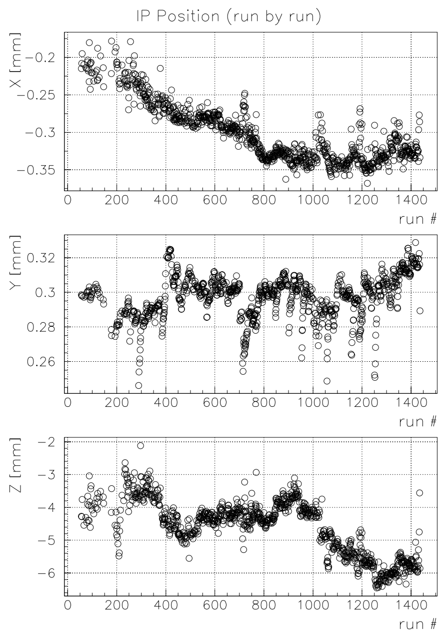

(b) width

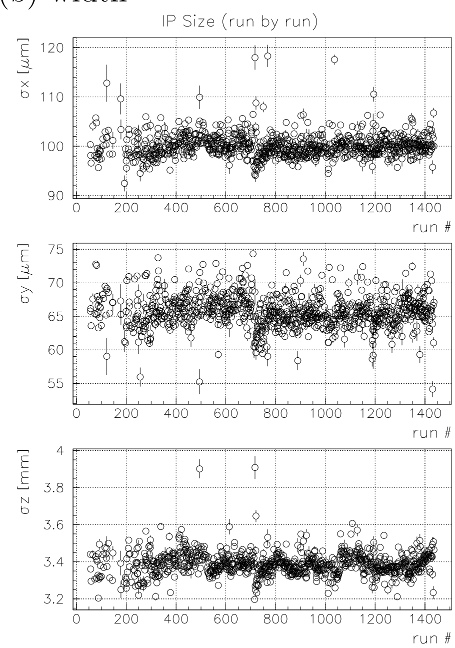

(c) rotation angle

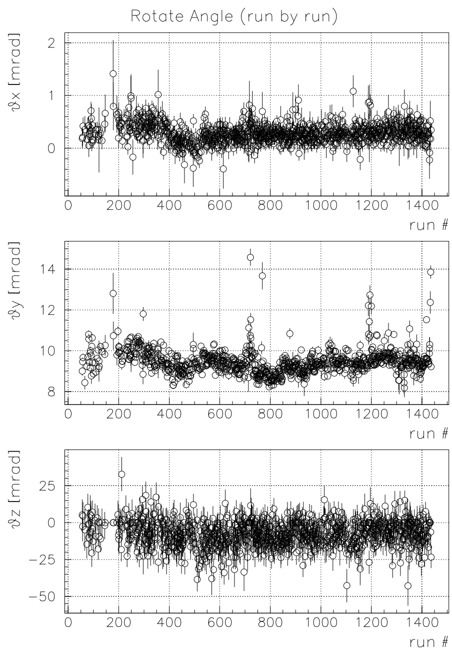

Figure B.2: Fit results of (a) the mean position, (b) the width, and (c) the rotation angle for a certain range of runs. Each figure contains the plots for x (top), y (middle), and z (bottom).

As Figure B.2 shows, the sizes of IP profile in x' and y' obtained from the fit are $\sigma_{x'} \sim 140\ \mu$m and $\sigma_{y'} \sim 80\ \mu$m. However, values expected from the designed parameters of the accelerator are $\sigma_{x'} \sim 80\ \mu$m and $\sigma_{y'} \sim 2\ \mu$m. This is due to the vertex resolution and the effect of the resolution must be removed.

Since the actual size in y is small enough, it is negligible with respect to the vertex resolution and the value of $\sigma_{y'}$ obtained from the fit can be regarded as the vertex resolution in r-ϕ. Therefore, the actual $\sigma_{x'}$ is obtained to be

$$\sigma_{x'} = \sqrt{\left(\sigma_{x'}^{\mathrm{fit}}\right)^2 - \left(\sigma_{y'}^{\mathrm{fit}}\right)^2}, \tag{B.3}$$

where the superscript "fit" means that it is the result of the fit.

To obtain the actual size of the IP profile in y', the information from the KEKB accelerator is used. The accelerator group measures beam sizes in x and y directions for HER and LER. The values at the times run starts and stops are averaged. These values are taken as the beam sizes of that run for both HER and LER. Then, the IP size in y' is calculated from the beam sizes of HER (σ_y^{HER}) and LER (σ_y^{LER}) as [77]

$$\sigma_{y'} = \frac{\sigma_y^{\mathrm{HER}} \sigma_y^{\mathrm{LER}}}{\sqrt{\sigma_y^{\mathrm{HER}\,2} + \sigma_y^{\mathrm{LER}\,2}}}. \tag{B.4}$$

In the z direction, the vertex resolution ($\sim 100\ \mu$m) is negligible since the size of the IP distribution is large ($\mathcal{O}(1\ \mathrm{mm})$). Therefore, no correction is applied.

Finally, the IP profile is obtained as the mean position calculated from the fit and the size of the distribution calculated from the widths of the three-dimensional Gaussian, its rotation angles, and the errors of the mean position.

References

[1] A. D. Sakharov, Pis'ma Zh. Eksp. Theor. Fiz. **5**, 32 (1967) [JETP Lett. **5**, 24 (1967)].

[2] J. H. Christenson, J. W. Cronin, V. L. Fitch, and R. Turlay, Phys. Rev. Lett. **13**, 138 (1964).

[3] M. Gell-Mann, Phys. Lett. **8**, 214 (1964).

[4] N. Cabibbo, Phys. Rev. Lett. **10**, 531 (1963).

[5] S. L. Glashow, J. Iliopoulos, and L. Maiani, Phys. Rev. D **2**, 1285 (1970).

[6] M. Kobayashi and T. Maskawa, Prog. Theor. Phys. **49**, 652 (1973).

[7] J. J. Aubert *et al.*, Phys. Rev. Lett. **33**, 1404 (1974); J. E. Augustin *et al.*, *ibid.* **33**, 1406 (1974).

[8] S. W. Herb *et al.*, Phys. Rev. Lett. **39**, 252 (1977).

[9] CDF Collaboration, F. Abe *et al.*, Phys. Rev. Lett. **74**, 2626 (1995); D0 Collaboration, S. Abachi *et al.*, *ibid.* **74**, 2632 (1995).

[10] A. B. Carter and A. I. Sanda, Phys. Rev. Lett. **45**, 952 (1980); Phys. Rev. D **23**, 1567 (1981); I. I. Bigi and A. I. Sanda, Nucl. Phys. **B193**, 85 (1981).

[11] D. Andrews *et al.*, Phys. Rev. Lett. **45**, 219 (1980); G. Finocchiaro *et al.*, *ibid.* **45**, 222 (1980).

[12] E. Fernandez *et al.*, Phys. Rev. Lett. **51**, 1022 (1983).

[13] ARGUS Collaboration, H. Albrecht *et al.*, Phys. Lett. B **192**, 245 (1987).

[14] L. Wolfenstein, Phys. Rev. Lett. **51**, 1945 (1983).

[15] A. J. Buras, M. E. Lautenbacher, and G. Ostermaier, Phys. Rev. D **50**, 3433 (1994).

[16] H. R. Quinn and A. I. Sanda, Eur. Phys. J. C **15**, 626 (2000).

[17] W. B. Atwood and J. A. Jaros, in *B* Decays, edited by S. Stone (World Scientific, Singapore, 1994), 2nd ed.

[18] I. I. Bigi, M. A. Shifman, and N. Uraltsev, Ann. Rev. Nucl. Part. Sci. **47**, 591 (1997).

[19] I. I. Y. Bigi *et al.*, in *B Decays*, edited by S. Stone (World Scientific, Singapore, 1994), 2nd ed.; M. Neubert and C. T. Sachrajda, Nucl. Phys. **B483**, 339 (1997).

[20] Particle Data Group, D. E. Groom *et al.*, Eur. Phys. J. C **15**, 1 (2000).

[21] H. Schröder, in *B Decays*, edited by S. Stone (World Scientific, Singapore, 1994), 2nd ed.

[22] A. Höcker, H. Lacker, S. Laplace, and F. Le Diberder, Eur. Phys. J. C **21**, 225 (2001) [`http://www.slac.stanford.edu/~laplace/ckmfitter.html`].

[23] N. Isgur and M. B. Wise, Phys. Lett. B **232**, 113 (1989); H. Georgi and F. Uchiyama, *ibid.* **238**, 395 (1990).

[24] KEK Report No. 2001-157, edited by E. Kikutani, 2001 [Nucl. Instrum. Methods Phys. Res. A. (to be published)].

[25] Belle Collaboration, A. Abashian *et al.*, Nucl. Instrum. Methods Phys. Res. Sect. A **479**, 117 (2002).

[26] G. Alimonti *et al.*, Nucl. Instrum. Methods Phys. Res. Sect. A **453**, 71 (2000).

[27] E. Nygård *et al.*, Nucl. Instrum. Methods Phys. Res. Sect. A **301**, 506 (1991): O. Toker *et al.*, *ibid.* **340**, 572 (1994).

[28] M. Yokoyama *et al.*, IEEE Trans. Nucl. Sci. **48**, 440 (2001).

[29] H. Hirano *et al.*, Nucl. Instrum. Methods Phys. Res. Sect. A **455**, 294 (2000); M. Akatsu *et al.*, *ibid.* **454**, 322 (2000).

[30] R. Früwirth, Nucl. Instrum. Methods Phys. Res. Sect. A **262**, 444 (1987); R. Harr, IEEE Trans. Nucl. Sci. **42**, 134 (1995).

[31] T. Iijima *et al.*, Nucl. Instrum. Methods Phys. Res. Sect. A **453**, 321 (2000).

[32] T. Iijima *et al.*, Nucl. Instrum. Methods Phys. Res. Sect. A **387**, 64 (1997).

[33] H. Kichimi *et al.*, Nucl. Instrum. Methods Phys. Res. Sect. A **453**, 315 (2000).

[34] H. Ikeda *et al.*, Nucl. Instrum. Methods Phys. Res. Sect. A **441**, 401 (2000).

[35] A. Abashian *et al.*, Nucl. Instrum. Methods Phys. Res. Sect. A **449**, 112 (2000).

[36] R. Santonico and R. Cardarelli, Nucl. Instrum. Methods**187**, 377 (1981); Yu. N. Pestov, Nucl. Instrum. Methods**196**, 45 (1982); R. Santonico, R. Cardarelli, A. Di Biagio, and A. Lucci, Nucl. Instrum. Methods Phys. Res. Sect. A **263**, 20 (1988); E. Gorini, Nucl. Phys. B Proc. Suppl. **23**, 249 (1991); L. Antoniazzi *et al.*, Nucl. Instrum. Methods Phys. Res. Sect. A **307**, 312 (1991).

[37] A. Yamaguchi, in *Proceedings of the Fourth International Workshop on Resistive Plate Chamber And Related Detectors: Applications In Partilc Physics And Astrophysics (RPC97), Naples, Italy, 1997*, p. 281.

[38] R. Akhmetshin *et al.*, Nucl. Instrum. Methods Phys. Res. Sect. A **455**, 324 (2000).

[39] Y. Makida *et al.*, Adv. Cryog. Eng. **37**, 401 (1991); **A43**, 221 (1998); H. Mukai *et al.*, in *Proceedings of the 15th International Conference on Magnet Technology (MT-15), Beijing, 1997*, edited by L. Lin, G. Shen, and L. Yan (Science Press, Beijing, 1998), p. 1044.

[40] Y. Ushiroda *et al.*, Nucl. Instrum. Methods Phys. Res. Sect. A **438**, 460 (1999).

[41] R. Itoh, Belle Note #161 (unpublished).

[42] The QQ B meson decay event generator was developed at the CLEO Collaboration [`http://www.lns.cornell.edu/public/CLEO/soft/QQ/`].

[43] D. J. Lange, Nucl. Instrum. Methods Phys. Res. Sect. A **462**, 152 (2001) [`http://www.slac.stanford.edu/~lange/EvtGen/`].

[44] CERN Program Library Long Writeup W5013, CERN, 1993.

[45] Belle Collaboration, K. Abe *et al.*, Phys. Rev. Lett. **87**, 091802 (2001).

[46] Belle Collaboration, K. Abe *et al.*, Phys. Rev. D **66**, 032007 (2002).

[47] B. C. K. Casey, Belle Note #390 (unpublished).

[48] G. C. Fox and S. Wolfram, Phys. Rev. Lett. **41**, 1581 (1978).

[49] J. Tanaka, Belle Note #193 (unpublished).

[50] F. Fang, Belle Note #323 (unpublished).

[51] M. Yokoyama, Ph.D. thesis, University of Tokyo, 2001.

[52] S. E. Vahsen, Belle Note #528 (unpublished).

[53] Belle Collaboration, K. Abe *et al.*, Phys. Rev. Lett. **88**, 171801 (2002).

[54] H. Cramér, *Mathematical Methods of Statictics* (Princeton Univ. Press, New Jersey, 1958).

[55] F. James and M. Roos, Comput. Phys. Commun. **10**, 343 (1975); F. James, CERN Program Library Logn Writeup D506, CERN, 1994.

[56] H. Tajima *et al.*(unpublished).

[57] ARGUS Collaboration, H. Albrecht *et al.*, Phys. Lett. B **241**, 278 (1990).

[58] Belle Collaboration, T. Tomura *et al.*, Phys. Lett. B **542**, 207 (2002).

[59] H. Kakuno, Belle Note #384 (unpublished).

[60] Belle Collaboration, K. Abe *et al.*, Phys. Rev. D **66**, 071102(R) (2002).

[61] Belle Collaboration, K. Abe *et al.*, Phys. Lett. B **538**, 11 (2002).

[62] I. Dunietz *et al.*, Phys. Rev. D **43**, 2193 (1991).

[63] H. Kakuno *et al.*(unpublished).

[64] Belle Collaboration, K. Hara *et al.*, Phys. Rev. Lett. **89**, 251803 (2002).

[65] Particle Data Group, K. Hagiwara *et al.*, Phys. Rev. D **66**, 010001 (2002).

[66] T. Skwarnicki, Ph.D. thesis, Institute for Nuclear Physics, Krakow, 1986.

[67] J. Tanaka, Belle Note #514 (unpublished).

[68] LEP B lifetimes working group, `http://lepbosc.web.cern.ch/LEPBOSC/lifetimes/lepblife.html` and references therein.

[69] Belle Collaboration, N. Hastings *et al.*, hep-ex/0212033 [submitted to Phys. Rev. D].

[70] D. Becirevic, in *High energy physics 2001*, proceedings of the International Europhysics Conference on High-Energy Physics (HEP 2001), Budapest, 2001, edited by D. Horvath, P. Levai, and A. Patkos (2001) [hep-ph/0110124].

[71] Working group on B oscillations,
`http://lepbosc.web.cern.ch/LEPBOSC/` and references therein.

[72] BaBar Collaboration, B. Aubert *et al.*, Phys. Rev. Lett. **89**, 201802 (2002).

[73] CDF Collaboration, T. Affolder *et al.*, Phys. Rev. D **61**, 072005 (2000); ALEPH Collaboration, R. Forty for the collaboration, in *B Physics and CP Violation*, proceedings of the Third International Conference on B Physiscs and CP Violation (BCONF99), Taipei, 1999, edited by H.-Y. Cheng and W.-S. Hou (World Scientific, Singapore, 2000), p. 121.

[74] KID Group, H. Hamasaki *et al.*, Belle Note #321 (unpublished).

[75] K. Hanagaki *et al.*, Nucl. Instrum. Methods Phys. Res. Sect. A **485**, 490 (2002).

[76] A. Abashian *et al.*, Nucl. Instrum. Methods Phys. Res. Sect. A **491**, 69 (2002).

[77] H. Yamamoto, Belle Note #269 (unpublished).